Experimental Implementations of Multidimensional Multi-photon States

By

Dr Andrea Tabacchini

A thesis submitted to Macquarie University
for the degree of Doctor of Philosophy
Department of Physics and Astronomy
August 2017

MACQUARIE
University
SYDNEY·AUSTRALIA

Typeset in LaTeX 2_{ε}.

Except where acknowledged in the customary manner, the material presented in this thesis is, to the best of my knowledge, original and has not been submitted in whole or part for a degree in any university.

Dr Andrea Tabacchini

To my grandma, Nonna Teresa.

Acknowledgements.

When I began the long path through the PhD, I couldn't imagine how hard the walk could be. General academic skills, both the technical and the soft ones, helps in the accomplishment of tasks. Developing strong ones is essential to get the workload done. However, I believe that in many cases - included mine, of course - the most difficult part is surviving the enormous pressure that may be associated with it. Yes, because the pressure can become stress, and the stress always obfuscate the perception of things.

The guide of my 3.5 years journey is A/Prof. Gabriel Molina-Terriza. He is one of the most brilliant (smartest?) persons I met. My esteem ain't limited to the academic sphere: he is also a great person on a personal layer, everybody knows it. I won't forget easily that time when he opened the door of his home to me, on a Sunday afternoon, during a hard personal moment during my first year.

I would have been impossible to even begin the PhD without the support of my family. Even from 16 thousands kilometers away I've never felt like they were far. They have been in fact very close to me. They suffered with me when I fell and enjoyed when I stood up again fulfilled by excitement.

The PhD takes and the PhD gives: it took the beautiful girlfriend I came with, it has given me a new wonderful one. To both of them goes my most sincere gratitude for the active support and trust in my abilities. Without you I couldn't have made it, this is for sure.

I still remember my first step on the ground of this beautiful land once known as *Terra Australis*. While I was excited for the new project I was about to undertake - both personal and academic - I was beginning it alone. I was the only friend of myself, but I knew that already before to arrive. What I didn't know, I couldn't imagine really, is that very soon I'd have run into wonderful people. To all of them go my many thanks, but to some of them - which I prefer not to mention here because I'd surely forget someone - goes something more than that: really they have been so passionate about my PhD. Thank you!

My gratitude also goes to the head of the department, prof. Mike Steel, as well as to the HDR A/dean Tracy Rushmer, for the trust placed in me when providing the financial support necessary to extend my candidature.

A final thanks to myself, who has never given up no matter what. I hope I'll never lose this very peculiar attitude of mine.

Personal outlook.

What follows here is a personal note regarding both the physical importance of the experiment that we've engineered and the experience of investigating many aspects of physics first hand. The main topic that I studied during my doctorate of research is, of course, Quantum Optics, and seeing Quantum Correlations in the states of light that we've been creating so often is a very fascinating experience. What I found even more fascinating, though, is seeing so many different aspects of physics playing a role, together, so harmoniously. Well established concepts of classical physics like conservation of energy and momentum work harmoniously together, very precise in selecting the modes that are phase matched within the non-linear crystal; Maxwell's equations of electromagnetism are flawless in describing the behaviour of collimated beams of both coherent and quantum light; the theory behind photoelectric effect rules the detection of light not caring whether those photons are "classical" or "quantum". Thinking about these - and other - concepts playing a role altogether in my little setup, blew my mind since the first tests that I've run. In this sense I feel like my PhD project hasn't been "just" *Experimental Implementation of Multidimensional Multi-photon States*, but rather an investigation of Physics as a whole: I've asked the Universe some specific new questions (the *innovative* part) using the well known still fascinating language of quantum optics and math behind it. This is what I consider the big progress of my PhD.

The present manuscript is the third thesis carrying my name. Now I can clearly see the whole process of accomplishing the PhD as a long path towards a personal growth under many aspects. Along the way, many times happened to me to feel like I had a good understanding of all the physical aspects involved in my investigations - whether that was the master degree thesis or the bachelor, or even just a hard exam. However, it has been only later that I realised how far I was, every time, from grasping those little - but at the same time fundamental - details. Writing this thesis I had the unique occasion to eventually shed light on them. Carrying with me a wide understanding of a relatively broad topic of research is perhaps the most relevant achievement, over and above a great personal triumph. I conquered it within four years of sorrows and joy, still uncountable hard work, which I'm glad prepared me at the best for my next appointment with Physics - in whatever form it will be.

A final note is about quantum mechanics, which has been driving my interests for so long. If one ain't astonished by the new paradigm of quantum mechanics, it certainly means that he/she didn't really understand it. And in fact I think that nobody on this Earth can possibly *understand* it. The quantum mechanical description of the Universe in which we live is so far from any possible everyday sensorial experience that I don't think one can honestly say to understand it. Quantum Mechanic is not something understandable, but rather something to be accepted. I'm honest person, I don't have any problem saying that I don't understand how can be that the spin of an electron is *at the same time* in state up *and* down. I can't even picture it in my mind!

This doesn't mean that I'm not fascinated by quantum mechanics. Actually, I can't stop being amazed every time I think about it, and personally I find by far more insightful the little details rather than the big pictures. An example discussed in this thesis (section 2.4) is the application of the Schmidt decomposition to the quantum information field. The final expression is so simple and at the same time so much loaded by quantum meaning!

Abstract.

I am a quantum engineer, but on Sundays I have principles.

John Stewart Bell

Multi-particle entangled states are becoming more and more interesting for different applications in quantum information, such as quantum multi-particle teleportation [1], entangled-based cryptography [2] [3] and quantum communication schemes based on multi-particle states [4], but also for fundamental reasons such as testing local realism by means of the Greenberger-Horne-Zeilinger states (GHZ) arguments [5] [6]. The advantage of multiparticle entanglement versus the most common two particle one lies in the fact that the greater the number of particles involved in the entangled state, the more clearly the quantum effects are exhibited. Our final goal is to exploit the multi-photon entangled states for quantum metrology. By the interaction of those states with nanostructures (mostly nanoholes, but in a future also nanospheres), we expect to reach sub-wavelength sensitivity phase measurements [7] [8] beating the Standard Quantum Limit [9] as well as to detect plasmonic effects.

In this thesis we present our work consisting on designing and building an experimental setup for the generation of states of 4-photon entangled in the transverse linear momentum. In the first part we explain some basics in the form of a technical introduction. We then adapt a general theoretical model to our particular case, explaining the physics of the process of generation of entangled states of photons. We proceed explaining the details of our setup, as well as the procedure of measurement. We then present the results of our tests in a "standard" 2-photon regime to show the correct functioning of the setup itself. Some more sophisticated measurements using structured light in the form of a first-order Hermite-Gaussian mode has been performed to generate entanglement in higher spatial modes are also presented. We conclude with theoretical and experimental details regarding the 4-photon experiments feasible with our setup.

Our source is based on Spontaneous Parametric Down-Conversion (SPDC). In the last two decades it has been extensively studied for the generation of two-photon entangled states, since Kwiat et al. published in 1995 the new scheme based on polarization entangled photons [10]. Most of the studies regarding entangled states involving more than two photons are indeed based on quantum correlations in the polarization [11] [12] or in the path of the down converted beams [13]. The great advantage of entangling a spatial degree of freedom (as we do) is related to the dimensionality of the Hilbert space in which the state is defined. In the particular case of linear momentum, which is a continuous variable, we are dealing with infinite dimensions. Since in each dimension of the state one quanta of information can be encoded, the advantage of having multidimension entanglement for the field of quantum communication and computing is clear.

The specs of our setup include a periodically-poled KTP crystals offering high conversion efficiency and cut for type-0 SPDC [14]. The photons generated are well known to be

inherently entangled in different degrees of freedom such as polarization, energy-time, linear momentum, and orbital angular momentum [15]. Since each single SPDC event generates one photon pair, in order to reach *four* photon we entangle two consecutive SPDC events per each state. Furthermore, it is possible to manipulate (to enhance) the dimensionality of the entanglement by properly tailoring the pump spatial profile.

The key point for the generation of four-photon entangled states is that, under some conditions, two consecutive pairs generated via SPDC cannot be described as two independent pairs but *necessarily* as a four-photon state showing genuine entanglement [11]. This can happen when using a pulsed laser to generate the entangled photons; in particular, in the regime in which the coherence time of the down-converted photons τ_c is (much) longer than the temporal length of the pumping pulse Δt [16]. In this condition the emission of a second pair is stimulated by the presence of the first one [16] [17]. That effect can be ultimately seen as a constructive multi-particle interference effect, the deep origin of which has to be sought in the boson statistic of photons [17].

Contributions.

We cannot teach people anything: we can only help them discover it within themselves.

Galileo Galilei

The contributions of the author and the collaborators are listed following the chronological flow of events.

The proposal of a source of 4-photon entangled states for nanophotonics experiment in a quantum regime belongs to A/Prof. Gabriel Molina-Terriza. The intuition of the need of entangled states in a spatial degree of freedom also belong to A/Prof. Molina-Terriza.

I entirely developed the design idea of the experimental setup. In particular, the need of using a very-short pulsed laser associated with a double-pass configuration and periodically-poled crystal. Those individual bits, taken individually, are of course not original: I have been inspired from several different papers read during the early stages of literature review.

The initial idea, very interesting indeed, of counting on entanglement in the Orbital Angular Momentum degree of freedom (later abandoned) belongs to the author and it has been inspired by the work of other members of the research group. We decided to take a turn only half way, after a research group in Europe had published a very similar investigation. The idea of the new direction undertaken belong as well to the author.

I found on the market all the components needed (apart from the lasers and few general purposes elements), some of which I needed to request to be customized according to the specs needed. All the purchasing have been processed by the author and founded by the ARC eQus budget of A/Prof. Molina-Terriza.

The practical building of the setup has been entirely carried on by me. In those stages, some useful technical discussions have been undertaken with Dr Mathieu Juan and Dr Xavier Vidal. I also calibrated and programmed the brand new Spatial Light Modulator and tested the setup in its different versions. Most of the data generated during the early stage tests is not presented in this thesis, but form a solid and necessary base for the experimental procedures implemented as described in this thesis.

The idea of investigating the spatial properties of entangled photons generated via structured light (ie, not Gaussian) belongs to A/Prof. Molina-Terriza. The experimental implementation of the setup has been carried on by the author with some initial help by Dr Alexander Büese.

The scripts powered by *LabView* needed to drive the different electronic devices on the setup (motorized rotational stages, Spatial Light Modulator, photon counter, saving of the raw data with some basic statistic) have been written by myself. The result is a fully automatized setup.

I developed the measurement protocols for the different experiments. Some of them have been update after discussions with A/Prof Molina-Terriza. All the measurements presented

here have been performed entirely by the author.

The analysis of the data, starting from the raw counts stored on **.txt* files by the *LabView* code that I created, to the final estimation of moments, correlations and entanglement witness, has been carried on entirely by the author. I wrote the several *MatLab* scripts necessary to analyse the raw data in different ways for different types of measurements, as well as to estimate the final uncertainties propagating the experimental errors.

Contents

List of Figures

List of Tables

1
Introduction.

Those who are not shocked when they first come across quantum theory cannot possibly have understood it.

Niels Bohr

The aim of this general introduction is to briefly address the motivations that drove us towards our goals. We want to explain why the topic that we investigated is important and what is so special about our own approaches.

1.1 Entanglement: the power of multidimensionality.

Quantum entanglement is the quintessence of quantum mechanics. Since its early stages of investigation it raised discussions among prominent physicists. The famous statement by Einstein defining the entanglement a *"spooky action at a distance"* is perhaps only one among the most famous comments on the topic. The *EPR paradox* (from the names of the authors, in order **E**instein A., **P**odosky B., and **R**osen N. [18]) embodies the skepticism around this property of a system. In that paper, published in 1935, EPR proposed a *gedanken* experiment that shows the contradiction between quantum mechanics (and the Heisenberg principle), and the common-sense assumption of *local-realism* [19]. This important assumption combines the idea that a system must have pre-existing values before and independently from any measurement (realism) with the constraints of the cause-effect principle to the speed of light (locality). In 1951 Bohm translated the paradox in a simpler form involving entanglement among two-level spin particles [20]. From Bohm's work, around 1965 John S. Bell derived the famous inequalities [21] [22] which have been then reformulated in an experimentally useful form in the work done by Clauser, Horne, Shimony, and Holt in 1969 [23]. The accepted conclusion is that quantum mechanics violates local-realism, in contradiction with the EPR assumption. On the other hand, there are compatible interpretations which are local, with uncertain outcomes, as well as other deterministic interpretations, favouring non-local behaviours.

Since then, the potentialities of quantum entanglement for fields such as (quantum) information and metrology have been seen as an important resource. Quantum communication schemes, for instance, heavily use entanglement as a resource [24]. Some of the most promising proposal for quantum computers also involve entanglement [25].

Entanglement has been therefore studied on different physical systems such as photons (the most recent record is led by Xi-Lin Wang et al. with a recent paper on the ArXiv demonstrating entanglement among *ten* photons [26]), ions [27] or superconducting circuits [28]. We restrict our research on photonic states.

One natural development direction to increase the impact of the engineered quantum systems is towards increasing the number of photons involved in the entangled system. In 2012 Yao et al. already demonstrated experimentally 8 entangled photons [29]. One needs at least three particles to demonstrate an "all-or-nothing" test of nonlocality [5, 6, 30]. In 2015 Chao Zhang et al. demonstrated for the first an "all-or-nothing" test of nonlocality with up to *six* photons [31]. Multipartite entanglement has been proven to be *necessary* for exponential speed-up of quantum algorithm versus classical ones (for Shor's algorithm in reference [32] as well as for Deutsch-Jozsa, Grover, and Simon algorithm in reference [33]).

Perhaps the easiest photonic degree of freedom to entangle is polarization: that's why most of the experiments in quantum optics focused on polarization entanglement. This limits the Hilbert space of the individual parties to $d = 2$. The amount of classical information storable *in each entity* is therefore only one bit. On the other hand, thanks to the phenomenon of quantum superposition which manifests when the state of a quantum system is described by a superposition of more than one discrete mode [34], a bidimensional Hilbert space can store what is called a quantum bit of information, or *qbit*.

Beyond the polarization degree of freedom, photons potentially carry a lot more information. Each of their degrees of freedom can be entangled. Therefore, another desirable direction for taking advantage from quantum entanglement is towards increasing the dimensionality of the Hilbert space. The power of dimensionality is already clear on one single particle: a three level one is enough to demonstrate quantum contextuality [35, 36].

Increasing the dimensionality leads to what is usually referred to as *multidimensional entanglement*, with many experiments recently exploring that direction [15, 37–41] [42]. In as early as 2006, for instance, Gröblacher et al. performed the first experimental verification of quantum key distribution with *qutrits* [43], increasing the encoding density as well as the security margin. Other studies demonstrating improved performances in quantum communication using multidimensional entanglement can be found in reference [44] and [45].

The final challenge is to merge multiparticle entanglement with multidimensionality, in other words to create multipartite systems prepared in entangled states involving multidimensional variables. One possible subfield of study is what is called asymmetric multiparticle entanglement [46] in which the dimensionality of each single entity involved in the entangled state can be different from each other. The first experimental demonstration has been published very recently on Nature Photonics [34], where Malik et al. also proposed a new kind of "layered" quantum communication protocol based on the states they generated.

Dealing with photons, the most convenient degrees of freedom for the encoding of multidimensional entanglement can be found perhaps in the spatial variables. For instance, in the just mentioned reference [34] the multidimensionality has been identified in the orbital angular momentum (OAM) of photons, which provides a discrete and unbounded state space [47]. Several experimental groups are investigating the applications of OAM entanglement. A very interesting experimental demonstration of entanglement of dimensionality up to $d = 11$

has been reported in 2001 by Dada et al. [48]. The record of dimensionality in OAM entanglement has been reported in [49], where the group leads by Anton Zeilinger created a biphoton state entangled in an Hilbert space of dimensionality 100×100.

In this brief literature review, we concentrate on photonic states. Most of the references cited in the previous paragraphs implicitly or explicitly rely on states generated via a process called *spontaneous parametric down conversion* (SPDC). Since the first proposal in 1995 by Kwiat et al. [10] of a new scheme for the generation of any of the four EPR-Bell entangled states, SPDC became quickly an affordable and easy to operate source of entangled photonic states. The process in its essence is fairly easy: one photon from a strong coherent field interacts with the atomic structure of a nonlinear crystal. With certain probability (very low, of the order of 10^{-10}) it can happen that one of the photons of the *pump* field undertakes *downconversion* into a pair of lower-energy photons. The process is probabilistic and happens respecting the fundamental laws of conservation of energy and momentum. As a consequence, the states of the two photons in each pair are entangled with each other in several degrees of freedom. Experiments showing quantum interference can easily highlight and confirm that the entanglement goes beyond classical concepts. The most typical test is in the form of violation of EPR-Bell inequalities.

However, despite many research groups investing energies in trying to understand the physics behind multiparticle multidimensional entanglement, there are still many unknowns regarding the generation and manipulation of entangled states of three or more photons when the dimensionality is higher than two [34]. For those systems that cannot be represented as qubits, the general structure of correlations is still quite obscure [46].

The work that we present here is directed in the investigation of exotic entanglement. In particular, we proceed with the analysis of multiparticle states entangled in the infinite-dimension domain of position and linear momentum. We produced those states via spontaneous parametric downconversion. Our contributions to the field are purely experimental. Within this thesis we describe the process of realisation of an optical setup for the generation of 4-photon entangled states in the transverse component of linear momentum. We designed and assembled a brand new apparatus ready for 4-photon states investigation. We tested it in the 2-photon regime, showing full control of spatial correlations. It is also versatile such that we can engineer many non-trivial two-photon states as we will show in the analysis of the results presented in chapters 4 and 5.

1.2 Chronology of our setup.

In April 2013 we started thinking how to engineer a source of 4-photon entangled states. The motivation was to use it for some nanophotonic experiments at that time already under investigation in our labs. The innovation would have been to use quantum light rather than classical lasers.

A first approach consisting in the development of a dedicated setup for the generation of two-photon entangled states began in parallel, around January 2013. That was the PhD project of Alexander Büese, which culminated in few interesting papers [50–52] (his PhD thesis: [53]).

The idea was to begin testing the nanophotonic setups with a standard source of 2-photon entangled states in polarization, while in parallel developing (from scratch) and testing the more complex source of 4-photon. Our *intuition* was twofold: first, scaling up the number of photons in the states would allows us to achieve novel quantum effects; second, we needed to

look at spatial entanglement to count on higher dimensionality.

The most challenging aspect lies in the fact that states produced by SPDC are in the form of *pairs* of photons. The single-pair events are quadratically more efficient than double-pair ones. Furthermore, among the double-pair emission there is a contribution due to independent pairs which does not lead to 4-photon entangled states, and a contribution due to stimulated emission which lead to states of highly correlated four photons [54].

From an experimental point of view there are also limitations. In a standard experimental setup, four-photon interferences due to consecutive pairs are usually very sporadic because of three common aspects of experimental SPDC: the conversion efficiency in common nonlinear crystals is quite low; the coherence time of a continuous wave (CW) laser usually employed to pump the crystal is very long; and the coherence length of downconverted photons is very short due to the broad spectrum characteristic of SPDC [55].

Our first approach to the 4-photon source was related to orbital angular momentum (OAM) entanglement. We performed a literature review from which we concluded that nobody had already published any work about 4-photon *OAM entangled* states from SPDC. Hence, we started designing the experimental proposal and presented it for the first time in December 2013 at the eQus[1] annual workshop.

A slightly refined version of the proposal was presented three months later in two international, peer reviewed conferences in Europe: at the *"Entanglement detection and quantification"* conference in Bilbao[2], and at the *Quantum Information and Measurement* OSA conference in Berlin (abstract available here: [56]).

The setup was based on a Titanium-Sapphire (Ti:Sap), femtosecond-pulsed laser as a pump, and on a double crystal configuration (Figure 1.1). We designed it such that the downconverted photons are phase-matched at non-degenerate frequencies; therefore we performed the separation of the two downconverted fields by using a dichroic mirror[3]. The nonlinear element was composed by two ppKTP crystals in a crossed configuration of the optical axes. The reason for the choice of a double-crystal configuration was that we wanted the entanglement to lie also in the polarization degree of freedom - as well as in the OAM. This implies that we had to account for the birefringence[4] of the nonlinear crystals, which means that we had to compensate for that delay effect. We also had to compensate for another temporal phase between signal and idler due to the wavelength dependence of refractive index associated to the non-degenerate configuration of our setup ($\lambda_s = 783nm$, $\lambda_i = 837nm$).

The standard manner to compensate such delays is by introducing on the path properly designed birefringent crystals. We needed two of them; we calculated the lengths required and we ordered two YVO_4 crystals (represented by the orange blocks in the setup in Figure 1.1). We eventually dropped the double-crystal configuration after we broke one of the crystals while mounting the setup; however, we also realised that this configuration was overcomplicating the setup, and the second crystal was in fact not essential for our purposes.

At the same conferences, especially at the OSA in Berlin, few other research groups proposed similar experimental apparatus such as the work presented by Wolfgang Löffler [57]. They found their way quicker than us and published the results on *Physical Review Letters* in February 2016 [58]. Another experiment going exactly in the same direction as our

[1] *eQus* stays for ***e**ngineered **Qu**antum **s**ystems*, and it is an ARC center of excellence. It has been the main founding subject (2013-2016) for the research presented in this thesis.

[2] Book of abstracts available here: *https://drive.google.com/file/d/0B0c3vCwp90arMk5OWU5pSTdKbjA/edit*

[3] A dichroic mirror (or beam splitter) is an optical component that reflects one range of wavelengths and transmits the rest.

[4] Birefringence is the property materials that have different refractive indexes (hence, different propagation velocities) for different polarizations of the propagating field.

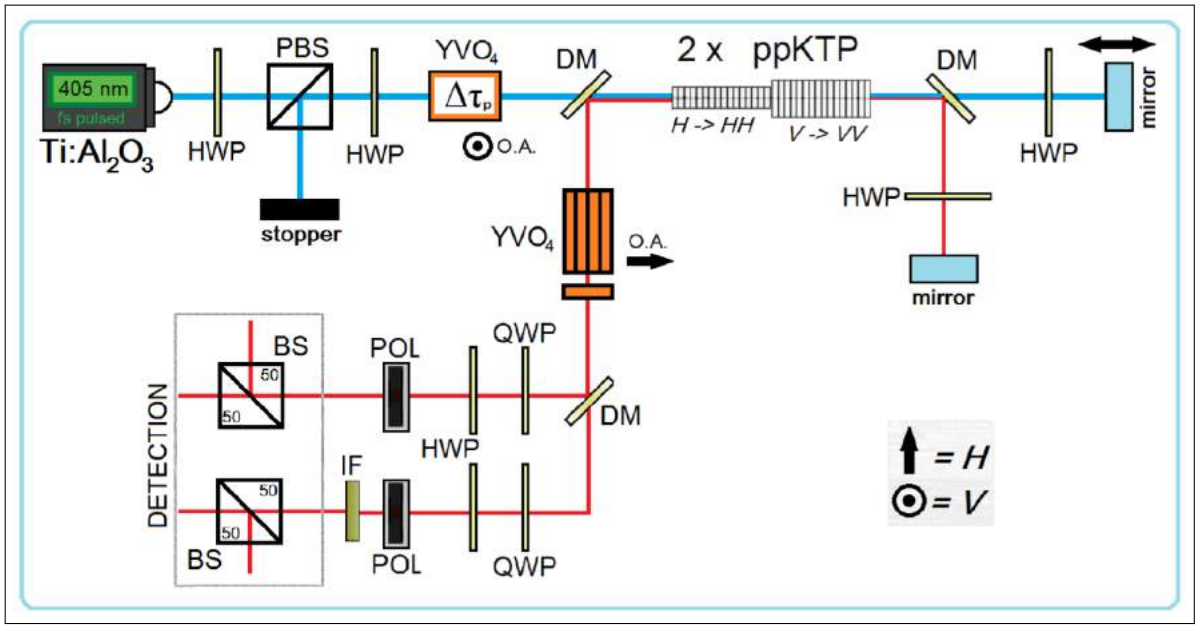

Figure 1.1: Sketch of the apparatus from the abstract presented at the *Quantum Information and Measurement* conference in Berlin, Germany, in March 2014 [56]. The same abstract has been submitted and presented the same month also at the *"Entanglement detection and quantification"* conference in Bilbao.

has been finished sooner and the authors published a letter on Nature Photonics in February 2016 [34].

While our setup was still unique in some experimental choices such as the double-pass configuration, we decided to slightly change also the final characteristics of the states from OAM to linear momentum entanglement. This would allow us to also explore the physics of continuous variables systems, while retaining the possibility of analysing OAM as well. We also included in the setup an innovative method for the detection of spatial correlations of downconverted fields using a spatial light modulator (SLM). The method, extensively explained in 5.1 theoretically and in 5.2 experimentally, had been recently and published by M. Hor-Meyll et al. in 2014 [59].

I presented our new proposal with a talk at the Australian Institute of Physics congress (AIP) 2014 held in Canberra (incorporating the Australian Optical Society Conference)[5].

Another small change in our experimental setup, this time due to a technical reason, regards the pump laser. Since our main goal has always been the generation of 4-photon states, we naturally started from the beginning aligning the setup with the pulsed laser[6]. When testing it with 2-photon states we had problems in measuring spatial correlations. In particular, the states did not show correlations at all. Therefore we decided to align also a CW, quasi-monochromatic laser, that we eventually utilized for all the experiments regarding the investigation of spatial correlations of 2-photon states.

[5]The abstracts can be found at: *http://aip2014.org.au/index.asp?IntCatId=14*.

[6]It is necessary only for the 4-photon experiments, while for the generation of 2-photon entangled states one can also use a CW.

1.3 Outline.

The structure of this thesis is thought to go along with the reader in the process of fully explaining the details of the experimental investigation undertaken during the course of my PhD. Reading through the chapters the reader will gain the necessary knowledge to grasp not only the big picture but particularly the details of the design and realization of the experimental setup. In particular, the manuscript is articulated as follows:

- In the first chapter after the introduction (chapter 2), we provide the mathematical model for the description of processes of Spontaneous Parametric Down Conversion (SPDC). We begin with a brief introduction for a general understanding of what spontaneous parametric down conversion is and what are the physical basic principles behind it. We then proceed working out the state of biphoton wavefunction from first principles. We explicitly account for approximations and comment them to show the high understanding of the topic needed to design our sophisticated setup. We then provide an overview of the discrete description of quantum states of light generated via SPDC in the case of continuous variable entanglement. We conclude with the study of entanglement criteria.

- Chapter 3 is where we describe the experimental aspects of SPDC. We begin with a brief overview to introduce the main components of a general setup; three important elements are examined extensively in subsections. We then proceed with the full, detailed description of our own experimental setup.

- In chapter 4 we explain our first method to measure spatial correlation both theoretically and experimentally. It concerns a double-raster performed by a Spatial Light Modulator (SLM). Results in the form of bidimensional spatial coincidence distribution are presented for four different configuration of the pump profile: Gaussian and first-order Hermite-Gaussian, both cases analysed with two different beam diameters. The final results, calculated from the spatial coincidences distribution, are the moments of the probability distribution describing the biphoton states produced by SPDC.

- In chapter 5 we describe an innovative method for the direct detection of the moments of the spatial probability distribution of biphoton states. We apply it to the standard case of Gaussian correlations as already done by Walborn et al. [59]; furthermore, we demonstrate its applicability to higher order correlations by analysing the spatial properties of photon pairs generated via SPDC with a first-order Hermite-Gaussian pump laser. In order to prove its reliability, we compare it with the more studied raster-scan method presented in the previous chapter. We also compare them with the theoretical predictions of our simulations. The experimental errors are thoroughly analysed.

- In chapter 6 we tackle the theory and experiment of 4-photon momentum entangled states from SPDC. More than an exhaustive analysis, it is a description of the state that we aim to generate proceeding from the theory of two photon states developed in chapter 2 and borrowing the discretization addressed in the section 2.4 of chapter

Spontaneous Parametric Down Conversion. The experimental setup described in section 6.2 is an improvement of the 2-photon setup. The differences are just few, but fundamental. Possible technical improvements to the experiment are also mentioned at the end of the chapter.

- In the Conclusions we summarize the work done and recall the most significative results and implications of our measurements.

2

Spontaneous Parametric Down Conversion.

I think I can safely say that nobody understands quantum mechanics.

Richard Phillip Feynman

Within this theoretical chapter we explore the process of Spontaneous Parametric Down Conversion (SPDC), from the basics to the deep analysis of the final quantum state. The analysis is based on a general pump laser spatial profile. It is then applied to the most standard case of Gaussian beam and to the more interesting one of first-order Hermite-Gaussian.

In the first part (section 2.1) we provide the adequate basis to understand the experiments from a theoretical point of view. We present the generalities of the process of spontaneous parametric down conversion (SPDC), which plays a central role in all our studies of spatial entanglement in photonic states.

We proceed concentrating on the theoretical model that describes the states of *two photons* produced by SPDC. First, we explain a general approach to the simpler case involving only Gaussian modes in section 2.2. Within its subsections, we work out the quantum state of SPDC from first principles (2.2.1 and 2.2.2). We then explain the important role played by approximations in section 2.2.3 and show the consequent final state in 2.2.4. This state refers to what is created at a certain position inside a nonlinear crystal. In order to provide some measurable predictions one needs to propagate the field from the source to the optical devices utilized for detection: we discuss that aspect in section 2.2.5. As a conclusion, in section 2.2.6 we present the useful exponential approximation of the *sinc* phase-matching function of the downconverted state.

The analysis of SPDC in this thesis is not limited to the most standard case of Gaussian modes. In section 2.3 we explore one case of higher order downconversion, consisting in employing structured light to generate the states. Such higher-order modes are relevant for our experimental conditions.

Sometimes it is convenient to describe the biphoton state on a discrete basis, even when the variables considered are continuous. How to do so, and why, is treated in 2.4, where few basic concepts of quantum information theory are introduced. A comparison between the

exotic case and the most standard one (Gaussian) follows in subsections 2.4.1, 2.4.2, 2.4.3, and 2.4.4.

In quantum mechanics an observable for the entanglement does not exists. Therefore, in most cases one has to rely on some entanglement witness in order to identify and/or quantify entanglement. A general criteria for continuous variable states is explained in section 2.5, where we derive a necessary and sufficient condition for negativity of the partial transposition (NPT), which in turn is a sufficient condition for entanglement. This condition uses the different moments of the photon distributions in real and Fourier spaces. It is then applied to the Gaussian pump case (section 2.5.1) and to the higher-order case (section 2.5.2). This will serve us as a motivation to implement the method in chapter 5.

2.1 Basics of SPDC.

SPDC is the physical phenomenon that we decided to take advantage of for engineering our sophisticated source of entangled states of light. In this section we give an overview of the process keeping a generic profile. In particular, we explain SPDC in the more intuitive and more generic case of *non-collinear* generation, even though our particular setup is optimized for *collinear* SPDC. At the end of this section the reader should have a clear idea of the physics behind SPDC in a non-linear crystal, as well as what can be achieved and what not using this technique.

Spontaneous Parametric Down Conversion is a process that belongs to the category of *three-wave mixing*. As the name suggests, it is a process involving three electromagnetic waves interacting within a crystal characterized by a particular crystalline structure. In particular, one photon of a strong coherent field (usually referred to as *pump* laser) occasionally decays in two lower-energy photons referred to as *signal* and *idler*[1]. The process happens respecting conservation of energy and momentum as indicated by figure 2.1.

There exist several varieties of SPDC, whose differences lie mainly in the kind of crystal and pump laser chosen, as well as in the characteristics of the resulting down-converted photons. However, all of them rely on the same parametric downconversion principle. A

[1]The tags "signal" and "idler" for the downconverted fields are due to historical reasons. They come from the classical counterpart of SPDC, where the nonlinear crystal is pumped not only with the pump laser but also with a "signal" beam. The goal there is to amplify the signal field through nonlinear processes happening within the crystal; the "idler" field in those experiment is often not-needed and hence discarded. While the origins of the two processes are conceptually different, the experimental similarities are clear.

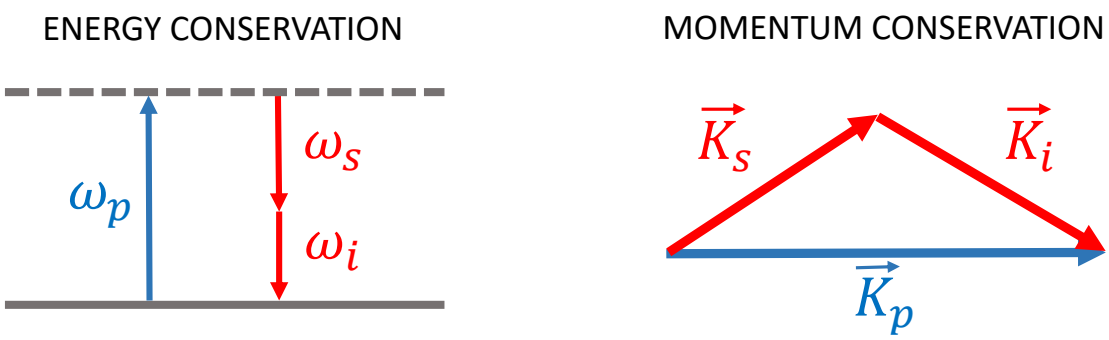

Figure 2.1: Representation of the conservation of energy (left) and linear momentum (right) in SPDC. The subscripts p, s, and i refer respectively to ***p**ump*, ***s**ignal*, and ***i**dler*.

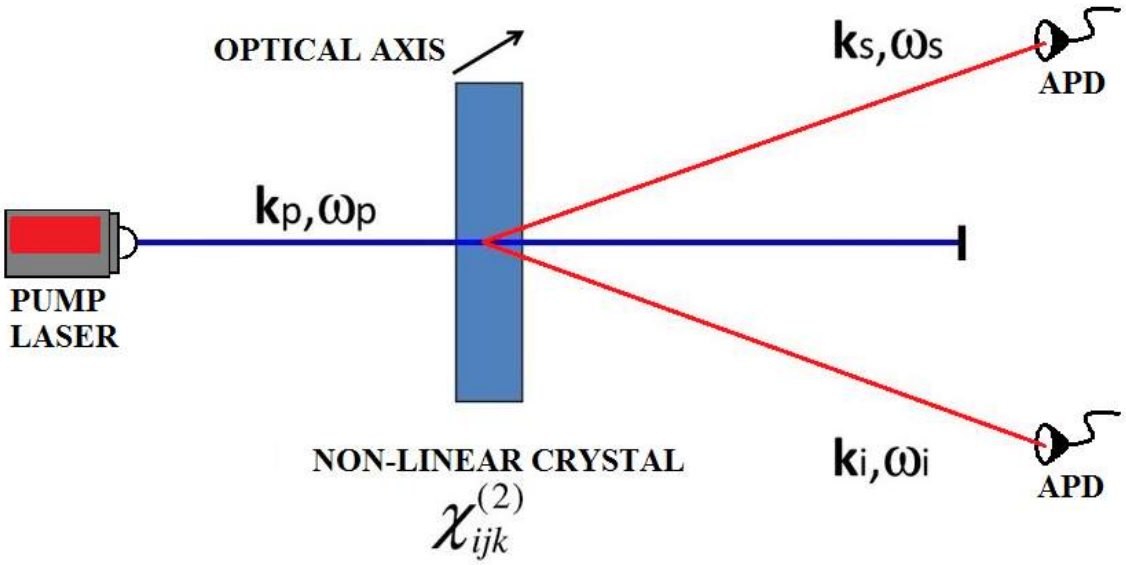

Figure 2.2: Simplified sketch to schematize a general process of SPDC. The (strong) pump laser is depicted in blue to indicate its higher frequency (typically in the near-UV); in red, the signal and idler lower energies down-converted beams. We label the nonlinear crystal with $\chi^{(2)_{ijk}}$ to indicate that the nonlinearity is of the second order in the susceptibility tensor. APD indicates ***A**valanche **P**hoto **D**iode*, which are the most commonly used instruments for single-photon detection. More details in the text.

general sketch to fix the idea is the one shown in figure 2.2.

The process of SPDC happens in *second order nonlinear crystals*; the nonlinearity lies in the susceptibility tensor, which in turn reflects in the nonlinearity of the polarizability vector. The latter is the physical quantity ultimately responsible for the interaction of light with matter. It can be shown that in some circumstances a second order nonlinearity in the polarizability vector implies the creation of two new fields when a strong enough pumping field interacts with the molecular structure of the material.

A strong electromagnetic field (a laser) is sent through a second-order nonlinear crystal (figure 2.2). Most of the power traverses the crystal with no interaction at all. However, if the laser is strong enough some of its photons can interact with the atomic structure of the crystal itself. The result can be the annihilation of one photon of the pump with emission of two photons respectively in the signal and idler modes. Although this process is forbidden classically in the absence of external noise, it is stimulated by the fluctuations of vacuum quantum states (virtual states). Through the interaction the state of the crystal is unchanged.

It can happen that one of the virtual states populated by vacuum fluctuations stimulates the emission of a pair of photons from the energy of one pump photon. Since the vacuum fluctuations are completely random, also the emission of pairs of photons is stochastic. This makes a deterministically description of SPDC impossible, and limits the process to be a probabilistic one. Consequently, there is no correlation between photons in successive pairs.

The sketch depicted in 2.2 is a two dimensional slice (say, the top view) of the complete picture. What really happens in the process of SPDC is that the two photons are not emitted on two fixed straight lines but rather over the surfaces of three-dimensional cones (figure 2.3). Spontaneous parametric down conversion can be classified by the polarization of the fields involved. In what is called *TYPE-II* SPDC, the two downvconverted photons are non-degenerate in the polarization d.o.f.. As a consequence, they are emitted over two cones whose vertices arise from the same generation point within the crystal. The cone axes are

symmetric relative to the direction of propagation of the pump beam only if signal and idler have the same wavelength. In *TYPE-0* and *TYPE-I* SPDC signal and idler are linearly polarized along the same direction, and the photons of each pair can propagate within the same cone (depending whether they are frequency degenerated or not).

Stimulated emission by vacuum fluctuations.

Vacuum fluctuations can be understood from the Heisenberg's principle written in the energy-time form [60] (English translation: [61]):

$$\delta E \delta t \geq \frac{\hbar}{2} \tag{2.1}$$

where $\hbar$ is the normalized Plank's constant, and δ represents the uncertainty of a variable. The importance of inequality 2.1 for what regards SPDC lies in the fact that conservation of energy can be violated by an amount δE provided that it happens for a time shorter or equal to δt.
The interpretation of this *quantum* non-conservation of energy is in the form of virtual states. An example of such states are the already mentioned *vacuum fluctuations*, which are fluctuations of the zero-energy (vacuum) state due to quick creation and annihilation of pairs of particle-antiparticle. This concept of vacuum fluctuations is applied to physical modelling in a whole range of fields (not only quantum optics). An interesting example can be found in the cosmological paper by Edward P. Tryon published on *Nature* in 1973, where he proposed the origin of the Universe as a fluctuation of a quantum vacuum state in the sense described above [62].

The general state generated via SPDC is what is called a *two-mode squeezed vacuum state* (containing only even terms since the photons are generated in pairs). We can approximate the 2-photon (4-photon) state considered as the first (the first two) term(s) of the complete two-mode squeezed vacuum. In general, squeezed states are a class of non-classical states of fundamental importance in quantum metrology.

The entire process of SPDC is fully described by a function of the polarization vector and linear momentum of pump, signal, and idler fields called *phase matching*. It comes from the non-complete fulfillment of the conservation of total linear momentum during the process of SPDC. Qualitatively speaking this can happen if we limit the three dimensional space to the volume of the nonlinear crystal. In Figure 2.4 we present a visual description of the linear momentum conservation equalities in the three dimensions. Given that the transversal cross section of the crystal is larger than the pump width (image on the left), we can mathematically extend the transversal sizes (x, y) of the crystal to infinity. As a result, within this approximation the transversal momentum will be conserved. On the other hand, the longitudinal momentum conservation is limited by the length of the crystal - which cannot be approximated to infinity in the z size (image on the right of Figure 2.4).

We can summarize the importance of the phase matching function saying that it accounts for the competition between conservation of *transverse* linear momentum and non-conservation of the *longitudinal* one. We will see that these two regimes can be controlled by one experimental parameter each, and the ratio between the two (parameters) can alone imply high values of entanglement [63].

What the phase matching function practically does is to select which modes of the

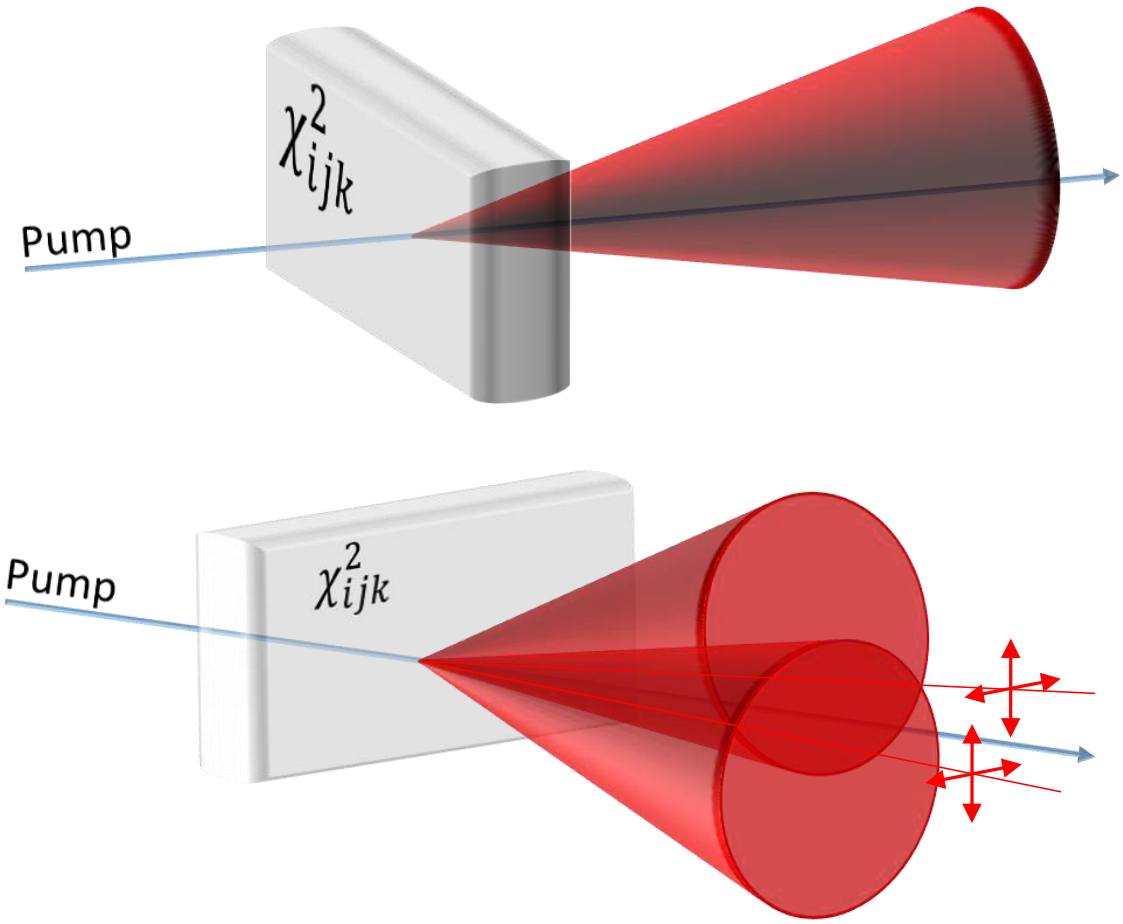

Figure 2.3: In TYPE-0 (and also TYPE-I) SPDC the photon pairs are generated over one single cone (sketch on the top figure). In the case of TYPE-II SPDC, the two photons of each pair are emitted on two cones which in general may or may not intersect.

downconverted electromagnetic fields are emitted efficiently via constructive interferences within the crystal. The selection has to satisfy, as said, the conservation of transverse momentum, and also the polarization constraint imposed by the geometry of the crystal. Different crystals or even same crystals cut in different ways[2], result in SPDC photons with different polarization. For the same reason, the orientation of the crystal can be a critical parameter for some schemes of SPDC. The procedure of tilting the angle in order to optimally satisfy the phase matching condition is called angle tuning.

The geometry of many nonlinear crystals used in SPDC is *uniaxial*; the term refers to the fact that for such crystals there is only one preferred axis. The presence of a preferred axis implies that there are two different refractive indexes within the crystal: ordinary or extraordinary. For instance, in negative uniaxial crystals a field propagating along the extraordinary direction feels a smaller refractive index than if propagating along the ordinary directions; this means that the beam travels at a faster group velocity ($v_g = c/n$, where c is the speed of light in vacuum and n is the refractive index in the material). Another implication is that for extraordinary waves the Poynting vector is not parallel to the propagation direction due to

[2]The cut of the nonlinear crystal here refers in particular to the angle between the optical axis of the crystal and the propagation direction of the pump laser - which is usually assumed to be perpendicular to the input face.

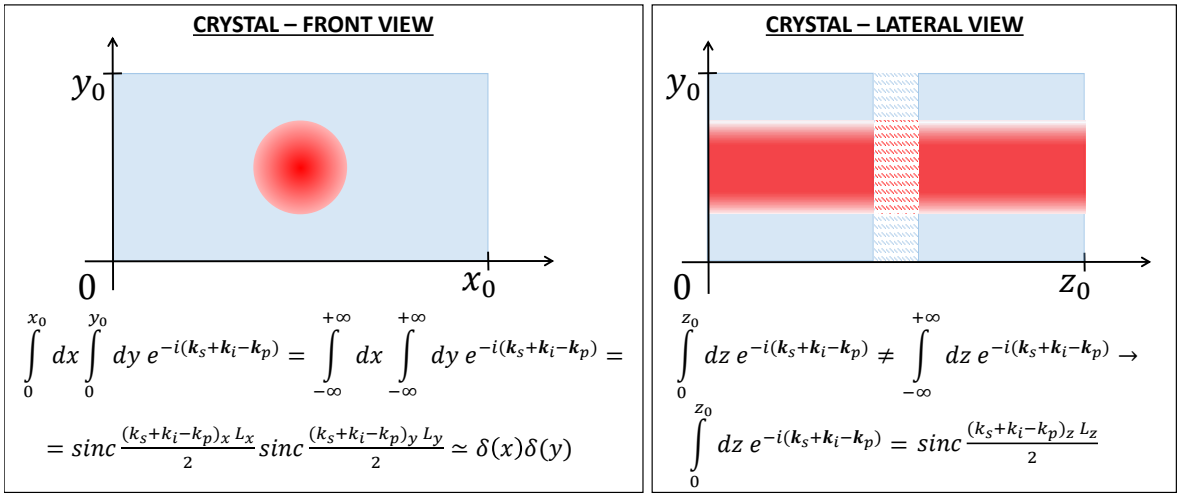

Figure 2.4: In the left figure is shown a front view of the nonlinear crystal (light blue) with the down converted beams in the middle. We can see that the entire beam is well confined within the x and y sizes of the crystal. As a consequence, for $L_x, L_y \gg w_p$ (where w_p is the pump waist) the two *sinc* approximate to a delta function (here we are not considering the spectral components in order to emphasize the spatial ones in the form of linear momentum). In the right hand figure is depicted the lateral view, with the fields propagating from left to right. It is clear why in this case the approximation is no longer valid.

the birefringence[3] of the crystal. This reflects in different propagation directions for ordinary and extraordinary waves, an effect usually referred to as transversal walk-off.

Because of the restrictions due to phase matching condition, the two photons of each pair generated via SPDC are in a state which can be inherently entangled in several degrees of freedom. Not only in polarization (already mentioned above), but also position, linear momentum, orbital angular momentum, photon number, and energy-time. Photons can also be entangled after their generation using, for instance, beam splitters. That procedure is possible for the polarization d.o.f. (certainly the most used d.o.f. in experimental entanglement of photonic states) and also in what is referred to as path entanglement.

With the work described in this thesis we explore other kinds of correlations: we are interested in entanglement in the spatial degrees of freedom. In particular, we generate signals and idlers which we will show being correlated in the emission position and anticorrelated in the transverse linear momentum. Those inherent correlations can result in entanglement, which needs to be detected and quantified with particular expedients.

Our experiments are based on a SPDC source of the kind TYPE-0 (all the photons are polarized along the same direction), wavelength non-degenerate (signal and idler have different central wavelengths: $\lambda_s = 783nm$, $\lambda_i = 837nm$). We use a $20mm$ long, periodically-poled Potassium titanyl-phosphate (ppKTP) nonlinear crystal, and we propagate along one of the optical axis. This way we minimize the distortion of the spatial properties of downconverted fields, that could raise due to the refractive indexes of the crystal being dependent on the angle between direction of propagation and optical axes.

[3]Birefringence is the property of anisotropic materials of having different refractive indeces for different polarizations of a field propagating through them.

2.2 Light-matter interaction in nonlinear crystals.

In this section we describe the full derivation, from first principles, of the biphoton wavefunction of photons generated via SPDC. The wavefunction fully characterizes the two-photon state for a given pump field distribution. Then, we will apply it to the most common case of Gaussian beam profile.

There exist many different approaches to the theoretical description of parametric down conversion (at this regard, see 2.4). In this section we follow the review paper by Walborn, Monken, P*á*dua, and Souto Ribeiro published in 2010 on Physics Reports [55]. They describe a fairly general approach which we adapt to our case. In particular, with our setup we do not create degenerate photons and the downconverted beams propagate collinearly. Also, some parts have been dropped, other expanded, and the nomenclature has been slightly changed. Walborn and co-workers in turn based their analysis on references [64] and [65]. We begin the modelling in a classical framework, and only at some point of the analysis we enter the quantum realm by quantising the electromagnetic fields.

Justification.

In the following section we derive the biphoton state produced by SPDC from first principles, that is starting from the interaction of an electromagnetic wave (the laser pump) with the atomic structure of a medium (the nonlinear crystal). Most of this analysis can be found in a few quantum optics books dealing with nonlinear interaction such as [66] or review papers such as [55]. We've chosen to include this detailed derivation here for three main reasons.

First of all, with the derivation of the state from first principles, passing through the mathematical approximations supported by their experimental justification, and landing with the final quantum state of SPDC, this thesis will be self consistent in this important aspect. Since the experimental setup is still in development, this thesis will be read by PhD students continuing the work there. They may have never seen this derivation, therefore we think it would be extremely useful for them to have everything in one place. In this sense, we could not find a suitable reference that satisfies the need of mathematical details and corresponding physical interpretations.

The second point we want to make here is the fact that we could not find a reference in which the derivation of the states with the characteristic of those that we generate in our experiment is described. The differences could be small, but sometimes meaningful. For instance, in the review paper from where we follow the structure of this section, the downconverted photons propagate at a certain angle with respect to each other, while in our case they are collinear. Furthermore, in their case they phase match degenerate frequencies for signal and idler while in our case we opted for non-degenerate.

Last, the notation can be sometimes a source of misunderstanding, especially when one has to compare analysis published by different authors on different journals/books. Our notation is slightly different from the one used in the principal reference and we justify those different choices along the way.

In conclusion, while this section can be skipped by the reader familiar with nonlinear interaction in the quantum regime, it is recommended for the reader who wants to understand the subtlety of the physics behind the generation of quantum light from classical electromagnetic waves.

2.2.1 The quantum operator of the Hamiltonian of interaction.

The description of light-matter interaction in dielectric materials, ultimately takes place with the effects of an applied electric field on the polarizability of the material. This is physically described by the *electric susceptibility* tensor $\tilde{\chi}$, which represents the mathematical proportionality between the *dielectric polarization density* $\vec{\mathbf{P}}$ and the applied electric field $\vec{\mathbf{E}}$ in a given dielectric medium. In general, the electric susceptibility is a tensor (which we indicate with a tilde in order to distinguish it from a vector). Its tensorial components reflect the characteristics of the material (which may be non-centrosymmetric) responsible for the interaction at a molecular scale. In vectorial formalism:

$$\vec{\mathbf{P}} = \epsilon_0 \tilde{\chi} \vec{\mathbf{E}} \tag{2.2}$$

The proportionality parameter is the electric permittivity of free space ϵ_0 (which is a constant).

Equation 2.2 implies that an electric field $\vec{\mathbf{E}}$ travelling through a medium characterized by susceptibility $\tilde{\chi}$ has the effect of polarizing the medium itself in a direction given by the incident electric field.

If the applied electric field is strong enough, the atomic transition modelled by the polarizability can reach a saturation level on other nonlinear effects [67]; this can be modelled by adding a nonlinear susceptibility [55] in the expression of $\vec{\mathbf{P}}$. For that reason, the dielectric polarization density is often modelled as a Taylor expansion which leads to terms that are nonlinear in χ as well as in the electric field [66, 68]:

$$P_i \simeq \epsilon_0 \left(\sum_j \chi^{(1)}_{ij} E_j + \sum_{jk} \chi^{(2)}_{ijk} E_j E_k + \sum_{jkl} \chi^{(3)}_{ijkl} E_j E_k E_l \right) \tag{2.3}$$

where with the subscripts of E we refer to different electric fields, that is to different components of the *total* electric field.

In some situations, some nonlinear terms can be dropped due to a symmetry argument. Any system, including bulk materials, that do not change under parity inversion are known as *centrosymmetric*. Both the polarizability $\vec{\mathbf{P}}$ and the single electric fields E_j, E_k, E_l, ..., because of their vectorial nature, are *not* invariant under spatial inversion, but rather acquire a minus sign. This makes clear that for respecting the parity inversion in centrosymmetric medium, the Taylor expansion of the the polarizability 2.3 must consist only of odd terms [67]. However, many systems such as anisotropic molecules and many forms of crystal, are not invariant under parity inversion. We refer to them as *noncentrosymmetric* systems. Hence, eq. 2.3 can (and actually in the case of noncentrosymmetric materials *has to*) include also even terms.

Therefore, while for centrosymmetric materials the first nonlinear term is the third, for non-centrosymmetric crystals the biggest contribution in the nonlinearity of the polarizability vector occurs in the second order. For that reason we can limit the Taylor expansion to the second term. Note that since we are describing a parametric process characterized by no losses and no dispersion (as an approximation), by definition the susceptibility is real [66].

The linear term in eq 2.3 represents a sum of the effects of all the components j of the total electric field (mediated by the first-order susceptibility tensor $\chi^{(1)}_{ij}$); the second-order nonlinear term involves the sum of the effects of pairs of electric fields j, k multiplied together (through $\chi^{(2)}_{ijk}$); the third-order nonlinear term involves three components of the electric field and so on.

The important remark here is that while the linear term implies (through P_i) an induced oscillation of the linear polarization at (only) the same frequency of the incident field, the non-linear terms allow for the induction of oscillating polarizations in more "new" frequencies [67]. Thus, while in the presence of a first-order susceptibility the effect on an electric field is limited to a modification of its free-space propagation (due to the atomic structure of the medium), in the case of nonlinear terms it is more complicated.

In particular, the term containing the second order susceptibility tensor is responsible for two-photon emission. The fundamental reason is indeed the fact that the second order term involves the interaction of one component of an input electric field E_i with one component of each of *two* further electric fields E_j and E_k (at different frequencies). Hence, from here on we will focus only on the second order nonlinear term.

Multiplication of more than one component of the electric field $E_j, E_k, etc.$ is responsible for the new frequencies mentioned above. For instance, in the case of the first non-linear term there is an explicit multiplication between *two* components of the total electric field. Considering a field made only by two frequencies constituents: $E(t) = A(\omega_1)\exp[-i\omega_1 t] + A(\omega_2)\exp[-i\omega_2 t] + c.c.$, the multiplication between two electric fields j, k results in:

$$\begin{aligned} E^2 = & [A(\omega_1)A^*(\omega_1) + A(\omega_2)A^*(\omega_2)]e^{-i(0)t} \\ & + [A^2(\omega_1)A^2(\omega_1)]e^{-i(2\omega_1)t} \\ & + [A^2(\omega_2)A^2(\omega_2)]e^{-i(2\omega_2)t} \\ & + 2[A(\omega_1)A(\omega_2)]e^{-i(\omega_1+\omega_2)t} \\ & + 2[A(\omega_1)A^*(\omega_2)]e^{-i(\omega_1-\omega_2)t} \\ & + c.c. \end{aligned} \tag{2.4}$$

From equation 2.4 we can conclude that the second-order nonlinear term in 2.3 allows for a total electric field composed by five new frequencies. In turn, the physical meaning of those oscillating polarizations is that they act as sources of electromagnetic waves at the (new) frequencies which may not be present in the incident field [67].

The nonlinear processes that describe the generation of the five new fields as expressed in 2.4 are known with the name of: optical rectification ($exp[-i(0)t]$), second harmonic generation ($exp[-i(2\omega_1)t]$ and $exp[-i(2\omega_2)t]$), sum frequency generation ($exp[-i(\omega_1 + \omega_2)t]$), and difference frequency generation($exp[-i(\omega_1 - \omega_2)t]$). Spontaneous Parametric Down Conversion (SPDC) is a particular case of sum frequency generation. Which process happens within the nonlinear crystal is selected by the phase-matching conditions and other crystal parameters.

Considering explicitly the temporal and spatial dependence of the fields involved, and integrating over the time of interaction of the field with the medium, the polarization density vector reads as [69], [70]:

$$\begin{aligned} P_i(\vec{\mathbf{r}}, t) = & \epsilon_0 \int_{-\infty}^{0} dt^{'} \chi_{ij}^{(1)}(t^{'} - t)E_j(\vec{\mathbf{r}}, t^{'}) + \\ & + \int_{-\infty}^{0} dt^{'} \int_{-\infty}^{0} dt^{''} \chi_{ijk}^{(2)}(t^{'} - t, t^{''} - t)E_j(\vec{\mathbf{r}}, t^{'})E_k(\vec{\mathbf{r}}, t^{''}) \end{aligned} \tag{2.5}$$

where ϵ_0 is the free space electrical permittivity, $\chi_{ij}^{(1)}$ and $\chi_{ijk}^{(2)}$ are respectively the first and the second order susceptibility tensors. The temporal integrals are evaluated from $-\infty$ to 0

meaning that for calculating the total effect of the electric field $\vec{\mathbf{E}}(\vec{\mathbf{r}}, t)$ on the polarizability vector $\vec{\mathbf{P}}(\vec{\mathbf{r}}, t)$ at time t, one needs to consider the contributions of the electric field from all the past moments, that is from $t = -\infty$ to the actual time of evaluation. In eq. 2.5, the summation over j and k is implicitly assumed.

The interaction of the light field within the crystal can be described with a Hamiltonian [71]:

$$H(t) = \frac{1}{2}\int_V d\vec{\mathbf{r}}[\vec{\mathbf{D}}(\vec{\mathbf{r}}, t) \cdot \vec{\mathbf{E}}(\vec{\mathbf{r}}, t) + \vec{\mathbf{B}}(\vec{\mathbf{r}}, t) \cdot \vec{\mathbf{H}}(\vec{\mathbf{r}}, t)] \tag{2.6}$$

where $\vec{\mathbf{D}}$ is the displacement vector, $\vec{\mathbf{B}}$ is the magnetic induction vector, and $\vec{\mathbf{H}}$ is the magnetic field vector. This is the classical expression from Maxwell's equations; but Hamiltonian will allows us to explore the evolution in the quantum regime. Notice also that all the necessary information about the crystal are provided by the tensor $\tilde{\chi}$, then we can isolate the nonlinear interaction term in the following way:

$$\vec{\mathbf{D}}(\vec{\mathbf{r}}, t) = \epsilon_0 \vec{\mathbf{E}}(\vec{\mathbf{r}}, t) + \vec{\mathbf{P}}(\vec{\mathbf{r}}, t) \Rightarrow H(t) = H_0(t) + H_{NL}(t) \tag{2.7}$$

According to the definition of the polarization vector given in equation 2.5, $H_0(t)$ contains the interaction of the applied field with the first order term of P_i, while in our notation we named $H_{NL}(t)$ the (second order) nonlinear interaction Hamiltonian. The latter explicitly reads as:

$$\begin{aligned} H_{NL}(t) &= \frac{1}{2}\int_V dr \vec{\mathbf{E}}(\vec{\mathbf{r}}, t) \cdot \vec{\mathbf{P}}_{NL}(\vec{\mathbf{r}}, t) \\ &= \frac{1}{2}\int_V d\vec{\mathbf{r}} \int_0^\infty dt' \int_0^\infty dt'' \chi^{(2)}_{ijk} E_i(\vec{\mathbf{r}}, t) E_j(\vec{\mathbf{r}}, t - t') E_k(\vec{\mathbf{r}}, t - t'') \end{aligned} \tag{2.8}$$

Since we want to reach an expression in the formalism of quantum operators, it is useful to expand the (classical) electric field vector in sum of positive and negative frequencies:

$$\vec{\mathbf{E}}(\vec{\mathbf{r}}, t) = \vec{\mathbf{E}}^+(\vec{\mathbf{r}}, t) + \vec{\mathbf{E}}^-(\vec{\mathbf{r}}, t) \tag{2.9}$$

where: $\vec{\mathbf{E}}^+(\vec{\mathbf{r}}, t) = [\vec{\mathbf{E}}^-(\vec{\mathbf{r}}, t)]^*$ are complex conjugated plane waves defined as:

$$\vec{\mathbf{E}}^+(\vec{\mathbf{r}}, t) = \frac{1}{\sqrt{v}} \sum_{\vec{\mathbf{k}}, \sigma} e_{\vec{\mathbf{k}}, \sigma} \varepsilon_{\vec{\mathbf{k}}, \sigma} \alpha_{\vec{\mathbf{k}}, \sigma} e^{i(\vec{\mathbf{k}} \cdot \vec{\mathbf{r}} - \omega(k, \sigma)t)} \tag{2.10}$$

$$\varepsilon_{\vec{\mathbf{k}}, \sigma} = \sqrt{\frac{\hbar \omega(k, \sigma)}{2\epsilon_0 n^2(\vec{\mathbf{k}}, \sigma)}} \tag{2.11}$$

where v is the quantization volume, $\vec{\mathbf{e}}_{\vec{\mathbf{k}}, \sigma}$ is the bidimensional polarization vector, $\vec{\mathbf{k}}$ is the wave vector, ω is the angular frequency (the dependence of the angular frequency on k and σ will be implicitly assumed), $\alpha_{k,\sigma}$ is the mode amplitude, $n(\vec{\mathbf{k}}, \sigma)$ is the linear refractive index of the anisotropic medium, and $\varepsilon_{\vec{\mathbf{k}}, \sigma}$ is the energy associated with the electromagnetic mode identified by $(\vec{\mathbf{k}}, \sigma)$. The sum over all possible orthogonal components of polarization directions in the (bidimensional) plane orthogonal to the propagation direction of the incident field, is explicitly accounted by the index σ; at the same time, $\vec{\mathbf{k}}$ is summed over all the possible wave vectors.

One can add an extra term to 2.10, as it is done in [55], which models an interference filter. In doing so, one has to be careful to consider it as the transmission function expressed in *amplitude* rather than intensity. We have decided not to include it here, because it might generate a physical inconsistency in the normalization. The argument is basic but meaningful. The normalised classical Hamiltonian of an electromagnetic field in a vacuum volume V reads as:

$$H = \frac{1}{2}\epsilon_0 \int_V d^3\vec{\mathbf{r}}(|E(\vec{\mathbf{r}},t)|^2 + c^2|B(\vec{\mathbf{r}},t)|^2) \tag{2.12}$$

where $E(\vec{\mathbf{r}},t)$ is the electric field, $B(\vec{\mathbf{r}},t)$ is the magnetic induction, and c is the speed of light. The physical meaning of the Hamiltonian is the total energy of a given system. From eq. 2.12 it is easy to deduct that in order for the meaning of total energy to be appropriate, the integral has to be evaluated over all the components of the electric field. Including a spectral filter $G(\omega)$ in the definition of electric field itself is dangerous in the sense that it would select only a range of modes from the entire spectrum (with the consequence that some of the $\varepsilon_{\vec{\mathbf{k}},\sigma}$ in 2.10 would not contributes to the electric field). The meaning of the integral in 2.12 then would change and such Hamiltonian would not represent the total energy anymore. Of course this effect can be accounted for by an appropriate normalization procedure. However, since we think that for the non-expert reader it could be confusing or misleading, we prefer to avoid to include the function of the spectral function until when needed.

The quantization of the electric field amplitude is ultimately obtained by interpreting the mode amplitudes of the plane wave components of the (classical) field with quanta of light, that is with the creation of single photon entities. The standard way to proceed is by the following substitution: $\alpha_{\vec{\mathbf{k}},\sigma} = \hat{\mathbf{a}}_{\vec{\mathbf{k}},\sigma}$, where $\hat{\mathbf{a}}_{\vec{\mathbf{k}},\sigma}$ is now an operator which represents the annihilation of a single photon in the mode described by the subscripts $(\vec{\mathbf{k}},\sigma)$.

$$\vec{\mathbf{E}}^{+}(\vec{\mathbf{r}},t) \rightarrow \hat{\mathbf{E}}^{+}(\vec{\mathbf{r}},t) = \frac{1}{\sqrt{v}} \sum_{\vec{\mathbf{k}},\sigma} \vec{\mathbf{e}}_{\vec{\mathbf{k}},\sigma}\varepsilon_{\vec{\mathbf{k}},\sigma}\hat{\mathbf{a}}_{\vec{\mathbf{k}},\sigma}e^{i(\vec{\mathbf{k}}\cdot\vec{\mathbf{r}}-\omega t)} \tag{2.13}$$

$$\hat{\mathbf{E}}^{+}(\vec{\mathbf{r}},t) = [\hat{\mathbf{E}}^{-}(\vec{\mathbf{r}},t)]^{\dagger} \tag{2.14}$$

By substituting 2.13 in 2.10 and 2.10, and in turn the result in the nonlinear hamiltonian 2.8, we obtain a *quantum operator* for the nonlinear Hamiltonian:

$$\hat{\mathbf{H}}_{NL} = \frac{1}{2\sqrt{V^{3/2}}} \sum_{\vec{\mathbf{k}}_s\sigma_s} \sum_{\vec{\mathbf{k}}_i\sigma_i} \sum_{\vec{\mathbf{k}}_p\sigma_p} g^{*}_{\vec{\mathbf{k}}_s\sigma_s} g^{*}_{\vec{\mathbf{k}}_i\sigma_i} g_{\vec{\mathbf{k}}_p\sigma_p} \hat{\mathbf{a}}^{\dagger}_{\vec{\mathbf{k}}_s\sigma_s} \hat{\mathbf{a}}^{\dagger}_{\vec{\mathbf{k}}_i\sigma_i} \hat{\mathbf{a}}_{\vec{\mathbf{k}}_p\sigma_p} e^{i(\omega_s+\omega_i-\omega_p)t}$$
$$\times \chi_{ijk}(\vec{\mathbf{e}}_{\vec{\mathbf{k}}_s\sigma_s})^{*}_i(\vec{\mathbf{e}}_{\vec{\mathbf{k}}_i\sigma_i})^{*}_j(\vec{\mathbf{e}}_{\vec{\mathbf{k}}_p\sigma_p})_k \times \int_V d\vec{\mathbf{r}} \left[e^{-i(\vec{\mathbf{k}}_s+\vec{\mathbf{k}}_i-\vec{\mathbf{k}}_p)\cdot\vec{\mathbf{r}}}\right] + H.c. \tag{2.15}$$

where $H.c.$ stays for *Hermitian conjugate*. As customary, we identified the three fields involved in SPDC using the subscripts s, i, and p which stay respectively for *signal*, *idler*, and *pump*. The first and second are the downconverted optical fields and the pump refers to the input (pumping) laser. The V now assumes the meaning of the volume of the nonlinear crystal in which the interaction happens.

The other terms in eq. 2.15 are:

$$g_{\vec{\mathbf{k}}_j\sigma_j} = i\sqrt{\frac{\hbar\omega(k_j,\sigma_j)}{2\varepsilon_0 n^2(k_j,\sigma_j)}} \tag{2.16}$$

$$\chi_{ijk} \equiv \chi^{(2)}_{ijk}(\omega = \omega' + \omega'') = \int_0^\infty dt' \int_0^\infty dt'' \left[\chi^{(2)}_{ijk}(t',t'')e^{-i(\omega' t' - \omega'' t'')}\right] \tag{2.17}$$

for different combinations of pump, signal, and idler angular frequencies.

2.2.2 Working out the quantum state of SPDC.

Now that we have an expression for the (quantized) Hamiltonian of interaction, we can use it to calculate the biphoton state at a given time t. We fix the time at which the nonlinear interaction begins to $t_0 = 0$. In order to obtain the state of the system at a (later) given time t, we evolve the initial state $|\psi(t_0)\rangle$ according to:

$$|\psi(t)\rangle = \hat{\mathbf{U}}(t)|\psi(0)\rangle \tag{2.18}$$

where the evolution operator is:

$$\hat{\mathbf{U}}(t) = e^{\frac{1}{i\hbar}\int_0^t d\tau \hat{\mathbf{H}}_{NL}(\tau)} \tag{2.19}$$

In order to proceed, we need to declare the first important assumption.

Assumption:*if the interval time between two successive SPDC processes is large enough compared to the interaction time, that is* ***if the pump field is sufficiently weak***, we can express the exponential in 2.19 in power series. Since we are interested only in the terms that describe the creation of two photons[4], we can then keep only terms up to the first order. This approximation is very common. In a real experiment, the researcher usually has full control over it in the sense that decreasing the power of the pump one can make sure to be in the two-photon regime. On the other hand, if one was interested in multiphoton events can (in principle) increase the power of the pump laser until reaching higher orders regimes (refer to section 6.1 for a theoretical discussion of what is usually referred to as the *multiphoton regime*).

The (quantum) evolution operator is then approximated to:

$$\hat{\mathbf{U}}(t) \simeq 1 + \frac{1}{i\hbar}\int_0^t d\tau \hat{\mathbf{H}}_{NL}(\tau) \tag{2.20}$$

Remembering the final expression of the quantum Hamiltonian of interaction 2.15, equation 2.20 implies integrations in both time and space. Let us evaluate first the integration along the temporal variable:

[4]Note that the first power in $\hat{\mathbf{H}}$ having only two creation operators leads to two photons in the down converted field; higher powers n of it, however, would lead to the creation of 2^n photons.

$$\int_0^t d\tau \hat{\mathbf{H}}_{NL}(\tau) = \frac{1}{2v^{3/2}} \sum_{\vec{\mathbf{k}}_s\sigma_s} \sum_{\vec{\mathbf{k}}_i\sigma_i} \sum_{\vec{\mathbf{k}}_p\sigma_p} {g^*}_{\vec{\mathbf{k}}_s\sigma_s} {g^*}_{\vec{\mathbf{k}}_i\sigma_i} g_{\vec{\mathbf{k}}_p\sigma_p} \hat{\mathbf{a}}^\dagger_{\vec{\mathbf{k}}_s\sigma_s} \hat{\mathbf{a}}^\dagger_{\vec{\mathbf{k}}_i\sigma_i} \hat{\mathbf{a}}_{\vec{\mathbf{k}}_p\sigma_p}$$

$$\times e^{i\frac{(\omega_s+\omega_i-\omega_p)t}{2}} \chi_{ijk} (\vec{\mathbf{e}}_{\vec{\mathbf{k}}_s\sigma_s})^*_i (\vec{\mathbf{e}}_{\vec{\mathbf{k}}_i\sigma_i})^*_j (\vec{\mathbf{e}}_{\vec{\mathbf{k}}_p\sigma_p})_k \tag{2.21}$$

$$\times t \cdot \mathrm{sinc}\left[\frac{(\omega_s+\omega_i-\omega_p)t}{2}\right] \int_V d\vec{\mathbf{r}} \left(e^{-i(\vec{\mathbf{k}}_s+\vec{\mathbf{k}}_i-\vec{\mathbf{k}}_p)\cdot\vec{\mathbf{r}}}\right) + H.c.$$

Similarly, we integrate over the (crystal) volume $V = l_x \times l_y \times l_z$, which means to evaluate the integral along the three spatial variables x, y, z with boundaries the three sizes of the crystal:

$$\int_0^\infty d\tau \hat{\mathbf{H}}_{NL}(\tau) = \frac{Vt}{2v^{3/2}} \sum_{\vec{\mathbf{k}}_s\sigma_s} \sum_{\vec{\mathbf{k}}_i\sigma_i} \sum_{\vec{\mathbf{k}}_p\sigma_p} {g^*}_{\vec{\mathbf{k}}_s\sigma_s} {g^*}_{\vec{\mathbf{k}}_i\sigma_i} g_{\vec{\mathbf{k}}_p\sigma_p} \hat{\mathbf{a}}^\dagger_{\vec{\mathbf{k}}_s\sigma_s} \hat{\mathbf{a}}^\dagger_{\vec{\mathbf{k}}_i\sigma_i} \hat{\mathbf{a}}_{\vec{\mathbf{k}}_p\sigma_p}$$

$$\times e^{i\frac{(\omega_s+\omega_i-\omega_p)t}{2}} \chi_{ijk} (\vec{\mathbf{e}}_{\vec{\mathbf{k}}_s\sigma_s})^*_i (\vec{\mathbf{e}}_{\vec{\mathbf{k}}_i\sigma_i})^*_j (\vec{\mathbf{e}}_{\vec{\mathbf{k}}_p\sigma_p})_k$$

$$\times \mathrm{sinc}\left[\frac{(\omega_s+\omega_i-\omega_p)t}{2}\right] \prod_{m=x,y,z} \mathrm{sinc}\left[\frac{(k_s+k_i-k_p)_m l_m}{2}\right] \tag{2.22}$$

$$\times e^{-i\left[\frac{(k_s+k_i-k_p)_z l_z}{2}\right]} + H.c.$$

where $(...)_m$ means the component m of the vectorial quantity in the parenthesis. The integration itself over the three spatial directions yields to the product of three *sinc* function. Without the last exponential, eq. 2.22 would refer to the fields at the interaction position (say, in the middle of the crystal). We included that term because want to evaluate the fields at a position $z = l_z/2$. This correspond to evaluate the state at the output (x, y) face of the crystal. We proceed that way expecting that at some point of our calculations the fields will propagate along the z-direction (at this stage the choice of z is purely arbitrary). The exponential could resemble a propagation, but since hitherto we did not say anything about $(k_s + k_i - k_p)_z$, the argument of the exponential function could turn out to be positive (I illustrate the propagation of the state in section 2.2.5).

We may refer to the z-direction as the *longitudinal* one. The spatial integration results in an exponential function of the wave vectors along the longitudinal direction multiplied by three *sinc* functions along each of the three spatial components of the wave vector. The latter are responsible for the *conservation of linear momentum* and are usually referred to as *phase matching* condition.

Finally we can work out the quantum state at a given time t by inserting eq. 2.22 in 2.20, and in turn the result in 2.18. In doing so, we consider no photons in the signal and idler modes at the time $t_0 = 0$; their initial state on the Hilbert space of the signal and idler only is the vacuum state. In Dirac notation we may refer to it as $|0\rangle|0\rangle$. Since in this thesis we

will often deal with two-photon (quantum) states, we adopt a short notation to refer to them. For instance, the aforesaid vacuum state is expressed as $|0,0\rangle\rangle$, where the double bracket explicitly refers to the 2-photon nature of the state.

For what concern the state of the pump, we considered it to be fairly represented as a classical field by its complex amplitude $A_p(\vec{\mathbf{k}}_p, \sigma_p)$. This practise is usually justified in literature stating that the pump field, being a strong one, is made by many photons and therefore does not face any depletion. However, the reality is slightly more devious here and it deserves a little explanation. Technically any system is quantum, and the pump field is not an exception. The quantum state of light that resembles most closely the emission of a laser is a *coherent state*. Without the need to explain the mathematical details of coherent states $|A_p\rangle$, for what concerns us it is enough to mention that coherent states are eigenstates of the annihilation operator: $\hat{\mathbf{a}}|A_p\rangle = A_p|A_p\rangle$. The physical meaning of which is that a coherent (quantum) state remains the same after annihilation of one particle. In formulae this reads as:

$$\hat{\mathbf{a}}^{\dagger}_{\vec{\mathbf{k}}_s\sigma_s}\hat{\mathbf{a}}^{\dagger}_{\vec{\mathbf{k}}_i\sigma_i}\hat{\mathbf{a}}_{\vec{\mathbf{k}}_p\sigma_p}|0,0,A_p(\vec{\mathbf{k}}_p\sigma_p)\rangle = A_p(\vec{\mathbf{k}}_p\sigma_p)|1(\vec{\mathbf{k}}_s,\sigma_s),1(\vec{\mathbf{k}}_i,\sigma_i),A_p(\vec{\mathbf{k}}_p\sigma_p)\rangle \tag{2.23}$$

The result of substituting 2.22 in 2.20, and then in 2.18 is:

$$\begin{aligned}|\psi(t)\rangle = &\sum_{\vec{\mathbf{k}}_p\sigma_p} A_p(\vec{\mathbf{k}}_p,\sigma_p)|0,0\rangle\rangle + \frac{Vt}{2i\hbar v^{3/2}}\sum_{\vec{\mathbf{k}}_s\sigma_s}\sum_{\vec{\mathbf{k}}_i\sigma_i}\sum_{\vec{\mathbf{k}}_p\sigma_p} g^{*}_{\vec{\mathbf{k}}_s\sigma_s}g^{*}_{\vec{\mathbf{k}}_i\sigma_i}g_{\vec{\mathbf{k}}_p\sigma_p}A_p(\vec{\mathbf{k}}_p,\sigma_p)\\ &\times e^{i\frac{(\omega_s+\omega_i-\omega_p)t}{2}}\chi_{ijk}(\vec{\mathbf{e}}_{\vec{\mathbf{k}}_s\sigma_s})^{*}_i(\vec{\mathbf{e}}_{\vec{\mathbf{k}}_i\sigma_i})^{*}_j(\vec{\mathbf{e}}_{\vec{\mathbf{k}}_p\sigma_p})_k\\ &\times \operatorname{sinc}\left[\frac{(\omega_s+\omega_i-\omega_p)t}{2}\right]\prod_{m=x,y,z}\operatorname{sinc}\left[\frac{(k_s+k_i-k_p)_m l_m}{2}\right]\\ &\times e^{-i\left[\frac{(k_s+k_i-k_p)_z l_z}{2}\right]}|1(\vec{\mathbf{k}}_s,\sigma_s),1(\vec{\mathbf{k}}_i,\sigma_i)\rangle\rangle\end{aligned} \tag{2.24}$$

The creation (quantum) operators of signal and idler, applied to the vacuum state $|0,0\rangle\rangle$, generate a single photon Fock state in the signal mode $(\vec{\mathbf{k}}_s,\sigma_s)$ together with a single photon Fock state in the idler mode $(\vec{\mathbf{k}}_i,\sigma_i)$. Again, our *bra-ket* notation for that two-photon state reads: $|1(\vec{\mathbf{k}}_s,\sigma_s),1(\vec{\mathbf{k}}_i,\sigma_i)\rangle\rangle = |1(\vec{\mathbf{k}}_s,\sigma_s)\rangle|1(\vec{\mathbf{k}}_i,\sigma_i)\rangle$.

In conclusion, we can affirm that the quantum state of the pump is not affected, and it is custom to treat the pump field classically. In 2.24 the classical amplitude $A_p(\vec{\mathbf{k}}_p,\sigma_p)$ is introduced in place of the annihilation operator acting on the (many-photon) initial state of the pump.

2.2.3 Approximations.

The final expression of the biphoton wavefunction obtained in 2.24 completely describes the state of the downconverted photons. However, for the sake of simplifying its form, it is convenient considering few reasonable approximations.

I **Assumption:** the time of interaction t is long, **so that** the term $sinc[(\omega_s + \omega_i - \omega_p)t/2]$ is non-zero only for $\omega_p = \omega_s + \omega_i$.
Justification: in order to justify this we request that $\frac{c}{L} > (\omega_p - \omega_s - \omega_i)$, where c is the speed of light and L is the length of hte crystal.

II **Assumption:** The spectral bandwidth of the down converted fields detected is small *compared to* the central wavelength, **so that** the dispersion of the refractive index $n(\vec{\mathbf{k}}, \sigma)$ is small and therefore a linear approximation can be adopted.
Justification: Interference filters can be set on signal and idler paths before the detectors.

III **Assumption:** The terms $g_{\vec{\mathbf{k}}\sigma}$ and χ_{ijk} vary slowly with $\vec{\mathbf{k}}$, **so that** they can be considered constants.

IV **Assumption:** The transversal dimensions of the crystal (l_x, l_y) are large enough to contain the whole beam profile and we can consider them infinitely long, **so that** the *sinc* functions of the transverse directions in eq. 2.24) are non-zero only for $k_{p,x} = k_{s,x} + k_{i,x}$ and $k_{p,y} = k_{s,y} + k_{i,y}$ and the product of sequences reduces to:

$$\prod_{m=x,y,z} \text{sinc}\left[\frac{(k_s + k_i - k_p)_m l_m}{2}\right] = \delta(\vec{\mathbf{q}}_s + \vec{\mathbf{q}}_i - \vec{\mathbf{q}}_p)\text{sinc}\left[\frac{(k_s + k_i - k_p)_z L}{2}\right] \tag{2.25}$$

where in our notation $\vec{\mathbf{q}} = \vec{\mathbf{k}}_x + \vec{\mathbf{k}}_y$ is the transversal wave vector (complementary to the longitudinal one k_z), and $L = l_z$ is the length of the crystal in the longitudinal direction. The first allows the delta functions in x and y to be written as the delta function of the transverse components $\vec{\mathbf{q}}$.
Justification: the pump beam waist is a parameter that can be controlled with telescope systems.

V **Assumption:** The (discrete) summations are replaced by (continuous) integrations.
Justification: We chose a volume of quantization large enough [55].

VI **Assumption:** The pump beam field contains only one linear polarization, **so that** the summations over the σ reduce to the only one polarization allowed. For negative birefringent crystals such as ours, the pump polarization is along the direction of the extraordinary index.
Justification: We can choose to filter only one linear polarization of the pump laser using a passive linear polarizer. In the experiment, we select only the one needed for optimal phase matching.

Of particular importance for its physical meaning is assumption (IV). For this reason, we had already mentioned it in the previous section of this chapter, when explaining the meaning of phase matching. A sketch useful for the understanding of this approximation was shown in Figure 2.4. With in mind the mathematical model just presented, we can recapitulate the phase matching discussion by saying that the *sinc* functions in the x and y directions reducing to Dirac deltas means that in those two directions we have *conservation of linear momentum*. This can be shortly addressed by saying that $\vec{\mathbf{q}}_p = \vec{\mathbf{q}}_s + \vec{\mathbf{q}}_i$. Conversely, in the longitudinal

direction we have to keep the *sinc* modulation because the approximation of infinite length of the crystal does not hold in this case. In conclusion, the linear momentum is *not* conserved in the z direction, and people usually refer to the *sinc* as the *phase-matching function*.

2.2.4 The final state.

Considering the six assumptions mentioned above, we can write the quantum state of two-photon generated by SPDC in a more familiar form. From 2.24, the state at a given time t is:

$$|\psi\rangle = |vac\rangle + \sum_{\sigma_s\sigma_i} \int d\omega_s \int d\omega_i \int d\vec{\mathbf{q}}_s \int d\vec{\mathbf{q}}_i \Phi_{\sigma_s\sigma_i}(\vec{\mathbf{q}}_s, \vec{\mathbf{q}}_i, \omega_s, \omega_i) |1(\vec{\mathbf{q}}_s, \omega_s, \sigma_s), 1(\vec{\mathbf{q}}_i, \omega_i, \sigma_i)\rangle\rangle \tag{2.26}$$

where $|1(\vec{\mathbf{q}}_s, \omega_s, \sigma_s), 1(\vec{\mathbf{q}}_i, \omega_i, \sigma_i)\rangle\rangle$ represents the two-photon Fock state of one photon being in the (signal) mode characterized by transversal wave vector q_s, at angular frequency ω_s, and polarization σ_s, and the other being in the (idler) mode characterized by transversal wave vector q_i, at angular frequency ω_i, and polarization σ_i. The amplitude $\Phi_{\sigma_s\sigma_i}$ is the so called *biphoton wavefunction*. In it, there are all the properties of the state:

$$\Phi_{\sigma_s\sigma_i} \simeq C_{\sigma_s\sigma_i} G_s(\omega_s) G_i(\omega_i) A_p(\vec{\mathbf{q}}_s + \vec{\mathbf{q}}_i, \omega_s + \omega_I) \mathrm{sinc}\left[\frac{(k_s + k_i - k_p)_z L}{2}\right] \tag{2.27}$$

where the terms $G_s(\omega_s)$ and $G_i(\omega_i)$ are respectively the transmission function of the signal and idler interference filters, and $C_{\sigma_s\sigma_i}$ is a coupling factor for polarizations σ_s ans σ_i dominated by the nonlinear susceptibility tensor $\chi^{(2)}_{ijk}$.

The quantum state in equation 2.26 is the mathematical expression of the biphoton state *generated* by SPDC somewhere within the nonlinear crystal. The next step in order to be able to predict the measurable properties of the state itself, is to account for the propagation of the field. This involves few more considerations and approximations.

2.2.5 Propagation of the two-photon field.

In this work we are interested in investigating the spatial - *ergo* transversal - properties of the optical field generated by parametric down-conversion. In order to describe the state at a given position along the optical axis, we need to propagate the state derived previously (eq 2.26). Most of the quantum theory at this regards are based on what is called *paraxial approximation*. A complete description of the topic can be found in most of the classic optics book such as [72, 73].

It is easy to picture a paraxial beam in geometric optics [72] as composed by rays which propagate within a small angle from the optical axis of the propagating field. So far we described the optical fields as optical (plane) waves. The equation that describes the motion of electromagnetic waves in free space is the wave equation, which in the vacuum reads as:

$$\nabla^2 \vec{\mathbf{E}}(\vec{\mathbf{r}}, t) - \frac{1}{c^2} \frac{\partial^2 \vec{\mathbf{E}}(\vec{\mathbf{r}}, t)}{\partial t^2} = 0 \tag{2.28}$$

where c is the speed of light in vacuum. It rewrites in the form of the Helmholtz equation if considering the wave to be monochromatic and with harmonic temporal dependence [55]:

$$\nabla^2\varepsilon(\vec{\mathbf{r}}) + k^2\varepsilon(\vec{\mathbf{r}}) = 0 \tag{2.29}$$

where $\varepsilon(\vec{\mathbf{r}})$ represents one single component of the electric field vector [74] expressed as: $E(\vec{\mathbf{r}}, t) = \varepsilon(\vec{\mathbf{r}})\exp[-i\omega t]$, with ω being the angular frequency. Now, let us extend the paraxial approximation to the wave framework by considering the propagating field to be composed only by waves whose wavefronts normals are paraxial rays. We can define such waves as *paraxial waves*. If we consider a collinearly propagating beam, that is described only by paraxial waves that propagate close to the optical axis z, the gradient of $\varepsilon(\vec{\mathbf{r}})$ in the transversal direction is small compared to the one in z. Strictly speaking this means that it keeps a plane wave structure at least within the distance of a wavelength. We can therefore write the spatial amplitude of the field as:

$$\varepsilon(\vec{\mathbf{r}}) = u(\vec{\mathbf{r}})e^{ikz} \tag{2.30}$$

where $u(\vec{\mathbf{r}})$ is a (spatially) slow-varying function. Inserting the expression for the complex amplitude 2.30 in the Helmholtz equation 2.29, and considering the paraxial approximation, we get the paraxial Helmholtz equation:

$$\left(\frac{\partial^2}{\partial x^2} + \frac{\partial^2}{\partial y^2} + 2ik\frac{\partial}{\partial z}\right)u(\vec{\mathbf{r}}) = 0 \tag{2.31}$$

Mathematically speaking, the paraxial approximation here is:

$$|(\partial^2 u(\vec{\mathbf{r}})/\partial x\partial y)| << |k(\partial u(\vec{\mathbf{r}})/\partial z)| \tag{2.32}$$

This corresponds to saying that the angle between the wave vector and its component in the direction of propagation z is small. The importance of 2.31 in our field is related to the fact that it admits several sets of well-known solutions, such as Laguerre-Gaussian modes and Hermite-Gaussian modes. From a mathematical point of view, the similarity of the (classical) Helmholtz paraxial equation and the Schrodinger equation of quantum mechanics is evident. The investigation of such similarities are beyond the purposes of this work, but the interested reader can find satisfaction in the demonstrations contained for instance in [75] and [76].

Now that we have an approximated but useful version of the wave equation (2.31), let us propagate the optical field. We define a solution of the paraxial Helmholtz equation $u(\vec{\mathbf{r}}) \equiv u(\vec{\boldsymbol{\rho}}, z)$ as the plane wave expansion [73]:

$$u(\vec{\boldsymbol{\rho}}, z) = \frac{1}{(2\pi)^2}\int_{\Re^2} d\vec{\mathbf{q}}A(\vec{\mathbf{q}}, z)e^{i(\vec{\mathbf{q}}\cdot\vec{\boldsymbol{\rho}})} \tag{2.33}$$

where we remind that we assume z to be the cartesian direction of propagation of the optical field, and $\vec{\mathbf{q}}$ and $\vec{\boldsymbol{\rho}}$ the transverse components of respectively wave vector and position. The weights of the plane waves $\exp[i\vec{\mathbf{q}}\cdot\vec{\boldsymbol{\rho}}]$ are given by the angular spectrum $A(\vec{\mathbf{q}}, z)$. Perhaps a more physically meaningful interpretation of the angular spectrum is in terms of the inverse Fourier transform of $u(\vec{\mathbf{q}}, z)$:

$$A(\vec{\mathbf{q}}, z) = \int_{\Re^2} d\vec{\boldsymbol{\rho}}u(\vec{\mathbf{q}}, z)e^{-i(\vec{\mathbf{q}}\cdot\vec{\boldsymbol{\rho}})} \tag{2.34}$$

We can therefore propagate the angular spectrum $A(\vec{\mathbf{q}}, z)$ by inserting 2.33 in the Helmholtz paraxial equation 2.31. If the angular spectrum is known at a given position z_0, then we can calculate it at any propagating position z and the result is:

$$A(\vec{\mathbf{q}}, z) = A(\vec{\mathbf{q}}, z_0)e^{ik_z(z-z_0)} \tag{2.35}$$

The last thing we need to do in order to be able to calculate the wave function at *any* position z by propagating eq. 2.26, is to remove the dependence from k_z. Since such a dependence lies directly in the *sinc* function, we ultimately need to express k_z for signal, idler, and pump as a function of the other components of the respective wave vector.

We already implicitly made use of the wave vector as expressed in two components, namely the longitudinal k_z component (one dimension) and the transverse $\vec{\mathbf{q}} = \vec{\mathbf{k}}_{x,y}$ component (bi-dimensional, in the (x, y) plane). The magnitude of the wave vector is $k^2 = k_z^2 + q^2$. We now work out k_z and rearrange the expression as following:

$$k_z = \sqrt{k^2 - q^2} = k\sqrt{1 - \frac{q^2}{k^2}} \tag{2.36}$$

Performing a Taylor expansion of the square root up to the second term in the variable q/k, we get:

$$k_z \simeq k(1 - \frac{q^2}{2k^2}) \tag{2.37}$$

The result in 2.37 is known as *Fresnel approximation*, and it is valid for $q^2/k^2 << 1$, that is[5] for $q^2 << k^2$. The hypothesis of wave vector transversal component being much smaller than the longitudinal one is nothing but the paraxial approximation. In fact, the Fresnel approximation is a particular application of the paraxial approximation. However, it is only valid for isotropic media [55], while the nonlinear crystals for SPDC are not by definition. For anisotropic crystals in general a more sophisticate analysis is required. The interested reader can find an exhaustive analysis on the Born-Wolf textbook [74].

Restricting the field to uniaxial crystals simplifies the analysis without missing any interesting aspects of the physics. Many papers can be found describing it clearly enough (see for instance the review paper by Walborn [55], pag. 97). The analysis is based on the different refractive index faced by different polarizations of the fields, namely the extraordinary and the ordinary refractive indexes. However, our nonlinear crystal is cut for Type-0 SPDC[6], which means that the three photons involved are all polarized along the same direction. The final result for the three fields involved is:

$$k_z, p = n_p\frac{\omega_p}{c} - \frac{c}{2n_p\omega_p}|\vec{\mathbf{q}}_s + \vec{\mathbf{q}}_i|^2 \tag{2.38}$$

$$k_z, s = n_s\frac{\omega_s}{c} - \frac{c}{2n_s\omega_s}|\vec{\mathbf{q}}_s|^2 \tag{2.39}$$

$$k_z, i = n_i\frac{\omega_i}{c} - \frac{c}{2n_i\omega_i}|\vec{\mathbf{q}}_i|^2 \tag{2.40}$$

Considering a monochromatic pump, the state of the two-photon 2.26 can now be approximated to:

$$|\psi\rangle \simeq |vac\rangle + \int d\vec{\mathbf{q}}_s \int d\vec{\mathbf{q}}_i \Phi_{oo}(\vec{\mathbf{q}}_s, \vec{\mathbf{q}}_i)|1(\vec{\mathbf{q}}_s, \omega_s, o), 1(\vec{\mathbf{q}}_i, \omega_i, o)\rangle\rangle \tag{2.41}$$

[5] In our case, since we evaluate the integral of q between $\pm\infty$, q could in principle be greater than k. However, since we assume the amplitude to be small for $q > k$ we recover the conditions for this approximation to apply.

[6] Three different kinds of SPDC are defined according to the polarization direction of the three photons involved. In Type-0, all the photons are polarized in the same direction: $o \rightarrow oo$ or $e \rightarrow ee$; in Type-1, the pump is polarized in one direction and the down converted photons in the complementary direction: $e \rightarrow oo$ or $o \rightarrow ee$; in type-2, the down converted photons are polarized in complimentary directions: $o \rightarrow oe$ or $e \rightarrow oe$

and the biphoton amplitude 2.27 takes the form:

$$\Phi_{oo}(\vec{\mathbf{q}}_s, \vec{\mathbf{q}}_i) \simeq C_{oo} G_s(\omega_s) G_i(\omega_i) A_p(\vec{\mathbf{q}}_s + \vec{\mathbf{q}}_i) \delta(\omega_s + \omega_i - \omega_p) \mathrm{sinc}\left[\frac{L}{4k_p}\left|\vec{\mathbf{q}}_s \frac{\omega_i}{\omega_s} - \vec{\mathbf{q}}_i \frac{\omega_s}{\omega_i}\right|^2\right] \quad (2.42)$$

The two ratios of signal and idler angular frequencies in the argument of the *sinc* function cancels out in the common framework of degenerate SPDC. In our experiment, as mentioned early, we aim to generate photons at different frequencies. The consequence is that we have two constant (but different) factors in front of signal and idler transverse momentum. In our case they differ only few percent from one, respectively 1.069 for the idler and 0.936 for the signal. When the spectral drift from the degenerate wavelength for signal and idler is small compared to their central wavelength, it is possible to approximate their ratio to one. Defining $\omega_s = \bar{\omega} - \delta\omega$ and $\omega_i = \bar{\omega} + \delta\omega$, where $\bar{\omega} = 2\omega_p$ is the degenerate wavelength, we can approximate $(\bar{\omega} \pm \delta\omega)/(\bar{\omega} \mp \delta\omega) \simeq 1$ for $\delta\omega << \bar{\omega}$.

While this approximation is not necessary when running simulations, it is useful to simplify the qualitative interpretation of the states produced with our setup. Unless explicitly specified, from now on we will consider it applied. Therefore, we can rewrite the final (approximated) expression of the biphoton amplitude as:

$$\Phi_{oo}(\vec{\mathbf{q}}_s, \vec{\mathbf{q}}_i) \simeq C_{oo} G_s(\omega_s) G_i(\omega_i) A_p(\vec{\mathbf{q}}_s + \vec{\mathbf{q}}_i) \delta(\omega_s + \omega_i - \omega_p) \mathrm{sinc}\left[\frac{L}{4k_p}|\vec{\mathbf{q}}_s - \vec{\mathbf{q}}_i|^2\right] \quad (2.43)$$

where now the argument of the *sinc* function depends only on the difference between the transverse wave vector of signal and idler.

We want to conclude this section by drawing few remarks and conclusions about the state just found:

- since also the interference filter function is included, the amplitude expressed by 2.43 can be considered the two-photon *detection* amplitude;
- the angular spectrum of the biphoton state factorizes in a particular form given by $\Phi_{oo}(\vec{\mathbf{q}}_s, \vec{\mathbf{q}}_i) \propto A_p(\vec{\mathbf{q}}_s + \vec{\mathbf{q}}_i) \times F_{pm}(\vec{\mathbf{q}}_s - \vec{\mathbf{q}}_i)$, where in our notation "F_{pm}" stays for "Phase Matching" function;
- the angular spectrum of the *pump* $A_p(\vec{\mathbf{q}}_s + \vec{\mathbf{q}}_i)$ is still explicit in the *signal-idler* amplitude 2.43, which means that the spatial properties of the pump are directly transferred to the downconverted fields [77];
- the function $\Phi_{oo}(\vec{\mathbf{q}}_s, \vec{\mathbf{q}}_i)$ is not a separable function of $\vec{\mathbf{q}}_s$ and $\vec{\mathbf{q}}_i$ (that is, $\Phi_{oo}(\vec{\mathbf{q}}_s, \vec{\mathbf{q}}_i) \neq f_s(\vec{\mathbf{q}}_s) f_i(\vec{\mathbf{q}}_i)$). In this fact many non-classical and non-local properties of SPDC two-photon states find justification;
- a common term well known as *spatial walk-off* is absent in this analysis because it is not relevant due to the nature of our SPDC (being TYPE-0).

The analysis done so far is in the momentum representation. For the sake of completeness, here we explicitly show how the state can be written in the coordinate space. A Fourier transform links the transverse wave vectors $\vec{\mathbf{q}}$ to the transverse positions $\vec{\boldsymbol{\rho}}$ for both signal and idler fields [78]. The state takes the form:

$$|\psi\rangle \simeq |vac\rangle + \int d\vec{\boldsymbol{\rho}}_s \int d\vec{\boldsymbol{\rho}}_i \Phi_{oo}(\vec{\boldsymbol{\rho}}_s, \vec{\boldsymbol{\rho}}_i)|1(\vec{\boldsymbol{\rho}}_s, \omega_s, o), 1(\vec{\boldsymbol{\rho}}_i, \omega_i, o)\rangle\rangle \tag{2.44}$$

In the biphoton wavefunction we can see that a physically interesting difference lies in the phase-matching function. In particular, in the paraxial approximation the *sinc* in momentum is substituted by a *sint* function [79]:

$$\Phi_{oo}(\vec{\boldsymbol{\rho}}_s, \vec{\boldsymbol{\rho}}_i) \simeq \tilde{A}(\vec{\boldsymbol{\rho}}_s, \vec{\boldsymbol{\rho}}_i)\text{sint}\left[\frac{k_p}{4L}|\vec{\boldsymbol{\rho}}_s - \vec{\boldsymbol{\rho}}_i|^2\right] \tag{2.45}$$

where the *sint* function is defined as follow: $sint(x) \equiv \frac{2}{\pi}\int_x^\infty \text{sinc}(t)dt \equiv 1 - \frac{2}{\pi}Si(x)$, where $Si(x)$ is the sine integral function [79].

2.2.6 Exponential approximation.

In the state 2.41 (in real space eq. 2.44), the phase matching function is expressed by a *sinc* (in real space, *sint*) function of the difference of the transverse components of signal and idler. That result is ultimately a manifestation of the non-conservation of linear momentum in the longitudinal direction. Such a function is often approximated by a Gaussian in order to simplify the analytical calculus [80–83].

The usual method to approximate the *sinc* function is to apply the substitution: $\text{sinc}(bx^2) \Rightarrow \exp(-\alpha bx^2)$ [79]. The idea is to match the central part of the *sinc* function with a Gaussian, as shown in figure 2.5. The parameter α clearly fits the width of the Gaussian. In different works the parameter of similarity of the *sinc* to the exponential has been defined in slightly different ways, and as a consequence α has been fixed to different values. For instance, in [63] and [84] they fixed it to 1; in [81–83] they choose it in order to equal the widths of the functions at $1/e^2$; while in [85] they chose to equal them at $1/e$. In our case, we opted for $\alpha = 0.455$ which results in the two functions (exp and $sinc$) coinciding at $1/e^2$ of the intensity [81].

The results for the momentum and the position representations respectively are:

$$\Phi_{oo}(\vec{\mathbf{q}}_s, \vec{\mathbf{q}}_i) \propto e^{\left[-\frac{w_p^2}{4}|\vec{\mathbf{q}}_s + \vec{\mathbf{q}}_i|^2\right]} e^{\left[-\frac{\alpha L}{4k_p}|\vec{\mathbf{q}}_s - \vec{\mathbf{q}}_i|^2\right]} \tag{2.46}$$

$$\Phi_{oo}(\vec{\boldsymbol{\rho}}_s, \vec{\boldsymbol{\rho}}_i) \propto e^{\left[-\frac{4}{w_p^2}|\vec{\boldsymbol{\rho}}_s + \vec{\boldsymbol{\rho}}_i|^2\right]} e^{\left[-\frac{\alpha k_p}{4L}|\vec{\boldsymbol{\rho}}_s - \vec{\boldsymbol{\rho}}_i|^2\right]} \tag{2.47}$$

where we substituted the general pump amplitudes $A(\vec{\mathbf{q}}_s, \vec{\mathbf{q}}_i)$ and $A(\vec{\boldsymbol{\rho}}_s, \vec{\boldsymbol{\rho}}_i)$ with the most common case of Gaussian profile.

The approximation gives very similar results with the advantage of providing analytical closed expression. On the other hand, the two expressions have subtle important differences. For what concerns the physics we are investigating, the *sinc* wavefunction is non-Gaussian and is always entangled in the signal and idler variables, while in the Gaussian case some choice of the parameters will make the wavefunction separable - as we will see later.

The numerical results for the two approaches confirm that the exponential approximation is justified. For an attentive analysis of the quantification of the non-Gaussianity, the interested reader may refer to [79].

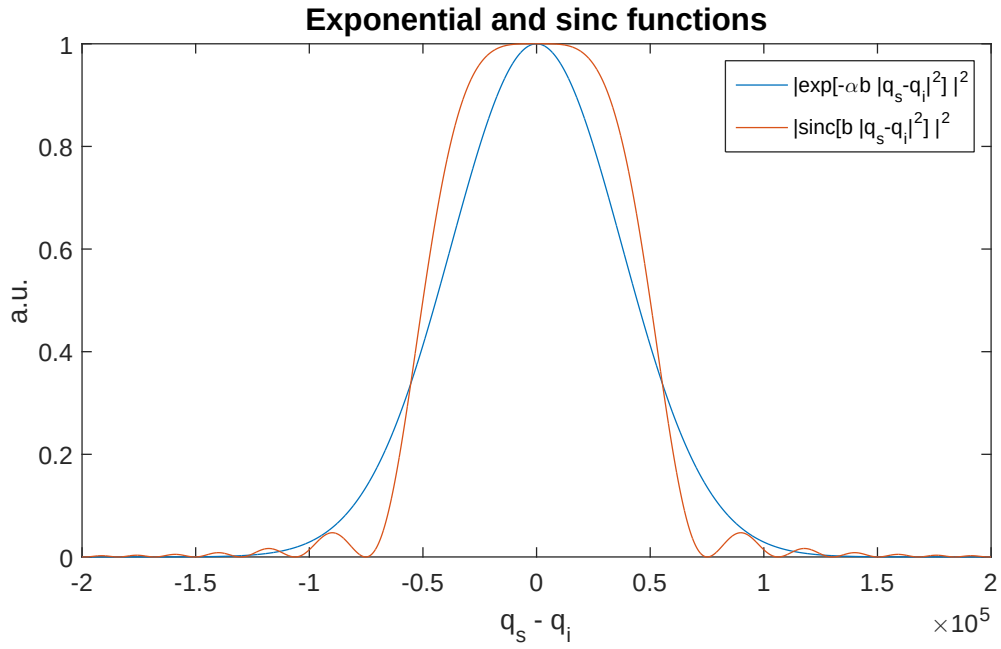

Figure 2.5: The phase matching *sinc* function plotted together with the exponential approximation. For our simulations we adopted $\alpha = 0.455$. Note that both of them has a maximum to one since here we only plotted the bare phase matching function, without the other terms present in the full wavefunction.

2.3 Higher order SPDC: Hermite-Gaussian modes.

Hermite-Gaussian modes form a natural (complete) bases for the states produced by SPDC. In many works they have been exploited as a discrete decomposition of the biphoton wavefunction (for instance [80, 86–89]). While the Laguerre-Gauss functions are defined in polar coordinates and therefore are more suitable for analysis of the Orbital Angular Momentum degree of freedom (OAM), the HG functions are expressed in cartesian coordinate. However, most of the physics research conducted in the field of quantum optics was only in the zero-order mode. In the work presented with this thesis, we are interested in stretching the analysis to a more general decomposition in Hermite-Gaussian modes.

In this section we will extend the result obtained in section 2.5 for general pump beam profile to the case of Hermite-Gaussian spatial profile. We will conclude the section presenting numerical simulations for the case of first-order Hermite-Gaussian profile of the pump beam. We just want to remember here that an interesting aspect of SPDC is that the pump beam profile is encoded in the spatial profile of the downconverted beams.

So, why a first-order Hermite-Gaussian mode? The reason is twofold. First, because it is an interesting state in the sense that the investigation of its spatial entanglement requires the development of elaborated criteria - at least under some experimental conditions (section 2.5.2); and second, because creating HG_{10} modes from a laser Gaussian mode HG_{00} is experimentally feasible with standard optical elements (as we will see in the next chapter, section 3.2.1). Apart from the experimental aspects, Hermite-Gaussian modes are interesting because they allow for a separation in the horizontal and vertical components.

2.3.1 Biphoton wavefunction with structured light.

In the previous sections, we derived the biphoton wavefunction expected by SPDC processes with a general pump profile $A(\vec{\mathbf{q}}_s + \vec{\mathbf{q}}_i)$. After some reasonable approximations regarding both the process of generation as well as propagation of the field, the resulting state 2.26 displays an explicit spatial modulation due to the pump field profile.

A property of SPDC processes is, again, that the spatial profile of the pump is modulated in the wavefunction of the biphoton state. For what concern the derivation of the quantum state, considering a non-Gaussian pump beam only imply the new higher-order profile to be inserted in place of $A(\vec{\mathbf{q}}_s + \vec{\mathbf{q}}_i)$.

Pumping the nonlinear crystal with a laser whose principal component is the HG_{01} mode, the biphoton amplitude (wavefunction) characterizing the probability distribution of the state follows from the general state we derived in the previous sections. In particular, we refer to equation 2.43, in which we substitute the pump amplitude with a first order Hermite Gaussian mode: $A_p(\vec{\mathbf{q}}_s + \vec{\mathbf{q}}_i) \propto (q_{s,x} + q_{i,x})\exp[-\frac{w_p^2}{4}(q_{s,x} + q_{i,x}) - \frac{w_p^2}{4}(q_{s,y} + q_{i,y})]$.

Since the point here is to show the effects of the Hermite-Gaussian distribution of the pump field, for the sake of simplicity we make use of a standard expression of the biphoton wavefunction composed only by the amplitude of the pump and the phase matching function (as used, for instance, in [90]):

$$\Phi_{oo}(\vec{\mathbf{q}}_s, \vec{\mathbf{q}}_i) \simeq N_{HG}(q_s + q_i)e^{-\frac{w_p^2}{4}|\vec{\mathbf{q}}_s + \vec{\mathbf{q}}_i|^2} e^{-\frac{\alpha L}{4k_p}|\vec{\mathbf{q}}_s - \vec{\mathbf{q}}_i|^2} \tag{2.48}$$

where N_{HG} is a normalisation factor that accounts for all the terms derived in the previous sections plus an additional part due to the normalization of the HG_{01} mode, and $(q_s + q_i)$ is the magnitude of the x component of the transverse wave vector.

2.4 Spatial entanglement in the SPDC bi-photon wave function.

The quantum description of the photonic states produced by SPDC relies on many parameters. They refer to several degrees of freedom that in general can all show entanglement among the states of the two individual photons. To refer to this multidimensionality of entanglement, in 1997 Paul G. Kwiat coined the term *hyperentanglement* [91, 92]. In this thesis we study multidimensional entanglement raising from the continuous variable (CV) nature of the spatial degrees of freedom.

Dealing with CV states it seems natural to express the quantum state in a form involving functions of continuous variables and (continuous) integral. In that regard, the description of the state provided by Eq. 2.41 with the wavefunction 2.43 is appropriate. However, when it comes to identify entanglement in an infinite dimensional Hilbert space, it is useful to rewrite the state on a discrete base. In the case of pure states the prevalent - if not universal - approach is known as *Schmidt-mode decomposition*. The theory has been developed at the beginning of 20^{th} century and published in 1907 by mathematician Erhard Schmidt and named after him[93][7]. First conceived for purely mathematical analysis, it was only more than 80 years later, in the 90's of the 20^{th} century, that it has been applied to quantum information theory [95] in articles like [96–98] to mention a few.

[7]The original paper is written in German language. English translation available here [94]

The Schmidt decomposition is a generic expression for representing a state $|v\rangle\rangle$ (mathematically: a vector) that belongs to a Hilbert space H_{12} which is obtained from the tensor product of two Hilbert (sub)spaces H_1 and H_2. The theorem says that there always exist two orthonormal basis $|i_1\rangle$ of H_1 and $|i_2\rangle$ of H_2 such that [99]:

$$|v\rangle\rangle = \sum_i \alpha_i |i_1\rangle|i_2\rangle \tag{2.49}$$

where between $|i_1\rangle$ and $|i_2\rangle$ the tensor product is implicitly assumed. The coefficients α_i are nonegative real numbers called Schmidt coefficients that for a normalised state have to obey: $\sum_i \alpha_i^2 = 1$. We apply 2.49 to our practical case, where the vector $|v\rangle\rangle$ is now the biphoton wavefunction 2.41 and the Hilbert spaces H_1 and H_2 are the spaces of the signal and idler respectively. The Schmidt decomposition of $C(\vec{\mathbf{q}}_s, \vec{\mathbf{q}}_i)$ corresponds to [63]:

$$C(\vec{\mathbf{q}}_s, \vec{\mathbf{q}}_i) = \sum_{n=0}^{\infty} \sqrt{\alpha_n} u_n(\vec{\mathbf{q}}_s) v_n(\vec{\mathbf{q}}_i) \tag{2.50}$$

where the Schmidt modes $u_n(\vec{\mathbf{q}}_s)$ and $v_n(\vec{\mathbf{q}}_i)$ are eigenvectors for the subspaces of the transverse wavevector of signal and idler respectively [98], [100] and they form a complete orthonormal set on the respective subspace [63].

Hence we can see how the discretization of a state which is naturally described on CV is not an artifact, but rather finds its roots in the fact that the trace of density matrices is always finite. In conclusion, the Schmidt decomposition of a state is always discrete independently of any box boundary condition chosen, also for naturally continuous states [63].

For our purposes, the importance of the Schmidt decomposition of a biphoton state such as the one produced by SPDC can be found in two aspects. First, the fact that the wavefunction 2.50 spreads over the two subspaces with a *single*-index sum fixes the matching of the states on the subspace of signal and idler one-to-one. That is, there is a certain probability $P_n = \alpha_n^2$ that the signal is found in the state $u_n(q_s)$; however, if that is the case, with certainty the idler is in the state $v_n(q_i)$. Second, from the eigenvalues α_n is possible to *quantify* the amount of entanglement. Intuitively, the greater the number of the non-zero coefficients α, the more the state is entangled over the two subspaces. The rigorous way to express entanglement on a bipartite system is in term of the entropy: $S = -\sum_n \alpha_n \log_2(\alpha_n)$ [63]. Another expression of the same quantity is given by the Schmidt number. For practical purposes it is a more convenient definition in the sense that it highlights the number of modes involved in the bipartite state:

$$K_{s,i} = \frac{1}{\sum_n \alpha_n^2} \tag{2.51}$$

where in our notation the subscripts s, i are explicit for reminding the reader that the concept of Schmidt number makes sense only for a bipartite state (composed by **s**ignal and **i**dler). Hence, the greater the Schmidt number, the higher the entanglement. The definition expressed in 2.51 is nothing but an average of the number of modes involved in the Schmidt decomposition. Remembering that the eigenvalues α_n sum up to 1 (hence $0 < \alpha_n < 1 \forall n$), the sum of the square of them is equal to 1 if and only if exists only one non-zero eigenvalue. In that case, $K = 1$ and the state is separable as: $|v\rangle\rangle = |u(q_s)\rangle \otimes |v(q_i)\rangle$. The maximum value tends to infinity (for $n \to \infty$); however in any practical case it is limited by the volume of the phase space which is restricted by physical constraints such as finite collection time [63].

Now let us apply the Schmidt decomposition argument to few different cases characterized by interesting biphoton wavefunction of the kind in 2.41. In particular, we will consider two

different pump profiles $\Theta(q_s + q_i)$ (Gaussian and Hermite-Gaussian) as well as two different phase-matching functions $\Lambda(q_s - q_i)$ (real and approximated).

2.4.1 Gaussian pump, Gaussian phase matching.

Let us consider the following (biphoton) wavefunction, which as we saw in 2.2.6 is a good approximation to the final wavefunction:

$$C_g^G(\vec{\mathbf{q}}_s, \vec{\mathbf{q}}_i) = N_g e^{-\frac{|\vec{\mathbf{q}}_s + \vec{\mathbf{q}}_i|^2}{\delta_p^2}} e^{-\frac{|\vec{\mathbf{q}}_s - \vec{\mathbf{q}}_i|^2}{\delta_{pm}^2}} \tag{2.52}$$

where in our notation capital G refers to "**G**aussian" pump profile, lowercase g to Gaussian phase-matching, and N_g is a normalization factor. We also introduced the parameters $\delta_p^2 = w_p^2/4$ for the width of the (Gaussian) **p**ump distribution (which relates to the pump beam waist w_p) and $\delta_{pm}^2 = (-\alpha L)/(4K_p)$ for the width of the **p**hase-**m**atching function (in this case, Gaussian).

In regards of the Schmidt decomposition, the importance of the exponential approximation considered in 2.52 lies in the fact that for this particular choice the Schmidt mode functions are the eigenfunctions of the energy levels of a two dimensional, isotropic harmonic oscillator [63]. The advantage is that the solutions can therefore be written as Hermite-Gauss (HG) or Laguerre-Gauss (LG) modes, and a closed expression for the Schmidt number can be found. As mentioned, the Schmidt number represents the average number of modes in the decomposition, which is related to the probabilities of each single mode to populate the distribution.

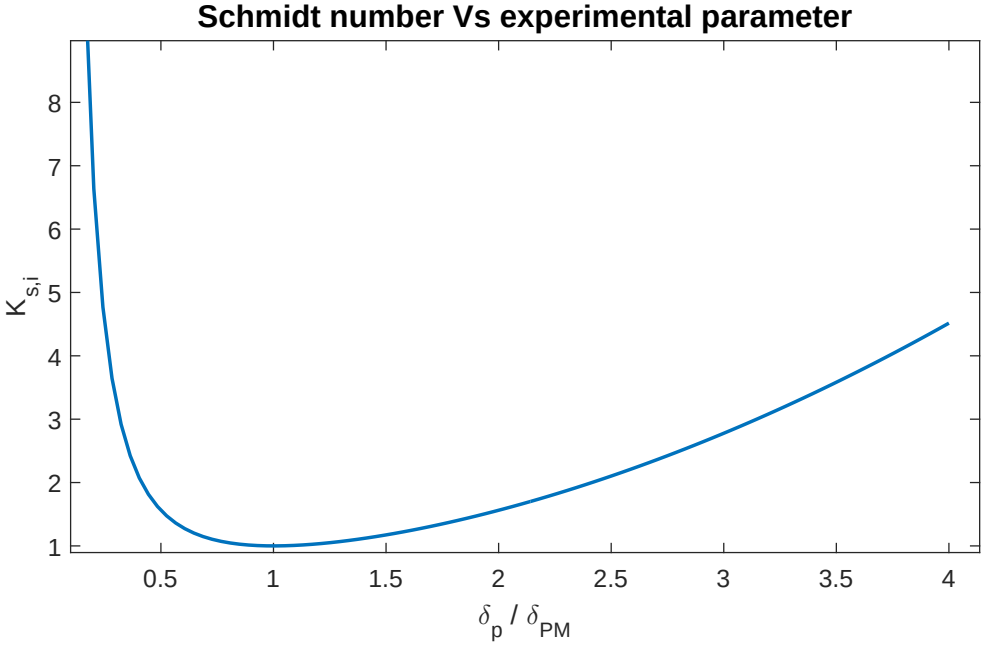

Figure 2.6: Schmidt number as a function of the control parameter expressed as the ratio of the widths of (Gaussian) pump profile and the (Gaussian) phase-matching function.

Defining the probability of the mode characterized by quantum numbers n, m (respectively the radial and angular number in polar coordinates) proportional to $\xi^{2n+|m|}$, with $\xi = (\delta_{pm} - \delta_p)^2/(\delta_{pm} + \delta_p)^2$ Law and Eberly [63] found the following (closed) solution:

$$K_{s,i}^{G} = \frac{1}{4}\left(\frac{\delta_p}{\delta_{pm}} + \frac{\delta_{pm}}{\delta_p}\right) \tag{2.53}$$

by matching the widths of the mode functions to the Schmidt mode function. The ratio between the widths of the two functions in 2.52 is the parameter that fixes the number of Schmidt modes - that is, the amount of entanglement - of the bipartite state. It is interesting to note how $K_{s,i}^{G}$ increases both for small and large values of the parameter, showing *the* minimum $K = 1$ for $\delta_p/\delta_{pm} = 1$ (see fig. 2.6).

2.4.2 Gaussian pump, *sinc* phase matching.

The actual phase matching function of the biphoton state generated by SPDC is not a gaussian, but rather a *sinc* function. A more realistic biphoton amplitude is therefore expressed as:

$$C_s^G(\vec{\mathbf{q}}_s, \vec{\mathbf{q}}_i) = N_s e^{-\frac{|\vec{\mathbf{q}}_s + \vec{\mathbf{q}}_i|^2}{w_p^2}} sinc\left(-\frac{|\vec{\mathbf{q}}_s - \vec{\mathbf{q}}_i|^2}{\delta_{pm}^2}\right) \tag{2.54}$$

where the superscript G refers to the **G**aussian pump, and s to the **s**inc function.

As far as we know, in this more complicated case a closed expression for the Schmidt number has not been found. However, a Schmidt decomposition of 2.54 can be accomplished as follows (adhering to the reasonings described in [63]). First, we reduce the dimensionality of the problem by making use of the polar coordinates which allows for the wavefunction to rewrite as:

$$C_s^G(\vec{\mathbf{q}}_s, \vec{\mathbf{q}}_i) = \sum_m e^{im(\theta_s - \theta_i)} \frac{\sqrt{P_m}}{2\pi} F_m(q_s, q_i) \tag{2.55}$$

where the transverse wave vectors are expressed as: $\vec{\mathbf{q}}_s \equiv (q_s cos(\theta_s), q_s sin(\theta_s))$ and $\vec{\mathbf{q}}_i \equiv (q_i cos(\theta_i), q_i sin(\theta_i))$, and $F_m(q_s, q_i)$ is a function of the magnitudes of the (transverse) wavevectors only. The latter has to obey $\int_0^\infty dq_s \int_0^\infty dq_i q_s q_i |F_m(q_s, q_i)|^2 \equiv 1$. The reduction of dimensionality is possible thanks to the fact that when written in polar coordinates, the function in eq. 2.54 depends only on the *relative* angles between signal and idler. This is ultimately a consequence of the symmetry of the pump.

In order to fully separate the dependence from the signal and idler variables, we need to apply again the principles of the Schmidt decomposition to expression 2.55, in particular to the function $F_m(q_s, q_i)$. Dealing with a function which depends on scalar variables (the *magnitudes* of the transverse wave vectors) simplify the derivation, and the result is: $F_m(q_s, q_i) = \frac{\sum_n \sqrt{\gamma_{n,m}} \phi_{n,m}(q_s) \phi_{n,m}(q_i)}{\sqrt{q_s q_i}}$.

We can now conclude the Schmidt decomposition of the wavefunction as 2.54:

$$C_s^G(\vec{\mathbf{q}}_s, \vec{\mathbf{q}}_i) = \sum_{m=-\infty}^{+\infty} \sum_{n=0}^{\infty} \sqrt{\lambda_{n,m}} u_{n,m}(\vec{\mathbf{q}}_s) v_{n,m}(\vec{\mathbf{q}}_i) \tag{2.56}$$

$$u_{n,m}(\vec{\mathbf{q}}_s) = \frac{1}{\sqrt{2\pi q_s}} e^{im\theta_s} \phi_{n,m}(q_s) \tag{2.57}$$

$$v_{n,m}(\vec{\mathbf{q}}_i) = \frac{1}{\sqrt{2\pi q_i}} e^{im\theta_i} \phi_{n,m}(q_i) \tag{2.58}$$

where the Schmidt eigenvalues are $\lambda_{n,m} = P_m \gamma_n, m$, hence given by the multiplication of the eigenvalues of the two Schmidt decompositions that we applied in succession to derive 2.56. In particular, from 2.55 we can conclude that P_m is the probability of finding the state of the signal in orbital angular momentum m and the idler in $-m$. Therefore we can conclude that in the present case of Gaussian pump profile and *sinc* phase matching function, the entanglement depends upon both the orbital angular momentum and the linear momentum.

The next step would be to derive the Schmidt number so that to estimate the entanglement. However, in the *sinc* case the final expression of the Schmidt decomposition 2.56 does not lead to a closed analytical expression.

2.4.3 HG pump, Gaussian phase-matching – a comparison.

As a last case we consider a first order Hermite-Gaussian pump $HG_{1,0}$ together with the Gaussian phase matching. The biphoton wavefunction is:

$$C_g^{HG}(\vec{\mathbf{q}}_s, \vec{\mathbf{q}}_i) = N_g^{HG} \cdot (q_{s,x} + q_{i,x}) \cdot e^{-\frac{|\vec{\mathbf{q}}_s + \vec{\mathbf{q}}_i|^2}{w_p^2}} e^{-\frac{|\vec{\mathbf{q}}_s - \vec{\mathbf{q}}_i|^2}{\delta_{pm}^2}} \tag{2.59}$$

where $(q_{s,x} + q_{i,x})$ refers to the x components of the transverse wavevectors $\vec{\mathbf{q}}$. The term $(q_{s,x} + q_{i,x}) \cdot e^{-\frac{|\vec{\mathbf{q}}_s + \vec{\mathbf{q}}_i|^2}{w_p^2}}$ represents the $HG_{1,0}$ mode of the pump angular distribution. The decomposition of 2.59 in Schmidt modes is further complicated by the factor $(q_s + q_i)$ and that analysis goes beyond the purposes of this thesis. However, it is interesting to highlight some differences between the present case and the one with Gaussian pump profile.

Comparing equation 2.52 with Eq. 2.59, we can see that in the particular case of $w_p = \delta_{pm} \equiv \delta$ the first wavefunction becomes completely separable in q_s, q_i while the second one is not:

$$C_g^{G}(\vec{\mathbf{q}}_s, \vec{\mathbf{q}}_i) = N_g^{G} e^{-\frac{|\vec{\mathbf{q}}_s + \vec{\mathbf{q}}_i|^2}{w_p^2}} e^{-\frac{|\vec{\mathbf{q}}_s - \vec{\mathbf{q}}_i|^2}{\delta_{pm}^2}} = N_g e^{-2\vec{\mathbf{q}}_s^2/\delta^2} \times e^{-2\vec{\mathbf{q}}_i^2/\delta^2} \tag{2.60}$$

$$\begin{aligned} C_g^{HG}(\vec{\mathbf{q}}_s, \vec{\mathbf{q}}_i) &= N_g^{HG} \cdot (q_{s,x} + q_{i,x}) \cdot e^{-\frac{|\vec{\mathbf{q}}_s + \vec{\mathbf{q}}_i|^2}{w_p^2}} e^{-\frac{|\vec{\mathbf{q}}_s - \vec{\mathbf{q}}_i|^2}{\delta_{pm}^2}} = \\ &= N_g^{HG} \left[q_s e^{-2\vec{\mathbf{q}}_s^2/\delta^2} e^{-2\vec{\mathbf{q}}_i^2/\delta^2} + q_i e^{-2\vec{\mathbf{q}}_i^2/\delta^2} e^{-2\vec{\mathbf{q}}_s^2/\delta^2} \right] \end{aligned} \tag{2.61}$$

I remind that the biphoton amplitude expressed as a function of the transverse wavevector represents indeed the angular distribution of the signal-idler biphoton state. In the first case (eq. 2.60) the angular distribution of the signal is completely uncoupled from that of the idler; hence, both the signal and the idler are in a single-particle state showing a Gaussian distribution: $e^{-2\vec{\mathbf{q}}^2/\delta^2}$. On the other hand, eq. 2.61 shows a final biphoton state which is still not separable in $\vec{\mathbf{q}}_s, \vec{\mathbf{q}}_i$. In particular, it is a superposition of the signal having a Gaussian profile and the idler a $HG_{1,0}$, and viceversa.

The important result here is that while in the case of Gaussian pump profile a particular choice of the parameters can "switch off" the entanglement generating an SPDC state which is separable, the same cannot be said for the *HG* case. No matter what, pumping the nonlinear crystal with a HG beam profile there is always some entanglement in the transverse momentum.

In figure 2.7 we show those differences appearing in the biphoton intensity distribution. First and second rows refers respectively to Gaussian and HG pump beam profile. From left

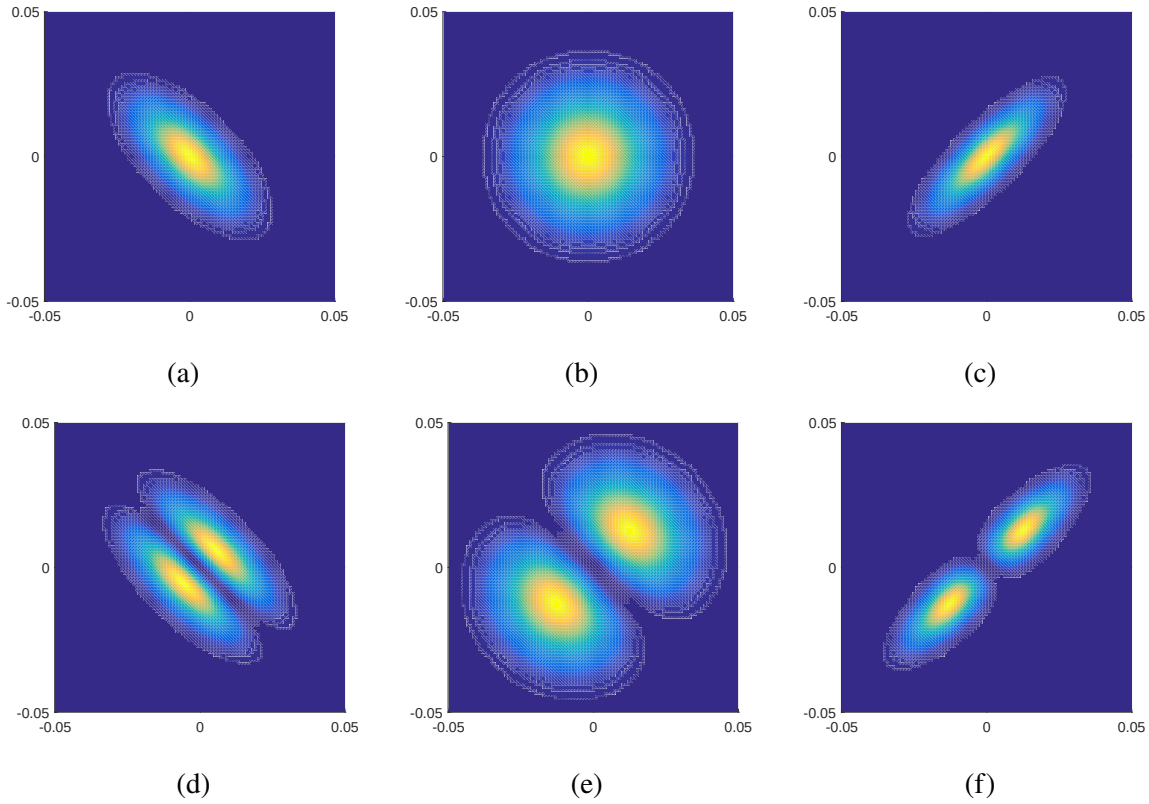

Figure 2.7: Angular distribution of the biphoton wavefunction as a function of signal (x-axis) and idler (y-axis) transverse wavevectors (horizontal component). The first row refers to a Gaussian pump profile $HG_{0,0}$ while the second one to $HG_{1,0}$. In (a) and (d), we fixed the control parameter to 10 and the state shows anticorrelations in both cases. In (c) and (f) the parameter is smaller than 1 (0.1) and the two photon show correlations in both cases. In (b) and (e) the parameter is equal to one and (anti)correlations are still present for the HG pump (e) but absent in the Gaussian case (b). Note that in typical experimental conditions only one of the two widths can be modified (by changing the pump waist). In that case, only one of the two diagonals of the ellipses on the first column would be affected. However, the qualitative result in the form of the shapes of the ellipsoids, would be the same as in the reported in the Figure above.

to right we decreased the control parameter δ_p/δ_{pm}. The interesting part is noticeable in the two plots of the middle column, where the parameter is fixed to 1. While for the Gaussian case the distribution of the two photons is completely uncorrelated, in the case of HG there is still some residual (as expected from 2.60 and 2.61).

This makes the state produced via SPDC using a higher modes pump profile a particularly interesting source of entangled states of light. Further analysis will be given in the following chapters.

2.4.4 Conclusion.

To close the discussion about the Schmidt decomposition, let us summarise the conclusions drawn in the current section. From the general expression of the biphoton wavefunction for SPDC derived in the previous sections (eq. 2.43), we can see that there is a sort of competition between two functions: the pump transverse profile and the phase matching function. They impose correlations in opposite directions, namely in $(q_s + q_i)$ and $(q_s - q_i)$. To regulate

which one of the two correlations leads the process, we introduced a control parameter given by the ratio of the sizes of the two functions: δ_p/δ_{pm}. We related it to experimental parameters as $\delta_p = w_p/2$ and $\delta_{pm} = 2\sqrt{(\alpha L)/(4k_p)}$, where w_p is the waist of the Gaussian pump, L is the length of the crystal, k_p is the wavenumber at the pump wavelength, and α is the factor that approximates the real phase matching function (a *sinc*) to the exponential approximation. By acting on the pump beam waist and the length of the crystal, for the gaussian pump with (approximated) gaussian phase matching we can move from a correlated regime to an anticorrelated regime passing through a completely uncorrelated (separable) regime (for $\delta_p = \delta_{pm}$ - Fig. 2.7). On the other hand, for HG pump and Gaussian phase matching we can see that it is not possible to switch off completely the correlations acting on the width parameters, not even in the case of same value. In that case, the biphoton state has the minimum entanglement possible in which signal and idler are in a superposition of a two-mode state (Eq 2.61).

Regarding the case of real phase matching function (*sinc*), we provided an expression for the Schmidt decomposition but not for the Schmidt number - which we shown to be a quantification of entanglement on a bipartite state. However, recalling the work done by Law and Eberly in [63], we can conclude that in comparison to the case of exponential approximation, with the *sinc* phase matching the trade curve of $K_{s,i}$ is shifted up towards higher values of the Schmidt number, indicating a higher number of modes involved in the state with respect to the approximated case. In particular, the minimum of the plot is not $K = 1$ (which means separability) but rather $K \simeq 1.4$. This translates in the fact that, according to this model, entanglement between signal and idler spatial modes is always present.

2.5 Entanglement criteria.

In the previous sections of this chapter, we derived the biphoton wavefunction generated via SPDC (section 2.2) and we presented a mathematical justification for entanglement based on the Schmidt decomposition (section 2.4). Now we move forward defining the entanglement criteria applicable to the CV states produced in our setup. As usual, we contextualize the final expressions and give a justification for them by starting from the basics.

In [101], Shchukin and Vogel showed that all the known entanglement conditions/inequalities can be derived from an infinite series of inequalities involving the moments of the probability distributions of the states. Their analysis is based on the *negativity of the partial transposition* (NPT) of the *density matrix operator* representing the bi-photon state.

In the matrix formalism, the object representing a quantum state is called density matrix operator. A density matrix operator $\hat{\boldsymbol{\rho}}$ has to obey the following rules:

I $\hat{\boldsymbol{\rho}} \geq 0 \Rightarrow$ real and nonnegative eigenvalues α_n;

II $Tr[\hat{\boldsymbol{\rho}}] \equiv 1 \Rightarrow$ the eigenvalues add up to 1: $\sum_n \alpha_n = 1$;

III $\hat{\boldsymbol{\rho}}$ is Hermitian: $\hat{\boldsymbol{\rho}} = \hat{\boldsymbol{\rho}}^\dagger \Rightarrow$ always diagonizable.

In this formalism, a state of two photons is represented by a density operator $\hat{\boldsymbol{\rho}}$ that lies in the Hilbert space defined by the tensor product of the two Hilbert (sub)spaces of signal and idler. The state of one of the two photons can be then represented by a *reduced* density matrix, which is obtained from the density operator of the total system by partial tracing on the space of the other photon. It can be proved that the operation of partial trace on a density

matrix operator preserves the properties listed above, which means that partial tracing on a density operator returns a density operator.

In general, a quantum state represented by the density matrix operator $\hat{\boldsymbol{\rho}}$ can be factorized on a certain base (not necessarily orthogonal), and expressed as a linear combination of the vectors $\rho^{(n)}$:

$$\hat{\boldsymbol{\rho}} = \sum_{n=0}^{\infty} p_n \rho^{(n)} \tag{2.62}$$

If ρ is a two-mode quantum state, it can be defined as a convex combination of two factorizable states as follow:

$$\hat{\boldsymbol{\rho}} = \sum_{n=0}^{\infty} p_n \rho_1^{(n)} \otimes \rho_2^{(n)} \tag{2.63}$$

where the subscripts 1 and 2 stays for first and second mode respectively. If an expression like 2.63 can be found, then the state ρ is said to be *separable*. On the other hand, if a two-mode state can't be expressed as in eq. 2.63, it is said to be *entangled*.

The concept of full transposition can be defined for both single-mode and multi-partite states. It can be demonstrated that the result of the full transposition of the density matrix representing a quantum state is a density matrix still representing a quantum state (i.e., it still satisfies the three rules mentioned in the previous section when defining the density matrix operator at page 36) [101]. For multipartite states what is called *partial transposition* can be defined as follow: it is the mathematical operation of transposition which acts only on one (or a part) of the mutlipartite state. In contrast with the case of full transposition, partially transposing a quantum state does not guarantee that the final state is still Hermitian.

For a bipartite separable state, ie a quantum state that can be written in the form 2.63, the result of the partial transpose is clearly still a quantum state:

$$\hat{\boldsymbol{\rho}}^{PT} = \sum_{n=0}^{\infty} p_n \rho_1^{(n)} \otimes \rho_2^{(n)T} \tag{2.64}$$

because all the $\rho_2^{(n)T}$ are quantum states. Therefore we can conclude that *the negativity of the partial transpose of a multipartite state is a sufficient (even though not necessary) condition for non separability* - ergo, for entanglement. This reasoning is known as the Peres-Horodecki condition [102–104].

The definition of non-negativity for a Hermitian operator is:

$$\langle \Psi | \hat{\mathbf{A}} | \Psi \rangle = \mathrm{Tr}[\hat{\mathbf{A}} | \Psi \rangle \langle \Psi |] \geq 0 \tag{2.65}$$

for any state $|\Psi\rangle$. Following the demonstration provided for instance in [101], it can be concluded that a necessary and sufficient condition for non-negativity of a Hermitian operator $\hat{\mathbf{A}}$ is that the following inequality is satisfied:

$$\langle \hat{\mathbf{f}}^\dagger \hat{\mathbf{f}} \rangle_{\hat{\mathbf{A}}} = \mathrm{Tr}[\hat{\mathbf{A}} \hat{\mathbf{f}}^\dagger \hat{\mathbf{f}}] \geq 0 \tag{2.66}$$

for any operator $\hat{\mathbf{f}}$ for which it exists a normally ordered form.

Using 2.66 to apply the Peres-Horodecki principle, for any operator $\hat{\boldsymbol{\rho}}$ the inequality 2.66 becomes:

$$\langle \hat{\mathbf{f}}^\dagger \hat{\mathbf{f}} \rangle^{PT} \equiv \langle \hat{\mathbf{f}}^\dagger \hat{\mathbf{f}} \rangle_{\hat{\boldsymbol{\rho}}^{PT}} = \mathrm{Tr}[\hat{\boldsymbol{\rho}}^{PT} \hat{\mathbf{f}}^\dagger \hat{\mathbf{f}}] \geq 0 \tag{2.67}$$

The (normally ordered) operator $\hat{\mathbf{f}}$ can be written as:

$$\hat{\mathbf{f}} = \sum_{n,m,k,l}^{\infty} c_{nmkl} \hat{\mathbf{a}}^{\dagger n} \hat{\mathbf{a}}^{m} \hat{\mathbf{b}}^{\dagger k} \hat{\mathbf{b}}^{l} \tag{2.68}$$

Inserting 2.68 in 2.67, one ends up with:

$$\langle \hat{\mathbf{f}}^{\dagger} \hat{\mathbf{f}} \rangle^{PT} = \sum_{n,m,k,l;p,q,r,s}^{\infty} c^{*}_{pqrs} c_{nmkl} M_{nmkl,pqrs} \geq 0 \tag{2.69}$$

where $M_{nmkl,pqrs}$ represents the general moment of the partial transposition [101]:

$$M_{nmkl,pqrs} = \langle \hat{\mathbf{a}}^{\dagger}_{q} \hat{\mathbf{a}}_{p} \hat{\mathbf{a}}^{\dagger}_{n} \hat{\mathbf{a}}_{m} \hat{\mathbf{b}}^{\dagger}_{s} \hat{\mathbf{b}}_{r} \hat{\mathbf{b}}^{\dagger}_{k} \hat{\mathbf{b}}_{l} \rangle^{PT} \tag{2.70}$$

where ultimately $\hat{\mathbf{a}}$ and $\hat{\mathbf{b}}$ are the annihilation operators of the two modes that we are considering.

According to the *Silvester criteria*,inequality 2.70 is satisfied for all possible coefficients c if and only if all the main minors of the expression 2.69 are nonegative.

Hence, one only has to write a non-negativity inequality for the minors, and to express the moments of the partially transposed state as a function of the moments of the original one. Defining an ordering in the indexes $(nmkl, pqrs)$, the moments of the original state can be written as [101]:

$$\langle \hat{\mathbf{a}}^{\dagger}_{q} \hat{\mathbf{a}}_{p} \hat{\mathbf{a}}^{\dagger}_{n} \hat{\mathbf{a}}_{m} \hat{\mathbf{b}}^{\dagger}_{s} \hat{\mathbf{b}}_{r} \hat{\mathbf{b}}^{\dagger}_{k} \hat{\mathbf{b}}_{l} \rangle^{PT} = \langle \hat{\mathbf{a}}^{\dagger}_{q} \hat{\mathbf{a}}_{p} \hat{\mathbf{a}}^{\dagger}_{n} \hat{\mathbf{a}}_{m} \hat{\mathbf{b}}^{\dagger}_{l} \hat{\mathbf{b}}_{k} \hat{\mathbf{b}}^{\dagger}_{r} \hat{\mathbf{b}}_{s} \rangle \tag{2.71}$$

The nonegativity condition for all the minors in 2.70 can then be expressed in a matrix form as [101]:

$$\forall N : D_N = \begin{vmatrix} M_{11} & M_{12} & \dots & M_{1N} \\ M_{21} & M_{12} & \dots & M_{2N} \\ \dots & \dots & \dots & \dots \\ M_{N1} & M_{N2} & \dots & M_{NN} \end{vmatrix} \geq 0 \tag{2.72}$$

is valid for each positive integer N, with:

$$M_{ij} = \langle \hat{\mathbf{a}}^{\dagger}_{q} \hat{\mathbf{a}}_{p} \hat{\mathbf{a}}^{\dagger}_{n} \hat{\mathbf{a}}_{m} \hat{\mathbf{b}}^{\dagger}_{l} \hat{\mathbf{b}}_{k} \hat{\mathbf{b}}^{\dagger}_{r} \hat{\mathbf{b}}_{s} \rangle \tag{2.73}$$

where the index i corresponds to the ordered set of indexes (n, m, k, l) and j to (p, q, r, s). It might be useful to rewrite the matrix 2.72 with the explicit moments of the two modes a and b. It reads:

$$D_N = \begin{vmatrix} 1 & \langle \hat{a} \rangle & \langle \hat{a}^{\dagger} \rangle & \langle \hat{b}^{\dagger} \rangle & \langle \hat{b} \rangle & \dots \\ \langle \hat{a}^{\dagger} \rangle & \langle \hat{a}^{\dagger} \hat{a} \rangle & \langle \hat{a}^{\dagger 2} \rangle & \langle \hat{a}^{\dagger} \hat{b}^{\dagger} \rangle & \langle \hat{a}^{\dagger} \hat{b} \rangle & \dots \\ \langle \hat{a} \rangle & \langle \hat{a}^{2} \rangle & \langle \hat{a} \hat{a}^{\dagger} \rangle & \langle \hat{a} \hat{b}^{\dagger} \rangle & \langle \hat{a} \hat{b} \rangle & \dots \\ \langle \hat{b} \rangle & \langle \hat{a} \hat{b} \rangle & \langle \hat{a}^{\dagger} \hat{b} \rangle & \langle \hat{b}^{\dagger} \hat{b} \rangle & \langle \hat{a}^{2} \rangle & \dots \\ \langle \hat{b}^{\dagger} \rangle & \langle \hat{a} \hat{b}^{\dagger} \rangle & \langle \hat{a}^{\dagger} \hat{b}^{\dagger} \rangle & \langle \hat{b}^{\dagger 2} \rangle & \langle \hat{b} \hat{b}^{\dagger} \rangle & \dots \\ \dots & \dots & \dots & \dots & \dots & \dots \end{vmatrix} \tag{2.74}$$

Necessary and sufficient condition for non-negativity of the partial transposition of a bipartite quantum state is that all the determinants of 2.74 are non-negative, that is:

$$\forall N : D_N \geq 0 \tag{2.75}$$

Table 2.1

CV		single-photon
many photons	$\rightarrow$	one photon
one mode	$\rightarrow$	many modes
$\hat{\mathbf{E}} \propto \hat{\mathbf{a}}^\dagger + \hat{\mathbf{a}}$	$\rightarrow$	$\hat{\mathbf{x}}_a = \frac{1}{\sqrt{2}}(\hat{\mathbf{a}} + \hat{\mathbf{a}}^\dagger)$
$\hat{\mathbf{B}} \propto \hat{\mathbf{a}}^\dagger - \hat{\mathbf{a}}$	$\rightarrow$	$\hat{\mathbf{p}}_a = \frac{i}{\sqrt{2}}(-\hat{\mathbf{a}} + \hat{\mathbf{a}}^\dagger)$

Therefore, if a negative determinant exist, that is if:

$$\exists N : D_N \leq 0 \tag{2.76}$$

the bipartite state is non-separable.

This result has been derived in the context of the electromagnetic field operators ($\hat{\mathbf{E}}, \hat{\mathbf{B}}$). Since they are continuous variable operators, the reasoning can be applied in the same way to the states of two and four photons that we generate in our setup. Indeed, we can map the many photons in one single mode of the first case to the many modes of one single photon of our case (table 2.1). In particular, we substitute the creation/annihilation operators $\hat{\mathbf{a}}, \hat{\mathbf{a}}^\dagger$ with the usual definition of position and momentum operator as:

$$\begin{aligned} \hat{\mathbf{a}} &= \frac{1}{\sqrt{2}}(\hat{\mathbf{x}} + i\hat{\mathbf{p}}) \\ \hat{\mathbf{a}}^\dagger &= \frac{1}{\sqrt{2}}(\hat{\mathbf{x}} - i\hat{\mathbf{p}}) \end{aligned} \tag{2.77}$$

where with $\hat{\mathbf{x}}$ and $\hat{\mathbf{p}}$ we identify respectively the position and momentum quantum operators in the mode identified by $\hat{\mathbf{a}}$.

To summarize, the inequality 2.76 is a *necessary and sufficient* condition for negativity of the partial transposition (NPT), which in turn is a *sufficient* condition for entanglement. This is a general result that applies to any CV bipartite state. Now we turn to the particular cases of Gaussian mode entanglement and genuine non-Gaussian entanglement that we investigated, appropriate combinations of the minors will be worked out respectively in section 2.5.1 and 2.5.2.

2.5.1 Non-separability criteria for Gaussian mode entanglement.

We have derived from first principles a general hierarchy of necessary and sufficient conditions for negativity of the partial transpose of a state, which in turn is a sufficient condition for entanglement (see section 2.5). The main conclusion we drew is that for continuous variable systems entanglement witnesses can be expressed in terms of the moments of the individual and join probability distributions (of the bipartite state). The power of the result just mentioned lies in the fact that it applies in general to any state [101]. entanglement witness for different states may require a different combination of the moments of the single and joint distributions, however they can be derived from the general result reached in 2.5.

Many of the most common second order separability criteria such as the ones presented in [105–107], can be derived from the general principle mentioned above as combinations of the determinants of different minors of the matrix constructed from 2.74 fixing $N = 2$ [101]:

$$D_2 = \begin{vmatrix} 1 & \langle\hat{a}\rangle & \langle\hat{a}^\dagger\rangle & \langle\hat{b}^\dagger\rangle & \langle\hat{b}\rangle \\ \langle\hat{a}^\dagger\rangle & \langle\hat{a}^\dagger\hat{a}\rangle & \langle\hat{a}^{\dagger 2}\rangle & \langle\hat{a}^\dagger\hat{b}^\dagger\rangle & \langle\hat{a}^\dagger\hat{b}\rangle \\ \langle\hat{a}\rangle & \langle\hat{a}^2\rangle & \langle\hat{a}\hat{a}^\dagger\rangle & \langle\hat{a}\hat{b}^\dagger\rangle & \langle\hat{a}\hat{b}\rangle \\ \langle\hat{b}\rangle & \langle\hat{a}\hat{b}\rangle & \langle\hat{a}^\dagger\hat{b}\rangle & \langle\hat{b}^\dagger\hat{b}\rangle & \langle\hat{a}^2\rangle \\ \langle\hat{b}^\dagger\rangle & \langle\hat{a}\hat{b}^\dagger\rangle & \langle\hat{a}^\dagger\hat{b}^\dagger\rangle & \langle\hat{b}^{\dagger 2}\rangle & \langle\hat{b}\hat{b}^\dagger\rangle \end{vmatrix} \tag{2.78}$$

For assessing Gaussian mode entanglement we can use the Mancini-Giovannetti-Vitali-Tombesi criteria [107] which is very useful for bipartite Gaussian state correlated in momentum-position. It can be derived from 2.78 by choosing the following minor:

$$d = \begin{vmatrix} 1 & \langle\hat{a}\rangle & \langle\hat{b}^\dagger\rangle \\ \langle\hat{a}^\dagger\rangle & \langle\hat{a}^\dagger\hat{a}\rangle & \langle\hat{a}^\dagger\hat{b}^\dagger\rangle \\ \langle\hat{b}\rangle & \langle\hat{a}\hat{b}\rangle & \langle\hat{b}^\dagger\hat{b}\rangle \end{vmatrix} \tag{2.79}$$

By imposing $d \geq 0$, a separable bipartite (Gaussian) state must satisfy the following inequality:

$$\langle\Delta^2(x_s \pm x_i)\rangle\langle\Delta^2(p_s \mp p_i)\rangle \geq 1 \tag{2.80}$$

where $\langle\Delta^2()\rangle$ indicates the expectation value of the variance; the variables x and p here indicate the position and the momentum of signal and idler (according to the definition 2.84). Those correlation functions can be ultimately expressed as a linear combination of the moments:

$$\langle\Delta^2(v_1 \pm v_2)\rangle = \langle v_1^2\rangle - \langle v_1\rangle^2 + \langle v_2^2\rangle - \langle v_2\rangle^2 \pm 2\langle v_1 v_2\rangle \mp 2\langle v_1\rangle\langle v_2\rangle \tag{2.81}$$

for variables v being either x or p.

2.5.2 Non-separability criteria for genuine non-Gaussian entanglement.

In the previous sections regarding the Hermite-Gaussian modes, we have seen how the spatial properties of the pump profile are transferred to the down converted fields. We have also shown how this does not mean that in all the cases a structured profile of the pump field, such as HG_{10}, is automatically observable in the biphoton state. In a few words, it depends on which term is more relevant in the wavefunction amplitude 2.27, whether the phase matching *sinc* function or the pump angular amplitude $A_p(q_p)$.

If the experimental conditions are such that the entanglement, or at least part of it, lies in the Gaussian mode of the SPDC fields, then the non-separability criteria introduced earlier for Gaussian states 2.80 *may* still hold. For all other cases, genuine non-Gaussian entanglement is present and a higher order separability criteria is needed in order to detect it. An example of such states is the one in 2.48, which is composed by a first-order Hermite-Gaussian term $HG_{10}(\vec{\mathbf{q}}_s + \vec{\mathbf{q}}_i)$ (which represents the pump profile) and a Gaussian term $HG_{00}(\vec{\mathbf{q}}_s - \vec{\mathbf{q}}_i)$ (the exponential approx of the phase matching function) multiplied together. It can be proven [90] that for some range of values of the widths of the exponentials, the state 2.48 while does not violate the entanglement criteria for Gaussian modes 2.80, it does violate the higher-mode criteria that we are deriving in the following paragraphs.

I recall here the arguments developed in section 2.5 about negativity of the partial transpose (NPT) and non-separability of the density operator. From the general matrix 2.74, chosen for $N = 4$, we can consider the following minor [90]:

$$M_4^{HO} = \begin{vmatrix} 1 & \langle \hat{\mathbf{a}}\hat{\mathbf{b}}^\dagger \rangle \\ \langle \hat{\mathbf{a}}^\dagger \hat{\mathbf{b}} \rangle & \langle \hat{\mathbf{a}}^\dagger \hat{\mathbf{a}} \hat{\mathbf{b}}^\dagger \hat{\mathbf{b}} \rangle \end{vmatrix} \tag{2.82}$$

where in our notation M stands for "minor", the superscript HO stays for "higher order" to emphasize that its scope is for modes higher than the fundamental HG_{00}, and the subscript 4 reminds that the matrix is a minor of the fourth order correlations matrix. Indeed we can see that the matrix element $M_4^{HO}(2,2)$ is a moment of the fourth order, involving the two modes $\hat{\mathbf{a}}$ and $\hat{\mathbf{a}}^\dagger$ for signal photon and the two modes $\hat{\mathbf{b}}$ and $\hat{\mathbf{b}}^\dagger$ for the idler.

For any separable state, $M_4^{HO} \geq 0$, which means that necessary and sufficient condition for entanglement is [90]:

$$det[M_4^{HO}] < 0 \tag{2.83}$$

In order to be able to apply the criteria 2.83 to a real experimental setup, one needs to express the operators $\hat{\mathbf{a}}, \hat{\mathbf{a}}^\dagger, \hat{\mathbf{b}}, \hat{\mathbf{b}}^\dagger$ as a function of some measurable quantity. In our case we are interested in measuring the momentum and position of the fields, therefore here again we involve the *quantum operators* for momentum ($\hat{\mathbf{p}}$) and position ($\hat{\mathbf{x}}$). From the usual definition of annihilation and creation operators:

$$\hat{\mathbf{a}} = \frac{1}{\sqrt{2}}(\hat{\mathbf{x}} + i\hat{\mathbf{p}}) \tag{2.84}$$

$$\hat{\mathbf{a}}^\dagger = \frac{1}{\sqrt{2}}(\hat{\mathbf{x}} - i\hat{\mathbf{p}}) \tag{2.85}$$

and by considering that as usual $\hat{\mathbf{x}}$ and $\hat{\mathbf{p}}$ do not commute: $[\hat{\mathbf{x}}, \hat{\mathbf{p}}] = i$, we can derive the position and momentum operators as [90]:

$$r\hat{\mathbf{x}}_a = \frac{1}{\sqrt{2}}(\hat{\mathbf{a}} + \hat{\mathbf{a}}^\dagger) \tag{2.86}$$

$$\frac{1}{r}\hat{\mathbf{p}}_a = \frac{i}{\sqrt{2}}(-\hat{\mathbf{a}} + \hat{\mathbf{a}}^\dagger) \tag{2.87}$$

with the commutator not being affected by the parameter r: $[r\hat{\mathbf{x}}_a, \hat{\mathbf{p}}_a/r] = i$. The subscript a stays either for signal or idler. Here r is a local parameter which does not affect the entanglement since it doesn't change the commutator - and therefore it can be chosen arbitrarily [108]. Applying the definitions 2.86 in the inequality 2.83, we can finally derive the criteria as a function of the following moments [90]:

$$\begin{aligned} &1 + r^4\langle\Delta^2(\hat{\mathbf{x}}_a\hat{\mathbf{x}}_b)\rangle + \langle\Delta^2(\hat{\mathbf{x}}_a\hat{\mathbf{p}}_b)\rangle + \langle\Delta^2(\hat{\mathbf{p}}_a\hat{\mathbf{x}}_b)\rangle + \\ &+ \frac{1}{r^4}\langle\Delta^2(\hat{\mathbf{p}}_a\hat{\mathbf{p}}_b)\rangle + 2\langle\hat{\mathbf{x}}_a\hat{\mathbf{p}}_b\rangle\langle\hat{\mathbf{p}}_a\hat{\mathbf{x}}_b\rangle - 2\langle\hat{\mathbf{x}}_a\hat{\mathbf{x}}_b\rangle\langle\hat{\mathbf{p}}_a\hat{\mathbf{p}}_b\rangle + \\ &- r^2\left[\langle\hat{\mathbf{x}}_a^2\rangle + \langle\hat{\mathbf{x}}_b^2\rangle\right] - \frac{\langle\hat{\mathbf{p}}_a^2\rangle + \langle\hat{\mathbf{p}}_b^2\rangle}{r^2} \geq 0 \end{aligned} \tag{2.88}$$

where $\langle\Delta^2 w\rangle$ is the expectation value of the variance of the operator w defined as: $\langle\Delta^2 w\rangle = \langle w^2\rangle - \langle w\rangle^2$.

As anticipated at the beginning of this section, the biphoton state generated by pumping the SPDC crystal with a Hermite-Gaussian profile 2.48 does not violate the Gaussian-mode entanglement criteria for $0.57 < \sigma_p/\sigma_{PM} < 1.73$; however, it does violate 2.88 for a narrower set of values $0.63 < \sigma_p/\sigma_{PM} < 1.58$ (using $r = 2/\sigma_{PM}$) [90]. That means that within this range of values $0.63 < \sigma_p/\sigma_{PM} < 1.58$, in general there is no second order non-separability criteria that can detect entanglement while the higher-order one does. Again, this is due to the fact that entanglement lies in spatial modes higher than the Gaussian.

3
Experimental setup.

What we observe is not nature itself, but nature exposed to our method of questioning.

Werner Heisenberg

In the present chapter we go through the experimental aspects of our investigations. Via the process of Spontaneous Parametric Down Conversion (SPDC) we create momentum entangled two-photon states. We tag the photons *signal* and *idler* and we distinguish between them by the wavelength, which is $783nm$ for the signal and $837nm$ for the idler. Other than the standard Gaussian profile, with our setup we can pump the nonlinear crystal also with structured light. For that purpose we transform the Gaussian profile of a diode laser into a first-order Hermite-Gaussian one, and the downconverted photons show correlations beyond Gaussianity.

We begin with a brief technical overview of the setup (3.1). Some among the most relevant elements will be described in the following subsections 3.1.1, 3.1.2, and 3.1.3; we mention their specifications as well as the basic working principles (when necessary). The aim here is to give enough background information to the non experimentalists in order for them to be able to follow and understand not only the principles and the results presented in this theses, but also to grasp the physics behind the experimental methods.

In the second part of the chapter (section 3.2) we give a complete and detailed description of the experimental apparatus. We split the presentation in five blocks following the block diagram shown in figure 3.1: pump laser 3.2.1; polarization control of the pump beam 3.2.2; generation of the SPDC states 3.2.3; conditioning of the downconverted fields 3.2.4; detection 3.2.5.

3.1 A brief overview of the apparatus.

In figure 3.1 is represented a block diagram of our experimental setup. It can be schematized in five separate blocks. First, one needs a laser as source of energy to be (down)converted

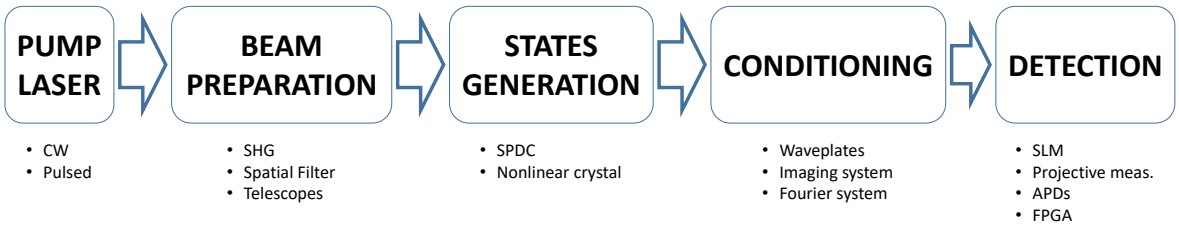

Figure 3.1: Block diagram of our experimental setup (description in the text).

in quantum states of light. For the experiments presented in this thesis we need to different kinds of lasers, as explained in section 3.1.1.

The pump preparation block consists of a nonlinear element for the upconversion of the pump laser frequency from the near-IR to the near-UV. This nonlinear process is called Second Harmonic Generation (SHG) and will be mentioned in section 3.1.1 too. Furthermore, the spatial profile as well as the beam waist of the pump laser need to be controlled and appropriately prepared through the utilization of spatial filters and telescopes.

The generation of quantum light happens within a periodically-poled second-order nonlinear crystal. This process is of fundamental importance for our experiments and therefore it was treated thoroughly in the (dedicated) previous chapter (chapter 2).

After the crystal we separate the residual pump laser from the downconverted (signal and idler) photon beams. The conditioning block represents waveplates for the preparation of the beams in the appropriate polarization state and two systems of lenses for accessing the real and Fourier spaces of the generated fields.

The detection involves the use of a Spatial Light Modulator (SLM) for imprinting a spatial dependent phase on signals and idlers photons (section 3.1.2). Finally, we perform a projective measurement in polarization states using waveplates and linear polarizers. An array of fiber coupled Avalanche Photo Diodes (APDs) converts the optical energy of single photons into TTL signals which are eventually counted by a four-channels FPGA unit specifically programmed.

3.1.1 Lasers.

There exist many different kind of lasers on the market. Their differences lie in the working principles, in the amount of power generated (high-power lasers are utilized, for instance, for metal cuts; lower-power lasers utilized for information communications), or other specific requirements such as spectral spreading or power stability. In our laboratories we have several different kinds of what we can consider low-power lasers. For the experiments described in this thesis we had to choose two different lasers. This is due to the complementarity of the specs required by the different measurements that we run.

A laser can be naively defined as a source of coherent light whose propagation is characterized by low divergence. From the temporal point of view we can separate lasers in two categories: **C**ontinuous **W**avelength (CW) and pulsed. In particular, the spectral emission of the former can be often considered single-frequency (monochromatic) for their spectral linewidth that can be very narrow.

For the simpler experiments in the two-photon regime we utilized a CW laser. The main advantage of CW lasers versus pulsed ones is that the narrow linewidth that allows us to consider them monochromatic. Indeed, optimally one would like to pump the nonlinear crystal with a single frequency source. The reason is that each single frequency of the pump

Table 3.1: Principal specifications of our continuous wave laser *TOPTICA TopMode 405-HP*.

Characteristic	Value	Units
Power	100	mW
Wavelength	404.0	nm
Linewidth	< 5	MHz
Coherence length	> 25	m
Linear Polarization	> 100:1	–
Beam diameter	1	mm
Power stability	< 0.5%	(STD/mean)/h
Wavelength stability	< 1	pm/h

Table 3.2: Principal specifications of our pulsed laser *Coherent Chameleon ULTRA*.

Characteristic	Value	Units
Power (@800nm)	3.3	$Watt$
Wavelength	680-1080	nm
Linewidth	1.2× FL[1]	
Repetition rate	80	MHz
Pulse width	140	fs
Linear Polarization	> 500:1	–
Beam diameter	1.2 ± 0.2	mm
Power stability	< 0.5%	(STD/mean)/h
Beam ellipticity	0.9-1.1	–

undertaking downconversion generates a photon pair with locked frequencies per each spatial mode. That is, in each direction, say at the angle θ from the pump propagation direction, only one frequency of the signal and consequently one frequency of the idler are phase-matched. By selecting one given angle of the downconversion, for instance with a pinhole, one only couples one single frequency for the signal and one single frequency for the idler.

Of course, a single-frequency laser is an idealization of what is realistically available on the market. However, lasers with very narrow linewidth can be considered single-frequency for many purposes. For our experiment we ordered a high-quality monochromatic laser from *TOPTICA Photonics*. The model is *TopMode 405-HP*. It is a fixed-frequency laser (ie, not tunable) with a linewidth of less than $5MHz$ (declared by the producer) around the wavelength $404.0nm$ (measured by us). The main specs are grouped together in table 3.1.

For the generation of the 4-photon spatially entangled states we need a very narrow pulsed pump. In that way we can ensure a temporal localization of the single pairs produced. We could rely on a sophisticated tunable titanium-sapphire (*Ti:Sap*) machine produced by *Coherent*. The model is a *Chameleon Ultra* and it lases pulses of about $140fs$ at a rate of $80MHz$ (further specs in table 3.2).

The gain of the active medium of this kind of lasers does not permit them to emit in the short wavelength regime needed for our experiment. Therefore, we *upconvert* the output of the Ti:Sap by exploiting a nonlinear process similar to SPDC, called **S**econd **H**armonic **G**eneration (SHG). For this purpose we utilized the built in Harmonic Generator System produced by *Coherent*. By pumping it with the Ti:Sap, we can convert pulses at $810nm$ to the near-UV frequency of $405nm$ with an efficiency of about $30-35\%$ (depending on the

alignment)[2]. The efficiency of the process ultimately limits the total accessible pump power to $1.6W$, which is still enough for our purposes since the estimated breakdown threshold of our nonlinear crystal is around $350mW$ of pump power.

Compared with the CW laser, for a pulsed coherent source the spectrum is determined by the temporal confinement of the energy: the shorter the pulse, the wider the spectrum. The reason of this can be ultimately found in the time-energy form of the Heisenberg principle or equivalently in the Fourier theorem. The theoretical limit is reached when the time-frequency product for the pulse saturates the Heisenberg inequality, reaching the so called *Fourier-limited* regime.

Therefore, the short temporal confinement of the pulses limit the minimum width of the power spectrum. This is true for any electromagnetic field, not only for lasers. The explanation of the technical details goes beyond the purposes of this thesis, since they would not add any discussion interesting for our experimental results. For what concerns us, it is enough to say that the limit fixed by the Heisenberg principle for the temporal confinement of the field (within the pulse) and the frequency spectrum depends on the temporal shape of the pulse itself. In the case of a Ti:Sap, the typical shape of the pulse is called hypersecant ($sech^2$) and the limit is [109]:

$$\Delta\nu\Delta\tau \geq 0.315 \tag{3.1}$$

When the inequality saturates, that is when the product of the temporal duration of the pulse and its bandwidth equals 0.315, we say that the pulse is Fourier Limited (NB: this number applies only for $sech^2$ pulses. For different temporal shapes of the pulse the numerical value of the product in Eq. 3.1 is different).

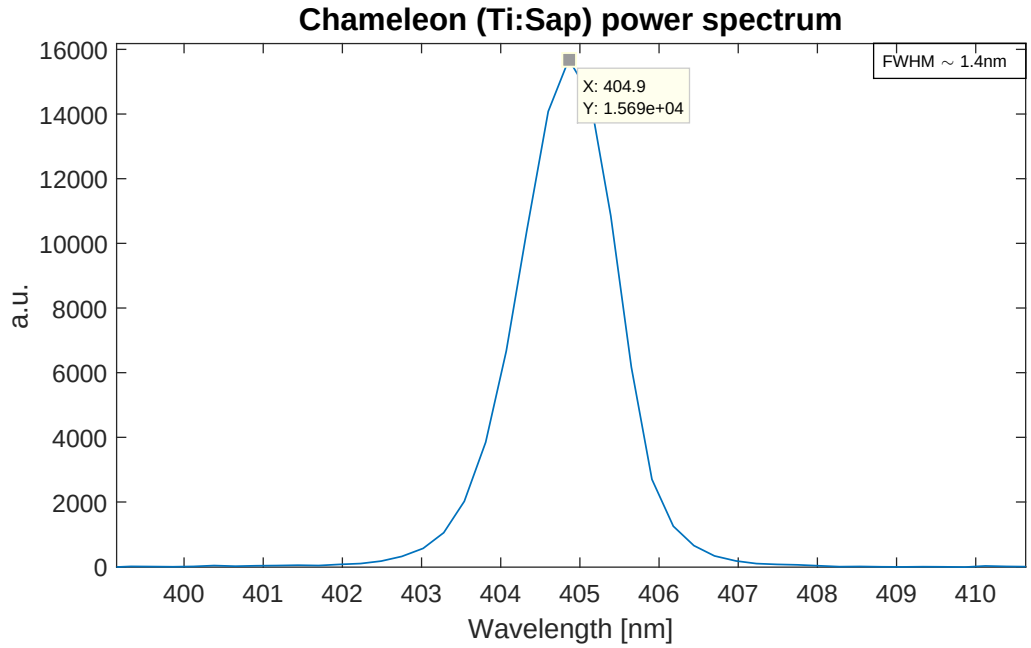

Figure 3.2: Typical spectrum of the TiSap laser after the radiation has been upconverted by the SHG. Detected by a commercial spectrometer produced by *Ocean Optics*.

In practise, a Fourier limited pulse is technically very challenging to achieve. The typical values for commercial Ti:Sap such as ours are 10 to 30 percent higher than the Fourier Limit

[2]https://www.coherent.com/lasers/laser/ultrafast-oscillator-accessories/harmonic-generator

[109]. In figure 3.2 we show the spectrum of the TiSap pump laser at the crystal plane, that is after the SHG and several optics.

3.1.2 Spatial Light Modulator (SLM).

In recent years Spatial Light Modulators (SLM) have been extensively used in several fields of optics. In quantum optics in particular they found employment from engineering high dimensional states (*qudit*) in Ref. [110], to implementation of quantum logic gates for continuous variables quantum computation [111], to the extensive study of Orbital Angular Momentum (OAM) [48, 112–114]. In this section we briefly introduce what a Spatial Light Modulator (SLM) is: main specifics, working principle, and why we choose a particular device for our experiment. The information given here should be enough for the reader to understand the experiment as well as the results.

There exists several kinds of spatial light modulators. All of them are electro-optical devices that introduces a spatially controllable modulation on an electromagnetic field (a beam of light) interacting with them. The first distinction is whether the SLM works in reflection or in transmission. There is not much to say about this point, the principles are the same: while in one case the photons pick up the modulation and are transmitted, in the other they are reflected by a passive mirror of some sort placed behind the active area of the device.

A more significant differentiation is found in the domain that is subjected to modulation. Some SLMs act on the (spatial) phase of the beam, some on the (spatial) amplitude, and some others modulate both. In our case we used a reflective, *phase-only* spatial light modulator, hence we concentrate in the analysis on that category only.

To give an idea of what we are talking about to the readers who have never seen an SLM, figure 3.3 shows a photo of the device that we used in our experiments. The active area is a matrix of electrodes that spatially controls a layer of liquid crystals forming de facto a very dense liquid crystal on silicon (LCOS) microdisplay. The dimensions of the display are about 15mm wide and 8.6mm high and with $8 \times 8 \mu m^2$ pixel size it has a full-HD resolution ($1920 \times 1080 Px^2$).

The liquid crystals are made by birefringent material. By applying an appropriate electric field to each pixel of the electrodes matrix, it is possible to tilt the birefringent molecules locally. Different electric fields imply different tilts (figure 3.4). Changing the tilt ultimately changes the optical path travelled by the photons of the incident beam through those birefringent materials. The effect is that of a different phase for different tilt of the local molecules.

Because of the birefringence of the liquid crystals molecules, the SLM affects only one direction of the linear polarization, say horizontal. The orthogonal one, ie vertical, is not affected by any phase modulation. The overall effect on the reflected beam is that of a two-dimensional, spatial phase $S(x, y)$ on the horizontal polarization, where x, y are respectively the horizontal and vertical dimensions on the display, and a phase zero on the vertical one. In formulae, the effect of a general phase on the input polarization state $|\psi\rangle = |H\rangle + |V\rangle$ can be expressed as:

$$|\psi^{'}\rangle = S(x, y)|H\rangle + I|V\rangle \tag{3.2}$$

where I is the identity operator acting on the general quantum state indicated in bra-ket notation $|...\rangle$. We will exploit in the following two chapters this spatial-polarization feature to explain an innovative detection method that we implemented in parallel to a more standard one.

Figure 3.3: Spatial Light Modulator. Producer: *Holoeye photonics AG*. Model: *PLUTO-NIR-015-HR*. The active area is limited to the mirror-looking rectangle in the bottom-right part of the photo. The black plastic box in the back encloses the driver unit. Source: http://holoeye.com/spatial-light-modulators/slm-pluto-phase-only/

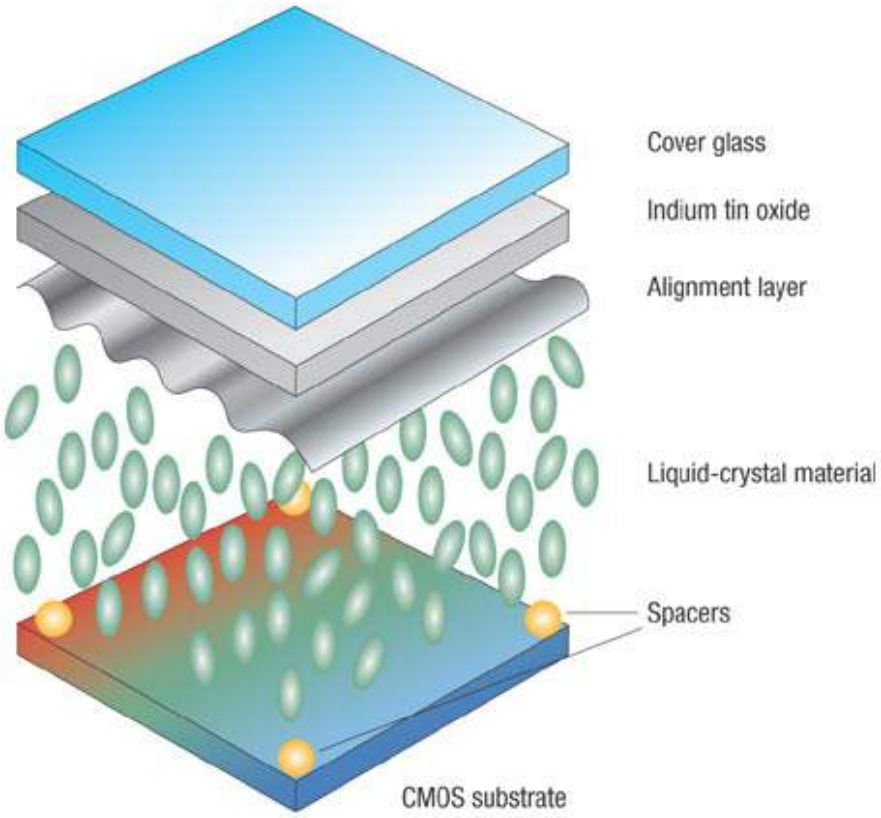

Figure 3.4: Spatial Light Modulator. The liquid crystals are deposited on a silicon substrate. The tilt of the ellipsoid molecules is driven by the potential between two electrodes - one being represented by the pixel itself. Source: http://www.nature.com/nphoton/journal/v1/n5/fig_tab/nphoton.2007.63_F1.html (in reference [115]).

The SLM is connected to a computer via a standard video cable and detected and driven by the computer itself as an extra monitor, through the video card. The pixels of the images sent to the SLM are read by the driver as phase levels and converted accordingly to an electric potential. The pixels are accessed independently, which means that each of the 2MPx can be set independently to a different potential, which in turn translate in different phases on the incident photons polarized in the sensitive direction.

The phases are encoded in the greylevels of the images sent to the SLM driver. In particular, the standard for this device is an 8-bit (256) greylevel image on the green channel of the RGB (Red Green Blue) standard. Since we needed to program the SLM with complex phases, we could not rely on the GUI (Graphic User Interface) provided by the producer. We built our own home made software based on the *LabView* programming language.

Before to be able to use the SLM it is a good practise to calibrate it. A precise calibration based on interferometric techniques is recommended by the producer. However, building a good look up table (LUT) can be enough.

The problems that one tackles by building a LUT are two: first, the nonlinearity of the phases introduced with respect to the greylevel (and in turn, the electric potential) passed to the SLM; second, the maximum interval of exactly 2π between greylevel zero and greylevel 255. The first is clear: one wants that whenever the greylevel is increased by each single greylevel $(1/256)$, the increasing in phase imposed on the incident beam is always of the same amount. The second regards the fact that it could happen - and in general it does - that the full range of phases available over the 256 greylevels is larger than 2π. In that case one needs to drop part of the greylevels such that when a pixel is passed greylevel 0 the phase is 0, and when the greylevel is 255 the phase is $(255/256) \times 2\pi$.

In our case we realised that building a LUT was enough. The procedure for applying such a correction is easy. One has to build the LUT which is nothing but a conversion table (figure 3.5) that translated the wanted greylevel, say 134, to the greylevel that is needed by the drivers for the particular potential that generates $(134/256) \times 2\pi$. The conversion table is in general different for each single pixel of the SLM; that's why the producer recommends a precise interferometric measurement. However, the larger differences are global rather than local. For this reason the measurement we performed in order to build the LUT consisted in a uniform flat-phase scan, from 0 to 2π, over the entire display. The experimental procedure is the following: we set the polarization of the incident beam to $+45°$; we set a polarization control before the detector such that only the $+45°$ (or $-45°$) polarization is detected; in this conditions, we run a scan of all the 256 greylevels on the entire SLM by sending a sequence of uniform images and recording the power coupled. The result of our measurement with the not-calibrated SLM is shown in figure 3.6.

For a linear response over a range of exactly 2π, what we aimed to see was one full period of a cosinusoidal curve. The result is usually not linear, neither limited to one full cycle (figure 3.7, left). By mapping the $[0 - 255]$ greylevels to the correspondent greylevels interval corresponding to $[0 - 2\pi)$ phase, we could account for both nonlinearity and extra-2π phase interval. Repeating the scan with the LUT applied one expect to reconstruct exactly one period of sinusoidal curve. The results of the scans with and without superimposing the LUT are shown for comparison in figure 3.7, where we plot only the selected interval from the full greylevel range.

Comparing the plots in figure 3.7, we can see that by applying the LUT the phase imposed by the SLM on the incident beam corresponds to the cosinusoid function on a full period. One further step is needed to finalise the LUT. We simply needed to shift the entire column of values by 29 positions in order to center the cosine function on the selected greylevel interval.

WANTED GREYLEVEL		MAPPED GREYLEVEL
1	→	16
2	→	17
3	→	17
4	→	18
5	→	19
6	→	19
7	→	20
8	→	21
9	→	21
10	→	22
11	→	23
12	→	24
13	→	24
14	→	25
15	→	26
16	→	27
17	→	27
18	→	28
19	→	29
20	→	30
21	→	30
22	→	31
...	→	...

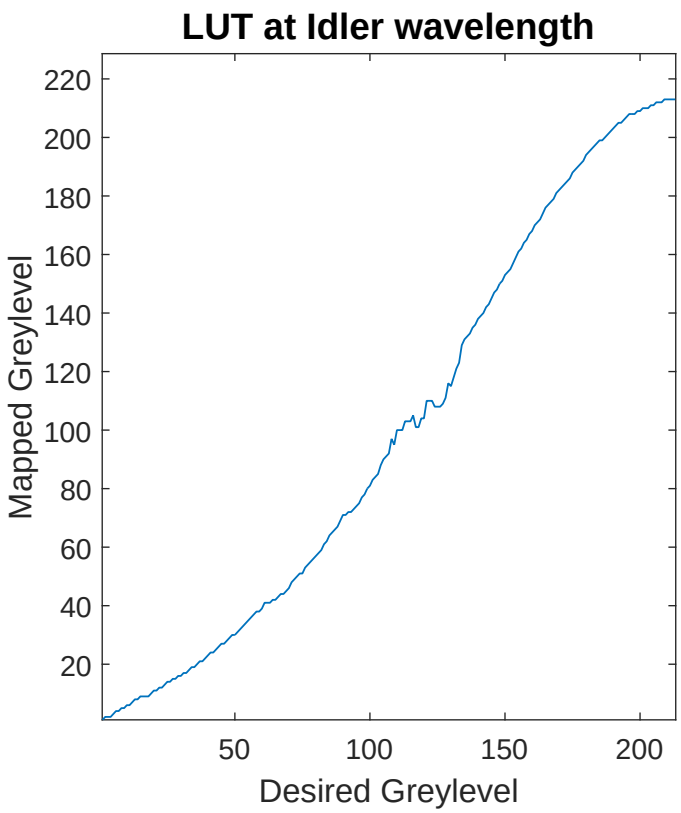

Figure 3.5: Example of a part of the LUT that we built to calibrate our PLUTO SLM (on the left). On the right, we plot the entire LUT. We note that it is limited to the maximum value of 213; this is due to the selection of the part of the greylevels range that provides a 2π phase interval (in particular we only use values between 44 and 255). The photonic beam utilized for the measurement is the idler produced via SPDC by pumping the crystal with the TiSap pulsed laser.

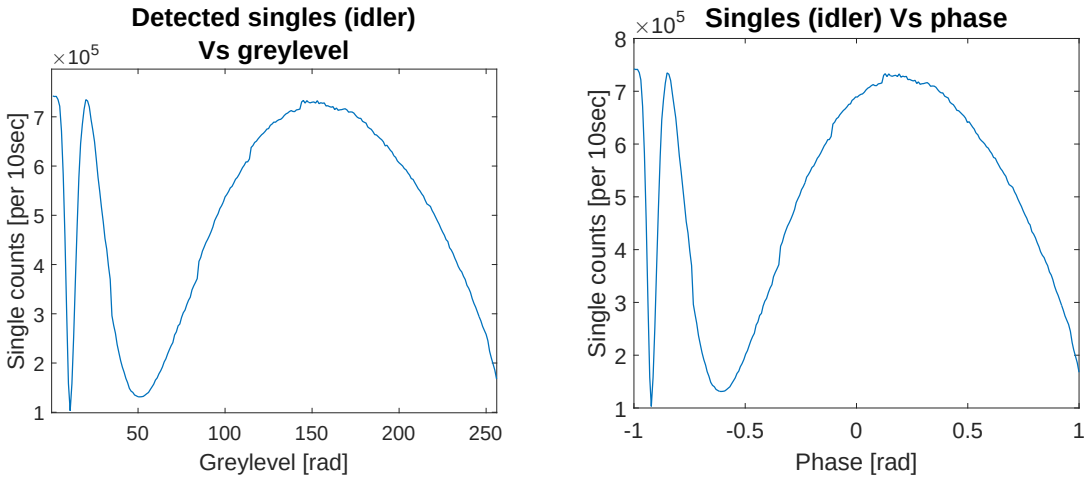

Figure 3.6: Result of a phase scan on the SLM before to add the calibration LUT. Incident light was polarized at +45°, and a polarizer set to transmit 45° polarization was placed before the detectors. We can see here that the response of the SLM does not satisfy neither the linearity of the response nor the 2π phase range. The photonic beam used for this measurement is the signal (at $\lambda = 837nm$) produced vie SPDC by pumping the crystal with the TiSap pulsed laser. On the left, the phase shift plotted Vs the greylevel value; on the right the same measurement is plotted Vs the desired corresponding phase (clearly not-calibrated).

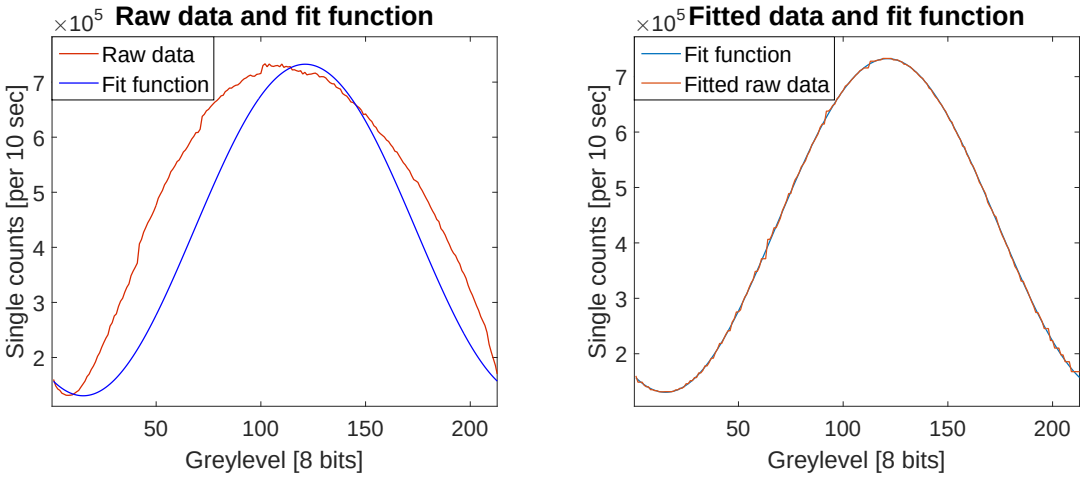

Figure 3.7: We plot the counts per unit time recorded when scanning the value of the uniform phase on the SLM. In blue are shown the experimental values (linearly interpolated to guide the eye) while in orange is shown the desired function. On the left, the result without implementing the LUT; on the right the result of the same measurement when using the LUT we built.

Table 3.3: Principal specifications of our SLM *HOLOEYE PLUTO-NIR*.

Characteristic	Value	Units
Resolution	1920×1080	Px^2
Pixel size	8×8	μm^2
Active area	15.36×8.64	mm^2
Addressing	$8bits$	greylevels
Fill factor	93%	–
Reflectivity	65%	@ $780nm$
Diffraction efficiency	$> 80\%$	–
Wavelength range	$650 - 1100$	@ nm

In the following chapters we describe two different measurements in which the SLM plays a main role. Therefore we leave the details about the utilization of the SLM for later. For what concern this technical introductory chapter, we close the section about SLM providing the specifications of our device (table 3.3).

3.1.3 Customized interference filters.

In general SPDC pairs are produced within a large spectrum both in frequency and linear momentum. It is customary to filter signal and idler fields both spatially and in the frequency domain [116]. The first task can be achieved by selecting the light before to coupling it into the APDs by means of small irises or narrow slits; the latter is usually accomplished by using interference filters.

The commercial filters normally available from companies such as *Thorlabs*, *Semrock*, or *Newport* (just to mention few large scale producers) are good enough for most of the experimental setups. The scope is selecting a range of frequencies (usually around $10nm$) from the whole SPDC spectrum (usually of the order of $100nm$) in order to reduce the frequency modes.

In our two-photon experiment we did not need any spectral filter. The reason is empirical: we tried to detect SPDC without filtering neither signal nor idler and we could already see good correlations, strong enough for deciding not to spectral filtering at all (with the advantage of higher brightness). This can be easily understood if we consider the two sources of broadening of the spectrum of detected SPDC. First, if the pump is not monochromatic photons with different frequencies downconvert into different frequency pairs of signal and idler. Second, in SPDC the phase matching conditions imply that each single frequency of the pump generates pairs of photons of a given frequency only in one particular direction. Therefore, different frequencies of the SPDC photons propagates along different angles, and collecting them with a finite aperture imply to collect more than one pair of frequencies.

Both in the 2- and 4-photon experiments we indirectly spatial filter the SPDC by coupling only a narrow angle. This is due to the finite dimension of the optics used, and limits the *detectable* spectrum of SPDC. For the 2-photon experiment, we pump the crystal with a continuous wave laser characterized by a very narrow bandwidth (section 3.1.1). Since it can be considered single-frequency, it reduces the spectrum of the *generated* downconversion, not requiring further spectral filtering at the detection stage.

On the other hand, for the 4-photon experiment we need to use a pulsed laser which for the reasons explained in 3.1.1 is characterized by a broad spectrum. A strong spectral filtering is therefore needed. Spectral filtering the downconverted photons is also essential to synchronize two consecutive downconverted pairs. In particular, to make them indistinguishable. For that purpose we need the *coherence time* of each photon pairs to be long enough - that is, longer than the pulse width of the pump. The coherence time of SPDC can be approximated as [116] [117]:

$$T_c \simeq 1/\Delta\omega_{spdc} \tag{3.3}$$

where $\Delta\omega_{spdc}$ is the bandwidth of the SPDC fields.

According to 3.3, with a $10nm$ full width at half maximum (FWHM) interference filter around the idler central frequency ($837nm$), we limit the coherence time of idler photons to: $T_c \simeq 1/(4.28 \cdot 10^{12}) = 234fs$. Recalling the pulse temporal length of the TiSap being approximately $140fs$, we see that the coherence time in this case is only $(234 - 140)/140 = 0.67 = 67\%$ longer. If on the top of that we consider that when reaches the crystal plane the TiSap pulse is a bit stretched due to group delay dispersion (mentioned in 3.1.1), we can assume $10nm$ filtering not enough to satisfy the condition of coherence time of SPDC (much) longer of temporal duration of the pump pulse.

For our 4-photon experiment then we needed a narrower interference filter. We aimed for a $1nm$ FWHM interference filter. With such a filter we could increase the coherence time of SPDC by one order of magnitude; according to 3.3, for the idler photons we get approximately $2.34ps$, that is a factor $2340/140 \simeq 17$ longer than the nominal pulse length of the TiSap. Searching the market, we found a company called *Andover Corporation* that could produce the filters customized according to our required specs. In figure 3.8 we show the transmission functions for signal and idler fields as provided by the producer.

As we can read in the vertical side bars, at the right of each of the two plots in figure 3.8, the measured values of the central wavelengths for signal and idler are respectively $783.20nm$ and $837.08nm$. The FWHM are $0.99nm$ for the signal and $1.10nm$ for the idler. The other important parameter is the peak transmission, which for signal (idler) is 72.97% (78.14%).

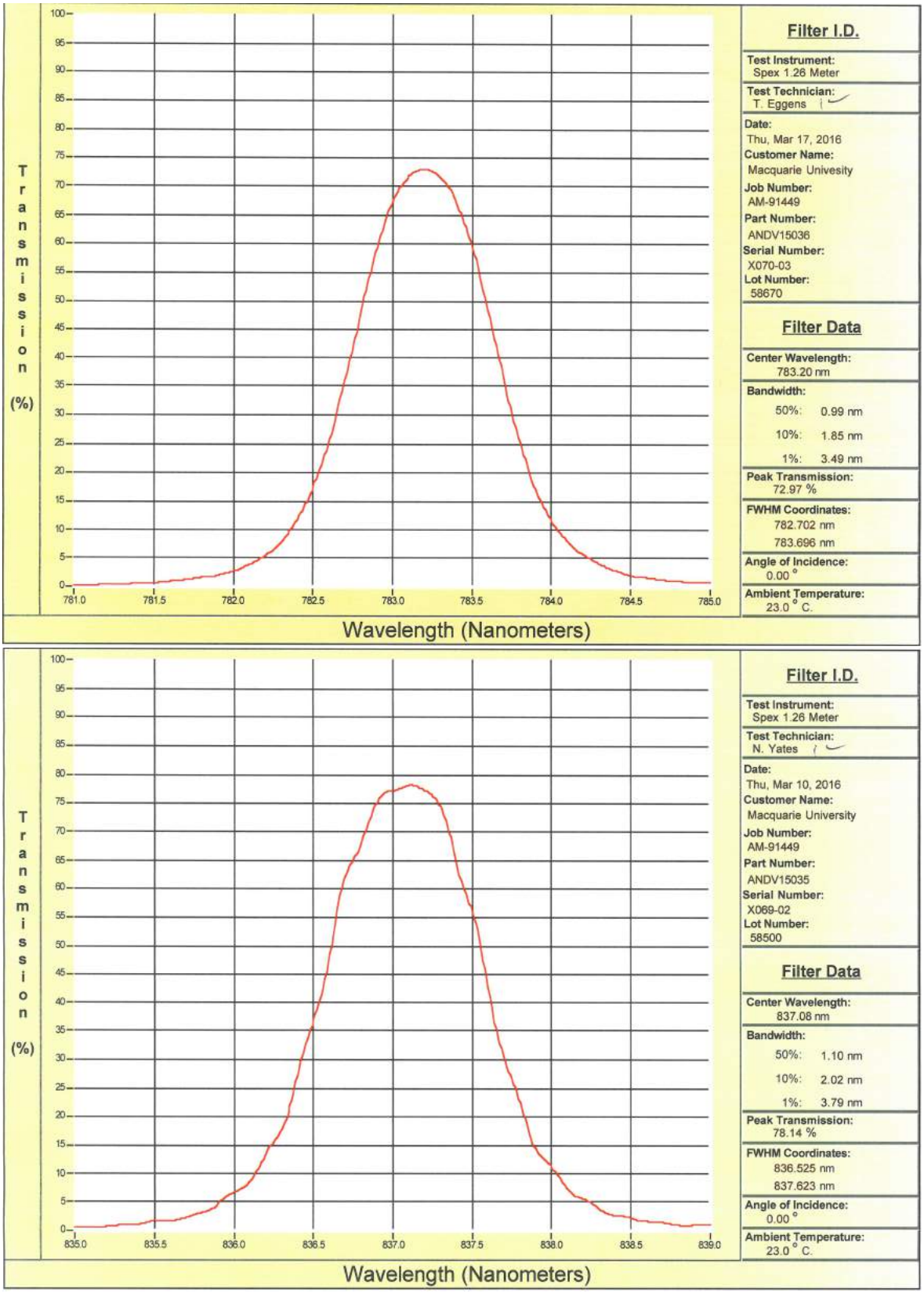

Figure 3.8: On the top, the transmission of the customized interference filter as a function of wavelength centered at the signal frequency; on the bottom, the transmission of the idler filter. These two plots have been provided by the producer.

3.2 Our experimental setup: Detailed description.

With our experimental setup we aim to control and measure spatial entanglement of 2- and 4-photon states generated via collinear, non-degenerate SPDC. We designed and developed a full setup capable which works for both of them, but due to time restriction within this thesis we could only test the 2-photon part. We did so by running two different types of experiments (results in chapters 4 and 5). This is why we thoroughly explain the 2-photon setup here and leave the parts needed for the 4-photon experiments for chapter 6.

In the previous sections of this chapter we gave a brief introduction about Spontaneous Parametric Down Conversion (SPDC). We presented a simplified scheme (Figure 2.2) with the only goal of fixing the ideas about the process itself rather than explaining a typical experimental setup. In addition to the optical elements needed for that purpose, one has to add several other optics and electronics elements depending on what are the degrees of freedom of interest. In general, there is some *preparation* to be done on the pump beam (mainly shaping the spatial profile and selecting the appropriate polarization), some *manipulation* of the downconverted fields (in our case phase transformation through a Spatial Light Modulator - SLM), and the measurement of the photon's states (polarization projection and fiber coupling).

Figure 3.9 shows the experimental setup used to investigate the two-photon states[3]. The pump is a continuous wave (CW) diode laser made by *Toptica Photonics*. We choose the model *TopMode* because of its very narrow linewidth of less than 5MHz. Hence, we can consider it monochromatic at the measured wavelength $\lambda = 404.0nm$.

For the first part of the experiment we want to pump the crystal with a Gaussian mode. The output of a diode laser is typically collimated, but the profile differs from that of a Gaussian field. The reason is that the beam starts slightly elliptical, and the collimation makes it astigmatic. To improve its quality, one has to correct for it. Also, the number of spatial modes amplified in the cavity of a diode laser can be greater than one and the Gaussian term (TEM_{00}) is just one of them. The result is a field with limited spatial coherence. The parameter accounting for that is the M^2 which for our laser the producer declares it to be smaller than 1.5 with a beam diameter of diameter $d = 1mm$.

There are two common solutions for obtaining a spatial profile that resembles a coherent term TEM_{00} from the output of a laser. One is to fiber couple the laser in a single mode fiber (SMF). The particularity of SMFs is that they transmit *efficiently* only one spatial mode, which is within a good approximation the Gaussian term TEM_{00}. Therefore, at the output of the fiber the spatial profile can be approximated as purely Gaussian. The behaviour of a typical SMF is shown in figure 3.10. The good thing about this method is that the quality of the resulting Gaussian profile is alignment independent, in the sense that the fiber output field is Gaussian even if the incoupling is not well centered. On the other hand, as any other filtering procedure part of the energy is lost. In the case of SMF, this is especially true when coupling light in the UV spectrum.

In our setup we first implemented this method. The main reason for that choice was practical: the fiber decouples the two parts of the setup. A misalignment in the pump laser would not reflects in a misalignment of the optical path through the nonlinear crystal as far as the outcoupling of the fiber is not moved. In those stages we were using the pulsed *TiSap* laser as our pump source and we encountered several problems related to practical procedures. In particular, we noticed that the amplitude was very unstable. Also, the filter (the SMF) got

[3]The setup for the 4-photon state investigation is slightly different and will be presented in chapter 6, section 6.2

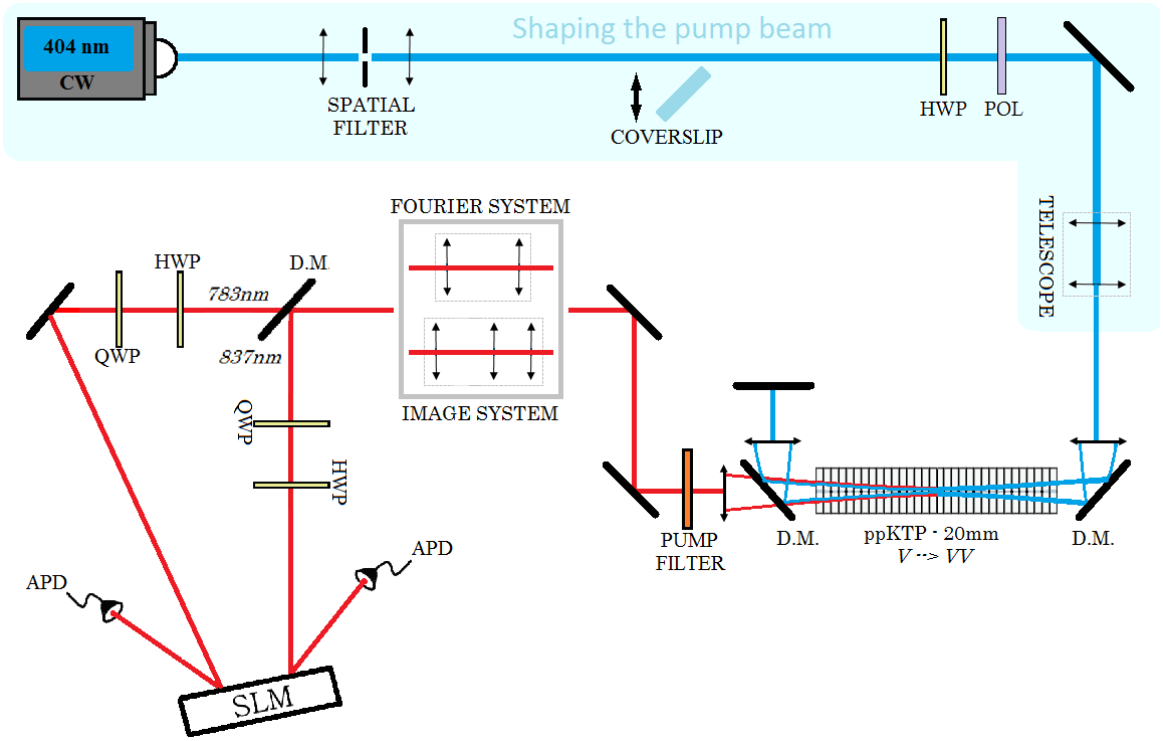

Figure 3.9: A continuous wave (CW) diode laser at 404nm is spatially filtered by means of a focusing lens, a pin-hole, and a collimating lens (details in the text). The thin coverslip used for transforming the Gaussian beam into a HG can be inserted into the path as needed. The combination of Half Wave Plate (HWP) plus polarizer (POL) are used to control the polarization of the pump field as well as its power. A telescope made by two planoconvex lenses can be flipped in or out the pump path to decrease or increase the diameter of the pump which eventually translates in increasing or decreasing the waist in the crystal plane. After the nonlinear crystal, a Dichroic Mirror (DM) reflects the pump while transmitting the signal and idler fields. A long-pass filter completes the filtering by absorbing the the residual pump field. Two sets of lenses are interchangeable thanks to flippable mirrors; one images the crystal plane on the Spatial Light Modulator (SLM) while the other does the Fourier transform. Signal and Idler fields are separated by a DM, and on each of the two resulting branches a pair of waveplates (HWP+QWP) prepares the the polarization state on 45°. The SLM applies the desired phase transformation and reflects the beams. Finally, signal and idler are coupled into multimode fibers and sent to the fiber-coupled Avalanche Photo Diodes (APDs).

easily damaged and the power coupled use to decrease dramatically after some time. The reason is twofold (at least). First, coupling light in a single mode fiber is harder in the UV than it is in other parts of the spectrum. Second, the fact that the laser is pulsed increases the likeability of damaging the optical fiber itself due to the high energy within the single pulses. The consequence is that we could not couple with an efficiency higher than 25 – 30%, and in one occasion we seriously damaged the fiber due to the high power of the laser. After that event we necessarily had to limit the incoming power to 100mW.

A different problem that we did not expect from the SMF method was an instability in the pump spectrum. In particular, from one measurement to the other not only the power decoupled from the fiber decreased (expected from an unperfect alignment of the fiber coupler), but later we also realised that the spectrum itself was shifting of few nanometers (indeed it was not only shifting, but also changing shape and size). It is quite predictable to see a temporal broadening of the pulse due to dispersion effects while propagating the field

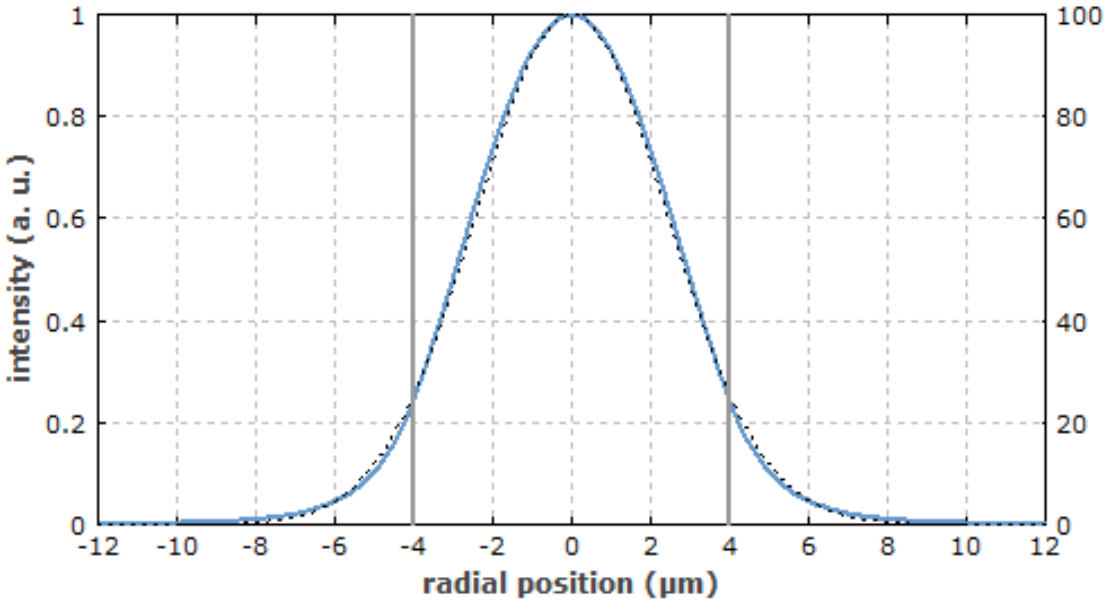

Figure 3.10: In blue, the intensity profile of the transmitted field in a typical single mode fiber. The dotted line is a Gaussian function - note the strong similarity of the two. The grey vertical lines represent the position of the border between core and cladding. Source: RP photonics, https://www.rp-photonics.com/passive_fiber_optics3.html

into the fiber, therefore we tried to solve the problem by purchasing a shorter optical fiber. We ordered a customized $30cm$ long optical patch cable built using single mode optical fiber designed for an appropriate range of wavelengths. However, the spectrum instability was still happening. Our understanding is that different parts of the laser beam profile (before to be filtered) are characterized by slightly different wavelengths. Considering that a small misalignment of the laser before the spatial filter implies the coupling of different parts of the field into the SMF, a spectral instability could be expected.

The second method requires the alignment of what is called a *spatial filter*. The working principle is fairly easy. It can be shown that when an optical field traverses a thin spherical lens, the result is an intensity distribution proportional to the Fourier transform of the input field [72]. The central part contains the slowly varying components of the field itself, and its distribution follow in good approximation the central part of a Gaussian profile. Slowly varying means also greater spatial coherence.

In order to select only the desired central part, one needs to insert a pin-hole on the optical axis of the beam, at the z-position corresponding to the focal plane of the lens. The pin-hole blocks the outer parts of the Fourier distribution and only allows the central, slowly varying field. With a second lens placed at a focal distance after the pin-hole, the diverging beam is re-collimated. The spatial profile at this stage is the typical Airy pattern as shown in top image of Figure 3.11. After eliminating the rings using an iris, the profile of the field is in good approximation Gaussian (Figure 3.11, bottom image) and is characterized by improved spatial coherence.

The drawback of this filtering method is that the output spatial profile is alignment sensitive in two ways: if either the pump beam before the spatial filter or the pin-hole is subject to misalignment, the field selected by pin-hole and iris is not circularly symmetric anymore and therefore its distribution changes with respect to the TEM_{00}.

Because of the problems described earlier with the SMF, we decided to switch to the

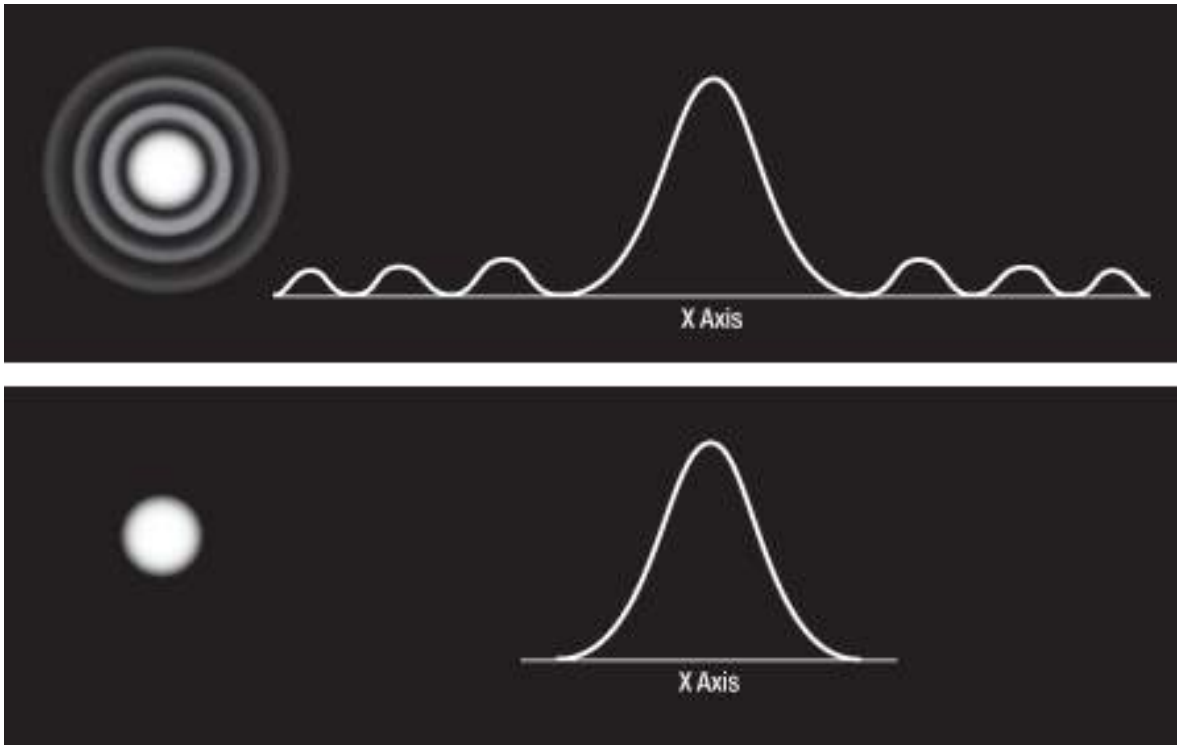

Figure 3.11: A typical laser beam profile spatially filtered. The top image represents the expected beam profile after a spatial filter: it is characterized by a typical Airy pattern. The bottom figure represent the Gaussian-like beam profile after cleaning the Airy pattern by placing a circular aperture coaxially with the beam to select only the central spot. Source: Thorlabs website.

spatial filter made with two lenses, a pin-hole, and the iris. This way we could count on more pump power, which turned out to be needed in some of the configurations analysed. The pinhole we used for filtering the CW laser in the 2-photon experiment (figure 3.12) has a nominal aperture $d = 10\mu m$.

The beam that we detect after our spatial filter shows the Airy pattern as expected. Using an iris (*Thorlabs ID25/M*) set on the path of the laser after the collimating lens we eliminate the rings by closing it up to the first circular minima.

In Figure 3.13a we show the profile of the beam focused at the z-position corresponding to the center of the crystal (about one and an half meters of propagation from the iris). The rings are not present anymore, but the profile of the beam is clearly not circularly symmetric as expected. The reason is twofold. First, the output field of diode lasers is not perfectly circular to begin with. Second, in choosing the size of the pin hole one has to find a good compromise between the amount of light discarded and the circularity of the filtered beam. By using a smaller pin hole we could have improved the circularity of the beam to the detriment of the available maximum power.

However, in our investigation of transverse (x, y) position/momentum distributions we focused only on one of the two transverse coordinates at a time (either x or y). Therefore, what matter is the Gaussianity of each of the two transverse components of the pump beam profile. In Figure 3.13b we show the horizontal and vertical cross sections of the bidimensional profile along the orthogonal directions intersecting the center of the beam. We can see that the detected values of intensity are well fitted by a Gaussian distribution in both cases, allowing us to consider the pump beam profile to be Gaussian in all of our measurements.

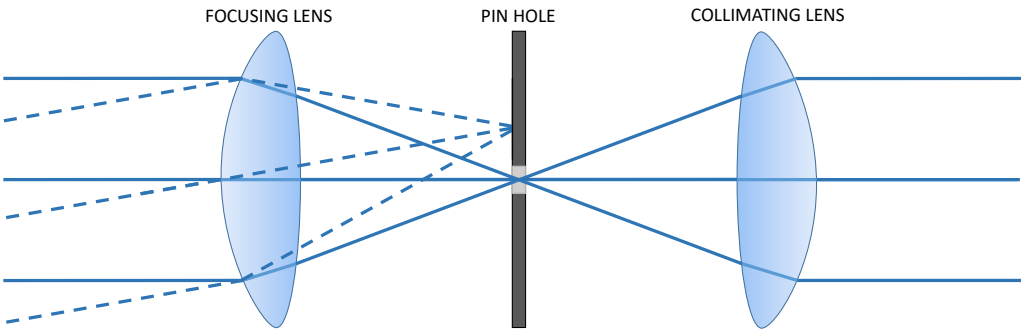

Figure 3.12: Spatial filter composed by a focusing lens, a pin hole in the focal plane, and a collimating lens. The sketch is shown in the ray-optic framework.

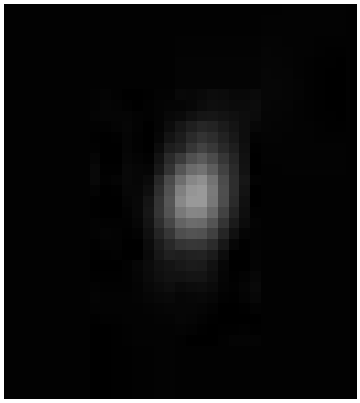

(a) Bidimensional profile.

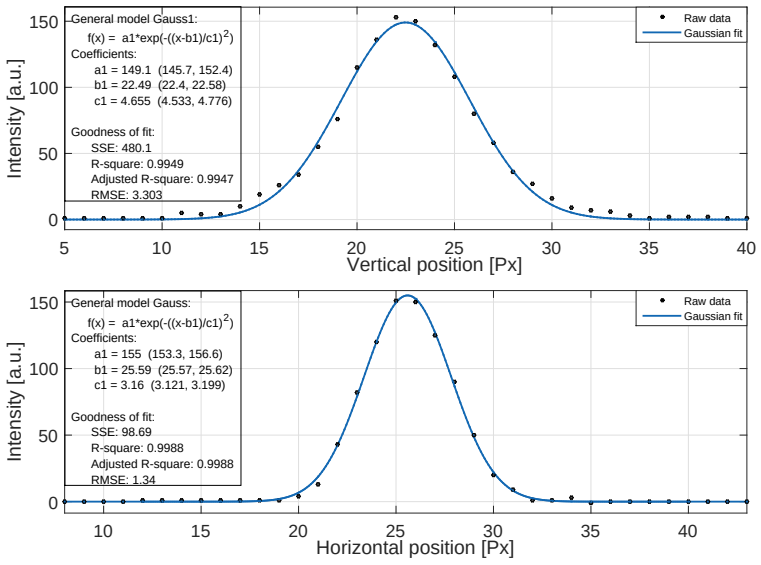

(b) Cross sections.

Figure 3.13: Pump beam profile at the z-position corresponding to the center of the crystal. In a) is shown the transverse profile captured with a CMOS (Complementary Metal Oxide Semiconductor) camera. In figure b) are shown the horizontal (top) and vertical (bottom) cross sections of the transverse beam profile.

3.2.1 Pump beam preparation: spatial profile.

The beam diameter after the filter is quite large (about $5mm$) and collimated. For the experiment with structured pump beam profile we need a higher order spatial mode. Starting from a profile approximately Gaussian, it is possible to transform the beam into a mode width that is approximately a first-order Hermite-Gaussian mode (HG_{10}) just by imprinting a π phase between two halves of the beam. We can do that by inserting on the path of half the beam a thin layer of glass (figure 3.14): half of the beam will propagate at speed of light in air ($n \simeq 1$), while the other half will experience a higher refractive index ($n \simeq 1.5$) which means lower group velocity. The temporal delay between the two translates in a reciprocal phase term.

In principle, the thickness of the glass should be such that the phase introduced is exactly half the period of the wave. The thickness needed is given by the difference in phase velocities:

$$\tau = d\left(\frac{1}{v_{glass}} - \frac{1}{v_{air}}\right) = d\left(\frac{n_{glass}}{c} - \frac{n_{air}}{c}\right) \tag{3.4}$$

Considering in good approximation that $n_{air} = 1$ and $n_{glass} = 1.5$, the desired thickness d of the glass turns out to be: $d \simeq (\lambda/2c) \times (c/0.5) = \lambda$. Our laser has a wavelength of $\lambda = 404nm$, which means that we would need a glass about half a micrometer thick. Technically, it is challenging and as far as we know no company provide such a thin glass. However, what is important for the transformation of the Gaussian beam into HG_{10} is not the absolute value of delay (phase) but rather the half-cycle. This is true as far as the total delay is shorter than the temporal coherence of the field, which can be approximated to the inverse of the bandwidth[4] ([118], pag. 572). In the case of our CW laser this condition is fulfilled thanks to the narrow spectrum, which implies a long temporal coherence of about $\tau_c \simeq 1/5MHz \simeq 0.2\mu s$. We prove it by showing that the coherence length L_c of the laser is much longer than the thickness d of the glass used:

$$L_c = \tau_c \times c \simeq 0.2 \cdot 10^{-6}s \times 3 \cdot 10^8 m/s = 60m \tag{3.5}$$

The thin glass we choose is a cover slip commonly used for placing microscopes samples. Its nominal thickness is anywhere between $100\mu m$ and $150\ \mu m$ (the precise value is not important), which is much shorter than the calculated coherence length.

We mounted the cover slip on a translational stage such that we can insert it or remove it from the pump path as needed. The correct phase value of $n+1/2$ cycles is obtained by tilting carefully the cover slip while checking with a camera that the resulting intensity distribution is a typical HG_{10}. In Figure 3.15 we show a screenshot of what detected by a commercial CMOS camera. The beam is focused on the sensor with a plano convex lens ($f = 75mm$) (we just needed the lens in order to mimic infinite propagation). The beam profiles utilized for each experiment are shown later in the corresponding section.

A telescope system is then used to control the size of the pump beam. It is aligned such that we can insert it or remove it without loosing completely the alignment. This allowed us to test the setup with two different pump waists - while keeping all the other parameters unchanged. Without using the telescope, the collimated pump beam is large which means that the waist in the focal plane at the center of the crystal is *small* (the measured value is about $16.2\mu m$). Using the telescope the beam profile is demagnified and consequently the focused waist in the crystal plane is *large* (about $74.2\mu m$ measured waist). The telescope,

[4]The approximation of the coherence time with the inverse of the bandwidth comes from the convolution theorem which in this case relates the Fourier transform of the spectrum to its auotocorrelation function

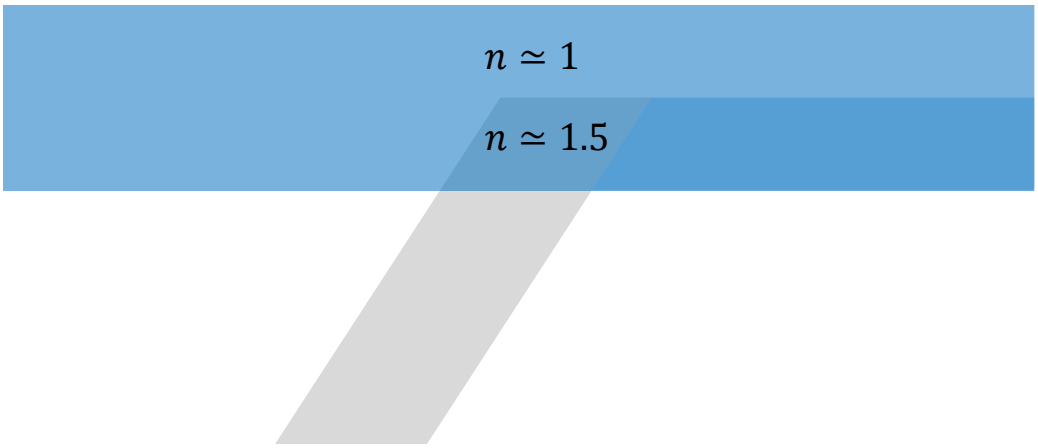

Figure 3.14: Sketch of the simple setup to transform a Gaussian beam to a HG_{01}. A thin sheet of glass is placed on half of the path of the Gaussian beam. Then we tilted the glass until reaching a phase difference of a multiple of π between the two halves of the beam.

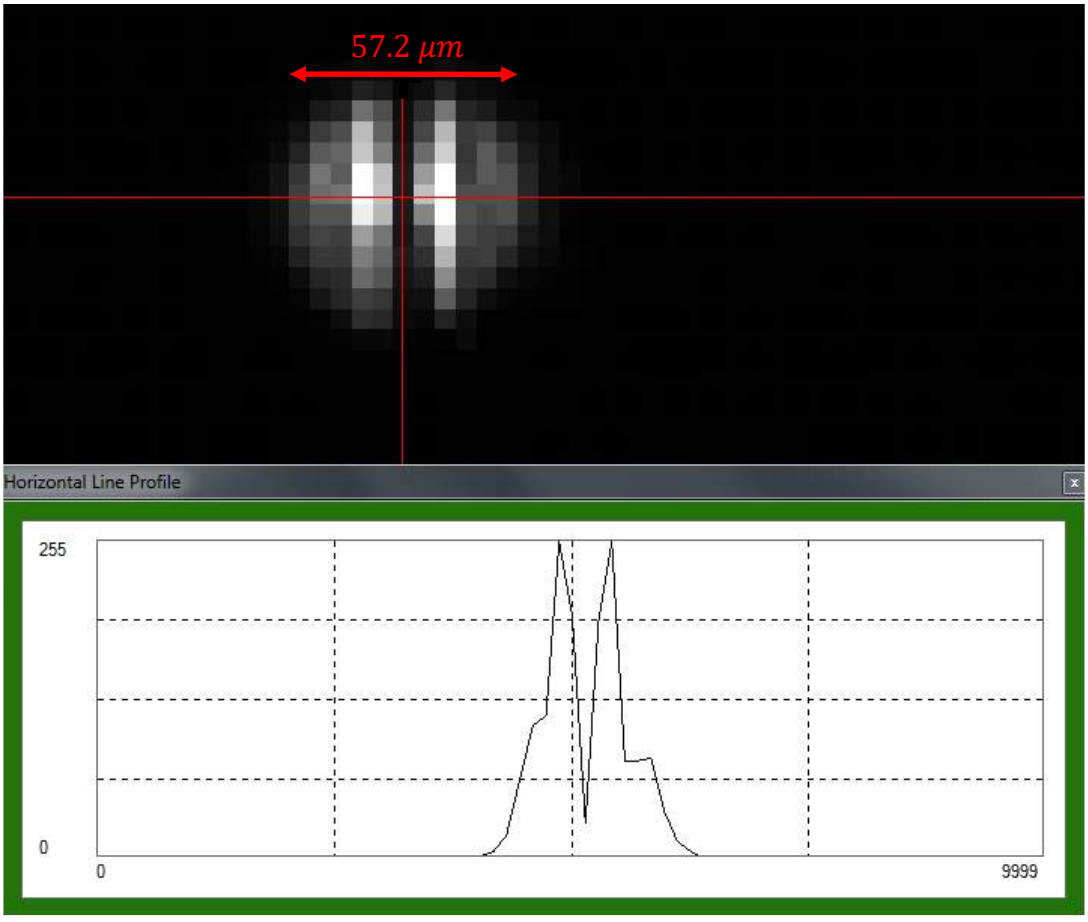

Figure 3.15: This is a screenshot from the GUI (Graphical User Interface) of our CMOS camera. The pixelization in the image reflects the physical pixels of the camera ($5.2 \times 5.2 \mu m^2$). The inset represent the horizontal cross section taken along the horizontal red line.

of course, works well for both the Gaussian and the Hermite-Gaussian settings of the pump profile. We built it using two planoconvex lenses of respective focal lengths $f_1 = 200mm$ and $f_2 = 75mm$. The magnification factor is therefore $M = f_2/f_1 = 0.375$.

3.2.2 Pump beam preparation: polarization and power control.

As explained in the previous sections polarization of the pump is a fundamental parameter for the downconversion of pump photons via SPDC. Although the output of our laser is linearly polarized with a high degree, the field oscillates in a direction that in general is not the one that we need. Furthermore, we experienced some unexpected changes in the properties of the output field when changing the power of the laser as well as when switching it off and on again. For instance, a well known instability in diode lasers is due to the temperature dependence of the output wavelength which can be triggered when changing the driving current. Therefore, we never changed the output power of the laser by acting on the current of the laser itself, but rather keep it lasing at maximum power. In order to control both the polarization direction and the power we then use a Half Wave Plate (HWP) followed by a linear polarizer set to filter the appropriate polarization direction.

The polarizer is set such that it selects only the polarization for optimal phase matching of Type-0 SPDC in our crystal. We chose a Glan-laser calcite polarizer produced by *Newport* (model: *10GL08*). The advantage of using a bulk polarizer with respect to other linear polarizers that work in absorption lies in the transmission efficiency. For comparison, the element we used has a nominal transmission efficiency greater than 95% and extinction ratio of 10^6; while a good absorptive linear polarizer such as the *Visible Wire Grid Polarizers 420 - 700 nm* by *Thorlabs* transmits about 87% in one polarization but with a small extinction rate on the other polarization (below 200), or the *nanoparticles linear films polarizers* by Thorlabs that has high extinction rate but only 47% transmission efficiency[5].

On the other hand, the drawback of using a cube beam splitter is that there is an appreciable tilt of the optical path due to the beam intersecting and propagating through surfaces with different refractive indexes (air-glass surface and glass bulk material). The effect is particularly annoying when the rotation of the cube is needed, since that would change the propagation direction of the beam at the output of the cube. For this reason we always keep the PBS in a fixed position and rotate the HWP instead. A linearly polarized beam passing through a HWP is subject to a rotation of the axis of (linear) polarization. The amount of rotation depends on the angle between the optical axis of the wave plate and the polarization direction of the beam. Therefore, by rotating the HWP we can control the amount of the pump optical field polarized parallel to the direction of polarization selected by the polarizing beam splitter.

Therefore the purpose of the HWP is limited to the control of the pump power. We chose the *WPH05M-405* by *Thorlabs*, which is a zero order HWP with half-inch aperture. The deflection of a beam passing through a wave plate perpendicularly to its surface is negligible in most of the cases - we tested that it is the case in our setup by looking at the beam with a camera placed in the crystal position and rotating the HWP: we could not see any detectable change in the beam position.

The last element to shape the pump beam profile is a plano-convex lens $f = 300mm$ which is used to focus the beam into the center of the crystal (also referred in this thesis as *crystal plane*). The lens is mounted on a translational stage that can be moved parallel to

[5]The transmission efficiency tells how much of the wanted light pass through, while the extinction rate refers to how much of the *unwanted* light is discarded.

the propagation direction, such that we can optimally control the exact focal position of the pump (we want it to be in the center of the crystal).

3.2.3 Generation of SPDC via ppKTP nonlinear crystal.

The non-linear crystal is a periodically poled Potassium titanyl-phosphate (ppKTP) produced by *Raicol Crystals*. For a KTP we can optimally control the phase matching with the temperature of the crystal itself. For what concerns this section, it is enough to say that changing the temperature of the crystal implies a change in the wavelengths of the downconverted fields propagating in a defined direction. In order to have full control about that, we home-built a temperature controller system consisting of: a thermoelectric cooler (TEC) element (*Thorlabs TEC3-2.5*) based on the Peltier effect, a temperature controller (*Thorlabs TED200C*), a block of copper to dissipate the heat, and a temperature transducer (*Thorlabs AD590*). A photo of the system is shown in figure 3.16. The ppKTP is sandwiched between two layers of glass, the bottom one sitting on the block of copper for better uniform diffusion of heat.

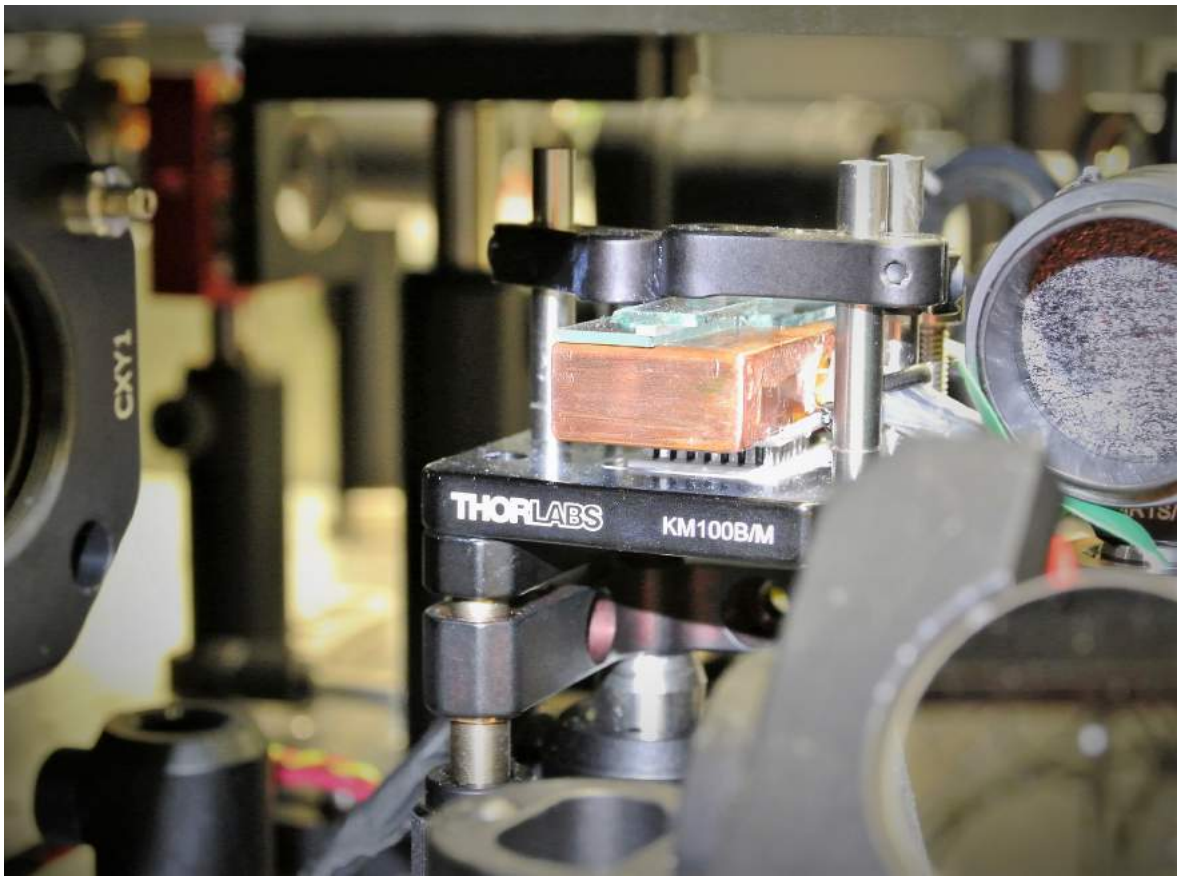

Figure 3.16: Photo of our home-made temperature controlled platform. The ppKTP is sandwiched between two thin layers of glass, which in turn are held on a block of copper. Inside the copper we drilled a hole in which we inserted a temperature sensor. The block of copper sits on the peltier element, and they are all fixed to a kinematic platform mount by *Thorlabs*.

Along the optical path, after the non-linear crystal, there is a dichroic mirror (*Thorlabs DMLP650*) that filters the downconversion removing large part of the pump optical field. Wavelengths shorter than $650nm$ are reflected - including the pump - while longer ones are transmitted (the downconverted fields). A plano-convex lens $f = 300mm$ is placed after the

crystal to collect the SPDC fields in a collimated, collinearly propagating beam. A high-pass spectral filter (*BLP02-561R-25* made by *Semrock*) completes the suppression of the pump field counting on an optical density above seven[6].

3.2.4 Conditioning of the downconverted fields.

Two sets of lenses are interchangeable by flipping them in and out the optical path. This is possible by mounting them on flip mount adapters such as the *FM90/M* by *Thorlabs*. One of the two sets is designed *to image* and the other to *Fourier transform* the downconverted fields from the crystal plane to the SLM. The imaging system consists of four lenses (including the $f = 300mm$ lens placed after the crystal, already mentioned above). The focal lengths are, from the closest to the farthest from the crystal: $f_1 = 300mm$, $f_2 = 200mm$, $f_3 = 19mm$ (achromatic doublet *Thorlabs AC127-019-B-ML*), and $f_4 = 400mm$. Assuming that they are placed in the proper z-position, the expected magnification factor is given by: $M = (400/18) \times (200/300) = 14.8$ (Figure 3.17).

The Fourier transform of the field at crystal plane is made by the first lens, $f = 300mm$ (which is also the first lens of the imaging system - this does not flip out). After that, a telescope consisting of two lenses, $f_1 = 250mm$, and $f_2 = 400mm$ (the last being, again, the same used in the imaging system) magnify the distribution of transversal momentum by a nominal factor of: $M = 400/250 = 1.6$. On the optical path between the first and the last lens of the imaging and Fourier system (as said, first and last lenses are shared by both optical systems), there are several other optics. First, we need a HWP in order to rotate the polarization from vertical to diagonal. Since the delay (or relative phase) introduced by waveplates is wavelength dependent, we needed two different models of waveplates, one designed for the signal wavelength and one for the idler.

In principle one of the two waveplates could be place on the common path of signal and idler and tuned for one of the wavelengths, while the other HWP handles the polarization of the other photon beam after separation via dichroic mirror. However, we realised that the dichroic mirror itself is strongly polarization dependence, while we want it to split the beams according to the frequencies only. Therefore we had to place both the HWPs after the dichroic mirror, that is one on the path of signals only and the other on the path of idlers only.

Each of the two waveplates is designed for introducing exactly half-cycle phase at a wavelength close to the expected wavelength of signal and idler respectively[7]. For the idler we chose the *Thorlabs WPH10M-830* which is a zero order HWP centered at $830nm$, while

[6]Source: Semrock website.

[7]Expected wavelengths for signal and idler are $783nm$ and $837nm$ respectively.

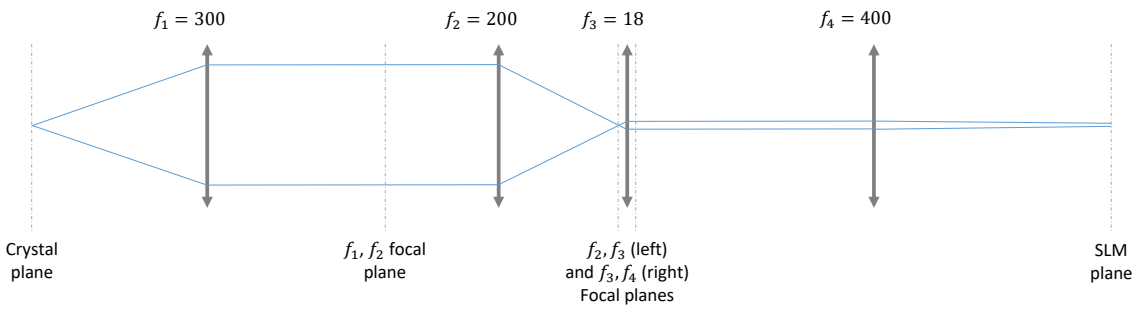

Figure 3.17: Diagram (in scale) of our imaging system. Focal lengths and focal planes are indicated.

for the signal we picked the *Thorlabs WPH10M-780* which belongs to the same family of waveplates but designed for the central wavelength 780*nm*.

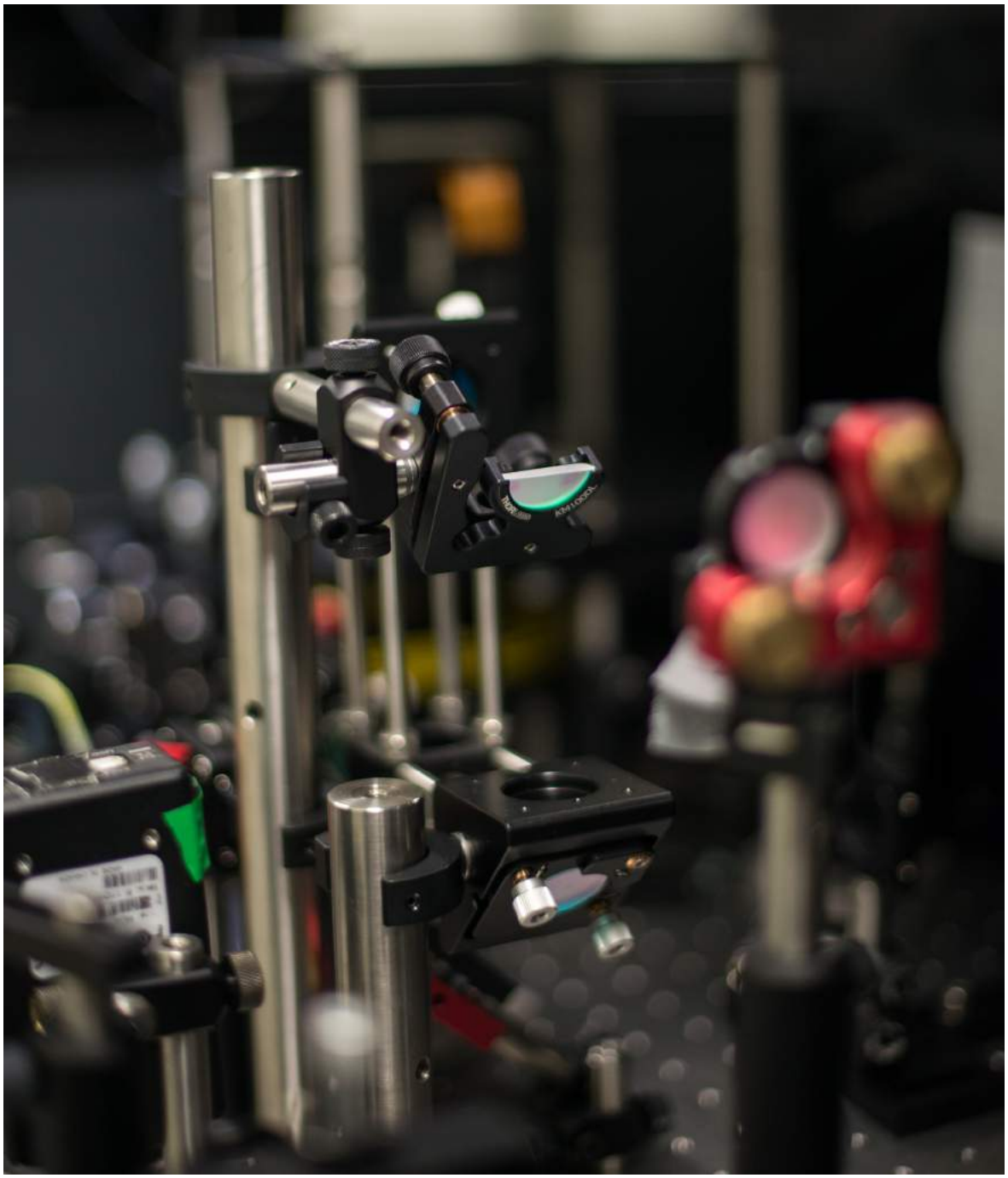

Figure 3.18: Details of the optics for accessing the upper level of the setup. The parallel beams (one signal and one idler) are reflected from the bottom (dielectric) mirror (one inch diameter, round) which is installed in the black, triangular shaped mount in the bottom of the photo. The upper mirror is a D-shaped one, designed for allowing the other two beams coming from the back of the D-shaped mirror itself (another one signal and another one idler) to propagate close to the reflected two.

Still for lack of space on the optical table, the detection block was set on an upper level (Figure 3.18). The experimental setup therefore extends on two parallel optical planes, separated (vertically) by about 30 cm. Besides some extra difficulties in alignment, this also means that we have to account for an imaginary phase between the s and p components

of polarization[8] of signal and idler. We can pre-compensate for the ellipticalyzation of the polarization by placing a Quarte Wave Plate (QWP) right after the HWP on each of the two paths. Again, the two QWPs have to be designed for the appropriate wavelength. We chose *Thorlabs WPQ10M-780* and *Thorlabs WPQ10M-830* for signal and idler respectively.

The dichroic mirror responsible for the split of signals and idlers beams is the *Thorlabs DMSP805*, which is a short-pass filter with cutoff wavelength $\lambda = 805nm$.

3.2.5 Detection block.

For being able to control the phase of both signal and idler beams using one SLM only, we need to propagate them parallel and close to each other. The sensitive area of our SLM - that is the area covered by the LCD pixels - is $15.36mm$ wide, which means that in an optimal case we want the two beams to propagate with a constant separation of about $7.68mm$. We do that exploiting the sharp edge of a D-shaped mirror (*Thorlabs BBD1-E03*): it allows for one beam to pass very close to the edge while another beam coming from an orthogonal direction to be reflected at 90°. The result is that both the beams propagates parallel and close to each other. The D-spahed mirror is installed on a dedicated kinematic mount (*Thorlabs KM100D*) not explicitly shown in the sketch of the setup in figure 3.9. The two beams are then translated to the upper level of the setup by a pair of dielectric mirrors placed parallel to each other.

Just before the SLM we have a linear polarizer placed perpendicularly to the optical path and set such that only light polarized diagonally (45 degrees) pass through. In this case, unlike for the pump laser, we opted for an absorbing nanoparticle linear film polarizer (*Thorlabs LPVIS100-MP2*). This choice has been driven by the fact that we might want to remove and replace the polarizer without misaligning the coupling of the downconverted beams, and for the reasons explained earlier a cube polarizer deflects the beam while an absorptive polarizer does not.

The Spatial Light Modulator has been described already in section 3.1.2. Here we just remind that it is a phase-only, full-HD $(1920x1080)Px^2$, reflective SLM produced by Holoeye (model: *PLUTO BB-HR NIR*). After the reflection on its pixelized surface, the two parallel propagating beams are separated by a second D-shaped mirror. Then, they both pass through an independent set for the polarization control (QWP, HWP, and linear polarizer). Again, the waveplates are chosen to match the wavelength of the downconverted fields (*Thorlabs WPH10M-780* and *Thorlabs WPQ10M-780* for the signal, *Thorlabs WPH10M-830* and *Thorlabs WPQ10M-830* for the idler). The selection of the linear polarization is made by two identical cube beam splitters (*Thorlabs PBS202* - one on each of the two arms). In principle, we would not need the QWPs in order to project to the diagonal/antidiagonal base vectors. However, since there is a reflection by the SLM for both beams and a further reflection by the D-shaped mirror for the signal, and that happens when the beams are not *p*-only nor *s*-only polarized, we need to take into account a possible rotation of polarization and compensate for it.

We mount QWPs and polarizers on manual continuous rotation mounts (either *RSP1/M* or *CRM1/M*, both by Thorlabs) so that we can find the correct angle during the process of alignment and fix it - since we don't need to rotate them anymore. Instead, the last HWP before fiber coupliing on signal and idler are mounted on a different mount. In order to automatize the full measurements, we need to rotate them to select the coupled states on

[8]The *s* and *p* formalism is useful when considering reflection of polarized fields. The *s* polarization is along the direction perpendicular to the incidence plane, while the *p* is the component parallel to it. The acronyms come respectively from the German terms *senkrecht* and *parallel*.

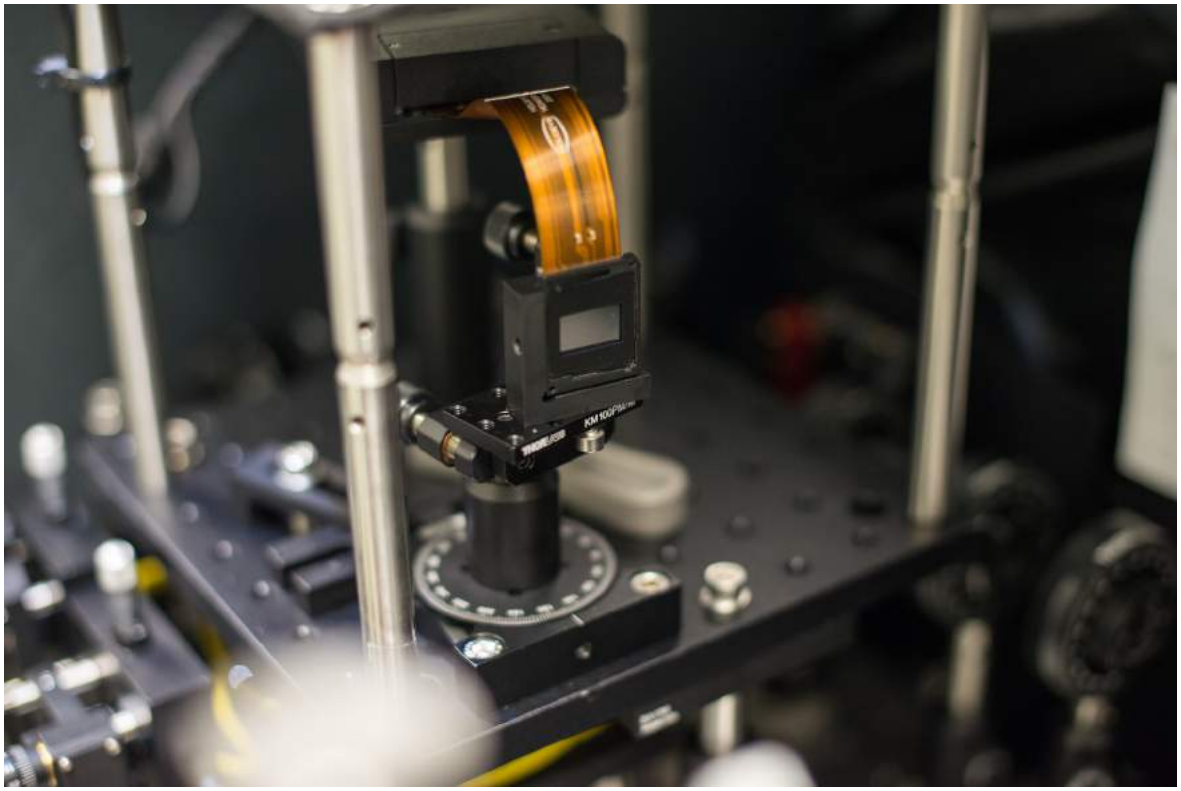

Figure 3.19: Photo of our Spatial Light Modulator (SLM) installed on our setup. Produced by *Holoeye*, model: *PLUTO BB-HR NIR*.

different combinations of diagonal and antidiagonal polarization direction. We then opted for mounting those HWPs on a motorized rotation stage (Thorlabs *KPRM1E/M*).

The fiber coupling is made using aspheric lenses *Thorlabs A397TM-B* ($f = 11.0mm$) with numerical aperture equal to 0.30, and Graded-Index multimode fiber optic patch cables (*Thorlabs M31L02*) characterized by core diameter equal to $62.52.5\mu m$ and designed for operative wavelength range: $800 - 1350nm$. We use multimode fibers since we do not need to - actually we do not want to - filter the spatial mode distribution selecting only the fundamental Gaussian mode, but rather we want all the spatial modes to be coupled and detected.

Regarding the detection unit and the coincidence logic, here we just mention few details. The detectors are four Avalanche Photo-Diodes (APDs) mounted on a single board. All the components are boxed in a home made metallic container provided of four optical inputs and four electronic outputs. For the detection of the two-photon states we chose channel zero and channel three, the furthest away from each other: this way one avoids any possible cross-talking produced by the electronics on the electronic board of the different APDs. The counting logic is implemented by a commercial FPGA board programmed for counting singles and coincidences from four input channels to eight output registers. The two boxes are connected through coaxial cables *RG-59/U*, 1 meter long each (for the two photon state we only need two of them). The FPGA box is eventually connected to a PC through a standard RS-232 serial cable.

All the lenses, mirrors and filters on the setup are one inch in diameter (unless differently mentioned). When used on the pump beam, the lenses are made by N-BK7 glass and anti-reflex coated in the range $350 - 700nm$ (*Thorlabs A-coated*), and the mirrors are protected silver mirrors *Thorlabs PF10-03-P01*. For the downconverted fields the lenses are still made

by N-BK7 glass but B-coated (range: $650 - 1050nm$), and we used broadband dielectric mirrors *Thorlabs BB1-E03* designed for the wavelength range $750 - 1100nm$.

Further improvements of the experimental setup are discussed at the end of the chapter regarding the generation of the 4-photon states, in section 6.2.1.

4

Spatial entanglement detection using raster scan with a phase-slit.

Experimental confirmation of a prediction is merely a measurement. An experiment disproving a prediction is a discovery.

Enrico Fermi

While in order to reach the final version of the experiment we needed to run several different tests to characterize and calibrate the setup, in this thesis we only present results regarding spatial correlations. Our final goal is to generate spatially correlated states of 4-photons via double emission of SPDC pairs. Experimentally the first step is to characterize the spatial correlations within each pair, that is in 2-photon states. We based our analysis on two conceptually different measurement methods. The first, more similar to the most conventional technique, is explained in this chapter; while the second, more innovative, will be discussed in chapter 5.

In this chapter we present the important topic of correlations (and eventually, entanglement) detection based on an updated version of the typical slit-scan. In particular, instead of performing a scan of the detector equipped with a metallic slit ([19, 82, 83, 119]), we scan the real and Fourier field of the SPDC with a phase-slit generated by a Spatial Light Modulator (SLM) - section 4.1.

Two slightly different approaches consisting respectively in the scan of one or both the downconverted fields have been implemented. The consequent results are presented respectively in section 4.2 and 4.3, with the latter case being applied to four different configurations of the pump beam profile. In particular, we show the experimentally measured biphoton wavefunction in the form of the coincidences distribution in one spatial dimension (horizontal) for the cases of: large Gaussian pump profile 4.3.1; small Gaussian pump profile 4.3.2; large first-order Hermite-Gaussian pump profile 4.3.3; small first-order Hermite-Gaussian pump profile 4.3.4.

We conclude the chapter with a section in which we show the estimation of some moments of the biphoton distribution from the measured data 4.4. To give meaning to any experimental result one needs to assess the experimental errors; uncertainties are extensively analysed in section 4.4.1.

4.1 Raster scan with a Spatial Light Modulator.

Most of the approaches to measure spatial distributions of photons requires some sort of discretization when projecting the fields[1]. In practice, this can be achieved in several different ways. The most intuitive is perhaps the detection of photon distribution through a Charged Coupled Device (CCD) camera, basically recording an image of the intensity of the electric field. This approach to SPDC became available in recent years thanks to the development of single-photon sensitive CCD such as Electron Multiplying Charged Coupled Devices (EMCCD) [122, 123] and Intensified CCD ICCD[124–126].

Another method, very widely used perhaps for its good balanced compromise between practicability and costs (a single-photon sensitive CCD can costs several tens of thousands dollars as well as a cooling system to operate), is the one commonly referred to as *slit-scan*. What links all the methods mentioned hitherto is the fact that all of them aim to reconstruct the marginal probability distribution of the biphoton state. A conceptually different approach, which does not require such a full probability reconstruction, will be explained in the following section 5.2. Here we concentrate on an improved version of the slit-scan.

The working principle of the typical slit-scan method is fairly simple and has been applied extensively to detect spatial properties of photon states generated by SPDC [19, 82, 83, 119]. In a two-photon setup, it requires to install a metallic screen with a slit cut in it in front of one or both the detectors. The only function of the metallic slit is to select a narrow part of the angular distribution of the downconverted fields. By spatially scanning one of the fields with such detector, say the signal scanned horizontally, and by recording the coincidence rate, one can reconstruct the marginal probability distribution. By comparing the coincidence distribution with the singles one, it is possible to estimate the amount of correlations between the photons of the two beams. Furthermore, by scanning both the detectors it is possible to reconstruct the bidimensional probability distribution as a function of one dimension of signal and idler (say, x_{signal} and x_{idler}). This way it is possible to build the probability distribution of coincidences as a function of $(x_s - x_i)$ to show anticorrelations or as a function of $(x_s + x_i)$ to show correlations. By applying this same approach to real and Fourier spaces consecutively, under certain experimental conditions (see section 4.3) one can expect that to detect correlation in position and anticorrelations in momentum. From there it is possible to eventually estimate entanglement with an entanglement witness.

An innovative approach to the slit-scan method was proposed in 2014 by E. C. Paul et al [127]. The principle is to substitute the metallic slit with a phase slit. They exploited the high versatility of Spatial Light Modulators (SLMs), namely the ability of applying a position-dependent phase on an optical field. Thanks to this unique feature, SLMs have been extensively utilized in quantum optics.

Since we utilize this method in our experiment, and it is a relatively recent one, we spend this section explaining its functioning principles. Our *phase-only*, reflective SLM

[1] Other approaches which do not require sampling are based on signal processing (compressed sensing [120]) or on a method proposed by Chan et al. in [81] that exploit interferometric techniques to estimate the Schmidt number (also in [121])

is produced by *Holoeye Photonics* (refer to chapter Experimental setup, section 3.1.2 for working principles and specs). The SLM will imprint a user defined spatial phase on one polarization component only of the field. In our case, we set the SLM such that the Horizontal polarization of an incident field picks up the phase, while nothing happen to the vertically polarized part (ie, it is simply reflected unaffected by the liquid crystals). Therefore we can describe the operation of the SLM on a linearly polarized field as:

$$T = |V\rangle\langle V| \otimes I + |H\rangle\langle H| \otimes U \tag{4.1}$$

where I is the unitary matrix, and $U = \exp[iS(x, y)]$ is the unitary transformation due to the SLM action when a bidimensional phase distribution $S(x, y)$ is applied. Since our modulator is programmable with 8-bit grey-levels images (section 3.1.2), the phase imprinted is $S(x, y) = 2\pi g(x, y)/256$, where $g(x, y)$ is the function associated to the grey-level image that we send to the SLM.

Thanks to the interaction expressed by Eq. 4.1, it should be clear that one can couple dynamically the polarization and the spatial degrees of freedom of a field. Exploiting this principle, in reference [128] the group lead by B. E. A. Saleh experimentally implemented several controlled quantum gates that utilizes the polarization parity as the control qubit and the spatial-parity-symmetry qubits as the targets.

From this working principle it is easy to show how it is possible to convert a phase-only SLM into an amplitude modulation device. In order to do so, let's prepare the incident field in a diagonal polarization state $|+\rangle$. Then, set a uniform zero-phase in the (x, y) positions of the field that we want to couple, and a π-phase everywhere else. The π-phase applied only to one polarization direction of the incident field rotates the linear polarization direction by $\pi/2$ radians, transforming the $|+\rangle$ incident states into $|-\rangle$ states. Finally, by projecting the field in the polarization direction $|+\rangle$ before detection we make sure that we only couple the field incident on the 0-phase positions.

We exploited the just explained reasoning to couple slices of the incident downconverted fields. To do so we designed phase-slits consisting of a given uniform phase within the slit area and a supplementary uniform phase elsewhere. We can mimic the raster of the physical metallic slit by engineering a proper sequence of those phase-slits. They are sent to the SLM via a computer software that we developed (powered by *LabView*). Eventually each phase-slit is imprinted on the transverse profile of the optical fields. Thanks to the mentioned polarization dependence of the action of the SLM, the phase-slits can be translated into an amplitude slit by coupling only the photons characterized by the phase inside the slit.

For instance, when we perform a scan on the horizontal x-direction, we implement a sequence of N vertical phase-slits. Each of them is an 8-bit greylevel images that once reaches the SLM translates to a phase slit $g_n(x, y)$, $n = 1, 2...N$, that can be expressed as:

$$g_n(x, y) = \begin{cases} 0 \text{ for: } n\Delta < x < (n+1)\Delta \\ \pi \text{ elsewhere.} \end{cases} \tag{4.2}$$

The slit size Δ can be chosen to optimize the outcome. Clearly, choosing narrower slits one can improve the sensitivity of the measurement at the expense of decreasing the counts. On the other hand, a large slit can be problematic in experiments aiming to estimate spatial entanglement [129, 130]. This is due to the fact that most of the entanglement witnesses eventually rely on some measurements of the variances. The discretized variance estimated using the slit method is a good approximation of the actual variance of the continuous variable field only for sufficiently narrow slit [131]. Indeed, the (estimated) variance would tend to

zero when the slit is large, because in that case most of the CV field would be associated to one position only.

For these reasons, one tends to work using narrow apertures while keeping an eye on the counts. Smaller aperture also translates in higher background which is mainly due to the photons reflected from outside the slit that fail to pick up the π-phase because of the limited efficiency of the SLM. On the top of that, we also have to consider that while the signal reduces, the dark counts of the APDs are constant. This makes them more influent (negatively) for smaller signal count rates. Diffraction effects can also be expected for very narrow slits. The typical slit size we implemented in our measurement is between 30 to 60 Px wide, that is 240 to 480 μm.

To show how we can reconstruct the entire coincidence distribution of the two-photon state, let us start writing the state as:

$$|\psi\rangle \simeq \int dx_s \int dx_i \Phi(x_s, x_i) |1(x_s, +), 1(x_i, +)\rangle\rangle \tag{4.3}$$

Eq. 4.3 represents the state derived in the previous chapter (eq. 2.44), where x is the monodimensional (horizontal) spatial transverse variable in real space. When analysing the Fourier distribution, that is when the lens system selected on the setup is the one that creates the Fourier space on the SLM plane, the variable to be considered is the monodimensional (horizontal or vertical) transverse momentum. Here we dropped the vacuum part since it does not interact with the SLM. We remind that the state in eq. 4.3 is valid in paraxial and monochromatic approximation (and s and i represents different wavelengths).

Applying a transformation 4.1 with a slit function 4.2 for each of the downconverted fields to the state 4.3, and consequently projecting the state onto the diagonal polarization $|++\rangle\rangle$, the coincidence probability reads [127]:

$$P(n, m) = \int_{n\Delta}^{(n+1)\Delta} dx_s \int_{m\Delta}^{(m+1)\Delta} dx_i |\Phi(\rho_s, \rho_i)|^2 \tag{4.4}$$

In this case we considered the slit functions on signal and idler to have the same width Δ. After a set of $N \times N$ measurements we can reconstruct the entire probability distribution of the two-photon state. One can do better by moving the slit by a fraction of the slit size, generating a convolution of the probability distribution by means of the rectangular step function representing the slit. While this would be a more accurate approach, it has the disadvantage of requiring longer measurement time.

4.2 Results using one fixed aperture.

Based on the raster scan method described in the previous section 4.1, in this section we explain two experimental procedures we employed in order to quick check for correlations. While it is possible to use them to *quantify* entanglement and correlations (one just has to repeat one of the two methods in position and momentum), we only exploited them for *qualitative* analysis. The quantification of correlations using a raster scan will be instead presented in the following section (4.3).

Based on the idea of selecting only part of the spatial distribution of signal and idler photons, we performed two slightly different tests. The first test is described here. It consists in comparing two coincidence distributions: the coincidence distribution obtained with a slit scanning channel 1 and the entire beam on channel 2 coupled (uniform zero-phase on

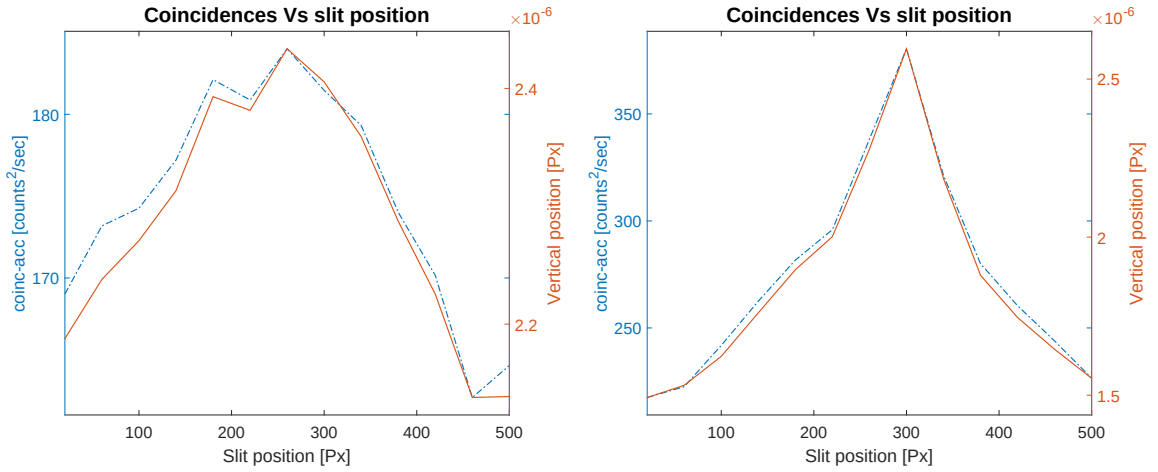

Figure 4.1: On the left, the coincidence distribution when the idler field is scanned vertically (ie, with a horizontal slit) and the signal field is all coupled. The size of the slit is $40Px$ (ie, $320.0\mu m$). On the right, the setup is exactly the same but with a fixed (phase) aperture $40Px$ wide imposed on the signal photons (at the center of the beam). The blue vertical axis on the left of each plot represents the raw coincidence counts (accidentals removed), while the orange one, on the right, represents the coincidences (minus accidentals) normalised by the singles on the fixed-phase channel (signal). On the x-axis the slit position in units of pixels on the respective quadrant of the SLM. A clear sign of spatial correlations is the shrinking of the coincidences distribution when on one field only photons from a narrow angular distribution are selected. The purpose of this measurement was to quickly test spatial correlations qualitatively, but the effect is clear.

the SLM); compared with the curve of the coincidences obtained with the same slit-scan on channel 1 and an aperture at a fixed position on channel 2. If the two fields are *not* spatially correlated (or anticorrelated), one would expect the two coincidences distributions to have same shape and width.

On the other hand, if the two beams were spatially (anti)correlated, the coincidence distribution measured by slit-scanning one channel and keeping a fixed aperture on the other would be a narrower curve. This is due to the fact that for (anti)correlated fields the photons contributing to coincidences are only the ones coming from the same angular position of the beam[2].

Although the method works independently of the position of the fixed slit (as far as it is intercepting the beam somewhere), more signal and therefore better signal-to-noise ratios are expected when it is held at the center of the beam. We applied this method for preliminary tests in order to quickly identify the presence of correlations, but we did not acquire sufficient statistic to *quantify* them. However, for our purposes at those preliminary stages, the results were satisfactory enough. In figure 4.1 we can see that the coincidences distribution for fixed aperture on channel 2 is slightly narrower than the one with zero-phase on channel 2 (ie, coupling the whole photon distribution).

This preliminary test allowed us to realise that in order to obtain better results one has to correct for background coincidences in a better fashion. We decided then to move to the next method which would automatically correct for the background thanks to our measurement protocol. This will give us better data useful for quantification of correlations.

[2] "same angular position" depends conceptually upon the amount of correlations - only maximum correlations gives Dirac delta. Experimetnally, it also depends on the size of the aperture (in our measurements between 240 to 480 μm).

The second test that we mentioned a few paragraphs above is very similar to the one just explained. Again, we aim to qualify spatial correlations by comparing two curves. Each of them is still based upon the scan of one of the two downconverted fields, say channel 1, by a phase slit on the SLM, but in this case on the not-scanned channel (2) we place both the times a fixed aperture (in two different positions). The comparison could also be implemented among more than two coincidence measurements, each of them with the fixed-aperture set at a different position. What we expected to see in the case of spatially correlated fields, is to be able to identify a narrow signal peak emerging from the broader coincidence distribution due to background counts. In particular, we expected the peaks to be centered at different abscissas of the coincidence distributions, corresponding to the position correlated (or anticorrelated) to the position of the fixed slit on the other field. The narrower the peak, the stronger the correlations.

We run many set of measurements of this sort during the early stages of testing the setup. Most of them gave negative outcomes; it was due to different reasons, some related to the parameters of the setup, other due to wrong data analysis protocols. An example of very noisy measurement is shown in figure 4.2.

We improved the measurements by adding one more background measurement to the detection. In figure 4.3 are shown two coincidence distribution curves from two (different) fixed positions of the slit on the idler while scanning the signal field. In that measurement we Fourier transformed the crystal plane on the SLM, therefore the coincidences are related to the distribution of the linear momentum of the down converted fields. This is clear by comparing the two plots: when the fixed aperture on the idler is closer to lower values of the SLM position ($x = 300Px$), the coincidence peak appeared closer to higher values of SLM position (about $x = 580Px$). In particular, with a relative distance of the fixed aperture position of exactly 240Px one would expect the peaks to be displaced exactly by that amount. The attentive reader may have realised that the two peaks are in fact separated by approx 200Px instead. The difference is most likely to be sought into the different magnifications experienced by the two beams, ultimately due to the fact that the fields have different wavelengths.

The experimental details for the plots in figure 4.3 are in the caption of the figure itself. Regarding the result, we can see that the visibility of the peaks is quite low. By defining it in the usual way as $(max - min)/(max + min)$, from the plotted data we calculate a value around 35%. This is due to a non-perfect account of the background, which we identify as the number of recorded counts due to the photons that should have picked up the desired phase but they did not because of the finite efficiency of the SLM[3].

The procedure for the data presented in Figure 4.3 was as follows. For each slit position of signal and idler, the protocol subtracted the number of coincidences recorded when a uniform pi-phase was set in place of the fixed-slit phase on one channel, and the fixed-slit was kept in position on the other one. Hence, this procedure accounted for the background in an asymmetric manner: the background removed is only given by the coincidences between the desired photons on one channel and the ones not desired on the other one. As a comparison, the plots in Figure 4.7 from section 4.3 refer to a measurement taken the same day and with the same conditions as in fig. 4.3 but using a symmetric subtraction of the background.

In particular, the cleaning of the data performed here only accounts for three aspects. First, the background given by all the coincidences detected when on the signal quadrant there is a slit of phase 0 on a uniform π-phase and on the idler channel there is a uniform flat π-phase. In an ideal case, i.e. if the SLM had 100% efficiency, there would be no *real* coincidences in

[3]The efficiency is defined as the fraction of the input photons that is actually affected by the phase change.

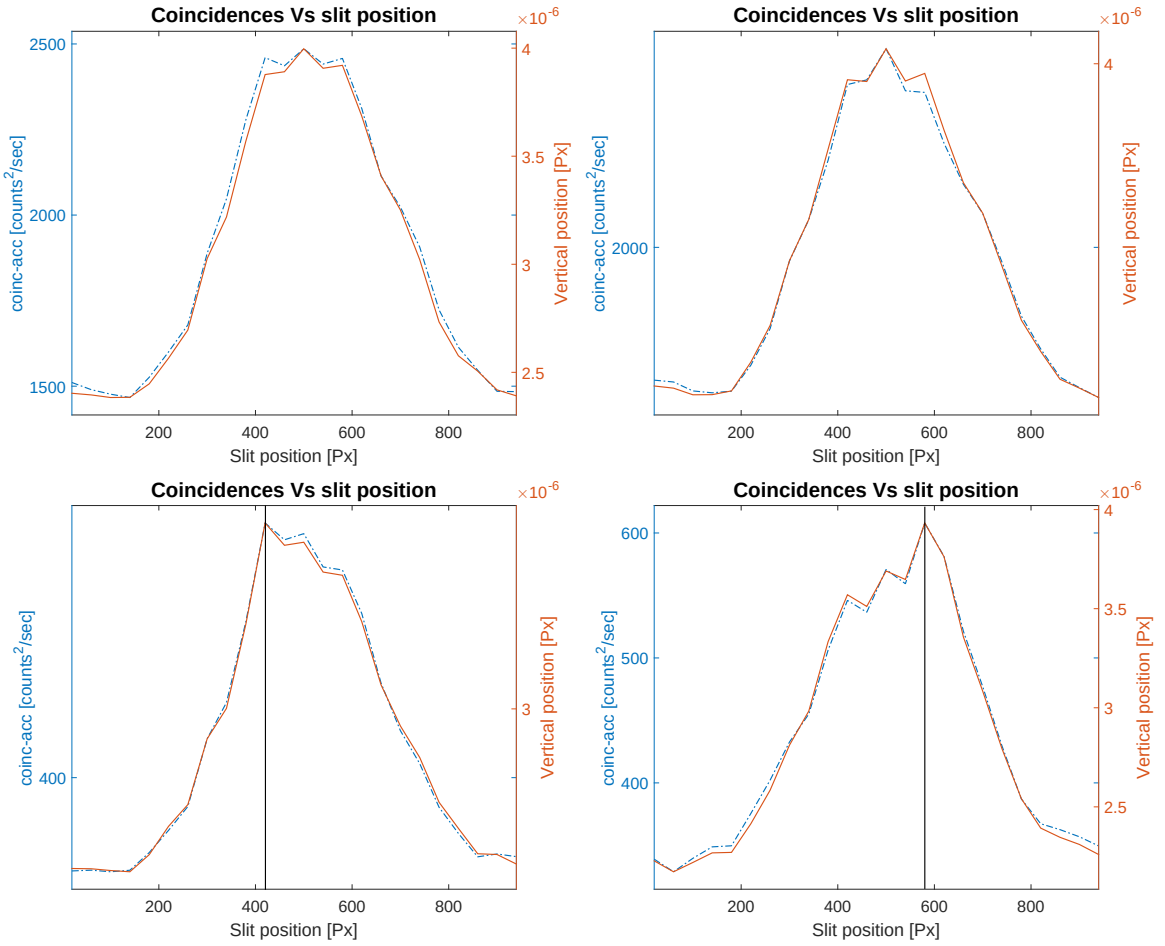

Figure 4.2: Example of qualitative detection of correlations leading to a very noisy result. The explanation of the axes is the same as in fig 4.1. In this case, the field scanned with a slit is the signal, while on the idler we set a fixed phase-aperture. The scan went horizontally, hence with a vertical slit. Comparing the bottom-left plot with the bottom-right, it is clear that there is a peak emerging from the wider coincidence distribution due to the background counts. At that time we could conclude that our photonic states were spatially correlated, but the data shown in this figure are clearly too noisy to estimate it. The data plotted in the upper figure of each column represents the coincidence distribution for uniform zero-phase on the idler channel. They are a control measurement taken while building the measurement set of the below plots. Their reason to be is that we wanted to make sure that the overall coincidence distribution did not change from the two consecutive sets of measurements (the one on the left and the one on the right).

this configuration but rather just accidental ones. After each single measurement with a given combination of slits positions, we took a measurement of such a background. We repeated this pair of measurements for each point of the scanning slit n times in order to collect more statistics. We then calculate the BG value for each slit position as the average over the n measurements of the coincidences recorded as BG. We subtract that value from each of the n measurements taken at the corresponding slit position; then we average among those n BG-removed data. While this approach does not affect the values detected, it decreases the dispersion of the error when the BG is removed.

A second aspect generally accounted for in cleaning the raw data are, of course, the accidental coincidences. This is a purely statistical effect. Given two sets of independent events being detected by two independent detectors at random times, there is a certain

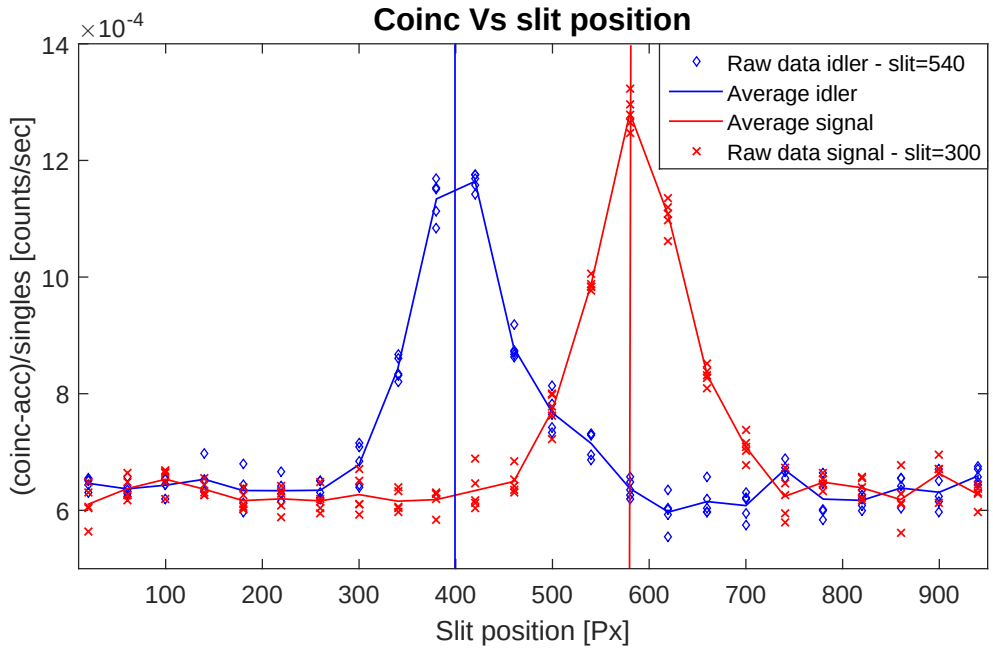

Figure 4.3: Demonstration of momentum anticorrelations in photons created by SPDC. For these two measurements we pumped the ppKTP crystal with the single frequency CW laser at 404.25*nm* and Gaussian profile. The slit size was 40 Px on both the signal and idler SLM quadrants. The scan has been performed horizontally therefore with a vertical slit. Coincidences per unit time on the vertical axis; slit position on the horizontal axis. The blue diamonds represents the experimental points for the slit-scan on the signal and fixed aperture on the idler centered at position $x = 540$Px, while for the red x the fixed aperture on the idler was set at $x = 300$Px. The curves are there to guide the eye, connecting the *average* of the experimental measurements (more details in the text). We plot all the experimental points recorded as an indication of the spread of the experimental uncertainty.

probability to detect one event on detector one and one event on detector two within a given *coincidence window*. Those coincidence-clicks can be truly accidental, no physical correlations are required. They can be approximated by:

$$C_{acc} = N_1 \times N_2 \times \tau \tag{4.5}$$

where N_1 and N_2 are the rates respectively on channel 1 and 2 (in clicks per second) and τ is the coincidence window. The accidental coincidences contribute as a form of statistical noise in the background of any coincidence measurements; however, they are easy to be calculated and removed. We just estimate them using 4.5 and subtract the number from the detected raw coincidences.

The last thing for cleaning the data consists in normalising the coincidences by the pump power. This is important in long measurements since the average power of the pump laser can in principle fluctuate due to several reasons such as, but not limited to, the temperature fluctuations. A more precise way to do so would be to divide the number of coincidences of a given scan by the number of singles on the channel in which the slit position did not change during the scan. This offers a direct measurement of the power fluctuations of the pump which directly reflects on the number of singles generated and in turn eventually detected. So we have a number that accounts for the power of the SPDC for each of the n repetitions that we record during a full measurement. Therefore, we divide each coincidence value by its corresponding singles value. That way we get n normalised coincidence values. The reason

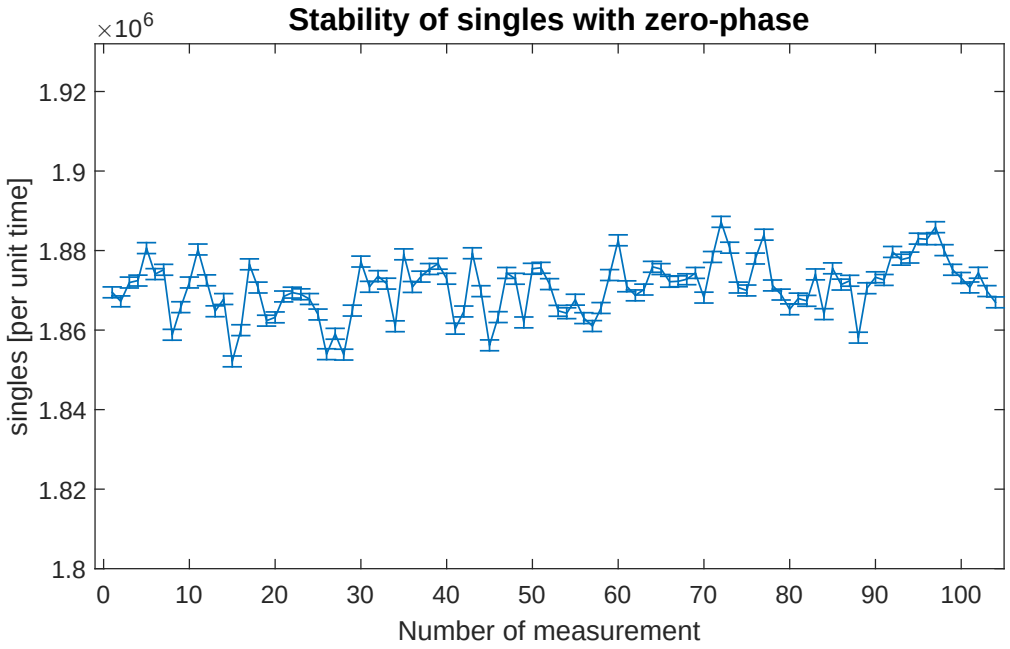

Figure 4.4: Singles on the signal channel with a flat, uniform zero-phase on its quadrant of the SLM. The separation between two successive points on the x-axis corresponds approximately to 5 minutes. The 104 points shown cover a temporal interval of 520 minutes, more than 8.5 hours. The constance of the single counts reflects the constants of the pump power.

for this approach lies in the fact that it makes sense to normalise the coincidences dividing by the power only if the value that we use to estimate the power refers exactly to the temporal interval in which we integrate the coincidence counts.

Within this section, the plots in figure 4.3 account for this normalization explicitly. In particular, each plot displays two similar curves. One represents the detected coincidences minus background minus accidentals (blue line, left vertical axis); the other represents the same numbers but also normalised as explained in the previous paragraphs (orange line, right vertical axis). As we can see, there are no substantial differences in the trends of the distributions. This is a clear sign of the fact that the singles were constant, from which we could assert that the pump laser was stable. A confirmation for that is the plot shown in Figure 4.4, where we demonstrate the stability of the singles in a sequence of more than 100 consecutive slit-slit position acquisitions. Each acquisition point is separate from the neighbours by approximately five minutes. For what concerns us at this stage, this demonstrates a stability of the pump over more than eight hours and an half, which is the typical duration of the measurements presented in this section. It also indirectly proofs the stability of our experimental setup in general. For this reason, we decided to ignore the power normalization in our successive measurements.

The imperfection of this procedure in removing all the unwanted background is clear by the fact that in the plots of all the measurements presented in this section (Figures 4.1, 4.2, and 4.3) do not show a zero value far from the center of the beam. In those regions, the detected coincidences are only due to the accidental ones (which we remove efficiently) and to the background which, as mentioned, we removed only asymmetrically. However, once again, we utilized this slit-aperture method only for qualitative analysis, and therefore we did not need to optimize it further.

4.3 Entanglement estimation by double raster scan.

In order to completely characterize the spatial properties of the state, to measure a few marginal probability distributions (slit scan with fixed aperture) is definitely not enough. A more complete analysis require a two dimensional scan in the Hilbert space of the biphoton state.

A full measurement consists in repeating N raster scans, one for each position of the slit on the not-scanned channel (either signal or idler). The entire set of measurements requires $N \times N$ acquisition points, where N is the number of (phase-)slit positions on each quadrant of the SLM, and fixing the quadrant size it depends on the choice of the slit width.

By reconstructing the entire 2-photon spatial coincidences distribution, we can test our theoretical model. In particular, we know that in the case of pump laser characterized by a Gaussian spatial profile, spatial (anti)correlations in position (momentum) are expected; furthermore, they should be higher for larger pump beam waists. The reason for this leads back to the *Schmidt decomposition* and the Schmidt number discussed in the chapter Spontaneous Parametric Down Conversion, section 2.4, as well as to the shape of the biphoton wavefunction.

In the following two (sub)sections we present the results for two different sizes of Gaussian pump beam (subsections *Pump: large Gaussian profile* and *Pump: small Gaussian profile*). That way we can show how spatial (anti)correlations can be switched on and off by changing the radius of the Gaussian pump beam. From now on we might refer to those two configurations as the *large* and the *small* pump beam waist respectively, corresponding to experimental values of about $74\mu m$ and $16\mu m$. Instead, in subsections *Pump: large Hermite-Gaussian profile* and *Pump: small Hermite-Gaussian profile* we present the results obtained when pumping the nonlinear crystal with structured light (first-order Hermite-Gaussian profile) in the cases, again, of large and small beam waist respectively.

4.3.1 Pump: large Gaussian profile.

As we said, for large pump beam waists we expect strong correlations in position and strong anticorrelations in momentum. The pump beam profile at the crystal plane is shown in figure 4.5. The value of the waist is calculated from the fit parameter $c1$ (in the inset of the cross sections, Figure 4.5) after multiplication by the pixel size of the camera. For the horizontal profile it gives: $w_H = 14.26Px \times 5.2\mu m/Px = 74\mu m$. As the scans were made in the horizontal directions, the width in the vertical direction provides no information for our purposes.

In the specific case of Gaussian pump, we also expect the spatial correlations (in position) and anticorrelations (in momentum) to translate in the typical elliptical distribution of coincidences in the $x + y$ and $x - y$ directions respectively (x and y being either the transverse position variables of signal and idler or the transverse momentum variables of signal and idler). The results of our measurements are shown in Figure 4.7: on the left column the plots for real space and the correspondent data for Fourier space on the right column.

Despite the pixelization due to the finite width of the slit, our results clearly show strong correlations in position and anticorrelations in momentum. The squares are $60 \times 60\text{Px}^2$, which correspond to $480 \times 480\mu m^2$. This choice was driven by the need to keep the execution time of the entire measurement not-too-long and to get a good contrast in the coincidences detected.

The visibility in the plots of Figure 4.7 are very high. For instance, in the position

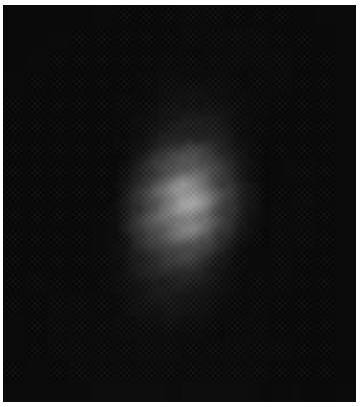

(a) Bidimensional profile.

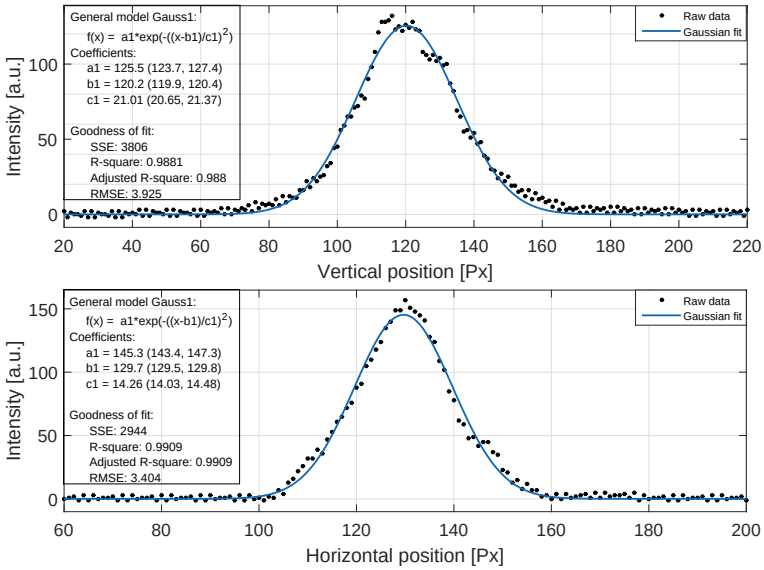

(b) Cross sections.

Figure 4.5: Pump beam profile at the z-position corresponding to the center of the crystal for the case of large Gaussian beam. In a) is shown the transverse profile captured with a CMOS camera. In figures b) are shown the horizontal (top) and vertical (bottom) cross sections of the transverse beam profile. The horizontal and vertical waists estimated from the fit parameters are: $w_H = 74\mu m$ and $w_V = 110\mu m$, showing that the pump beam was still elliptical (see section 3.2.1).

distribution if we consider Poissonian statistic[4] we calculate a visibility of 0.996 ± 0.04. This very high value is due to the average minimum value being estimated to be as little as 6 ± 31. In order to achieve such result we had to improve the suppression of the background, with respect to the previous section. Here, we consider the finite efficiency of the SLM over *both* channels.

For each point in the plots of Figure 4.7, we took a series of four measurements to account properly for the background. The accidental coincidences were accounted for separately on each single measurement by estimating them in the usual way. The procedure is explained as follow. When a 0-phase slit is programmed on each of the two quadrants (ie, for both signal and idler fields), the number of detected coincidences are: $N^{1,2}_{det} = N_{real} + N^{1,2}_{acc} + N^{1,2}_{BG}$. The background coincidences in this case are given by all those signal and idler photons that pass through the pixels of the SLM which are outside the slits, but fail to be transformed from $|+\rangle$ to $|-\rangle$ polarization state. Changing the SLM phase from a slit-like to a uniform π-phase on one of the two channels only, say channel 2, the detected coincidences are given by: $N^1_{det} = N^1_{acc} + N^1_{BG}$. In this case there are no real coincidences since we would expect all the photons reflected on the second quadrant to pick up a π-phase which would prevent them to reach the optical fiber due to the polarizer. The photons that are not affected by the SLM because of efficiency limitations are accounted for in N_{BG}. Repeating the same change in phase but on the other channel, channel 1, the detected coincidences corresponds to: $N^2_{det} = N^2_{acc} + N^2_{BG}$. Finally, one last measurement with uniform π-phase on both the SLM quadrant is performed, which brings to detect: $N_{det} = N_{acc} + N_{BG}$.

[4]The uncertainties can be estimated according to a Poissonian distribution: for a measured value n, its uncertainty is $\pm\sqrt{n}$.

For each slit-slit position (i, j) on signal and idler quadrants		
REPETITION:	PHASE: (ϕ_s, ϕ_i)	MEASUREMENT:
1 times	(slit, *0*)	$(C_{i,0}$ - $A_{i,0})$
n times	(slit, slit) (slit, π) (π, slit) (π, π)	$(C_{i,j}$ - $A_{i,j})$ $(C_{i,\pi}$ - $A_{i,\pi})$ $(C_{\pi,j}$ - $A_{\pi,j})$ $(C_{\pi,\pi}$ - $A_{\pi,\pi})$
1 times	(slit, *0*)	$(C'_{i,0}$ - $A'_{i,0})$

Figure 4.6: Experimental protocol for double raster scan measurements. The complete measurement of a bidimensional joint coincidences distribution requires the scan of the entire quadrant of one channel for each position of the slit on the other one. The procedure in figure refers to the scan on the signal channel.

Clearly the number of expected background coincidences changes along the four measurements. In the first case are due only to out-of-slit photons on both signal and idler; in the second, by out-of-slit photons from channel 1 and all quadrant from channel 2; then the other way around; finally in the fourth measurement the BG comes from the photons reflected in the entire quadrant on both channels. However, those numbers are connected. In particular:

$$\begin{aligned} N^1_{BG} &= N^{12}_{BG} + \delta^1 \\ N^2_{BG} &= N^{12}_{BG} + \delta^2 \\ N_{BG} &= N^{12}_{BG} + \delta^1 + \delta^2 \end{aligned} \tag{4.6}$$

where the δ represent the surplus of BG counts of the specific configuration with respect to the slit-slit one due to the fact that there is an extra part of the quadrant contributing to BG counts (ie, the area previously dedicated to the 0-phase of the slit). Hence, we can recover the real number of coincidences - that is the ones due to the photons coming only from the slits on both quadrants - with an easy operation: $N_{real} = (N^{1,2}_{det} - N^{1,2}_{acc}) - (N^1_{det} - N^1_{acc}) - (N^2_{det} - N^2_{acc}) + (N_{det} - N_{acc})$.

In conclusion, for each slit-slit position our protocol consists of taking four measurements for estimating a single value of real coincidences. On the top of that, we usually repeat each point a number n of times in order to produce some statistic for decreasing the value of the variances. Furtheremore, before and after each of the aforesaid set of measurement per single slit-slit point, we record a measurement with slit-phase on the scanning channel and uniform zero phase on the other (procedure sketch in Figure 4.6). The meaning of this is just to have a control measurement. With that we can make sure that between one slit-slit point and the others we have the same amount of singles on one channel - indication of the stability of the pump. We can also use it to reconstruct the entire joint distribution as a sum of the joint distributions of each slit-slit configuration.

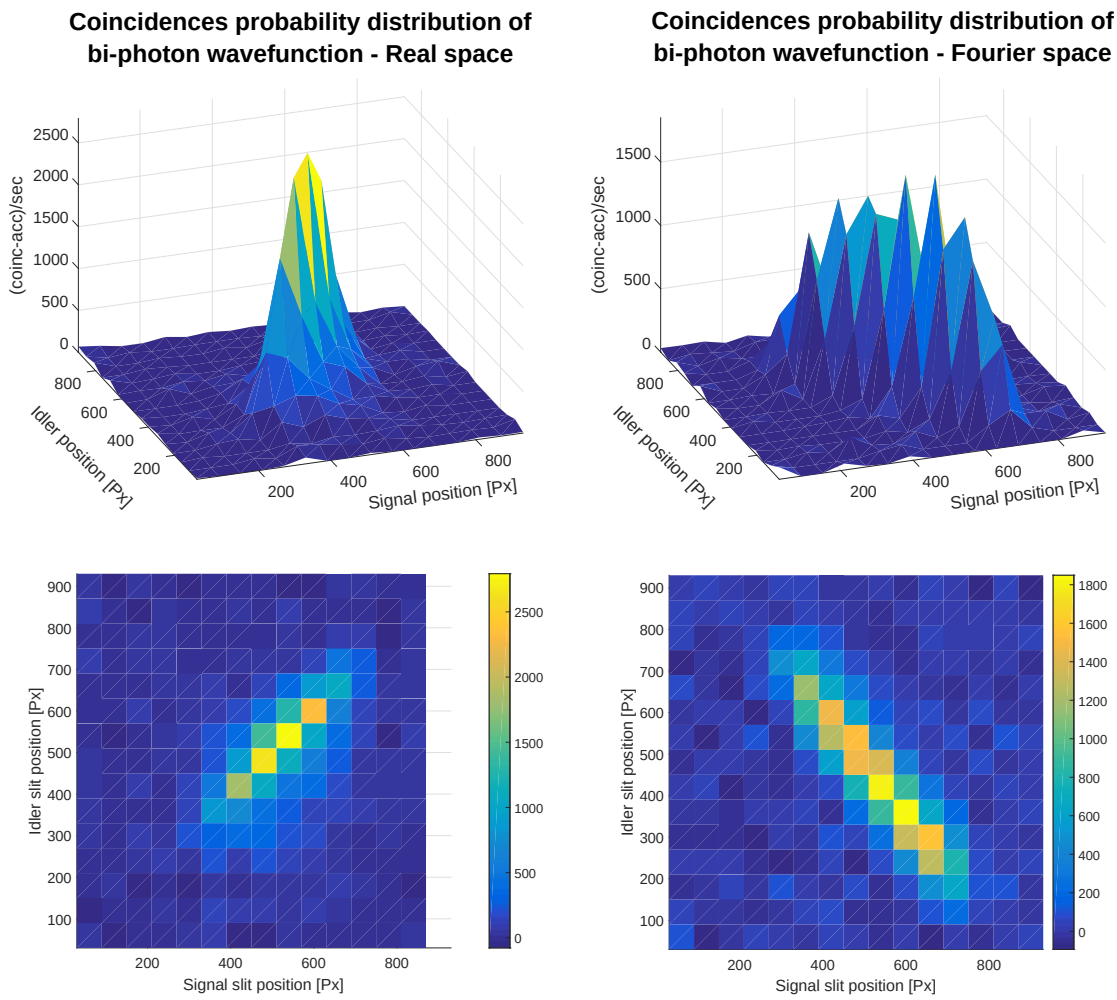

Figure 4.7: Experimental coincidences distribution of biphoton wavefunction in real space (top left and bottom left plots) for the case of large waist, Gaussian pump profile. The figures in the bottom row depict the *(x-y)* view of the distribution, with the x and y axis representing respectively the signal and idler horizontal position (expressed in pixels on the SLM). The colour bar is in units of coincidences per second (accidentals removed). On the top row, we show a 3D view of the same bidimensional probability distribution (the explanation of the axis is the same).

4.3.2 Pump: small Gaussian profile.

From the result already shown in equation 2.46:

$$\Phi_{oo}(\vec{\mathbf{q}}_s, \vec{\mathbf{q}}_i) \propto e^{\left[-\frac{w_p^2}{4}|\vec{\mathbf{q}}_s+\vec{\mathbf{q}}_i|^2\right]} e^{\left[-\frac{\alpha L}{4k_p}|\vec{\mathbf{q}}_s-\vec{\mathbf{q}}_i|^2\right]} \tag{4.7}$$

we can see that if the pump waist is exactly $w_p = \sqrt{(\alpha L)/(K_p)}$, that is if the widths of the two exponentials are equals, then the state assumes a separable expression. We recall that α is the parameter used to approximate the *sinc* phase matching function to an exponential, L is the length of the crystal, w_p is the pump waist, and k_p is the wavenumber at the pump wavelength. For values of the widths close to that regime, the entanglement is very small and the correlations may be hidden by the finite size of the slit. In order to detect them, in those cases the method of the slit-slit raster scan would not work.

Perhaps the easiest way to show this is to decrease the pump beam waist below certain value that prevent spatial correlations in the SPDC processes. It corresponds to decrease the

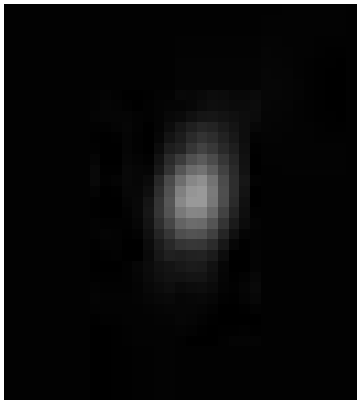

(a) Bidimensional profile.

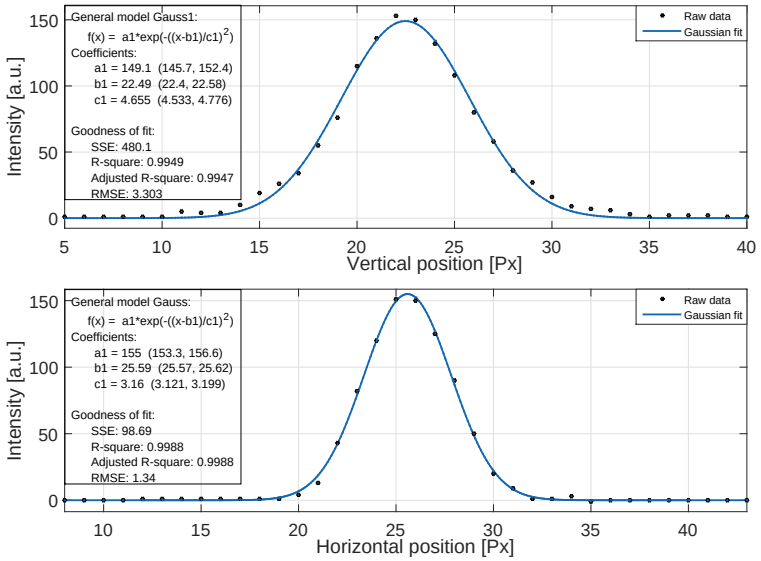

(b) Cross sections.

Figure 4.8: Pump beam profile at the z-position corresponding to the center of the crystal for the case of small Gaussian beam. In a) is shown the transverse profile captured with a CMOS camera. In figures b) are shown the horizontal (top) and vertical (bottom) cross sections of the transverse beam profile. The horizontal and vertical waists estimated from the fit parameters are: $w_H = 16\mu m$ and $w_V = 24\mu m$.

denominator of the first exponential of the biphoton wavefunction. We obtained a reduction in the pump beam waist of a factor $3.16/14.26 \simeq 1/4.5$ by removing from the setup the telescope system made by two plano-convex lenses. Apart from flipping-off the telescope system from the setup, the rest does not change with respect to the measurements for the large waist (results shown in the previous subsection).

We recorded the small pump beam waist at the z-position corresponding to the center of the crystal using a commercial CMOS camera. In Figure 4.8, we show the spatial profile of the CW laser as used to pump the crystal. From a Gaussian fit function we can estimate the waist in the direction of interest (horizontal) to be $16\mu m$.

Using the small Gaussian beam to pump the ppKTP crystal, we collected all the collinear SPDC fluorescence without any spectral filter. The results of the slit-slit raster scans in real space and momentum space are shown in Figure 4.9.

It can be observed that any possible spatial correlations would be hidden by the finite size of the slit or within the statistical error of coincidences count rates. The data processing method is the same as described above.

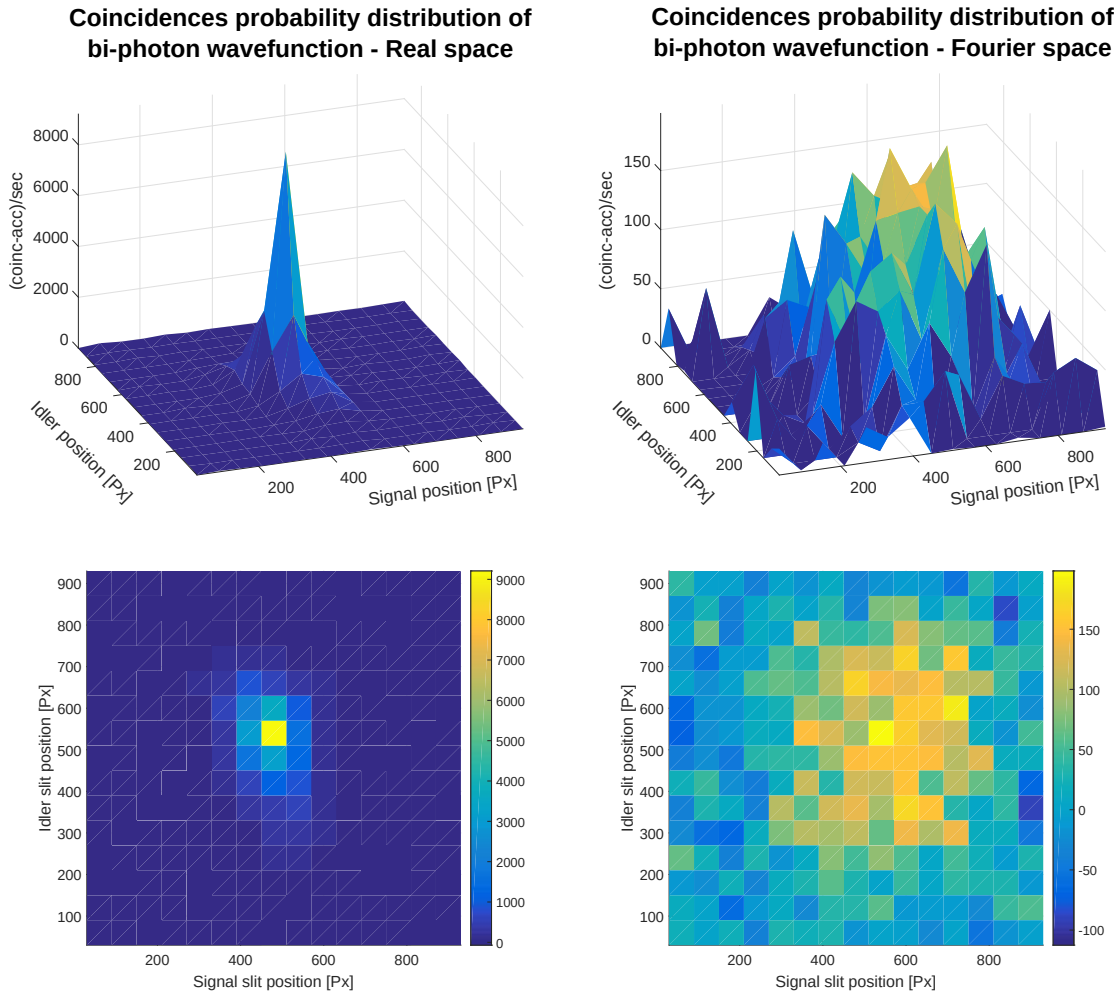

Figure 4.9: Experimental coincidences distribution of biphoton wavefunction in real space (top left and bottom left plots) for the case of small waist, Gaussian pump profile. The figures in the bottom row depict the *(x-y)* view of the distribution, with the x and y axis representing respectively the signal and idler horizontal position (expressed in pixels on the SLM). The colour bar is in units of coincidences per second (accidentals removed). On the top row, we show a 3D view of the same bidimensional probability distribution (the explanation of the axis is the same).

4.3.3 Pump: large Hermite-Gaussian profile.

We investigate the spatial characteristics in real and Fourier space of photons generated by SPDC using a large beam waist to pump the nonlinear crystal. The pump profile is shown in Figure 4.10. In Figure 4.11 we demonstrate that correlations and anticorrelations are visible in a similar way as for the Gaussian pump case. Very interesting is the split of the correlations (anticorrelations) diagonal (antidiagonal) coincidences distribution.

In the momentum space the split of the anticorrelation peaks is very clearly highlighted by a one-pixel line of almost zero counts. We expected a similar behaviour in real space as well, but in that case we can only see a thickening of the peak (from one pixel thick for the Gaussian case to a two pixels thick in the case of real space depicted in Figure 4.11, left column). The reason for this is again the finite size of the slit.

(a) Bidimensional profile.

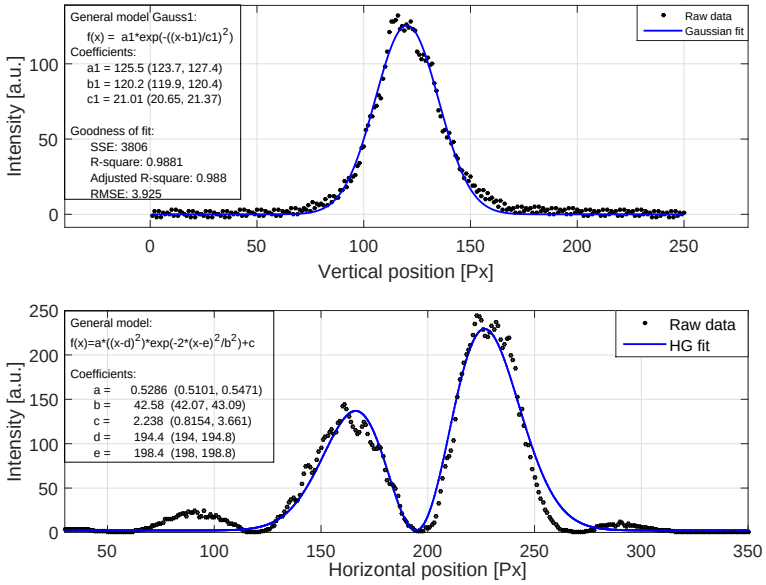

(b) Cross sections.

Figure 4.10: Pump beam profile at the z-position corresponding to the center of the crystal for the case of large Hermite-Gaussian beam. In a) is shown the transverse profile captured with a CMOS camera. In figures b) are shown the horizontal (top) and vertical (bottom) cross sections of the transverse beam profile. The horizontal and vertical waists estimated from the fit parameters are: $w_H = 111\mu m$ (Hermite-Gaussian) and $w_V = 107\mu m$ (Gaussian).

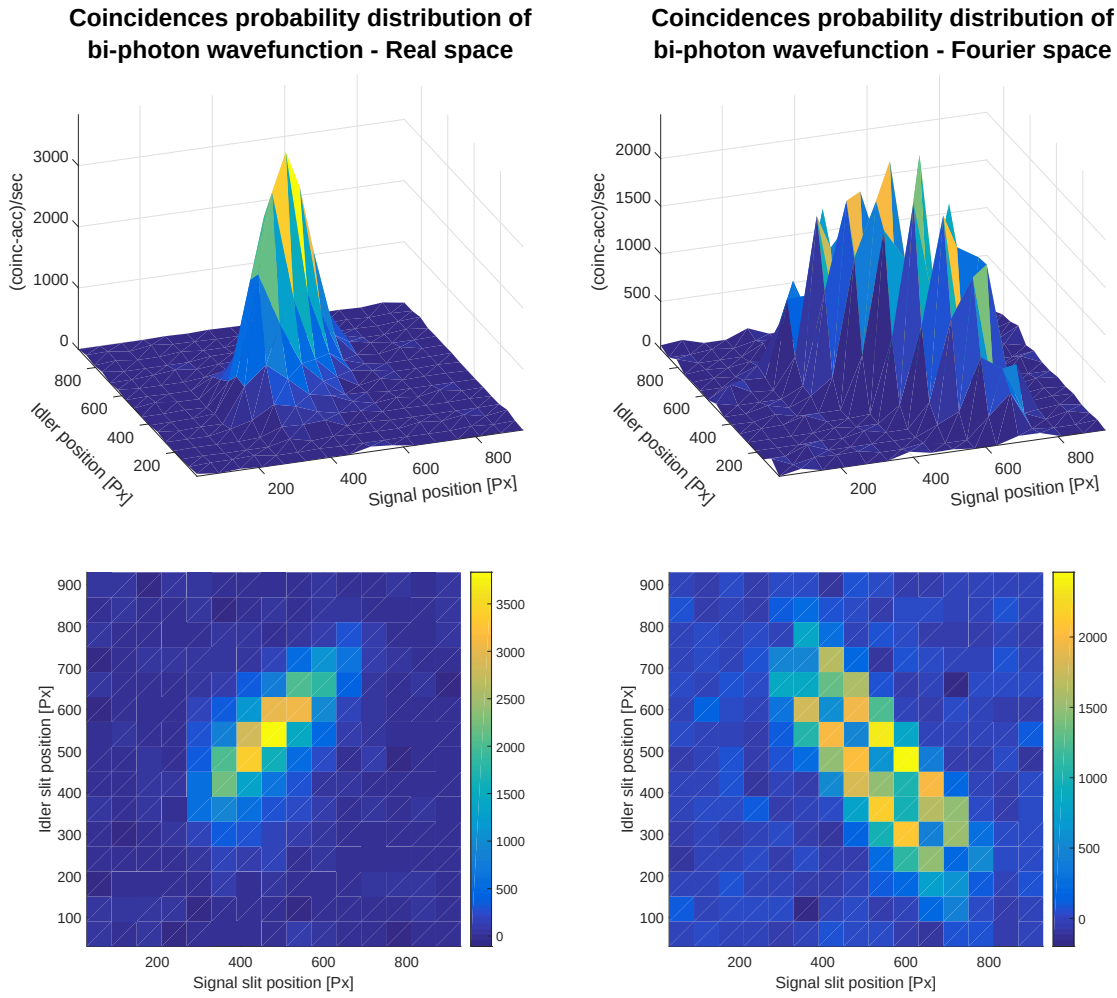

Figure 4.11: Experimental coincidences distribution of biphoton wavefunction in real space (top left and bottom left plots) for the case of large waist, Hermite-Gaussian pump profile. The figures in the bottom row depict the *(x-y)* view of the distribution, with the x and y axis representing respectively the signal and idler horizontal position (expressed in pixels on the SLM). The colour bar is in units of coincidences per second (accidentals removed). On the top row, we show a 3D view of the same bidimensional probability distribution (the explanation of the axis is the same).

4.3.4 Pump: small Hermite-Gaussian profile.

For small $HG_{1,0}$ pump beam, the spatial distribution of the coincidences detected with the raster scan method is peculiar; however, it does not highlight clear information about spatial entanglement of the source. As usual the intensity distribution of the pump field at the crystal plane is presented together with horizontal and vertical cross sections (Figure 4.12). The important value from the fit is the horizontal (Hermite-Gaussian) waist, which we measured to be: $w_H = 51.4\mu m$.

In Figure 4.13 are shown the results of our measurements for the double-slit raster scan in near and far field.

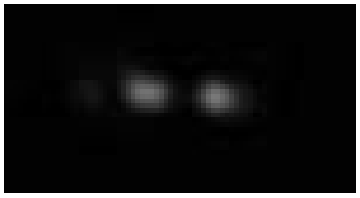

(a) Bidimensional profile.

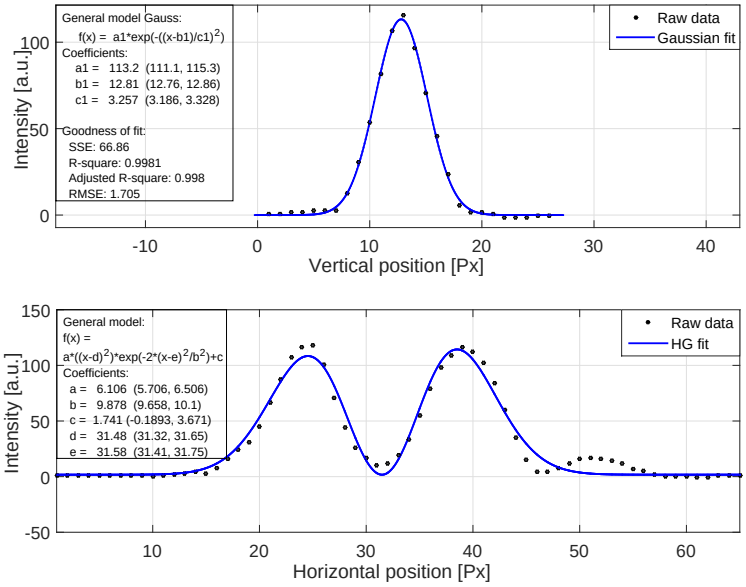

(b) Cross sections.

Figure 4.12: Pump beam profile at the z-position corresponding to the center of the crystal for the case of small Hermite-Gaussian beam. In a) is shown the transverse profile captured with a CMOS camera. In figures b) are shown the horizontal (top) and vertical (bottom) cross sections of the transverse beam profile. The horizontal and vertical waists estimated from the fit parameters are: $w_H = 51.4\mu m$ (Hermite-Gaussian) and $w_V = 17.1\mu m$ (Gaussian).

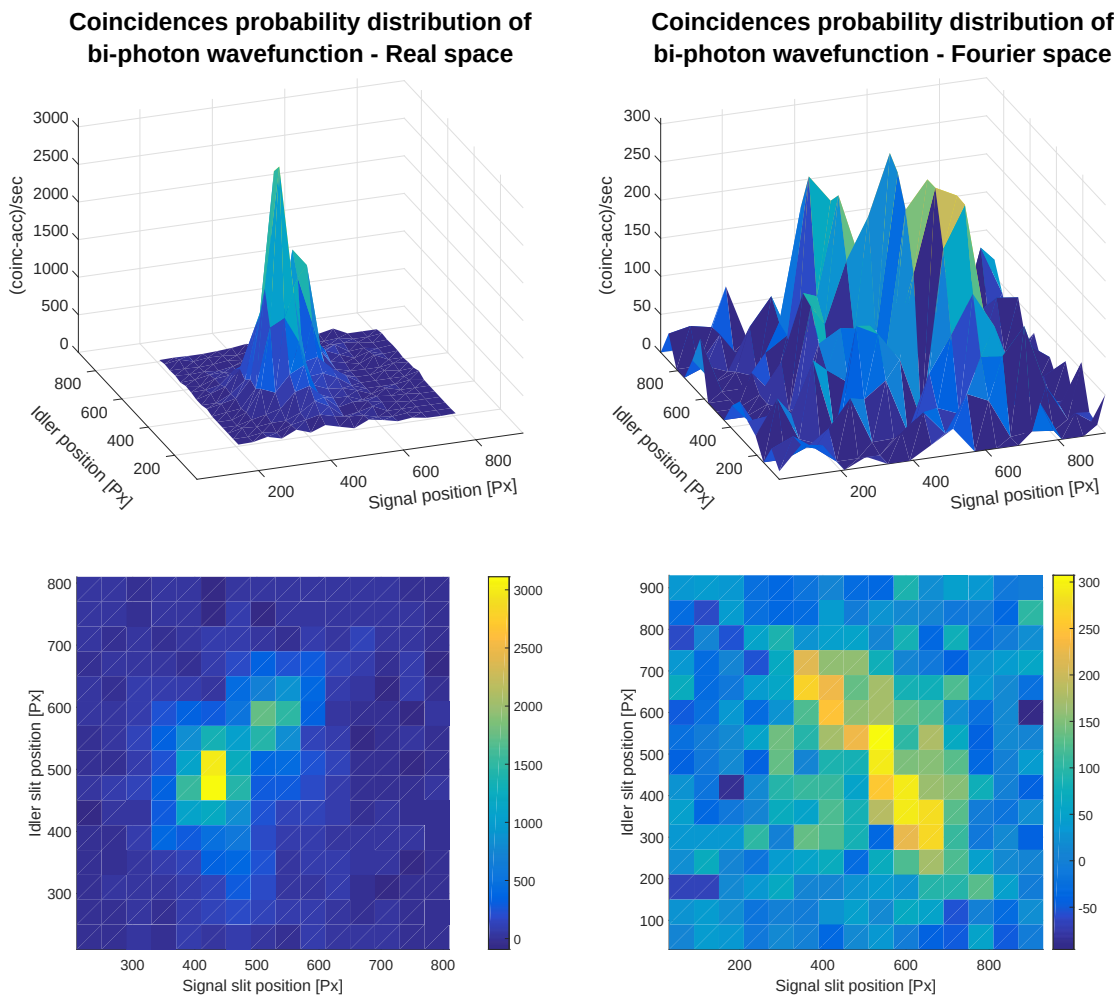

Figure 4.13: Experimental coincidences distribution of biphoton wavefunction in real space (top left and bottom left plots) for the case of small waist, Hermite-Gaussian pump profile. The figures in the bottom row depict the *(x-y)* view of the distribution, with the x and y axis representing respectively the signal and idler horizontal position (expressed in pixels on the SLM). The colour bar is in units of coincidences per second (accidentals removed). On the top row, we show a 3D view of the same bidimensional probability distribution (the explanation of the axis is the same).

4.4 Estimation of the moments of the distribution.

Given a probability distribution $P(x_1, x_2)$, it is possible to calculate any moment of such a distribution using the general formula (in two dimensions):

$$\langle x_s^n x_i^m \rangle = \frac{1}{N_{x_s^n, x_i^m}} \int_{-\infty}^{+\infty} dx_1 \int_{-\infty}^{+\infty} dx_1 x_1^n x_2^m P(x_1, x_2) \tag{4.8}$$

where $N_{x_s^n, x_i^m}$ is a normalisation factor. The variables x_s and x_i in our cases can be either the horizontal transverse position or the horizontal transverse momentum of signal and idler respectively.

By identifying the probability distribution of SPDC photons $P(x_1, x_2)$ as one of the empirical bidimensional coincidences distributions reconstructed and plotted in the previous four sections, we can calculate the experimental expectation values of the moments. For instance, in the Fourier space the general two-variables moment can be estimated from our

data as:

$$\langle p_s^n p_i^m \rangle = \frac{1}{N_{p_s^n, p_i^m}} \sum_{i=1}^{N} \sum_{j=0}^{N} p_1^n(i) p_2^m(j) P(x_1(i), x_2(j)) \tag{4.9}$$

where in the experimental case the integrals are replaced by sums over the discrete variables corresponding to the slit positions on the signal and idler fields.

The results from equation 4.9 are of course expressed in units of (Px^n, Px^m) at the SLM z-position. In order to assess the values of the moments in natural units at the crystal plane (i.e., where the photons are generated) we need first to convert from *pixels* to *mm*, and then account for the lens system that conjugates the two planes. For the case of real space (position distribution) the lens system is composed by a pair of telescopes which total magnification factor is $M = 13$. From the SLM to the crystal plane it corresponds to a *de*magnification $M' = 1/13$. The linear pixel size of the SLM is 8μ; therefore the conversion from px at the SLM plane to mm at the generation plane is given by:

$$\langle x_s^n, x_i^m \rangle_{mm}^{crystal} = \langle x_s^n, x_i^m \rangle_{\mathrm{Px}}^{SLM} \times \left(\frac{8 \cdot 10^{-3} \mathrm{mm/Px}}{13} \right)^{n+m} \tag{4.10}$$

For the case of transverse momentum the conversion is slightly different. In this case the three-lenses Fourier system applies a transformation that maps the momentum distribution of the SPDC photons at the crystal plane to the position distribution at the SLM plane described by:

$$\langle p_s^n, p_i^m \rangle_{mm}^{crystal} = \langle x_s^n, x_i^m \rangle_{\mathrm{Px}}^{SLM} \times \left(8 \cdot 10^{-3} \mathrm{mm/Px} \cdot \frac{2\pi}{\lambda_s} \cdot \frac{250\mathrm{mm}}{300\mathrm{mm} \times 400\mathrm{mm}} \right)^n \tag{4.11}$$

$$\times \left(8 \cdot 10^{-3} \mathrm{mm/Px} \cdot \frac{2\pi}{\lambda_i} \cdot \frac{250\mathrm{mm}}{300\mathrm{mm} \times 400\mathrm{mm}} \right)^m \tag{4.12}$$

where $\langle x_s^n, x_i^m \rangle_{Px}^{SLM}$ is the expectation value calculated from eq. 4.9 (which we left expressed in x since it has the physical meaning of moments of the position distribution of photons at the SLM plane). In the momentum case we see that the conversion factor is wavelength dependent due to the Fourier transform implemented with a lens system, therefore it has to be considered separately for signal and idler. The scalars 250, 300, and 400 represent the focal lengths of the lenses used in the Fourier system expressed in millimiters.

From the expectation values of the first and second moments is possible to calculate the variances using equations of the kind: $\langle \Delta^2 p \rangle = \langle p^2 \rangle - \langle p \rangle^2$. Eventually, with the variances we can provide the experimental value of the correlations from:

$$C(p_1, p_2) = \frac{\langle \Delta^2 (p_1 p_2) \rangle}{\sqrt{\langle \Delta^2 p_1 \rangle \langle \Delta^2 p_2 \rangle}} \tag{4.13}$$

with $\langle \Delta^2 (p_1 p_2) \rangle = \langle p_1 p_2 \rangle - \langle p_1 \rangle \langle p_2 \rangle$.

4.4.1 Estimation of the experimental uncertainties.

In order to estimate the uncertainty on the experimental values of the moments of the distribution we need to account for two types of errors. There is a statistical error related to the statistical nature intrinsic in the photon counting, and there is the sensitivity of the

instruments utilized. The latter is related to the size of the slit: when we fix the slit at position x_0 [Px], the complete reading of that position should be: $x_0 \pm D/2$ [Px], where D is the width of the slit (in pixels).

The definition of the generic moment of a probability distribution $P(x_1, x_2)$ is given by equation 4.8. Paying attention to the proportionalities: $\langle x_1^n, x_2^m \rangle \propto x_1^n x_2^m P(x_1, x_2)$, we can locate the statistical error $\sigma_{stat,nm}$ only in the term $P(x_1, x_2)$ while we can write the instruments error in the variables as: $x_1^n \pm \sigma_1^{inst}$ and $x_2^m \pm \sigma_2^{inst}$ (where the σ^{inst} are equal to half the slit width).

Regarding the statistical aspect, we follow the analysis carried on in reference [132], where the authors started by considering the recorded events to be all independent. This allows us to apply Poissonian statistic, and the error can be estimated as:

$$\sigma^2_{stat,nm} = \frac{1}{N} \int dx_s \int dx_i |x_s^n x_i^m|^2 (P(x_s, x_i) - P(x_s, x_i)^2) \tag{4.14}$$

with the normalisation factor N being equal to the double integral of $P(x_s, x_i)$ over the two coordinates x_s and x_i.

If we consider the domain of the integrals to be the entire SLM surface discretized by N_{slit} positions, then $P(x_s, x_i) = 1/N^2_{slit}$. The result of the integrals in 4.14 brings us to the final expression of the statistical error, which is:

$$\sigma^2_{stat,nm} = \left(\frac{1}{N \times N^2_{slit}} - \frac{1}{N \times N^4_{slit}} \right) \times \frac{2}{2n+1} \left(\frac{N_{slit}}{2} \right)^{2n+1} \times \frac{2}{2m+1} \left(\frac{N_{slit}}{2} \right)^{2m+1} \tag{4.15}$$

The total error on the estimation of the moment $\langle x_s^n x_i^m \rangle$ is:

$$\sigma^2_{nm} = \sigma^2_{stat,nm} + n^2 \sigma^2_{int} + m^2 \sigma^2_{int} \tag{4.16}$$

As a general remark, we can see that the instrument uncertainties on the identification of positions x_s and x_i are both multiplied by a factor which depends on the moment of the distributions, that is higher moments higher uncertainty. Furthermore, we can argue that the statistical error is much smaller than the instrumental error since the first can be reduced by incrementing the number of events recorded, and therefore we can always find a regime in which it is negligible with respect to the instruments one. For this reason, we consider the total error in the estimation of the moments using the double raster scan method to be proportional to the slit width as:

$$\sigma^2_{nm} \simeq (n^2 + m^2) \sigma^2_{int} \tag{4.17}$$

with $\sigma^2_{int} = (D/2)^2$, D being the slit width. This approximation also accounts for the method of removing the background counts explained in Pump: large Gaussian profile of the previous section. In there we explained how our final experimental coincidences distribution is calculated by summing and subtracting four consecutive measurements. The *statistical* error of the final result is therefore formally given by the error propagation of variances of the form 4.14 and 4.15; however, that is just a statistical error, which again can be managed by increasing the coincidences statistic.

4.5 Conclusion.

As a general conclusion regarding the double raster method we can say that, while it generates a very convenient output, the entire procedure requires long time. With N_s slit positions on the signal and N_i slit positions on the idler field, it requires $\simeq N_s \times N_i$ experimental points. To them one needs to add the extra measurements required in order to normalize the data and to account for imperfections and depolarization effects of the SLM (as explained in section 4.3.1). The total number of acquisitions needed for reconstructing the bidimensional coincidences distribution is $[(4n+2) \times N_s] \times [(4n+2) \times N_i] \simeq (4n+2)^2 \times N^2$ (where n is the number of times a single point measurement is repeated for statistical accuracy). If the target is spatial entanglement, one need to reconstruct the probability distribution in both the position and momentum. In that case, the total number of acquisition doubles.

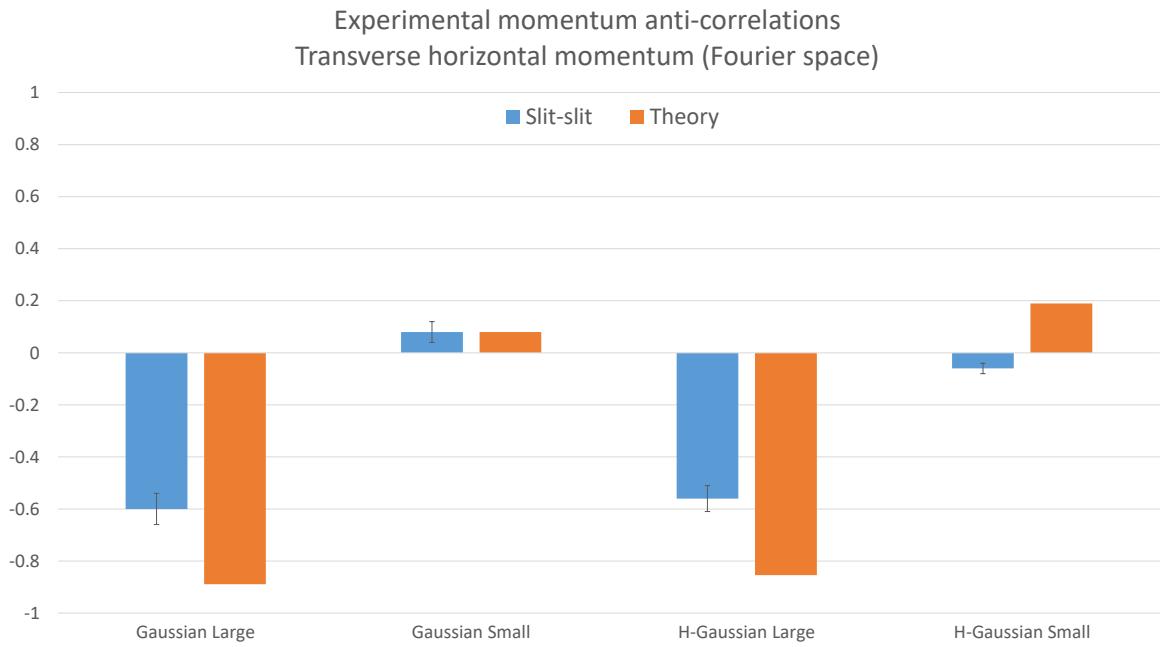

Figure 4.14: Momentum anticorrelations detected with the double-raster scan method in four experimental conditions. From left to right: Large Gaussian pump, small Gaussian pump, large Hermite-Gaussian pump, small Hermite-Gaussian pump.

As a representative example of estimated correlations we present in Figure 4.14 the values of correlations calculated using equations 4.9 to 4.13 for the momentum distributions in the four cases presented in the four previous subsections (Gaussian pump: large and small; Hermite-Gaussian pump: large and small). We picked momentum rather than position since in the Fourier case we have better resolution on th SLM plane due to the beams being larger and therefore covering more pixels.

What we expected to detect with this method is anticorrelations in the large waist cases and no correlations in the small ones. Therefore, the experimental results have confirmed theoretical expectations. However, the fact that the experimental error in the momenta increases dramatically with the orders n, m, together with the long integration time required to acquire enough counts (inversely proportional to the width of the slit), makes this method suitable for limited applications. In the next chapter we will describe an innovative one which fix both these problems and allows for the measurement of higher orders of the moments with no direct increase of the error.

5

Direct detection of the moments of spatial probability distribution.

It doesn't matter how beautiful your theory is, it doesn't matter how smart you are. If it doesn't agree with experiment, it's wrong.

Richard Phillip Feynman

In the previous chapter we have seen the results on the spatial correlations and how to control them. We obtained such results applying an interesting updated double-slit scan method. Another detection method, more sophisticated, has also been employed in our experiments. Its experimental implementation is again based on a Spatial Light Modulator (SLM); this time the novelty consists on measuring directly the moments of the biphoton state rather than detecting the whole marginal and joint probability distributions. The advantage of this method is also that the direct access to the moments provides information about the spatial entanglement of the photons.

This method was experimentally implemented by S.P.Walborn and his collaborators in 2014 [59], one year after having been proposed by some of the same authors in [132]. While they implemented it to the Gaussian case, we advanced by applying it also to correlations in Hermite-Gaussian modes. In the following sections we will show the results of the direct measurement of only the (few) moments of the distribution needed to detect correlations and/or entanglement. However, in our setup we also measured higher moments (up to the fourth in both horizontal and vertical direction), and we could measure even higher ones.

The basics and theoretical background of the method are explained in section 5.1. It is based on the entanglement criteria analysis carried out in section 2.5 of chapter Spontaneous Parametric Down Conversion. Here, in particular in section 5.2, we explain its implementation in our setup. The measurement protocol for estimating the moments of the distribution is address in the dedicated subsection 5.3.

In order to prove the reliability of such an innovative method, we first present in section 5.4.2 the results for a typical configuration of the setup (Gaussian profile). We compare them

with the double-slit scan method as well as with the theoretical predictions of the moments and variances of probability distributions.

With the reliability of the direct method tested, we proceed and conclude the chapter by measuring the moments of the probability distribution in the case of correlations beyond Gaussian modes. We achieve that by pumping the crystal with a first-order Hermite-Gaussian spatial profile (section 5.4.2) and we detect correlations in both real and Fourier spaces.

5.1 Theoretical analysis of the ideal case.

Perhaps the most intuitive notion of multidimensional entanglement refers to a system composed by N particles. If each of them has dimensionality 2 (for instance spin-up or spin-down), the entire system has $2N$ degrees of freedom. By entangling some of them we have multidimensional entanglement. However, as anticipated in the introduction of this thesis, multidimensional entanglement is also identified in continuous variables (CV) systems [133]. The problem is that the quantification of entanglement in systems described in infinite-dimensional Hilbert spaces in general is quite difficult [134, 135].

In sections 2.5.1 and 2.5.2 we have derived non-separability crteria respectively for Gaussian and non-Gaussian modes entanglement. Both of them are based on some combinations of the moments of the biphoton wavefunction. Therefore, experimentally one would need to be able to access to the moments of the probability distribution, in our case up to the 4^{th} order. In 2004 Walborn and co-workers [59] successfully demonstrated a method that allows to *directly* measure the moments of the spatial distribution of a field. The method relies on some peculiarities of Spatial Light Modulators (SLM), and it has been demonstrated using entangled photons produced by SPDC.

In this section I'm going to review this innovative method which we applied to our experiment. It's not only very handy to experimentally measure higher order moments of a probability distribution (as we will see later in next chapter, section 5.2), but it also speeds up the measurements of the first and second moments. Therefore we acknowledge its benefits both for the case of Gaussian and Hermite-Gaussian modes entanglement.

The method.

This method works in general for states of any number of photons. For a state of *single* photon described by its marginal probability distribution $\rho(x)$, let us consider an *ancilla qubit* prepared in the state $|+\rangle = (|0\rangle + |1\rangle)/\sqrt{2}$ by a Hadamard gate[1]. The state of the single photon is therefore fully described by the pair: $(\rho(x), |+\rangle)$. The ancilla qubit is used to drive a unitary transformation designated by the operator U. A second Hadamard gate is performed on the ancilla qubit, which then is measured in its natural base $(|0\rangle, |1\rangle)$. In figure 5.1, a quantum circuit schematizes the process for the case of 2-photon states (refer to the caption).

The detection probabilities in the computational base read as follow:

$$Q_0 = Tr[(U^\dagger + I)\rho(U + I)] \tag{5.1}$$

$$Q_1 = Tr[(U^\dagger - I)\rho(U - I)] \tag{5.2}$$

[1]A quantum gate is the basic quantum circuit corresponding to the classic logic gates. The Hadamard gate in particular is the transformations of the qubits $|0\rangle$ and $|1\rangle$ to a superposition state of the two. In particular the Hadamard gate is responsible for the following transformation: $H|0\rangle = \frac{1}{\sqrt{2}}(|0\rangle + |1\rangle)$, and : $H|1\rangle = \frac{1}{\sqrt{2}}(|0\rangle - |1\rangle)$

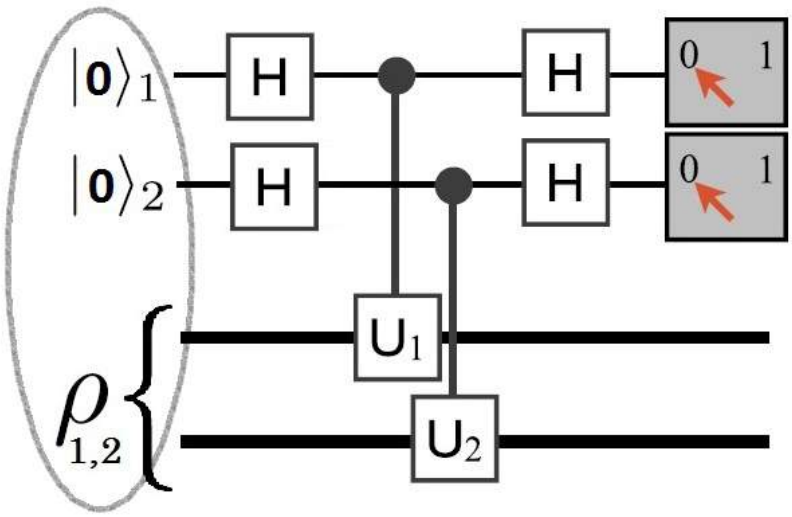

Figure 5.1: The quantum circuit in figure represents the procedure of preparation and reading of the 2-photon state following the method described in the text. The input (2-photon) state is represented by the marginal probability distribution ρ together with the two ancilla qubits. So far they can be *any* qubit, so for simplicity we indicate their value as $|+\rangle = (|0\rangle + |1\rangle)/\sqrt{(2)}$. The "H" boxes represent the Hadamard gates for preparation of the qubits; the "U_i" ($i = 1, 2$) represent the unitary operation made *locally* on both the modes of the state; the grey box represents the measurement on the natural basis of the ancilla qubits.

Now the idea is to choose the unitary transformation U such that a combination of the outcome probabilities Q_0 and Q_1 corresponds to the desired expectation value. For instance, it can be shown [132] that if the unitary operator is defined as:

$$U = e^{i \arccos(X_\phi^n)} \tag{5.3}$$

the expectation value of the $n-th$ moment of the marginal probability distribution ρ in the variable indicated by x_ϕ is given by:

$$\langle X_\phi^n \rangle_\rho = Q_0 - Q_1 \tag{5.4}$$

where with x_ϕ we indicate either the transverse momentum or the transverse position.

Therefore, we can calculate any moment of the marginal probability distribution of a state ρ, which is defined in an infitite-dimensional Hilbert space, by subtracting detection probabilities of a system defined in a bidimensional Hilbert space. With a reference to the experimental implementation of this method, we can see that in principle it would be possible to access any moment of the marginal probability distribution of a single-photon state with only two detection measurements.

Let us now consider the more interesting case of a d-particle state. Now the marginal probability distribution of the total state is defined by ρ_d. We then need d ancilla qubits, one for each mode (photon). The quantum circuit is sketched in figure 5.1.

Following the same reasonings, one can show that any moment of the distribution ρ_d can be calculated from the detection probabilities of the d ancilla qubits [132]:

$$\langle X_{\phi_1}^{n_1} X_{\phi_2}^{n_2} ... X_{\phi_d}^{n_d} \rangle_{\rho_d} = \sum_R s_R^{(n)} Q_R \tag{5.5}$$

where R is an array that contains the 2^d possible outcomes combinations of the d ancilla qubits, Q is the detection probability for the combination indicated by R, and $s_R^{(n)} = \pm 1$ depending on the specific moment that has to be calculated.

In order to have a notion of the accuracy of this method, one can estimate the uncertainty of the measurement of a single Q_R by considering a Poissonian distribution of the counts [59]. For a total number of detected events N the uncertainties are:

$$\Delta_N^2 = \frac{1}{N} \sum_{R=0}^{2d-1} (Q_R - Q_R^2) \tag{5.6}$$

Clearly the sum of all the Q is equal to the integer 1 as they are probabilities. Therefore the uncertainty is upper bounded by $\Delta_N^2 \leq 1/N$. The important thing about this upper bound, is that it doesn't depend upon the number of modes d. Reconstructing the marginal probability distribution of a system with d degrees of freedom, for instance using the double-slit method described in the previous chapter, requires in general a number of measurements proportional to N^d (where N is the number of points for each d.o.f.). Hence, the efficiency of the direct method goes exponentially (with the number of photons) better than the standard one.

When it comes to the experimental implementation of the method, one needs to take into account experimental imperfections. In the next section (5.2), we will explain how to actually use this method in a real setup, and show the corrections needed.

5.2 Accounting for experimental imperfections.

As pointed out in section 5.1, if one is just interested in identify/quantify the amount of entanglement, there are more economical ways than reconstructing the whole marginal probability distribution(s). Since most of the entanglement witnesses are based only on the first two moments of the distribution, in this section we explain how to experimentally access them directly. Eventually we will show the results for the states generated in our setup.

5.2.1 Spatial probability distribution of single photon.

This method has been first experimentally tested in 2014 by the group by Walborn [59]. It allows to directly access the moments of the spatial distribution of photons generated by SPDC. In order to understand it better, let's first discuss how it works for measuring the moments of one of the two fields produced by our SPDC source.

The single photon has marginal probability distribution $\rho(a)$ and initial polarization $|H\rangle$. To keep the flow from the result obtained in section 5.1 for a general system characterized by a probability distribution and a qubit, in the present case the ancilla qubit is represented by the polarization of the photon. Let's identify the $|0\rangle$ with horizontal polarization $|H\rangle$ and the state $|1\rangle$ with the vertical polarization $|V\rangle$. Also, the variable a can be one component of either the transverse linear momentum or the position of the single mode considered. Let's refresh our notation: the horizontal and vertical positions are addressed respectively by x and y; while for the transverse momentum, the horizontal component is p while the vertical is q.

To get to Fourier space we implement the Fourier transform using a plano-convex lens [136]. Experimentally we can swap from one space to the other (and vice versa) by flipping in and out of the setup a system of lenses and mirrors.

We perform the first Hadamard gate in polarization by using a combination of waveplates only. That procedure prepares the ancilla qubit (polarization) in the desired state, which is the

diagonal state $|+\rangle = \frac{1}{\sqrt{2}}(|H\rangle + |V\rangle)$. During the first tests we assumed that all the generated photons were due only to the process of SPDC that we designed the setup for. In particular, we assumed that all the photons in the signal and idler beams were linearly polarized along the same direction, and therefore all of them would be transformed by the Hadamard gate in the same diagonally polarized state. For this reason we decided not to filter the states with any polarizer in order to limit the losses. However, the results of the first measurements were very noisy and in particular we could not identify any spatial correlations. Our intuition was that the imperfections in polarization control of the pump as well as the number the frequencies in its broad spectrum (we were using the pulsed laser) could be responsible for fluorescence processes other than TYPE-0 SPDC. One example could be TYPE-I SPDC, in which the polarization direction of downconverted light is orthogonal with respect to the one expected for TYPE-0. To overcome this problem we placed a linear polarizer right before the SLM to filter only the photons polarized along the diagonal direction. This solution showed to work well allowing us to clearly identify correlations in our measurements. Therefore, we kept the polarizer in the setup.

It is important to underline that in implementing the Hadamard gate in polarization the spatial marginal distribution $\rho(a)$ is not affected. Following the quantum circuit depicted in fig. 5.1, the controlled unitary operator is experimentally implemented by a phase-only spatial light modulator (SLM). We recall here that such a device can imprint a user-defined phase on one linear polarization of the incident beam and acting as an identity transformation on the orthogonal one. Both polarizations are then reflected and keep propagating although carrying a new relative phase. In our setup it represents the means that allows us to implement a *controlled* unitary transformation. For one monochromatic field this transformation can be written as [137]:

$$T = |H\rangle\langle H| \otimes U + |V\rangle\langle V| \otimes I \tag{5.7}$$

For our purposes the unitary transformation implemented by the SLM has to be of the form: $U = \exp(i\arccos(a^n))$.

After the transformation we implement the second Hadamard in a very similar way, that is using another set of waveplates (and polarizer) before the APD. Since we didn't need to spectrally filter the source, the power detected was quite high.

Based on the explanation we gave in section 5.1, we can now calculate the probability of detecting a photon in the states $|H\rangle$ or $|V\rangle$ as [132]:

$$P_+(x) = \langle sin^2(arcos(x^n))\rangle \tag{5.8}$$
$$P_-(x) = \langle cos^2(arcos(x^n))\rangle \tag{5.9}$$

$$P_+(y) = \langle sin^2(arcos(y^n))\rangle \tag{5.10}$$
$$P_-(y) = \langle cos^2(arcos(y^n))\rangle \tag{5.11}$$

for position, and:

$$P_+(p) = \langle sin^2(arcos(p^n))\rangle \tag{5.12}$$
$$P_-(p) = \langle cos^2(arcos(p^n))\rangle \tag{5.13}$$

$$P_+(q) = \langle sin^2(arcos(q^n))\rangle \tag{5.14}$$
$$P_-(q) = \langle cos^2(arcos(q^n))\rangle \tag{5.15}$$

for transverse momentum. Here P has the meaning of probability; experimentally speaking it corresponds to the normalised coincidences, that is to the coincidence counts detected with a particular choice of SLM phase and polarization projection, divided by the total number of coincidences detected with that particular SLM phase in all the polarization states of the base.

Finally, the single-particle moments of its spatial probability distribution can be calculated by :

$$\langle x^n\rangle = P_+(x) - P_-(x) \tag{5.16}$$
$$\langle y^n\rangle = P_+(y) - P_-(y) \tag{5.17}$$
$$\langle p^n\rangle = P_+(p) - P_-(p) \tag{5.18}$$
$$\langle q^n\rangle = P_+(q) - P_-(q) \tag{5.19}$$

The simplification in the experimental procedure with respect to the standard slit-scans is clear. With only two measurements we could in principle measure any moment of the spatial probability distribution of single photon. We say "in principle" because in order to account for experimental errors and especially polarization imperfections introduced of the SLM, two measurements only are not enough to get a clear signal. The mentioned imprecisions can be found, for instance, in a non-optimal preparation of the photons in the desired polarization state. Or very similarly in a non-optimal projection of the photons' polarization state in the detection part. These two unwanted matters can be due both to not-optimal alignment of the setup (fixable) and to the not-ideal behaviour of the optics utilized.

Regarding the SLM, the effect is due to the fact that the limited efficiency implies that not all the photons reflecting on its surface pick up the desired phase. This effect, again, cannot be compensated. Hence, a more sophisticated protocol of measurement has to be implemented, but, since the characterization of single photon spatial probability is not of interest in this thesis, we leave a more comprehensive discussion of the methods for later. Now, let's focus on the analysis of the bi-photon wavefunction.

5.2.2 Spatial distribution of entangled photons.

While accessing the moments of the distribution of a single, independent photon doesn't lead to great excitement, investigating the characteristics of 2-photon states should. New physics emerges when describing a system of two photons with respect to the one photon case. For our particular case we are referring to entanglement, which is a fundamental quantum resource that by cannot exist in single-particle systems by definition. Furthermore, the investigation of the moments of the probability distribution of biphoton states is very exciting since most of the entanglement witnesses are indeed defined upon combinations of different moments.

The method applies in the same way as for one independent photon. The only difference is that now we do on both photons what earlier we did for the one field. The initial state is now described spatially by $\rho_{s,i}$, where s stays for signal and i for idler. The polarization part of the state is $|HH\rangle\rangle$, and with two independent and wavelength matched sets of waveplates we carry out the transformation that sets the polarization state of each of the two photons on the desired balanced superposition of horizontal and vertical: $|+\rangle = \frac{1}{\sqrt{(2)}}(|H\rangle + |V\rangle)$.

Using one system of lenses we can image the center of the crystal plane onto the SLM; using the second system of lenses we can do the Fourier transform of the same plane on the SLM. Swapping from one to the other is done in the same way as described for the one photon: just by flipping in and out some optics. Even though the setup can be expanded for measuring mixed moments of position of one field and momentum of the other, here we only access moments of the kind $\langle x, x\rangle$, $\langle x, x^2\rangle$, $\langle p^2, p\rangle$, and so on.

The polarizer before the SLM is common for both beams, therefore we expect some noise coming from it's imperfect behaviour at the difference wavelengths on the two down converted fields. However, for each moment that we measure we implement a sequence of different phases on the SLM and this should account for several imperfections including the one just mentioned. This will be explained in more details in the following sections of this chapter.

The unitary transformation has to be applied independently on each of the two optical fields. One can do this by using two separated, independent SLM, or more sophisticated by splitting one SLM in two halves and drive them independently. However, the concept on both the channels is exactly the same: a desired phase $U = \exp(i\arccos(a^n))$ has to be imprinted on the spatial profiles of the two beams. The horizontally polarized photons of each of the two picks up that phase, while its vertically polarized ones will pick up nothing. Of course there is an efficiency to be considered, but that will be discussed later.

We eventually project the bounched beams into combinations of $|\pm\rangle$ states and couple the light in multimode fibers. The coincidence probability in each of those bi-photon states in the ideal case are [59]:

$$P_{++}(x) = \langle sin^2(arcos(a^n))sin^2(arcos(b^n))\rangle \tag{5.20}$$
$$P_{+-}(x) = \langle sin^2(arcos(a^n))cos^2(arcos(b^n))\rangle \tag{5.21}$$
$$P_{-+}(x) = \langle cos^2(arcos(a^n))sin^2(arcos(b^n))\rangle \tag{5.22}$$
$$P_{--}(x) = \langle cos^2(arcos(a^n))cos^2(arcos(b^n))\rangle \tag{5.23}$$

Here a refers to the signal field, while b refers to the idler. They can both refer to either of the four considered degrees of freedom x, y, p or q. We recall from the previous section that the experimental correspondences of the probabilities P are the coincidence counts - which ultimately corresponds to the intensity of the electric field.

The detection of a specific moment is eventually given by the following linear combination of the probabilities (here is the general case):

$$\langle a^n, b^n\rangle = P_{++} + P_{--} - P_{+-} - P_{-+} \tag{5.24}$$

More details regarding the settings of the experimental setup as well as the analysis procedures - including the procedure to remove background and account for imperfections - will be given in the following sections where we present the results.

Table 5.1: First moments of the normal distribution with mean equal to zero.

Order	Moment
1	0
2	σ^2
3	0
4	$3\sigma^4$
5	0
6	$15\sigma^6$
7	0
8	$105\sigma^8$

5.3 Experimental implementation.

For the case considered in this section, ie SPDC generated by Gaussian pump beam, the outcomes of this method do not add any new information to the results obtained with the slit-slit scan presented in the previous subsection. In fact, running the direct method measurements what we aimed in the first place was to show that we are able to replicate the results with this innovative method. What we mean when saying that we do not get any new information is that for a normal distribution all the moments of order higher than two are proportional to the second moment (which is the variance - Table 5.1). However, proving that the method works for the estimation of the first and the second moments of the distribution means that it is reliable for higher moments too. Ultimately, the results presented here are just to prove that the method works and that we have good control of it.

From an experimental point of view, the advantage of running this test of the correlation lie mainly in the fact that the measurement is much faster. Being a measurement much faster imply not only saving time but also avoiding to deal with instability issues.

Regarding the results presented in this thesis, for a slit-slit scan the entire measurement takes about 12 to 15 hours, while the same measurement following the direct method (measuring up to 4 moments, even though as said in this case we only need two) takes about 2 hours. Also, the procedure to clean the results from the imperfections of the setup (especially polarization decoherence introduced by the SLM and imperfections on the polarization optics) is the same for all the measured moments. Which is the part that takes most of the time during the entire measurement process. Therefore, adding the detection of one or a few extra moments does not increase dramatically neither the duration of the measurement nor the analysis of the data.

Said that, let us go through the details of the experimental procedure. The setup is the one described in the first part of section 3.2 and depicted in figure 3.9. In order for the comparison of the two detection methods to be consistent, the results presented here have been taken either right before or right after the corresponding measurement with the slit-slit method presented in the previous section. This ensures that the experimental conditions were as close as possible. The parameters of the experiment as well (apart from the pump power) were the same. We recap that the temperature of the crystal was controlled and kept fixed at 30.05 degrees; the pump laser was the CW by Toptica with $5MHz$ bandwidth around $404.25nm$.

Apart from the power control of the pump laser, our setup is fully automatized for running any of our measurements. This means that from one measurement procedure to the other, the

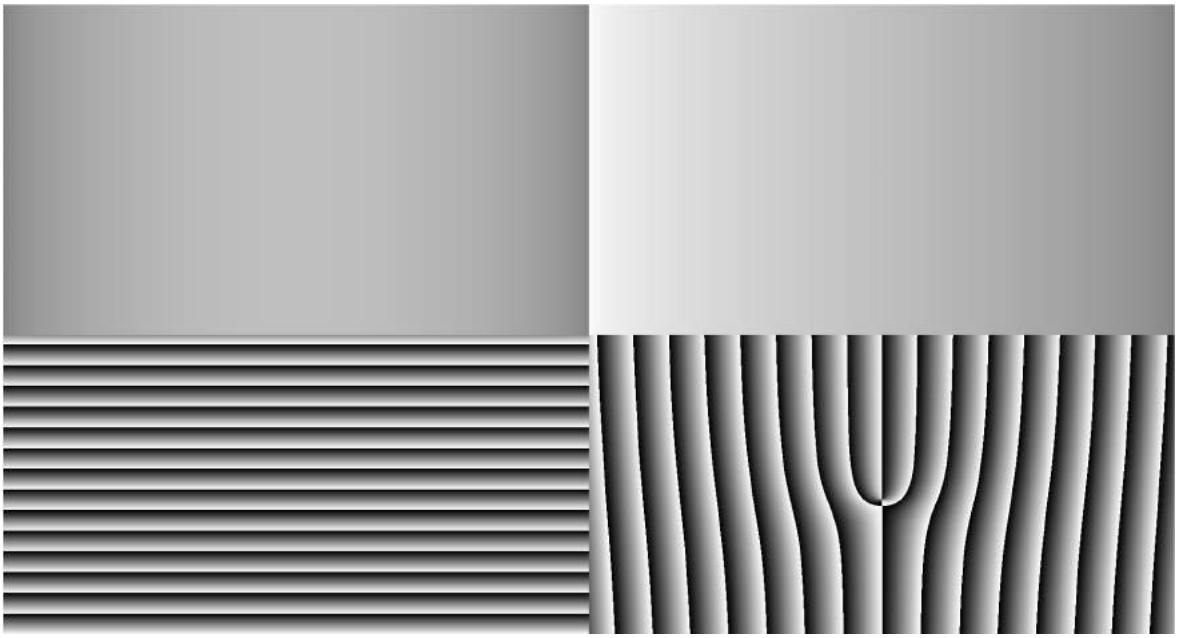

Figure 5.2: Screenshot of a 256 greylevels image sent to the SLM. The patterns are created with a home-made program witten in *LabView* code.

only one element we have to manually act on is the half-wave plate that regulates the power of the pump. We do not *have to* change it, in principle we could keep it at a fixed value. The reason why we act on it is to maximize the pump power, where the limiting factor is the number of single counts detected by any of the two APDs: above about 2 million counts per seconds the APDs stop to have a linear response to the electric field of the photons detected. Therefore we decided to limit the maximum counts in a single detector to about $1.5MHz$. As we will explain in the next paragraphs, this method requires a certain set of phases to be sent to the SLM; it includes a flat zero-phase all over the SLM which gives a maximum in single counts. On the other hand, for the slit-slit scan method the maximum single counts are detected when the slit is placed in the center of the beam with the rest of the optical field bouncing on a π-phase area and therefore not being coupled (in the limit of the SLM efficiency). For this reason, the pump power in the phase-slit method can be set higher.

Following the definition of the moments as a function of coincidence counts (eq. 5.24) in subsection 5.3, we want to measure the following first and second order moments of the distribution in position (real space): $\langle x_s \rangle$, $\langle x_i \rangle$, $\langle x_s^2 \rangle$, $\langle x_i^2 \rangle$, and $\langle x_s, x_i \rangle$. For each moment we need to apply on the SLM the appropriate phase and then record coincidence counts in the four polarization eigenstates: $|++\rangle\rangle$, $|+-\rangle\rangle$, $|-+\rangle\rangle$, and $|--\rangle\rangle$. According to the theoretical model presented in 5.3, the phase to be imprinted on the SLM is essentially an $\arccos(a^n)$ function. Here the spatial variable a can be either the horizontal (x) or the vertical (y) direction on the slm surface; the power of n is used for the detection of the moment of order n ($n = 1$ for the expectation value of the mean; $n = 2$ for the expectation value of the square and so on). Therefore, for instance, the $\arccos(x^n)$ functions are constant in the vertical direction and their full domain $x \in [-1; +1]$ is defined on the horizontal dimension of the liquid crystal display of the SLM.

In Figure 5.2 we show a screenshot of the SLM display when driven with a typical 8-bit image (256 greylevels) as required by the electronic of the SLM itself. That image has been generated by a home-made software written in *LabView* code, and it is sent to the SLM's electronic board via standard HDMI cable. The phases are encoded in the greylevel of the

image itself. As mentioned earlier, the SLM is divided in four quadrants driven independently (for the reason behind the choice of 4 quadrants rather than 2, please refer to the description of the setup given at the beginning of section 3.2). The top-left quadrant is where the idler field is reflected, while the signal bunches on the top-right. The bottom two quadrants are not used at all in the two-photon experiments, therefore we usually keep them at the uniform phase that rotates the polarization to the non-detectable direction (ie, to rotate polarization to $|+\rangle$ if we are coupling only $|-\rangle$). In the particular example of figure 5.2, the functions encoded are $\arccos(x^2)$ on the idler and $\arccos(x)$ on the signal, while the two unused quadrants are set to different phase patterns of no interest here. The independent variable x in both quadrants ranges from -1 for the first pixel on the left to +1 for the last on the right on each quadrant. Consequently, the zero is set in the centers.

In an actual measurement, the detection of a given moment would not be successful if we considered only the coincidence counts for a given phase (say, $\arccos(x_s)$ to detect the first horizontal moment of the signal field). In a real case, we need to consider two corrections: first, to account for the background due to imperfections of the SLM (depolarization) and of polarization control optics; second, to define a visibility for any given phase that we want to imprint on a beam. These two requirements, which are purely practical, gives prominence to the need of defining a long sequence of phases to be encoded sequentially on the SLM. Let us analyse those two corrections in more details.

We can define the visibility as a combinations of the counts taken at different polarization angles ±45°. For the simpler case of one optical field, given a phase n the visibility V_n reads:

$$V_n = \frac{C_+ - C_-}{C_+ + C_-} \tag{5.25}$$

where the C_+ and C_- represents the detected (single) counts respectively in the polarization state $|45\rangle$ (or: $|+\rangle$) and $|-45\rangle$ (or: $|-\rangle$). To account for the experimental errors due mainly to the known polarization decoherence intrinsically induced by the SLM, the non-ideal behaviour of the waveplates and polarizers, as well as the power fluctuations of the pump, we can express the above visibility as a fucntion of the experimental parameters that we identify with A and B [59]:

$$V_n = A + B \int dx I(x^n) x^n \tag{5.26}$$

The integral clearly represents the n^{th} moment of the probability distribution in the variable x. Recalling the notation introduced in section 5.3, x^n comes from the cosine function of $a(x)$, which in turn correspond to the $arcos$ function of x^n. Therefore, when fixing that function $a(x^n) = const = \pi/2$, it yields to the integrand in 5.26 to be equal to zero. In turn, the visibility $V_{\pi/2}$ obtained when we set the phase of the SLM to a uniform $\pi/2$ phase allows us to measure the parameter A (directly).

Following a similar reasoning, we can experimentally estimate the parameter B: in this case we need to set $a(x^n) = const = 0$. Summarising:

$$V_{\pi/2} = A \tag{5.27}$$

$$V_0 = A + B \tag{5.28}$$

Now we have all the experimental parameters to estimate the general n^{th} moment of the marginal distribution in the variable x, namely $\langle x^n \rangle$, for single beam as[2]:

[2]For the sake of clarity we keep referring to the variable x which refers to the horizontal *position*; obviously the same analysis is true for y, p or q (vertical position and horizontal and vertical transverse momentum).

$$\langle x^n \rangle_{raw} = \frac{V_n - V_{\pi/2}}{V_0 - V_{\pi/2}} \tag{5.29}$$

The subscript "raw" refers to "raw data" and it will be clear later in this section why we specified it. The moment expressed by equation 5.27 is the n^{th} moment of the spatial distribution of the one single photon at the plane of the SLM; because we chose the x-variable to span the half-width of the SLM from -1 to +1 (with the zero centered in the center of the quadrant), the units are $([\text{pixels}]/[\text{SLM-half-width}]_{px})^n$. In order to estimate the moment in natural units (millimeters, for instance) of the generated fields, we would need to convert the pixels to natural units ($8\mu m$ per pixel) and to account for the magnification of the field itself due to the lens system. We will explain those details in few paragraphs when dealing with the more interesting case of biphoton state.

Let us now apply the method to the higher dimensional case of two photons. For similarity, we define C_{+-} as the *coincidence* counts when the signal is projected to the $|45\rangle$ polarization state and idler to the $|-45\rangle$ polarization state; we define C_{++}, C_{--}, and C_{-+} accordingly. For measuring the general moment of two particles $\langle x_s^n, x_i^m \rangle$, the visibility $V_{n,m}$ corresponding to the phase indicated by the index n on the signal and m on the idler is defined as:

$$V_{n,m} = \frac{C_{++} + C_{--} - C_{+-} - C_{-+}}{C_{++} + C_{--} + C_{+-} + C_{-+}} \tag{5.30}$$

To account for experimental imperfections and errors, we write the above visibility as a linear combinations of several terms that can raise errors:

$$V_{n,m} = A + B_1 \int dx_s I(x_s^n) x_s^n + B_2 \int dx_i I(x_i^m) x_i^m + B_{12} \int dx_s \int dx_i I(x_s^n) I(x_i^m) x_s^n x_i^m \tag{5.31}$$

To experimentally determine the parameters A, B_1, B_2, and B_{12} we proceed as follow. Setting the phases on both channels to $\pi/2$ all the expectation values represented in 5.31 by the integrals are zero; that let us measure A. Setting $\Phi_{SLM}(s) = \pi/2$ and $\Phi_{SLM}(i) = \arccos(x^m)$ what we measure is $(A + B_2 \langle x_i^m \rangle)$. Swapping the phases in the two channels, ie $\Phi_{SLM}(s) = \arccos(x^n)$ and $\Phi_{SLM}(i) = \pi/2$, we get $(A + B_1 \langle x_s^n \rangle)$. Finally, by setting the phases to zero on both channels, all the integrals in eq 5.31 gives the unity. Summarizing:

$$V_{\pi/2,\pi/2} = A \tag{5.32}$$
$$V_{\pi/2,m} = A + B_2 \langle x_i^m \rangle \tag{5.33}$$
$$V_{n,\pi/2} = A + B_1 \langle x_s^n \rangle \tag{5.34}$$
$$V_{0,0} = A + B_1 + B_2 + B_{12} \tag{5.35}$$

Rearranging 5.31 to work out the desired 2-photon moment $\langle x_s^n, x_i^m \rangle$, and considering the expressions in eqs 5.32, we achieve:

$$\langle x_s^n, x_i^m \rangle_{raw} = \frac{V_{n,m} - V_{\pi/2,m} - V_{n,\pi/2} + V_{\pi/2,\pi/2}}{V_{0,0} - V_{\pi/2,0} - V_{0,\pi/2} + V_{\pi/2,\pi/2}} \tag{5.36}$$

With this method one could in principle measure any bidimensional moment of the marginal probability distribution of two entangled photons by taking only 7 acquisitions - one for each of the 7 different combinations of phases expressed in the equation above. The scaling of the number of measurements with the number of photon modes is $4N - 1$. In

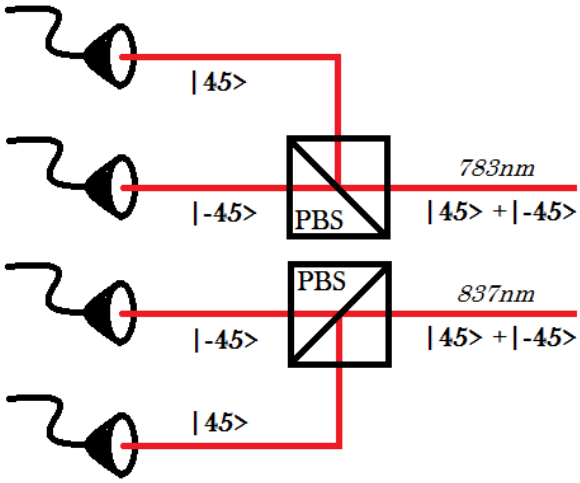

Figure 5.3: Detection scheme with 4 APDs. It allows to calculate any 2-photon distribution moment with 7 measurements only.

order to do so, one would need to detect at the same time the coincidences in all of the 4 combinations of $|\pm 45\rangle$ polarization states. Which means, by recording at the same time all the values needed for calculating a given visibility $V_{n,m}$ as defined in eq 5.30. Though, a setup with 4 detectors would be necessary for that purpose (see figure 5.3). Instead in a two-APD setup such as our, we have to perform 28 measurements, 7 in each of the 4 combinations of $|\pm 45\rangle$.

In our setup we opted for a 2-APD detection. In order to project onto the different polarization directions, right before the fiber coupler of each channel we placed a HWP followed by a (cube) PBS. Another wave plate (a quarter wave-plate, QWP) is set right before the HWP in order to account for any ellipticity of the polarization. Such an effect might happen when a diagonally polarized beam is reflected on a surface. Since the reflectivity is in general polarization dependent, and in particular s-polarization is reflected differently from p-polarization[3], the reflected beam could pick up a phase between two components of the polarization. In our setup we expect this to happen in the reflections on the SLM and on the d-shaped mirror (for a detailed sketch of the setup, please refer to the beginning of section 3.2).

As mentioned before, our setup is fully automatized. Which means that also the HWPs for the projective measurement do not need any manual operation. We equipped each of them on a motorized rotational stage produced (*Thorlabs KPRM1E/M*). We found the angles at which the rotation in the linear polarization due to the HWP allows the desired polarization to pass through the PBS to be eventually coupled into the optical fiber that goes to the APD. After the first calibration, no further intervention is needed. We wrote a *LabView* code that once provided with the four angles - one for +45° and one for −45° on each of the two channels - handles the entire measurement. In particular, the procedure is as follow: it sets the HWPs on signal and idler for one eigenistate projection (say, $|+-\rangle$); it sets the proper sequence of phases on the SLM storing for each combination of pases (Φ_s^{SLM}, Φ_i^{SLM}) the counts (singles and coincidences) on a matrix; it saves a *.txt* file with the counts matrix plus some statistical pre-analysis; it repeats the same procedure for the other 3 eigenstates of the complete bases.

[3]In this particular case p is vertical and s is horizontal.

Thanks to this automatization we also make sure that the HWPs always set the polarization on the same angles.

The procedure described makes it easy to measure the moments of the spatial distribution of the fields at the SLM plane (whether that is the near or far field). From that we can calculate the moments of the distribution at the generation position (say, at the center of the crystal) considering the set of lenses utilized. We can do that for both the image and Fourier systems.

On top of that, we have to consider that the units of the moments as derived so far are still expressed in $([Px]/[\text{SLM-half-width}]_{px})^n$. To convert a single field moment from the SLM units (the pixel) to its natural units (meters) we have to consider the SLM pixel size and for the magnification factor due to the lens system between the crystal plane and the SLM plane. Therefore, we need to multiply the raw data moments for the number of pixel in the quadrant to the power of n, and again multiply the result by the pixel size to the power of n. The result is the expectation value of the moment, in mm, at the position of the SLM:

$$\langle x_s^n \rangle_{mm}^{SLM} = \langle x_s^n \rangle \times (960Px)^n \times (8.0 \cdot 10^{-3} mm/Px)^n \tag{5.37}$$

The magnification factor is given by the focal lengths of the lens system. In the case of the imaging system we used two telescopes. The first composed by $f_1 = 300$ and $f_2 = 200mm$; the second composed by $f_3 = 18mm$ and $f_4 = 400mm$. The magnification factor then is:

$$M = \frac{200}{300} \times \frac{400}{18} = 14.8 \tag{5.38}$$

The calculated magnification is an approximated number: the focal lengths of the lenses can slightly differ from their nominal value; furthermore, they are intrinsically wavelength dependent. And even more important is the positioning of the lenses on the optical axis: in order for the nominal magnification value calculated in Eq. 5.38 to be correctly implemented on the optical table, the relative distances between the lenses have to correspond to their focal lengths (or better, to the sum of the focal lengths of two consecutive lenses). Aligning the lenses with the technique of back-propagating laser beams makes it very hard to place them in the correct z position.

In order to be more precise we measured the value of the magnification empirically. In back-propagation we set on the SLM a phase aperture with sharp edges and took an image of the aperture at the crystal plane by using a CMOS camera. First, we finely tuned the z-position of one of the lenses of the imaging system until when the image on the camera gained very sharp edges - a sign, this, of a proper image formation. Once happy with the fine tuning of the imaging system, we recorded an image. By measuring the size of the imaged aperture on the camera (knowing the pixel size of the camera being $5.2\mu m$), and by comparing that number with the size of the aperture programmed on the SLM (knowing the SLM pixel size being $8.0\mu m$), we could estimate the magnification factor (Figure 5.4).

We repeated the measurement for three different sizes of the programmed phase-aperture: in all cases the result is the same within the measurement uncertainties: $M = 13 \pm 0.5$ (table 5.2). The value is not far from the nominal one, and it agreed in the three different measurements. Therefore, we are confident using the empirical value rather than the calculated (nominal) one. For this reason, from now on we will always consider the magnification of the image system to be $M = 13$.

The same arguments apply to the case of far field. The procedure to convert from SLM units to natural units is slightly different though. In this case the lens system is composed by three lenses: $f_1 = 300mm$, $f_2 = 250mm$, and $f_3 = 400mm$. The action of the first lens is to Fourier transform the crystal plane. The momentum distribution at a focal distance after f_1

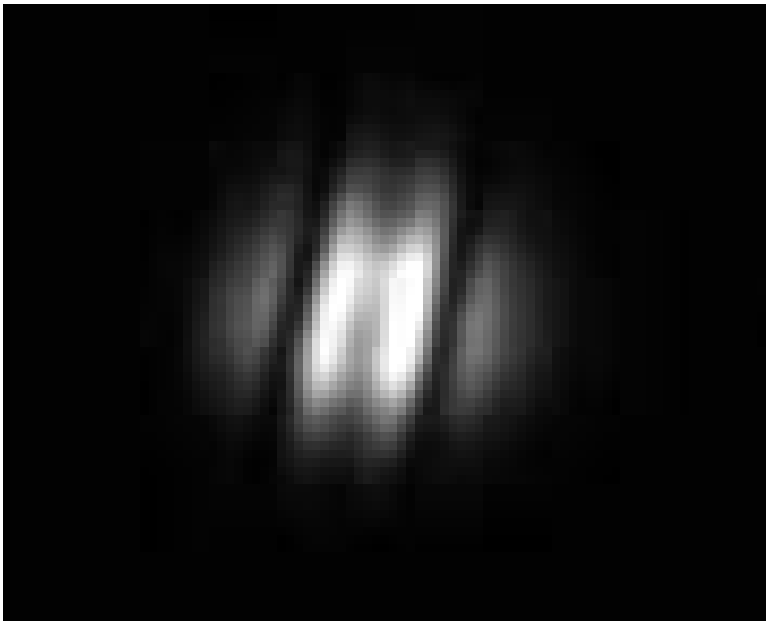

Figure 5.4: Image of the conjugation of the SLM plane on the z-position of the center of the crystal taken with a CMOS camera at the crystal position. The distance between the minima is given by the width of the phase-box on the SLM multiplied by the (de)magnification factor of the image lens set.

Table 5.2: .

Aperture size @ SLM pos.	Aperture size @ crystal pos.	Magnif.	Final value
$50Px \times 8.0\mu m/Px = 400\mu m$	$6Px \times 5.2\mu m/Px = 31.2\mu m$	12.8205	13 ± 0.5
$100Px \times 8.0\mu m/Px = 800\mu m$	$11.5Px \times 5.2\mu m/Px = 59.8\mu m$	13.3779	13 ± 0.5
$150Px \times 8.0\mu m/Px = 1200\mu m$	$17.5Px \times 5.2\mu m/Px = 91.0\mu m$	13.1868	13 ± 0.5

can be calculated to be: $p = \frac{2\pi}{\lambda}\frac{1}{f_1}x$, where p is the transverse momentum in units of $1/\text{length}$, λ is the wavelength, and x is the transverse position coordinate at a focal distance from the lens f_1 (i.e., at the crystal plane). The following two lenses can be seen as a telescope which magnification operates inversely (being in Fourier space) $M = f_2/f_3$. Putting everything together we can convert the detected values on the SLM (in mm) to the momentum at the crystal plane (in mm^{-1}) as:

$$p = k\frac{f_2}{f_1 f_3}\langle x_s^n \rangle_{mm}^{SLM} \tag{5.39}$$

In summary, the conversion factors for the two lens systems (near and far field) are:

$$K_{pos}(n,m) = \left((960\text{Px}) \times 8 \cdot 10^{-3}\frac{mm}{\text{Px}} \times 13\right)^{n+m} \tag{5.40}$$

$$K_{mom}(n,m) = \left(\frac{2\pi}{\lambda_s}\right)^n \cdot \left(\frac{2\pi}{\lambda_i}\right)^m \cdot \left(\frac{250}{300 \times 400}960\text{Px} \cdot 8 \cdot 10^{-3}\frac{mm}{\text{Px}}\right)^{n+m} \tag{5.41}$$

where we remind that the powers n and m represent the order of the moment of the signal and idler respectively. For instance, when estimating $\langle p_s^2 \rangle$ we need to fix $n = 2, m = 0$. Using equations 5.40 and 5.41 we can assess the expectation values of position and momentum on the crystal plane (ie, at the SPDC generation plane) from the value measured on the SLM.

The conversion is:

$$\langle x_s^n x_i^m \rangle_{mm}^{crystal} = \langle x^n \rangle_{\mathrm{Px}}^{SLM} \times K_{pos}(n,m) \tag{5.42}$$

$$\langle p_s^n p_i^m \rangle_{mm^{-1}}^{crystal} = \langle x^n \rangle_{\mathrm{Px}}^{SLM} \times K_{mom}(n,m) \tag{5.43}$$

where we would like to underlie that in the case of transverse momentum, the real-to-Fourier conversion is included in the definition of the scaling factor $K_{mom}(n,m)$, which explains why in the right side of the second equation in 5.42 appears the expectation value expressed in real space units.

5.3.1 Estimation of the experimental uncertainties.

The uncertainty connected to the estimated values of the moments descend from two conceptually different causes. First, we have to account for the sensitivity of the instrument used for the detection. Second, we need to infer the error due to the statistical nature of the photon counting.

In the present case of direct measurement of the moments, the precision of the instrument is the linear size of the single pixels of the SLM ($8\mu m$). In [132], S. Machado et al. argued that the SLM accuracy in reproducing a function can be considered good for functions with spatial frequency as small as $0.5Px^{-1}$. Their conclusion is based on the Nyquist-Shannon theorem [138]. For the particular case of inverse cosine function, the spatial frequency is proportional to the power of n at which the argument is raised. However, it has been showed that this bandwidth limitation of the SLM can be neglected for $\arccos(x^n)$ up to $n = 15$ [132]. Therefore, we can conclude that in good approximation the total experimental error on the estimation of the moments of the distribution using the direct method corresponds to the statistical one.

In an ideal case of perfect experimental setup (100% efficiencies, perfect alignment, infinite resolution, and so on), the expectation values of the moments can be estimated by the algebraic sum of four coincidences measurements according to eq. 5.24 derived in section 5.2: $\langle a^n, b^n \rangle = P_{++} + P_{--} - P_{+-} - P_{-+}$, where the P represent the detection probabilities in the $|\pm 45\rangle$ base. In the experimental analysis those probabilities assume the meaning of normalised coincidences and we name them $C_i = R_i/N$, where R_i is the coincidence rate in the i-th configuration and N is the total number of events summed over the four configurations. In this case, the statistical error σ_{nm}^2 connected to the empirical value of the moment $\langle x_s^n x_i^m \rangle$ can be estimated as:

$$\sigma_{nm}^2 = \frac{1}{N} \sum_{i=0}^{3} \left(C_i - C_i^2 \right) \tag{5.44}$$

$$N = \sum_{i=0}^{3} C_i$$

where C_i is the number of coincidences detected in the four combinations of $\pm 45^\circ$ polarization directions of signal and idler, and N is the normalisation factor.

In a real case we need to account for several experimental imperfections and a more complicated measurement protocol needs to be implemented (as explained in section 5.3). For extracting the final value of each moment of the biphoton distribution we need to repeat several times, for different phases on the SLM, the following measurements (already eq.

5.30):

$$V_{n,m} = \frac{C_{++} + C_{--} - C_{+-} - C_{-+}}{C_{++} + C_{--} + C_{+-} + C_{-+}} \tag{5.45}$$

The statistical error over $V_{n,m}$ is given by the propagation of error. For both numerator and denominator we can apply equation 5.44 and the σ^2 we get is actually the same for both of them. On the function $z = \frac{x}{y}$, the error σ_z^2 over z is given by $\sigma_z = \frac{z}{x}\sigma_x + \frac{z}{y}\sigma_y$. In our case it reads:

$$\sigma_{V_{n,m}} = \left(\frac{V_{n,m}}{C_{++} + C_{--} - C_{+-} - C_{-+}} + \frac{V_{n,m}}{C_{++} + C_{--} + C_{+-} + C_{-+}} \right) \sigma_{nm} \tag{5.46}$$

where $\sigma_{nm} = \sqrt{\sigma_{nm}^2}$.

The next step in the protocol calculate $\langle x_s^n x_i^m \rangle$ from a linear combination of seven different V. In particular (eq. 5.36):

$$\langle x_s^n, x_i^m \rangle_{raw} = \frac{V_{n,m} - V_{\pi/2,m} - V_{n,\pi/2} + V_{\pi/2,\pi/2}}{V_{0,0} - V_{\pi/2,0} - V_{0,\pi/2} + V_{\pi/2,\pi/2}} \tag{5.47}$$

The statistical error over $\langle x_s^n x_i^m \rangle$ can be calculated, again, from the propagation of errors. In particular, we have to apply the same reasoning as above. The result is:

$$\sigma_{\langle x_s^n x_i^m \rangle} = \frac{\langle x_s^n x_i^m \rangle}{V_{n,m} - V_{\pi/2,m} - V_{n,\pi/2} + V_{\pi/2,\pi/2}} \sigma_{num} + \frac{\langle x_s^n x_i^m \rangle}{V_{0,0} - V_{\pi/2,0} - V_{0,\pi/2} + V_{\pi/2,\pi/2}} \sigma_{den} \tag{5.48}$$

where with σ_{num}^2 and σ_{den}^2 we refer to the variance of respectively the numerator and denominator of 5.47 calculated as:

$$\sigma_{num} = \sqrt{\sigma_{nm}^2 + \sigma_{\pi/2,m}^2 + \sigma_{n,\pi/2}^2 + \sigma_{\pi/2,\pi/2}^2} \tag{5.49}$$

$$\sigma_{den} = \sqrt{\sigma_{0,0}^2 + \sigma_{\pi/2,0}^2 + \sigma_{0,\pi/2}^2 + \sigma_{\pi/2,\pi/2}^2} \tag{5.50}$$

5.3.2 Experimental technicalities: centering the beam.

Because we aligned the optical paths using a back-propagating technique, we couldn't identify clearly the center of the beams on the SLM. For the purpose of detecting spatial correlations by raster scanning with the SLM, that is not an issue since the whole quadrant is scanned by the (phase) slit. On the contrary, for detecting the correlations based on the method explained theoretically in section 5.1, the centering of the phase pattern with the center of the two beams is desirable. The requirement is that the phase pattern on beam 1 is centered with respect to an *(anti)correlated* position on beam 2. To this end one could exploit the preliminary measurements taken with the fixed aperture on one channel while scanning the other. An example of such a result is the one showing momentum anticorrelations represented by the plots in Figure 4.3: we can see that the photons selected by the slit centered at pixel position 540 on one channel gives a peak of coincidences with the photons at position $420Px$ (plot on the left), and when moving the fixed slit from $540Px$ to $300Px$ the coincidence peak moves from $420Px$ to $580Px$.

That procedure works well enough and we used it for our preliminary measurements. For our final measurements, however, we opted for a more sophisticated way to find the center of the beams. We used a standard approach consisting in a scan of the whole surface of the SLM

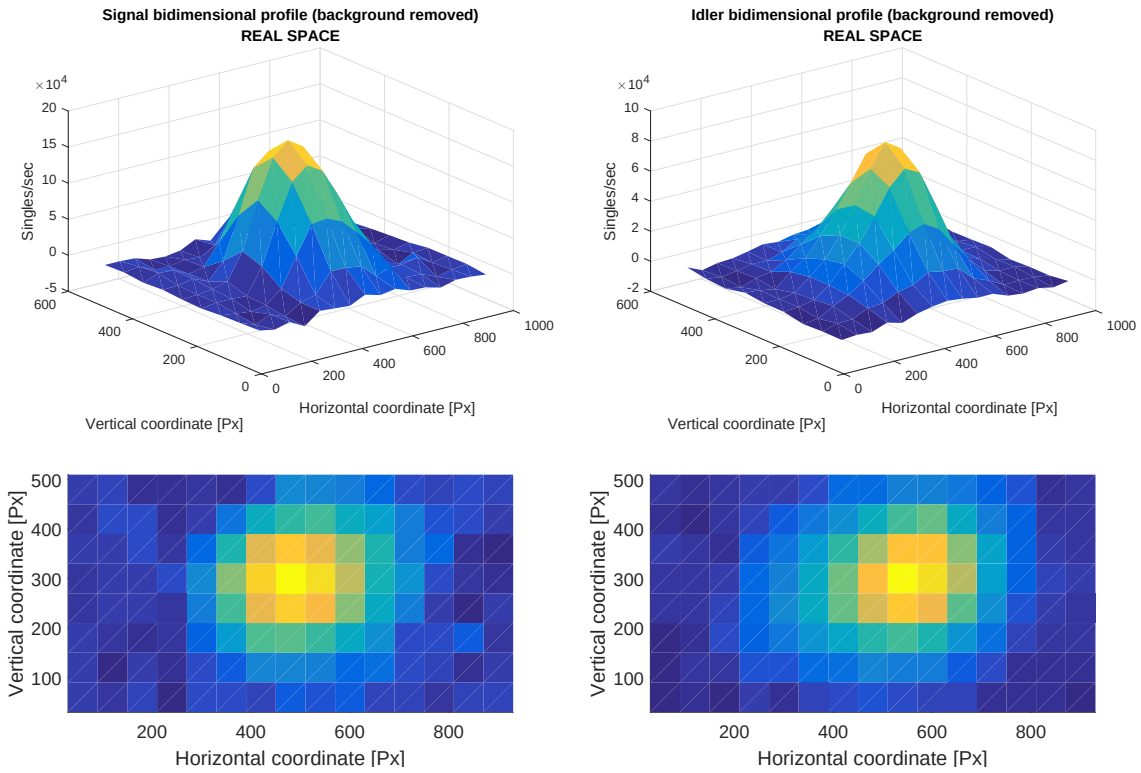

Figure 5.5: Spatial bidimensional distribution of signal (left column) and idler (right column). The intensities are given by the single counts recorded independently on each of the two channels and after efficiently subtracting the background. In the bottom line the x-y plane view of the corresponding plot above (bottom-left the signal; bottom-right idler). The data represented here have been collected with a pixelized scan made by $60 \times 60\text{Px}^2$. Details of the method in the text.

with a small, squared aperture. We prepared the optical fields to a polarization state of 45 degrees (in second quantization: $|++\rangle\rangle$). We set the polarization waveplates before the APDs at 45 degrees too, such that only the state $|+\rangle$ on each of the two channel would be coupled. Then, by setting the phase inside the squared aperture to zero and a flat, uniform π phase everywhere else, we aimed to couple only (restricted by efficiency) the photons reflected in that little square. Scanning that aperture all over the surface of the SLM, one can reconstruct the spatial distribution of the two down converted beams just plotting the detected singles. An example of the result is shown in figure 5.5.

The SLM we utilized is characterized by a very high efficiency (section 3.1.2 for the full specs). We will provide the experimentally measured number later on, in the results section; for now let us keep in mind that it is around 90%. This means that most of the light polarized along the working polarization of the SLM (in our setup: vertical) picks up the desired phase. Therefore one could expect a large contrast in such a measurement with phase apertures. However, the signal to noise ratio here is given in the largest part by the *little* amount of photons that are reflected in the surface of the aperture with 100% efficiency (since they don't have to pick up any phase) over the *large* number of photons reflected from everywhere else that with probability $\simeq 0.10$ will *not* pick up the π phase and therefore will be detected (as noise).

Numbers add up very quickly when the aperture is a small $60\times60Px^2$ or even $40\times40Px^2$ with respect to the whole SLM quadrant which measure $960 \times 540Px^2$. Therefore, in order to see any signal at all, also in this kind of measurement we need to properly account for the

background and accordingly remove it from the measurements.

In this case we are interested only in the singles counts, so the background requires less efforts (and less measurements) in order to be removed. If one was not interested in decreasing the uncertainties of the measurement with statistic, could in principle just acquire one measurement of the background with plain π phase all over the quadrant of the SLM and directly subtract it from the counts recorded when the aperture is in place. The background should be the same for all the possible positions of the aperture.

In our case, however, we decided to be a little more sophisticated and we took one measurement of the background after each acquisition with the squared slit in given position (x, y). This way we also account for possible fluctuations of the pump power as well as temperature of lab and/or crystal.

5.4 Results: direct method Vs double raster scan.

In this section we test the direct method against the raster scan with phase-slit described in section 4.1 (and related subsections). The terms for comparison are the estimated first and second moments of the distributions and some interesting combinations of them including the important result of correlations. The estimation of the moments and the relative experimental errors from the experimentally reconstructed joint probability distribution, is made according to the method explained in section 4.4.

Other than comparing the two experimental methods, we will also show the theoretical predictions provided by the model explained earlier, in chapter 2. We highlight the correspondences and explain the reasons for the non-correspondences.

This section is divided in subsections in which we present the results for some of the experimental conditions that we tested. The structure is the same in each of the subsections and therefore it will be explained in the first and disregarded in the following ones.

Regarding the direct method, the experimental procedure has been extensively described in section 5.3. The important conclusion was that with this method one can in principle measure any moment of the distribution with only $4N - 1$ measurements (where N is the number of photons). That's true as far as one is willing to use $2N$ detectors instead of the minimum possible which is, of course, N. In our setup we use indeed only two detectors, which means that we only collect the counts for one polarization projection at a time, discarding the orthogonal states. This imply that we need to record the counts for the orthogonal state in a separate measurement.

In conclusion, for the correct estimation of each moment of the distribution with our setup we need $2 \times (4N - 1)$ measurements. However, the average number per moment can be decreased by running a full set of measurement that targets more than one moment. This is explained by the fact that some of the correction measurements (see section 5.3) are the same for all or some of the moments. And if the pump can be considered constant - or, otherwise, if the counts can be normalised with respect to the pump power - one can avoid to repeat the same (correction) measurement several times in a set.

In our standard protocol we measure the moments up to the 4^{th} order. A a full set of measurement consists on a sequence of 50 different phases; the coincidences corresponding to each sequence need to be recorded four times, once for each of the four polarization combination ($|++\rangle\rangle$, $|+-\rangle\rangle$, $|-+\rangle\rangle$, $|--\rangle\rangle$). We therefore run a total of $4 \times 50 = 200$ measurements. With such a set we can measure 24 different moments (table 5.3), with an average number of measurements per moment of 8.3.

Table 5.3: List of the moments that we can measure with our measurement protocol.

Order:	First	Second	Third	Fourth
	$\langle x_s \rangle$	$\langle x_s^2 \rangle$	$\langle x_s^3 \rangle$	$\langle x_s^4 \rangle$
	$\langle x_i \rangle$	$\langle x_i^2 \rangle$	$\langle x_i^3 \rangle$	$\langle x_i^4 \rangle$
	$\langle y_s \rangle$	$\langle y_s^2 \rangle$	$\langle y_s^3 \rangle$	$\langle y_s^4 \rangle$
	$\langle y_i \rangle$	$\langle y_i^2 \rangle$	$\langle y_i^3 \rangle$	$\langle y_i^4 \rangle$
		$\langle x_s x_i \rangle$	$\langle x_s^2 x_i \rangle$	$\langle x_s^2 x_i^2 \rangle$
		$\langle y_s y_i \rangle$	$\langle x_s x_i^2 \rangle$	$\langle y_s^2 y_i^2 \rangle$
			$\langle y_s^2 y_i \rangle$	
			$\langle y_s y_i^2 \rangle$	
Total number:	4	6	8	6

In order for the results in near and far field to be comparable with each other, we took the two measurements in sequence, without switching off the laser nor changing any other part of the experimental apparatus - except for switching in the Fourier lens system.

5.4.1 The standard case of Gaussian correlations.

In the previous sections of the present chapter we explained extensively our experimental setup as well as the details of the detection procedure(s). With the theory explained in the previous chapter in mind, we have all the tools to proceed analysing the results.

In this section we present our results for a typical and extensively studied case of Gaussian pump beam. Not only this is useful in order to calibrate the setup (as reminded by the header of this section), but it is also a good occasion to test the theoretical model. Comparing the results of two different configurations of small and large pump (Gaussian) beam waists, we show how the correlations can be "switched on and off" according to the biphoton wavefunction derived in chapter *Spontaneous Parametric Down Conversion*.

The following three subsections encapsulate the results obtained by applying the two different detection approaches presented previously (in the case of raster scan we also briefly describe a simplified version 4.2).

Small Gaussian pump profile.

In this section we present the results for the case of small Gaussian pump beam. The pump waist at the crystal plane was set to $w_p^0 = 16\mu m$ by flipping off the telescope system on the pump path. Its profile was recorded with a CMOS camera and shown already in Figure 4.8 (together with the fit from which we estimated the waist). Instead, the (bidimensional) profiles of the downconverted fields at the SLM plane were reconstructed using the pixel-scan method described in section 5.3.2. The scans were performed *before* to start the measurements presented in this section; the results are shown in the plots of Figures 5.6 and 5.7 for the far and near field respectively.

We proceed presenting the measured moments of the probability distributions of both position and momentum. We compare the values calculated with this method with the ones estimated from the raster scan from chapter 4. For the present case of small Gaussian pump, the comparisons refer to the measurements presented in section 4.3.2.

The moments of the momentum distribution are summarized in table 5.4. In the first

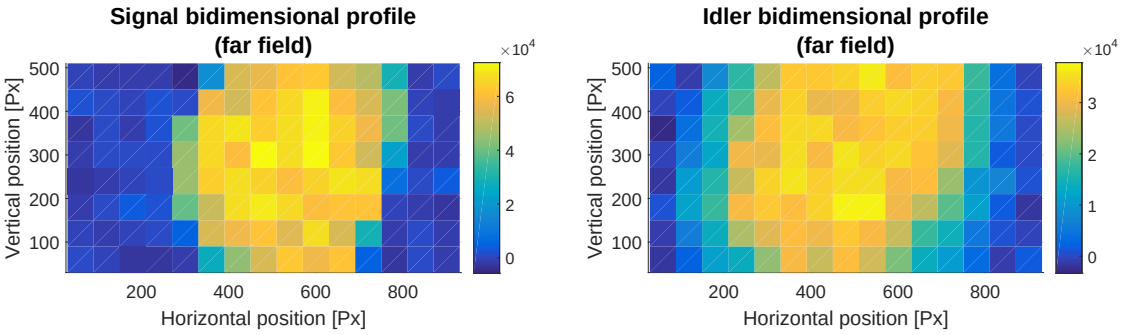

Figure 5.6: Signal (left) and idler (right) profiles at the SLM plane - momentum distributions. The counts, indicated by the color system, are single counts per unit time. The background counts have been removed.

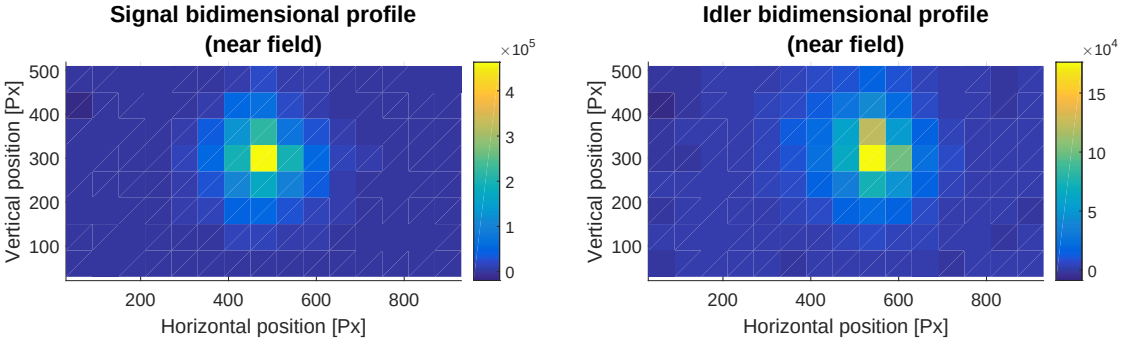

Figure 5.7: Signal (left) and idler (right) profiles at the SLM plane - position distributions. The counts, indicated by the color system, are single counts per unit time. The background counts have been removed.

column of data, we show the moments measured with the double-raster method while in the second we can see the results of the measurements performed with the direct method. In the last two columns we show two theoretical predictions. In the third column, *Theory 1*, we list the results from the simulation with the functions naturally centered at zero (the center of the axis). In that case, we would expect to measure the mean values of position and momentum to be zero, which in the simulation translates to the lowest number according to the computational precision. Indeed in the table we report a zero, but the actual number generated by the simulation is of the order of 10^{-18}. While in the last, fourth column, we show the theoretical predictions in which we shifted the center of the axis according to the experimental conditions.

In both the experimental methods the center of our coordinate system is set at the center of the SLM quadrant of each of the two downconverted fields. This does not necessarily correspond to the center of the downconverted fields, which are very difficult to perfectly align on the SLM. In the experiments the distributions of signal and idler are always a bit out of center, as can be seen in Figures 5.7 and 5.6 for the distribution of the *singles* in the near and far fields respectively.

The experimental values of the moments for signal and idler refer, of course, to those shifted centers. We can see this effect especially in the estimation of the first moments. In order to provide reliable predictions (especially for the first-order moments), we need to account for the not-perfect centering of the optical fields on the SLM. By adding such a shift

Table 5.4: Expectation values of the moments of the probability distribution of transverse-momentum. In the first, second, and third column the values calculated from the slit-slit scan, the direct method, and the theoretical model respectively. In the fourth column, we show the results from the simulation when we use the measured displacement of the signal and idler beams.

Moment	Slit-scan $[mm^{-1}]$	Direct method $[mm^{-1}]$	Theory 1 $[mm^{-1}]$	Theory 2 $[mm^{-1}]$
$\langle p_s \rangle$	4 ± 3	-3.3 ± 0.5	0	3.6242
$\langle p_i \rangle$	0 ± 3	1.0 ± 0.5	0	-1.1593
	$[mm^{-2}]$	$[mm^{-2}]$	$[mm^{-2}]$	$[mm^{-2}]$
$\langle p_s^2 \rangle$	360 ± 10	340 ± 30	1532.5	1543.0
$\langle p_i^2 \rangle$	390 ± 10	260 ± 30	1532.5	1533.6

Table 5.5: Expectation values of the moments of the probability distribution of transverse-position. In the first, second, and third column the values calculated from the slit-slit scan, the direct method, and the theoretical model respectively. In the fourth column, we show the results from the simulation when we use the measured displacement of the signal and idler beams.

Moment	Slit-scan $[mm]$	Direct method $[mm]$	Theory 1 $[mm]$
$\langle x_s \rangle$	-0.02 ± 0.02	0.0063 ± 0.002	0
$\langle x_i \rangle$	0.01 ± 0.02	-0.0360 ± 0.001	0
$\langle x_s x_i \rangle$	-0.0007 ± 0.0003	-0.001 ± -0.0005	-0.00001
	$[\mu m^2]$	$[mm^2]$	$[mm^2]$
$\langle x_s^2 \rangle$	0.0032 ± 0.0003	0.0021 ± 0.0005	0.00014807
$\langle x_i^2 \rangle$	0.0046 ± 0.0003	0.0013 ± 0.0004	0.00014807

in the simulation we can see in the last column of Table 5.4 that the predicted values of the first moments correspond to the measured ones.

We estimate the centers of the signal and idler distributions form the profiles shown in Figures 5.7 and 5.6. The protocol for a full-set of measurements therefore include a preliminary quick scan of the two fields with a squared aperture (corresponding to the pixelization of the singles distributions seen in the figures). In those cases what we record are the single counts on both channels. Plotting the results we can see the spatial distribution of the coupled single photons at the SLM plane. If necessary, that is if the beams are particularly off-center, we correct for it by finely tuning the alignment of the downconverted beams and we take a pixel-scan again before to begin the set of measurement.

With the final distribution of the signal's and idler's singles, we can estimate where the center of the two beams is, and eventually calculate the offsets to be passed to the code. Regarding the corrected theoretical predictions for momentum distribution, from Figures 5.6 we estimated the center of the signal beam at +30Px and the center of the idler at −10Px. We then transform those values from *Px* at the SLM plane to *1/mm* at the crystal plane by using the correction factors calculated in the previous sections (eq. 5.41).

The results for the moments of the position distribution are shown in table 5.5.

More important for the quantification of the correlations - and eventually of the spatial entanglement - are the variances. We calculated them from the measured first and second moments presented in Tables 5.6 for the momentum, and 5.7 for the position. The estimation

Table 5.6: Variances of the probability distribution of transverse-momentum calculated from the first and second moments presented in table 5.4. In the first, second, and third column the values calculated from the slit-slit scan, the direct method, and the theoretical model respectively. In the fourth column, we show the results from the simulation when we use the measured displacement of the signal and idler beams.

Variance	Slit-scan	Direct method	Theory 1	Theory 2
	$[mm^{-2}]$	$[mm^{-2}]$	$[mm^{-2}]$	$[mm^{-2}]$
$\langle\Delta^2 p_s\rangle$	400 ± 600	330 ± 30	1532.5	1529.9
$\langle\Delta^2 p_i\rangle$	400 ± 9000	260 ± 30	1532.5	1532.3
$\langle\Delta^2(p_s + p_i)\rangle$	800 ± 9000	530 ± 80	3309.2	3305.8
$\langle\Delta^2(p_s - p_i\rangle$	700 ± 9000	650 ± 80	2821.0	2818.6
$\langle C(p_s, p_i)\rangle$	0.08 ± 0.04	-0.1 ± 0.1	0.0796	0.0795

Table 5.7: Variances of the probability distribution of transverse-position calculated from the first and second moments presented in table 5.5. In the first, second, and third column the values calculated from the slit-slit scan, the direct method, and the theoretical model respectively. In the fourth column, we show the results from the simulation when we use the measured displacement of the signal and idler beams.

Variance	Slit-scan	Theory 1
	$[mm^2]$	$[mm^2]$
$\langle\Delta^2 x_s\rangle$	0.0028 ± -0.004	0.00014807
$\langle\Delta^2 x_i\rangle$	0.005 ± 0.02	0.00014807
$\langle\Delta^2(x_s + x_i)\rangle$	0.0064 ± 0.02	0.00027
$\langle\Delta^2(x_s - x_i\rangle$	0.008 ± 0.02	0.00032229
$\langle C(x_s, x_i)\rangle$	-0.1 ± 0.2	-0.0883

is based on the standard equation [59]:

$$\langle\Delta^2 w\rangle = \langle w^2\rangle - \langle w\rangle^2 \tag{5.51}$$

where in general w represents any of the spatial measurable variables, in our case: x, y, p, and q. Again, the comparison between the two detection methods and the theory is shown.

In the last row of Tables 5.6 and 5.7 we have shown the estimated correlations. A convenient expression for assessing them is expressed by eq. 5.52 [59] that we rewrite here for simplicity:

$$\begin{aligned} C(v_1, v_2) &= \frac{\Delta(v_1, v_2)}{\sqrt{\langle\Delta^2(v_1)\rangle\langle\Delta^2(v_2)\rangle}} \\ \langle\Delta(v_1, v_2)\rangle &= \langle v_1, v_2\rangle - \langle v_1\rangle\langle v_2\rangle \end{aligned} \tag{5.52}$$

It follows that $-1 < C(v_1, v_2) < +1$, where $C = 1$ ($C = -1$) means perfect correlations (anticorrelations). In Figure 5.10 we plotted the values of the calculated correlations I remind that those results are taken with the pump size set to *small* and the profile being Gaussian.

Finally, we can quantify the amount of entanglement. We make use of the Mancini-Giovannetti-Vitali-Tombesi criteria [107] expressed by equation 2.80. Considering our experimental definition of correlations 5.52, it can be written as:

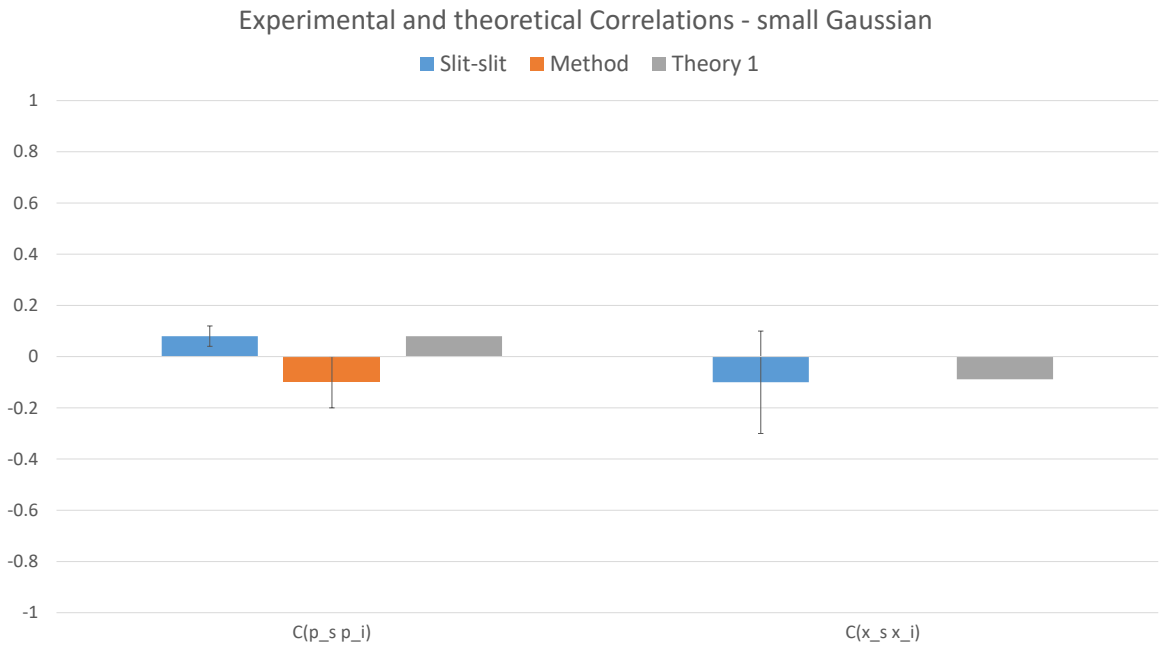

Figure 5.8: Correlations for the case of small Gaussian pump.

$$|C(x_s, x_i)| + |C(p_s, p_i)| \leq 1 \tag{5.53}$$

for all bipartite states to be separable. Violating 5.53 is a *necessary and sufficient* condition for entanglement of the state in the considered spatial variables. For the case of small Gaussian pump beam waist considered here, the results for the different methods employed are:

- **Slit-slit scan:** $(|C(x_s, x_i)| + |C(p_s, p_i)|) = 0.2068$;
- **Direct method:** $(|C(x_s, x_i)| + |C(p_s, p_i)|) = 0.1048$;
- **Theoretical model 1:** $(|C(x_s, x_i)| + |C(p_s, p_i)|) = 0.1679$;
- **Theoretical model 2:** $(|C(x_s, x_i)| + |C(p_s, p_i)|) = 0.1678$.

The results all agree in clearly showing no entanglement. This is due to the fact that the Gaussian profile being small, its width - which is then mapped on the downconverted fields - becomes comparable to the width of the phase matching function. That leads to very low values of the spatial correlation in both real and Fourier spaces, which eventually translate in no (or very low) entanglement. Further comments on the results will follow in the Conclusions of this chapter.

Large Gaussian pump profile.

In the case of large Gaussian profile, we only present data for the position distribution. The reason is a wrong protocol applied when taking measurements with the direct method in the far field. We realised the mistake after we finished the set and already began the following one. Due to a lack of time, we could not repeat the measurement. However, results for the momentum distribution in the case of large Gaussian pump although based on the slit-slit method only, were presented in the previous chapter (4.3.1).

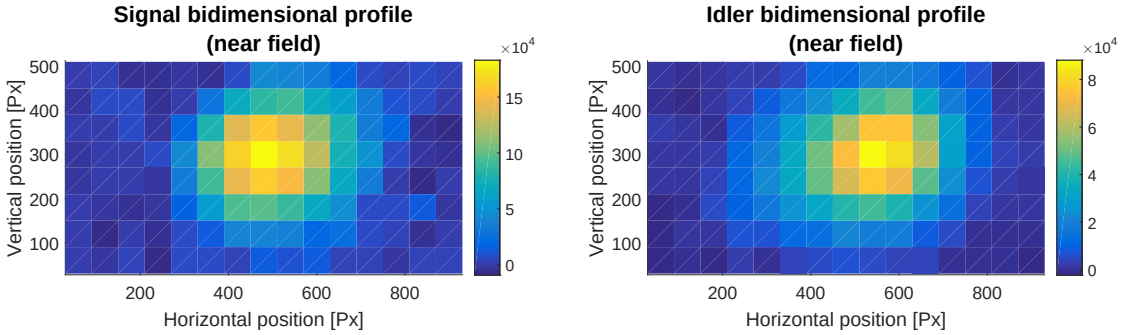

Figure 5.9: Signal (left) and idler (right) profiles at the SLM plane - position distributions. The counts, indicated by the color system, are single counts per unit time. The background counts have been removed.

Table 5.8: Expectation values of the moments of the probability distribution of transverse-position for the case of large Gaussian pump. In the first, second, and third column the values calculated from the slit-slit scan, the direct method, and the theoretical model respectively. In the fourth column, we show the results from the simulation when we use the measured displacement of the signal and idler beams.

Moment	Slit-scan $[mm]$	Direct method $[mm]$	Theory 1 $[mm]$
$\langle x_s \rangle$	0.004 ± 0.02	0.0162 ± 0.002	0
$\langle x_i \rangle$	-0.006 ± 0.02	-0.0164 ± 0.001	0
$\langle x_s x_i \rangle$	0.0018 ± 0.0003	0.0026 ± 0.0005	0.0013
	$[\mu m^2]$	$[mm^2]$	$[mm^2]$
$\langle x_s^2 \rangle$	0.0065 ± 0.0003	0.0038 ± 0.0005	0.0014
$\langle x_i^2 \rangle$	0.0077 ± 0.0003	0.0042 ± 0.0004	0.0014

In Table 5.8 we present the results of the moments measured following the direct method and also with the slit-slit scan described in the previous chapter. The telescope system on the pump was set off, and consequently the pump beam waist (radius) in the horizontal direction at the crystal plane was set to large: $w_H^0 = 74\mu m$. In this case we expect to see correlations in position and anticorrelations in momentum, as predicted by the model.

The correlations detected are summarized in Figure 5.10 and have been calculated using 5.52.

After having estimated the variances of the expectation values, we can calculate the correlations. We can only estimate the entanglement from the slit-slit scan detection and from the theoretical model. We report the results for the sake of completeness:

- **Slit-slit scan:** $(|C(x_s, x_i)| + |C(p_s, p_i)|) = 0.8461$;
- **Theoretical model 1:** $(|C(x_s, x_i)| + |C(p_s, p_i)|) = 1.7760$.

Comments of the results will follow at the end of this chapter.

Table 5.9: Variances of the probability distribution of transverse-position calculated from the first and second moments presented in table 5.8 for the case of large Gaussian pump. In the first, second, and third column the values calculated from the slit-slit scan, the direct method, and the theoretical model respectively. In the fourth column, we show the results from the simulation when we use the measured displacement of the signal and idler beams.

Variance	Slit-scan	Direct method	Theory 1
	$[mm^2]$	$[mm^2]$	$[mm^2]$
$\langle \Delta^2 x_s \rangle$	0.007 ± 0.06	0.0036 ± 0.0004	0.0014
$\langle \Delta^2 x_i \rangle$	0.008 ± 0.05	0.0039 ± 0.0004	0.0014
$\langle \Delta^2 (x_s x_i) \rangle$	0.0019 ± 0.0003	0.0029 ± 0.0004	
$\langle \Delta^2 (x_s + x_i) \rangle$	0.02 ± 0.08	0.0133 ± 0.001	0.0054
$\langle \Delta^2 (x_s - x_i) \rangle$	0.01 ± 0.08	0.0017 ± 0.001	3.2161e-04
$\langle C(x_s, x_i) \rangle$	0.26 ± 0.04	0.8 ± 0.2	0.8870

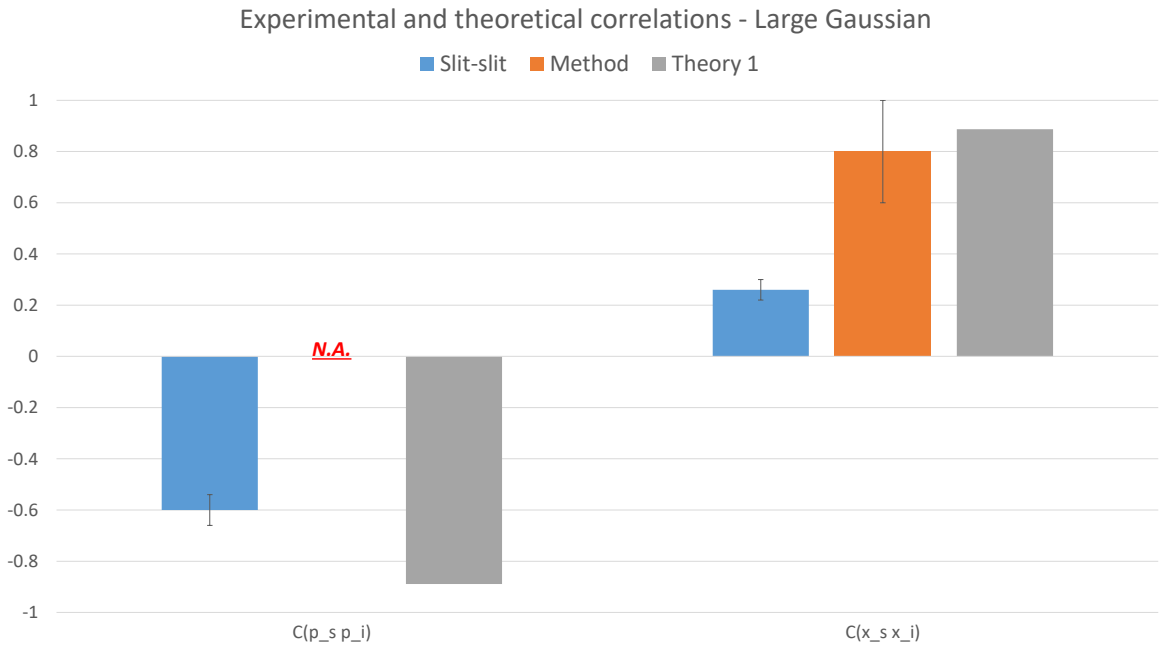

Figure 5.10: Correlations for the case of large Gaussian pump.

5.4.2 Higher modes correlations.

After having shown in the previous section that the direct method for determination of moments of probability distribution is reliable, in this section we show the results for a complete set of measurements with structure light.

We inserted the cover slip into the path of the Gaussian pump, after the spatial filter of the pump, in order to create a Hermite-Gaussian profile $HG_{1,0}$ as described previously (section 3.2.1 of the experimental chapter).

Hermite-Gaussian small pump.

The pump waist at the crystal plane was set to small by flipping-off the pump telescope system. For the Gaussian case, this experimental setting corresponds to a pump beam waist at the crystal plane of about $w_p^0 = 16\mu m$ (horizontal cross section). The beam profile for this Hermite-Gaussian case is shown in Figure 4.12. From that profile we measured the distance between the center of the two lobs to be $15Px \times 5.2\mu m/\text{Px} = 78\mu m$. Still from the same profile, by fitting the horizontal cross section with a Hermite-Gaussian function, we calculated the waist to be $w_H = 51.4\mu m$. The vertical profile of the lob on the right has also been analysed. It fits with a Gaussian function, and the resulting waist is $w_V = 17.1\mu m$.

Following the scheme utilized in the previous sections, let's move on and present the measured values of the moments of the distribution. They are shown in table 5.10 and 5.11. The profiles of signal and idler are showed in Figure 5.11 for the momentum distributions and 5.12 for the position distributions. They are needed in order to estimate the center of the axis for simulation purposes.

The variances are reported in tables 5.12 and 5.13 for position and momentum respectively. As usual, they have been assessed based on eq. 5.51: $\langle \Delta^2 w \rangle = \langle w^2 \rangle - \langle w \rangle^2$.

We calculated the expectation values of correlations in the spatial variables x and p (horizontal position adn horizontal transverse momentum respectively) by using the same formula as for the Gaussian case: $C(v_1, v_2) = \frac{\Delta(v_1,v_2)}{\sqrt{\langle \Delta^2(v_1) \rangle \langle \Delta^2(v_2) \rangle}}$ with $\langle \Delta(v_1, v_2) \rangle = \langle v_1, v_2 \rangle - \langle v_1 \rangle \langle v_2 \rangle$. The correlations detected are summarized in Figure 5.13.

Also for estimating the value of the entanglement witness we can use the same equation as for the Gaussian case. The results are:

- **Slit-slit scan:** $(|C(x_s, x_i)| + |C(p_s, p_i)|) = 0.3300$;

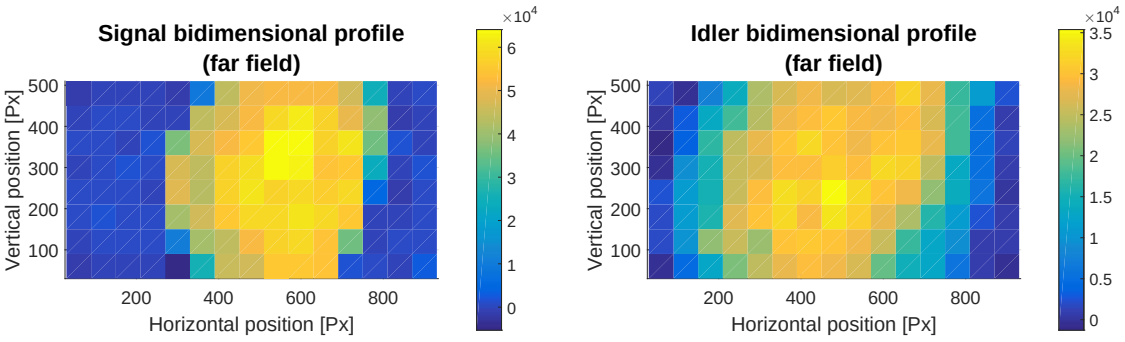

Figure 5.11: Signal (left) and idler (right) profiles at the SLM plane - momentum distributions. The counts, indicated by the color system, are single counts per unit time. The background counts have been removed.

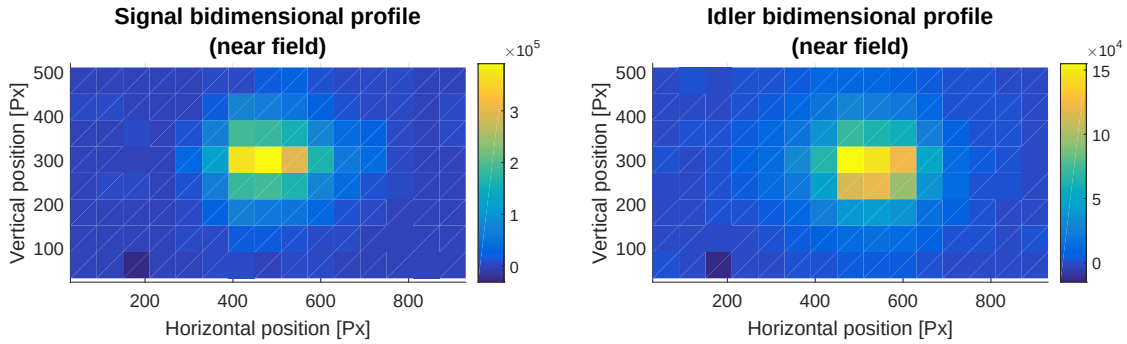

Figure 5.12: Signal (left) and idler (right) profiles at the SLM plane - position distributions. The counts, indicated by the color system, are single counts per unit time. The background counts have been removed.

Table 5.10: Expectation values of the first and second moments of the probability distribution of transverse-position for the case of small Hermite-Gaussian pump (horizontal) of signal and idler. In the first column the values calculated from the direct method compared to the theoretical predictions simulated with *MatLab* (second column).

Moment	Slit-slit	Direct method	Theory 1
	$[mm]$	$[mm]$	$[mm]$
$\langle x_s \rangle$	-0.02 ± 0.01	-0.0006 ± 0.002	0
$\langle x_i \rangle$	0.006 ± 0.01	-0.034 ± 0.001	0
$\langle x_s x_i \rangle$	0.0008 ± 0.0002	0.0012 ± 0.0005	0.00041378
	$[mm^2]$	$[mm^2]$	$[mm^2]$
$\langle x_s^2 \rangle$	0.0031 ± 0.0002	0.0026 ± 0.0004	0.00057475
$\langle x_i^2 \rangle$	0.0042 ± 0.0002	0.0026 ± 0.0004	0.00057475

Table 5.11: Expectation values of the first and second moments of the probability distribution of transverse-momentum for the case of small Hermite-Gaussian pump (horizontal) of signal and idler. In the first column the values calculated from the direct method compared to the theoretical predictions simulated with *MatLab* (second column) using the HG waist parameter from the fit: $w_p^{hg} = 0.0257$.

Moment	Slit-slit	Direct method	Theory 1
	$[mm^{-1}]$	$[mm^{-1}]$	$[mm^{-1}]$
$\langle p_s \rangle$	-20 ± 30	-3.1 ± 0.5	0
$\langle p_i \rangle$	20 ± 30	1.6 ± 0.5	0
	$[mm^{-2}]$	$[mm^{-2}]$	$[mm^{-2}]$
$\langle p_s^2 \rangle$	40000 ± 900	410 ± 30	1911.2
$\langle p_i^2 \rangle$	40000 ± 900	300 ± 30	1911.2

Table 5.12: Variances of the probability distribution of transverse-position (horizontal) calculated from the first and second moments presented in table 5.10. In the first column the values calculated from the direct method compared to the theoretical predictions simulated with *MatLab* (second column).

Variance	Slit-slit	Direct method	Theory1
	$[mm^2]$	$[mm^2]$	$[mm^2]$
$\langle\Delta^2 x_s\rangle$	0.003 ± -0.004	0.0026 ± 0.0004	0.00057475
$\langle\Delta^2 x_i\rangle$	0.004 ± 0.02	0.0014 ± 0.0004	0.00057475
$\langle\Delta^2(x_s x_i)\rangle$	0.0009 ± 0.0002	0.006 ± 0.001	
$\langle\Delta^2(x_s + x_i)\rangle$	0.009 ± 0.02	0.006 ± 0.001	0.0020
$\langle\Delta^2(x_s - x_i\rangle$	0.005 ± 0.02	0.002 ± 0.001	0.00032193
$C(x_s, x_i)$	0.27 ± 0.02	0.6 ± 0.2	0.7199

Table 5.13: Variances of the probability distribution of transverse-momentum (horizontal) calculated from the first and second moments presented in table 5.11. In the first column the values calculated from the direct method compared to the theoretical predictions simulated with *MatLab* (second column).

Variance	Slit-slit	Direct method	Theory 1
	$[mm^{-2}]$	$[mm^{-2}]$	$[mm^{-2}]$
$\langle\Delta^2 p_s\rangle$	$0.4 \cdot 10^5 \pm 2 \cdot 10^5$	400 ± 30	1911.2
$\langle\Delta^2 p_i\rangle$	$0.4 \cdot 10^5 \pm 1 \cdot 10^5$	300 ± 30	1911.2
$\langle\Delta^2(p_s + p_i)\rangle$	$0.7 \cdot 10^5 \pm 2 \cdot 10^5$	520 ± 70	4546.7
$\langle\Delta^2(p_s - p_i\rangle$	$0.8 \cdot 10^5 \pm 2 \cdot 10^5$	860 ± 70	3098.2
$C(p_s, p_i)$	-0.06 ± 0.02	-0.24 ± 0.09	0.1895

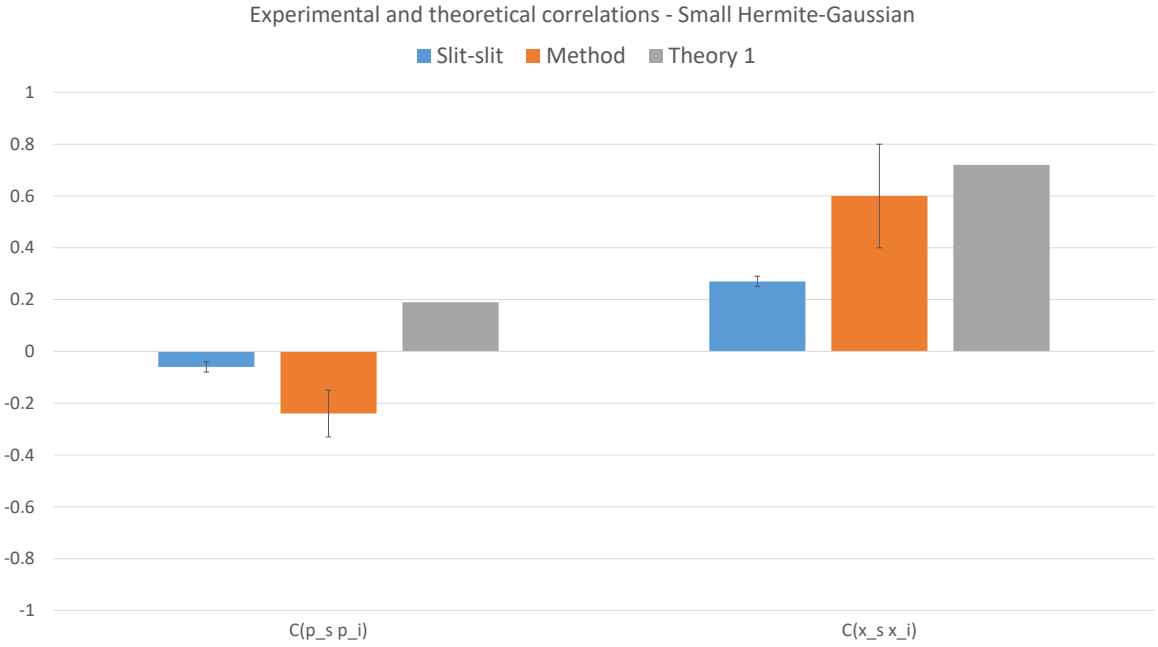

Figure 5.13: Correlations for the case of small Hermit-Gaussian pump.

- **Direct method:** $(|C(x_s, x_i)| + |C(p_s, p_i)|) = 0.8334$;
- **Theoretical model 1:** $(|C(x_s, x_i)| + |C(p_s, p_i)|) = 0.9094$.

5.4.3 Conclusions.

In this section we give some general conclusions regarding the results presented in the three previous subsections. In there, we presented our results for spatial correlations of our SPDC source in different scenarios of pump profile. We also showed how to control the amount of correlations, or better said, how to go from a regime in which spatial correlations are easily seen in the second moments of the spatial probability distribution to a regime in which investigating the probability distribution up to the second moment doesn't highlight any correlations. We did so just by changing the size of the pump beam waist.

Measurements of the moments.

First, a comment regarding the measurements of the first and second moments estimated. We could see that both the experimental methods provided similar results in all the measurement sets analysed (we presented a total of six complete measurements sets, three in position and three in momentum distribution). From this result we can conclude that we applied the innovative direct method correctly, both in the cases of Gaussian pump and Hermite-Gaussian. The only exception being the analysis of the SPDC generated with the small Hermite-Gaussian pump beam in the Fourier space. The values are clearly wrong, the reason to some experimental mistake could not be identified due to the time required to analyse the data. Indeed, when we realised the nonsense of the data the settings of the setup were already changed.

The theoretical predictions also confirm the experimental results in the cases of position distribution. In particular, the predictions of second order moments are correct with both the theoretical approaches proposed. On the other hand, we showed that we can predict correctly the first moments in position by slightly modifying the equations in the code in order to include the imperfect centering of the beams on the SLM.

Regarding the experimental errors, we can see that they are very similar in the results provided by the two experimental methods. We remind that the experimental uncertainties for the slit-slit scan method have been calculated considering only the low sensitivity of the instrument, that is the finite width of the phase slits used. We neglected the statistical error being much smaller. In the case of the direct method, the estimation of the errors - exclusively statistical errors - is more complex, and it has been extensively explained in section 5.3.1.

While we are happy to be able to confirm one experimental method with the other within experimental uncertainties, this is not the only result we were expecting. We expected the statistical error in the direct method to be few order of magnitude smaller than with the slit-slit scan not only in the determination of the variances (and therefore correlations) but also in the estimation of the moments. Analysing deeply the raw data of all the available sets, we could conclude that in all the sets of measurements an error in the polarization preparation of the state and/or in the polarization projection of the states in detection must have happened.

When knowing the input state on the SLM and the projecting state at in detection, it is easy to estimate the amount of (normalised) coincidences expected when placing on the SLM a known flat phase. The known *flat* constant phases we set on the SLM during each set of measurements are zero and $\pi/2$. So we tabulated the normalized coincidences in the four combinations of those constant phases (an example is reported in Table 5.14).

Table 5.14: Set of measurements: small Gaussian profile, in Fourier space. The values are normalized with respect to the sum of the total number of coincidences per second recorded in the four states. In the squared parenthesis the values expected in an ideal case.

Projected state	$C_{0,0}$	$C_{\pi/2,0}$	$C_{0,\pi/2}$	$C_{\pi/2,\pi/2}$
$\langle\langle + + \vert$	0.6544 [1]	0.4267 [0.5]	0.4100 [0.5]	0.2784 [0.25]
$\langle\langle + - \vert$	0.0293 [0]	0.0446 [0]	0.3116 [0.5]	0.1940 [0.25]
$\langle\langle - + \vert$	0.2491 [0]	0.4766 [0.5]	0.1541 [0]	0.2858 [0.25]
$\langle\langle - - \vert$	0.0293 [0]	0.0522 [0]	0.1244 [0]	0.2418 [0.25]

Since all the available sets were showing very similar values for same choices of projective state and phase on the SLM, we realised that some sort of systematic error affected the measurements. The mistake is very likely to be due to an error in the preparation of the polarization states. However, what matter is that the detected state is projected in combinations of states parallel and orthogonal to the original one (before the interaction with the SLM).

It is clear that there are some residual imperfections identifiable, for instance, in the 25% probability (instead of *zero*) of detecting the state in the state $\langle\langle - + \vert$ when the input state is prepared in $\langle\langle + + \vert$ and the phases on the signal and idler quadrants of the SLM we set zero phase. It is definitely *not* a negligible imprecision; however, the outcomes of the measurements are still in good agreement with what expected (as commented few paragraphs above). This should convince about the reliability of the direct method in regard of experimental errors. On the other hand, the fact that the uncertainties in the assessment of the moments are much larger than what expected is directly caused by this considerable error in polarization preparation and/or detection.

The problem just described is an experimental imperfection that can be easily found and removed. The reason why we did not repeat the measurements has to be found in the lack of time at the end of my PhD.

Another general comment regarding the estimation of the moments regards the results for the second order ones in momentum. While in position ($\langle x_s^2 \rangle$ and $\langle x_i^2 \rangle$) the measured values are always similar to the theoretical ones, in the case of momentum they are always much smaller. The second order moments reflect the width of the distribution; the fact that in position we measure the expected value while in momentum we do not, means that in the latter case we are cutting the beam somewhere. To understand that this conclusion makes sense it is enough to look at the spatial profiles of signal and idler: the beams in the momentum space are always much bigger than the correspondent in real space. Furthermore, it is also clear that the beam is already cut by the edges of the SLM. On the other hand, the simulation consider all the generated SPDC in calculating the expectation values.

As a further development, it is possible to include this experimental limitation in the mathematical model. This would be easy, and would allow to estimate the correct value of correlations and therefore entanglement which are possible to detect in an actual measurement.

Measurement of the variances and correlations.

We can draw one last conclusion and it is in favour of the direct method. In all the cases analysed it showed to be more reliable than the slit-slit scan in the measure of the variances. In particular, we can see how the instrumental error characteristic of the measurements with the double-slit method explodes when propagating it, while the same is not true for the case

of direct measurements. We can see that while the errors on the moments are similar, the final errors on the variances become much larger in the slit-slit scan with respect to the direct method. The difference become of the order of one or more often two orders of magnitude.

Comparing values of correlations measured with the two methods, we can see that in general the ones from the direct measurements of the moments are closer to the expected value calculated with the simulation. This behaviour is in turn reflected on the assessment of entanglement, which is more accurate using the direct method. In particular, we did not expect entanglement in the configuration with small Gaussian pump, and indeed the test with the entanglement witness was negative (in both methods).

In the case of large Gaussian pump we expected entanglement. From the simulation, the witness was expected to show a value of 1.7760, which is much larger than 1 and therefore identify entanglement. However, the direct method was not applicable in that case due to an error in the experimental procedure when measuring in the far field. The slit-slit method, instead, fail in revealing entanglement but, as mentioned, the experimental error was very large (larger than the value itself). This produced an underestimation of the correlation in position (0.264 ± 2.9) against the theoretical prediction of 0.8870 and the measured value with the direct method of 0.7725. Just to speculate, if we use the experimental value of momentum anticorrelations from the slit-slit scan ($|C(p_s, p_i)| = 0.5821$) together with the measurement of position correlations with the more accurate direct method ($|C(x_s, x_i)| = 0.7725$), the entanglement witness would return a value of 1.3546.

The last batch of measurements, the one referring to the Hermite-Gaussian pump profile with small waist, also confirm the better reliability of the direct method to measure entanglement with respect to the slit-slit method. the values of the entanglement witness are as far from each other as 0.3300 for the slit-slit and 0.8334 for the direct method. In neither of the cases is highlighted any entanglement through this witness. However, the simulation showed that entanglement is in fact not detectable in this experimental conditions, providing a value of the entanglement witness of 0.9094. Rather concluding that there is no entanglement in the small waist, Hermite-Gaussian states investigated, we should limit our conclusions stating that *with the standard method* (the Mancini-Giovannetti-Vitali-Tombesi criteria 5.53) is not possible to highlight entanglement in the present experimental condition.

This paves the way for further development on the theoretical aspects as well, encouraging to deepen the study of entanglement criteria for higher-than-Gaussian spatial modes.

6

Spatial entanglement: towards 4-photon momentum entangled states.

We all know that in principle it should work; what is more interesting, is to understand why in fact it doesn't.

AT

In the present chapter we describe our experimental setup for the generation of 4-photon momentum entangled states. *Spatial* entanglement among more than two particles had been demonstrated only in one experiment at the time we began the project described in this thesis [139]. The main difficulty lies in the fact that spontaneous parametric down conversion (SPDC) is a process that involves the generation of photons in pairs. While the photons within each pair are strongly correlated with each other, in most general conditions that is not true for the photons of consecutive pairs, limiting the possibilities to generate states that show 4-photon interference.

In section 6.1 we tackle a bit of theory showing the 4-photon states that we aim to create with our setup. It continues naturally from the derivation of the states of 2-photon derived in chapter 2.

The following section is dedicated to the experimental aspects. In 6.2 we describe the modifications needed to be applied to the setup used for the 2-photon states to adapt it for the 4-photon experiments. In particular, we mention the practical issues connected to the high losses and low efficiency of the new setup, starting from the 50/50 beam splitter needed in order to equally separate two beams of entangled photons in four beams, the need of a narrow-pulse laser, and finishing with the need of very-narrow interference filters in order to extend the coherence time of the detected beams.

Finally, in section 6.2.1 we briefly mention few very practical modification of the experimental setup that would improve it.

6.1 Theoretical model.

In this section we begin describing the states of photons generated via SPDC focusing on the 4-photon terms. We then conclude explaining how to work in the desired regime.

SPDC can also emit multipairs at the same time when the crystal is pumped with enough power. Still, each single event is a 2-photon emission and can be described following the reasoning carried on in chapter 2. The biphoton state has been derived (from first principles) and its final form is obtained in section 2.2.4, equation 2.26. We report the state here for simplicity:

$$|\psi\rangle = |vac\rangle + \sum_{\sigma_s\sigma_i} \int d\omega_s \int d\omega_i \int dq_s \int dq_i \Phi_{\sigma_s\sigma_i}(q_s, q_i, \omega_s, \omega_i) |1(q_s, \omega_s, \sigma_s), 1(q_i, \omega_i, \sigma_i)\rangle\rangle \tag{6.1}$$

where $|1(q_s, \omega_s, \sigma_s), 1(q_i, \omega_i, \sigma_i)\rangle\rangle$ are the two-photon Fock state of one photon being in the (signal) mode characterized by transversal wave vector q_s, at angular frequency ω_s, and polarization σ_s, and the other being in the (idler) mode characterized by transversal wave vector q_i, at angular frequency ω_i, and polarization σ_i. The amplitude $\Phi_{\sigma_s\sigma_i}$ is the biphoton wavefunction.

The reason why in 6.1 there are only 2-photon contributions to the total state $|\psi\rangle$ is due to the fact that we dropped higher photon number terms. We did so when we expanded in a Taylor series the evolution operator $U(t)$ (eq 2.20) and decided to keep only the linear term. Since here we are interested in the 4-photon emission, we need to consider also the first nonlinear order. Therefore we can express the state of SPDC as:

$$|\psi\rangle = e^{-i\frac{t}{\hbar}\hat{\mathbf{H}}}|0\rangle \simeq \left(1 - \frac{it}{\hbar}\hat{\mathbf{H}} - \frac{t^2}{2\hbar^2}\hat{\mathbf{H}}^2\right)|0\rangle \tag{6.2}$$

where in this case we ignored all the terms higher than *two*.

With respect to the analysis done in chapter 2, here we are less interested into the details of the interaction Hamiltonian and more in the multiphoton emission. We recognise that the toy model shown below is a strong simplification of the complete model proposed in the previous chapter. Several interesting aspects of the physics are dropped due to its approximations. However, we believe this approach helps us to focus on the multiphoton emission.

It is convenient to express the state on a discrete basis rather than continuous. This is possible thanks to the Schmidt decomposition explained earlier, in the Spatial entanglement in the SPDC bi-photon wave function (section 2.4). Therefore, we can write the (approximated) interaction Hamiltonian in a discrete form as [139]:

$$\hat{\mathbf{H}} = \gamma \sum_{i}^{N} \hat{\mathbf{a}}^\dagger_{q_i} \hat{\mathbf{a}}^\dagger_{-q_i} + H.c. \tag{6.3}$$

where $\hat{\mathbf{a}}^\dagger_{q_i}$ is the creation operator for a single photon in the state identified by the transverse momentum q_i, and γ represents the strength of the interaction that accounts for all the factors that we calculated in chapter 2.

The linear term in the Taylor expansion 6.2 is responsible for the two-photon state. In this discrete framework just introduced, using the Hamiltonian 6.3, the two-photon state results:

$$|\psi\rangle\rangle_2 = -\frac{it}{\hbar}\hat{\mathbf{H}}|0\rangle = -\frac{it\gamma}{\hbar}\sum_{i}^{N}|1_{q_i}; 1_{-q_i}\rangle\rangle \tag{6.4}$$

which is a superposition of all the accessible 2-photon states for signal and idler in the transverse momentum basis ($|1_{q_i}; 1_{-q_i}\rangle\rangle$ represents a two-photon state composed by one single photon in the signal mode with transverse momentum q_i and one single photon in the idler mode with transverse momentum $-q_i$). Of particular interest in 6.4 is the evident anticorrelation between signal and idler transverse momentum modes.

Similarly, the nonlinear term in 6.2 requires to apply twice the Hamiltonian operator to the vacuum state. The result is the 4-photon state described by [54, 139]:

$$|\psi\rangle_4 = -\frac{\gamma^2 t^2}{2\hbar^2}\left(\sum_{i=1}^{N}\sum_{j=1, j\neq i}^{N}|1_{q_i}, 1_{q_j}; 1_{-q_i}, 1_{-q_j}\rangle + 2\sum_{i=1}^{N}|2_{q_i}; 2_{q_j}\rangle\right) \tag{6.5}$$

where here $|1_{q_i}, 1_{q_j}; 1_{-q_i}, 1_{-q_j}\rangle$ refers to a state of four photons composed by one single photon in the signal mode with transverse momentum q_i and one with the transverse momentum q_j, plus one single photon in the idler mode with transverse linear momentum $-q_i$ and one with transverse momentum $-q_j$. Similarly, the term $|2_{q_i}; 2_{q_j}\rangle$ refers to a state of four photons composed by two single photons in the signal mode both with transverse momentum q_i and two single photons in the idler mode both with transverse linear momentum $-q_i$.

Therefore, in equation 6.5 there are two terms contributing to the 4-photon states. The first highlights no correlations between photons generated in two consecutive pairs and can be described as a state of two independent pairs of photons. The second is the term in which we are interested. Due to interference, the state results in not just the product of two pairs [11]. Correlations among all the four photons are evident, with two (signal) photons being in a mode of the transverse momentum q_i and the two corresponding (idler) photons both in the $-q_i$ state. In this case the four photons are in a genuine multipartite quantum entangled state of four photons. Furthermore, we can see that the 4-photon entangled states are more probable due to the multiplying factor 2. This factor comes from the stimulated emission mentioned in the *Introduction*.

It can be shown that the optimal experimental conditions for the generation of 4-photon states in the two-separate-pair regime are opposite to the experimental conditions optimal for stimulated emission [16]. In particular, when the coherence time of the biphoton wavefunction t^c_{dc} is much longer than the temporal duration Δt of the pulse of the pump laser, the four photon states are described by the 4-photon genuine entangled term. Viceversa, when t^c_{dc} is much shorter than Δt, the four photons are in a state of two separate pair [16]. Any intermediate case can be described by a visibility χ which is a function of t^c_{dc} and Δt.

It is clear that while for generating two-photon states we do not need a pulsed laser, for creating genuine entanglement among four particles we do need a pulsed pump. We can define our experimental parameter as the ratio between the coherence time of the downconverted photons t^c_{dc} and the temporal duration of the pump pulse Δt:

$$r = \frac{t^c_{dc}}{\Delta t} \tag{6.6}$$

The case of two separate pairs corresponds to $r << 1$; in that case there can be many independent SPDC events happening within the same pulse. It is due to the fact that their coherence time is short and in particular completely contained within the pump pulse, where there is room for temporally containing more than one biphoton wavefunction. Since in this regime each $2n$ photon state can be satisfactorily described in term of individual, independent pair, the Poisson statistic can be applied. It follows that the probability of creating n pairs is [16]: $P_n = exp[-\mu]\mu^n/(n!)$, where μ is the average of the distribution. For small values

of μ the probability of creating four photons is: $P_4 \simeq P_2^2/2$, and in this regime they must be interpreted as two independent pairs. We refer to these double pair photons as *Poisson distributed*.

In the opposite case when $r >> 1$, the pulse duration is much shorter than the coherence time of any downcovnerted pairs, creating indistinguishability among consecutive pairs. In this case, thanks to stimulated emission, the probability of generating four photons is $P_4 = P_2^2$, and they must be described by a 4-photon genuine entangled state [16]. We refer to these events as *stimulated emission*.

To the visibility parameter χ can be attributed a continuum of values between zero and one. We can therefore use it to describe the states between Poisson distributed (independent pairs) and stimulated emission (4-photon entangled) as:

$$P_4 = \frac{P_2^2}{2}(1 + \chi) \tag{6.7}$$

with $\chi \epsilon [0, 1]$. The connection between the visibility and the experimental parameter r in the limit cases has to be $\chi = 1$ for large r, and $\chi = r$ for small r (this is valid in the case of a large number of events N). For the cases in between an expression is derived in [16] and it reads:

$$\chi = \frac{r}{\sqrt{1 + r^2}} \tag{6.8}$$

which ultimately depends on the number of temporal and spatial modes created in the SPDC fields [16, 139].

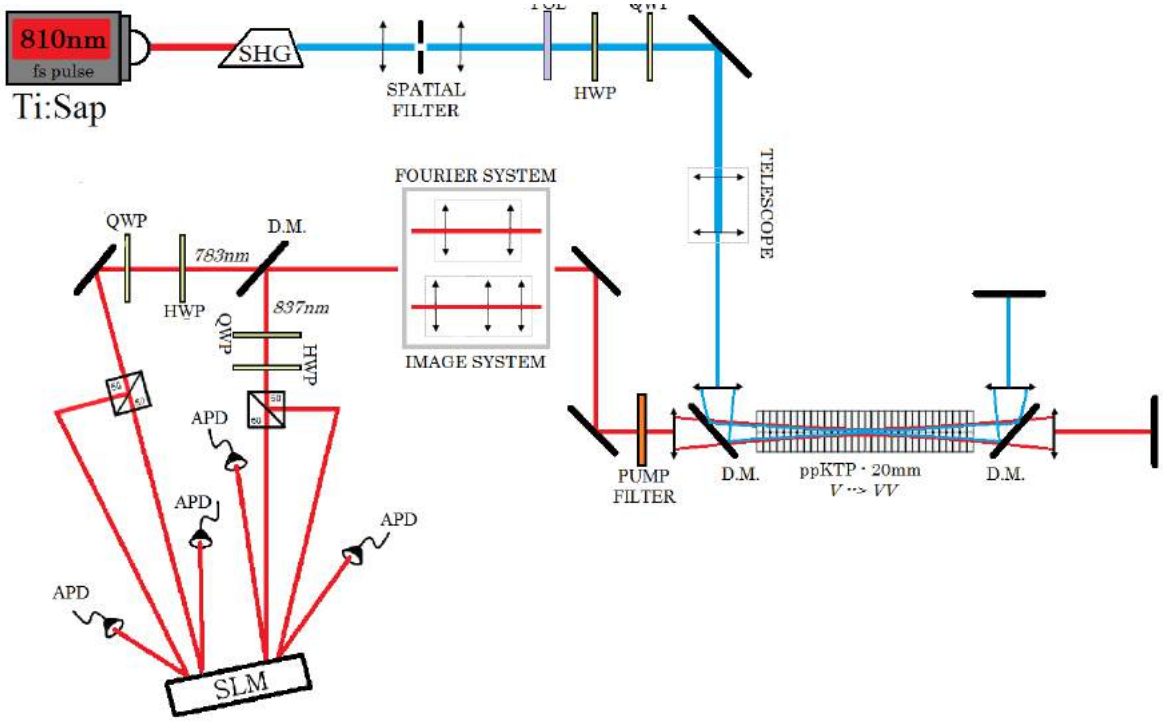

Figure 6.1: A tunable femtosecond-pulsed laser set around 810*nm* is upconverted to 405*nm* through a Second Harmonic Generator (SHG). Then it is spatially filtered by means of a lens - pin-hole - lens system. The combination of Half Wave Plate (HWP) plus polarizer (POL) are used to control the polarization of the pump field as well as its power. A telescope made by two planoconvex lenses can be flipped in or out the pump path to decrease or increase the diameter of the pump which eventually translates in increasing or decreasing the waist in the crystal plane. The laser enter the nonlinear crystal in a first pass from left to right; the SPDC produced is separated by the pump through a dichroic mirror; both the beams are reflected and refocused into the crystal traversing it in a second pass from right to left; then the pump is separated from SPDC and discarded. A long-pass filter completes the filtering of the SPDC by absorbing the residual pump field. Two sets of lenses are interchangeable: one images the crystal plane on the Spatial Light Modulator (SLM) while the other does the Fourier transform of the same plane. Signal and Idler fields are separated by a dichroic mirror (DM), and on each of the two resulting branches a pair of waveplates (HWP+QWP) prepares the polarization state on 45°. Both the beams are separated in two by a 50/50 beam splitter (BS). The resulting four beams are reflected by the SLM. Finally, the two signals and the two idlers are spectral filtered using customized interference filters and coupled into multimode fibers to be detected by an array of four Avalanche Photo Diodes (APDs).

6.2 Experimental setup.

The experimental setup for the generation and detection of 4-photon spatially entangled states is ready to be finely aligned and tested. Most of the optics are the same as for the 2-photon setup. However, few key elements needed to be added or substituted (figure 6.1).

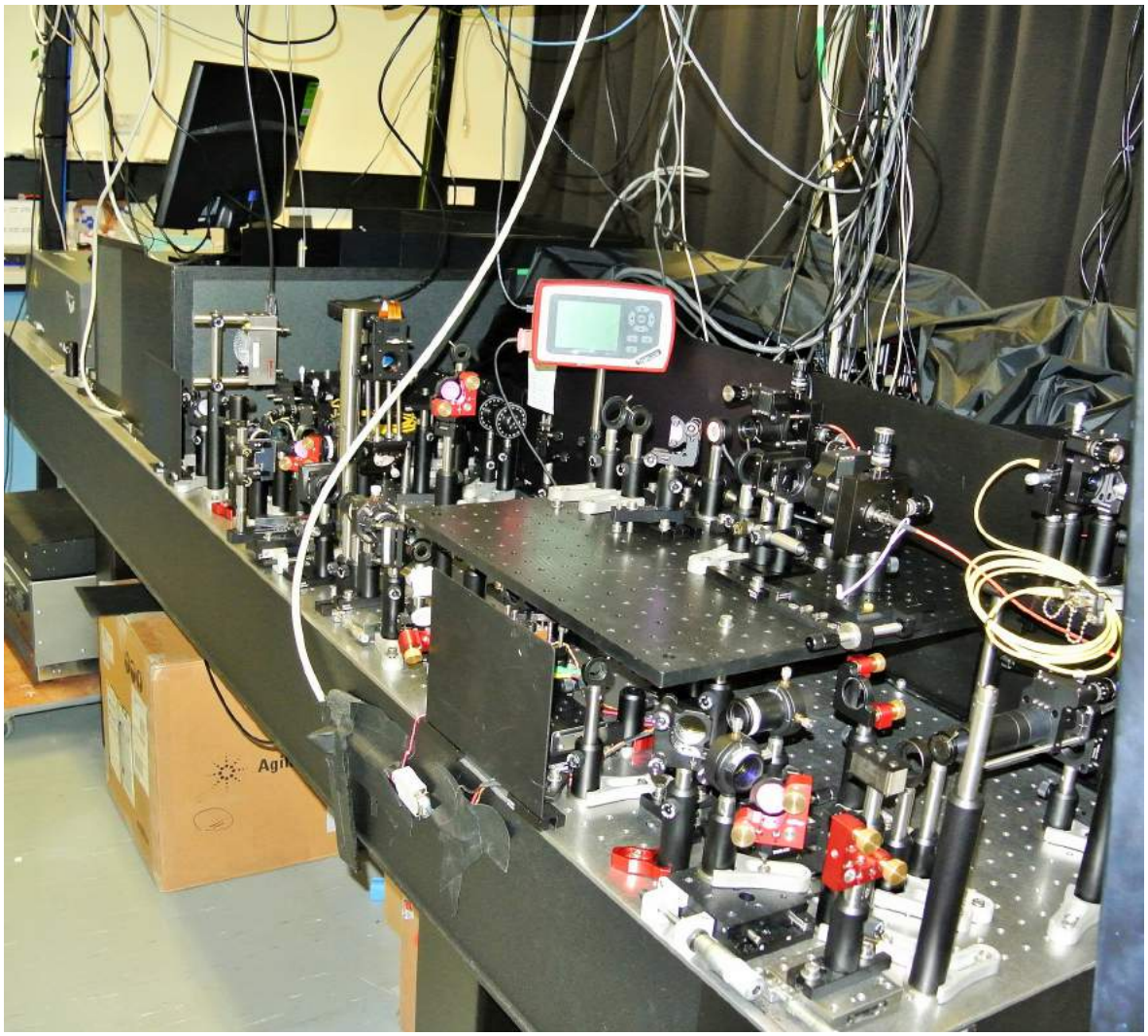

Figure 6.2: Experimental setup at an early stage. At the very left can be seen the rectangular grey box embedding the *Chameleon* pulsed laser. A CW diode laser used only for alignment during a time when the TiSap broke down can be seen below the monitor, in the top left corner. The CW diode laser used for the 2-photon experiment instead is injected into the setup from a hole in the black separation wall in the bottom right corner of the photo.

The first element we need to change is the pump laser. As explained in the theoretical section 6.1, for the 4-photon experiment is essential to pump the nonlinear crystal with a narrow pulsed laser. We opted for the Titanium sapphire (TiSap) *Chameleon ULTRA* produced by *Coherent* (described in the technical introduction, particularly in section 3.1.1). Through flippable mirrors we can swap from the CW (continuous wave) laser utilized for the 2-photon experiment to the TiSap.

For the preparation of the TiSap pump beam we follow the same steps already described for the CW case. Briefly: we used a linear polarizer (polarizing beam splitter, PBS) to select

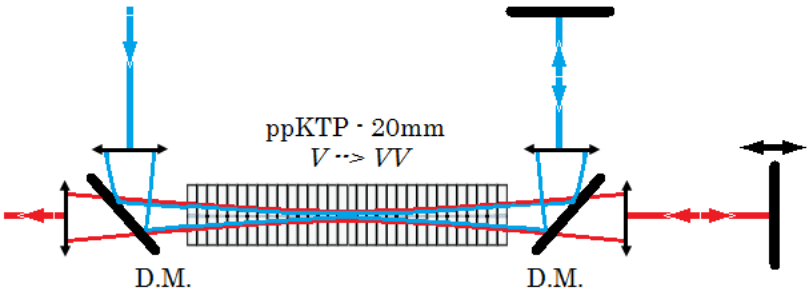

Figure 6.3: Sketch of the double-pass configuration. The pump field (blue) is first injected into the crystal from left to right. Then a dichroic mirror separates the pump from the downconverted fields. The two beams are reinjected into the crystal synchronized by the use of a micrometer controlled translational stage on the mirror of the spdc photons. After the second pass into the crystal (from right to left) the pump laser is removed by a dichroic mirror and the spdc fields are transmitted towards the detection apparatus.

only one direction of linear polarization. A half wave plate (HWP) is placed right before the PBS and works in conjunction with it to control the power of the pump laser. A spatial filter similar to the one described in section 3.2 is used to clean the spatial profile of the TiSap. Last, a telescope system made by two lenses is used to select the proper size of the pump beam waist (it can be removed to obtain a smaller diameter). The only one optical element placed between the laser and the crystal that is not present in the 2-photon experiment is a second harmonic generator (SHG). In the case of TiSap we need this element in order to upconvert the laser field to the wanted near-UV frequency (more details are given in section 3.1.1).

The second important feature regards the path of the laser through the crystal. While for the 2-photon experiment we opted for a standard single-pass of the pump into the crystal, for generating the 4-photon states we decided to install a more sophisticated double-pass configuration. A dichroic mirror is then used to reflect the pump into the crystal. While this element is not necessary for the two-photon experimental setup - actually its action is detrimental due to the finite reflection efficiency - its role will be clear when explaining the setup for the 4-photon experiment (section 6.2). To highlight the difference in the setup, the first case can be described as follow: the pump pass into the crystal from *right to left*; at the output of the crystal there are three collinearly propagating beams: pump, signal and idler; the pump is removed by a dichroic mirror; the downconverted photons are directed towards the detection apparatus. On the contrary, for the double-pass we can say: the pump pass into the crystal from *left to right*; at the crystal end facet there are signal, idler, and pump beams; we separate pump from downconverted fields through a dichroic mirror; we independently reflect the two beams with independent mirrors; a second pass into the crystal from *right to left* now involves both the pump and the SPDC generated in the first-pass; at the output of the crystal we have the usual three fields; we remove the pump by using a dichroic mirror while we let signal and idler beams propagate through the detection optics (figure 6.3).

We regard at the double-pass configuration as a method for enhancing the emission probability of a second pair in the same spatial modes of the first pair through the process of stimulated emission.

In order to split the collinearly propagating signal and idler beams into four separate modes we first split the signals from the idlers through the same dichroic mirror used in the 2-photon apparatus. Successively, we use a 50/50 beam splitter (BS) to separate *probabilistically* the signal and the idler beams into *two* signal and *two* idler beams. In normal conditions we have

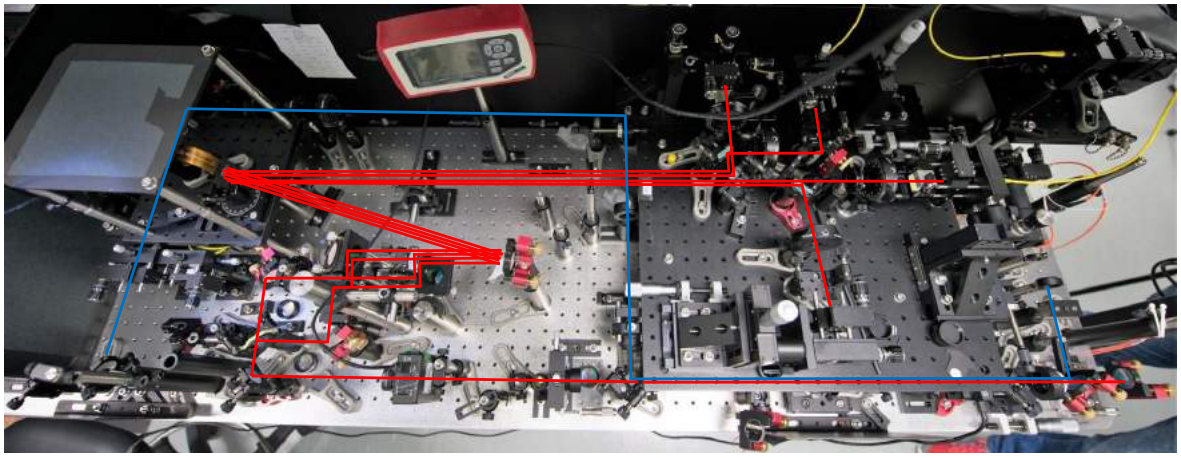

Figure 6.4: Experimental setup - top view. In blue is represented the path of the pump beam, that goes from left to right. The TiSap is not in the photo, neither is the SHG (which are both placed further on the left). The red lines represent the SPDC photon beams. The generation happens in the middle of teh segment where both pump and SPDC propagates collinearly. On the far right of the photo, both the SPDC (from the first-pass) and the pump are reflected back into the crystal form two individual mirrors. The second split of SPDC, ie where two beams become four, happens in conjunction with the vertical translation to the upper part of the setup. This photo was taken approx one year before completion of the thesis; the only optics missing for the 4-photon experiment are the two fibers for the 3^{rd} and 4^{th} photon.

50% probability that two signal photons reaching the beam splitter togetherare actually split (one transmitted and the other reflected); the same argument applies to two idler photons. Therefore, each four photon state reaching the BS is separated in four modes with an efficiency equal to 25%.

We then propagate the four beams parallel to each other. The position and the function of the spatial light modulator (SLM) are the same as for the 2-photon experiment. The only difference is that for the 4-photon experiments we use the entire SLM display, divided in four independent quadrants, while earlier we were utilising only two fourths of it.

For the detection part there is nothing new to say. We only added two more fiber couplers which work in the same way as for the 2-photon experiment (Figure 6.5). Our APDs box was already compatible to the 4-photon detection having four independent optical inputs. Its TTL output is coupled to the coincidence logic which we programmed for the counting of four different combinations of 2-, 3-, and 4-fold coincidences.

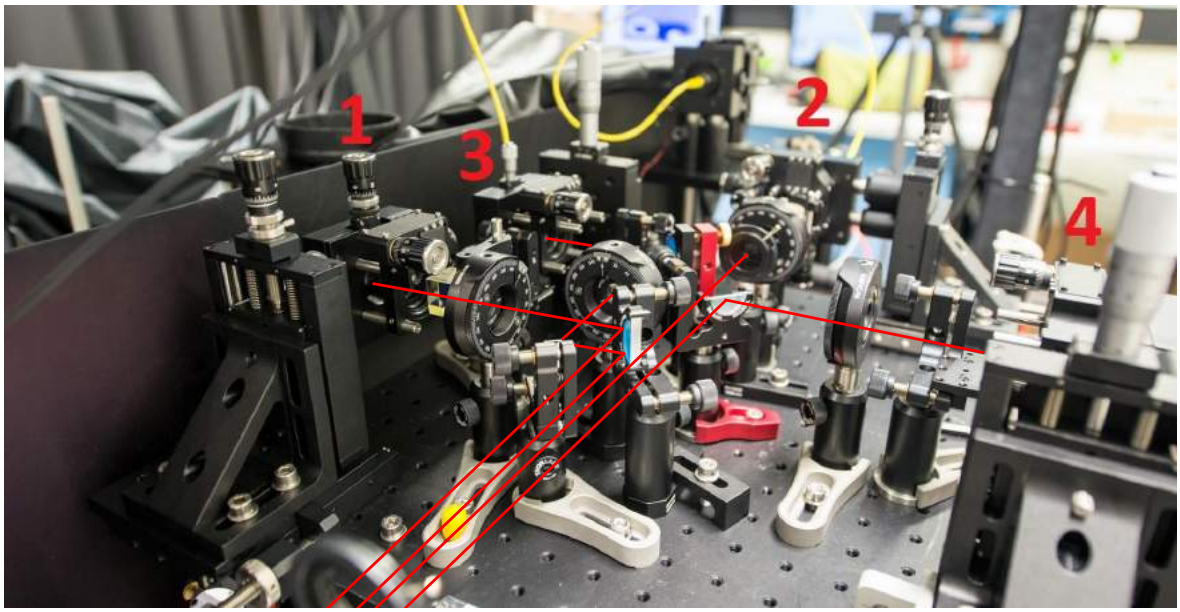

Figure 6.5: In the photo we can see the four independent fiber couplers for detection of 4-photon states. The numbers from 1 to 4 indicates sequentially: first signal, first idler, second signal, second idler. At the time when the photo was taken we were aligning the first idler in backpropagation coupling a diode laser into the fiber coupler 2 through a single mode fiber (which can be easily recognised by the yellow color of the external cladding).

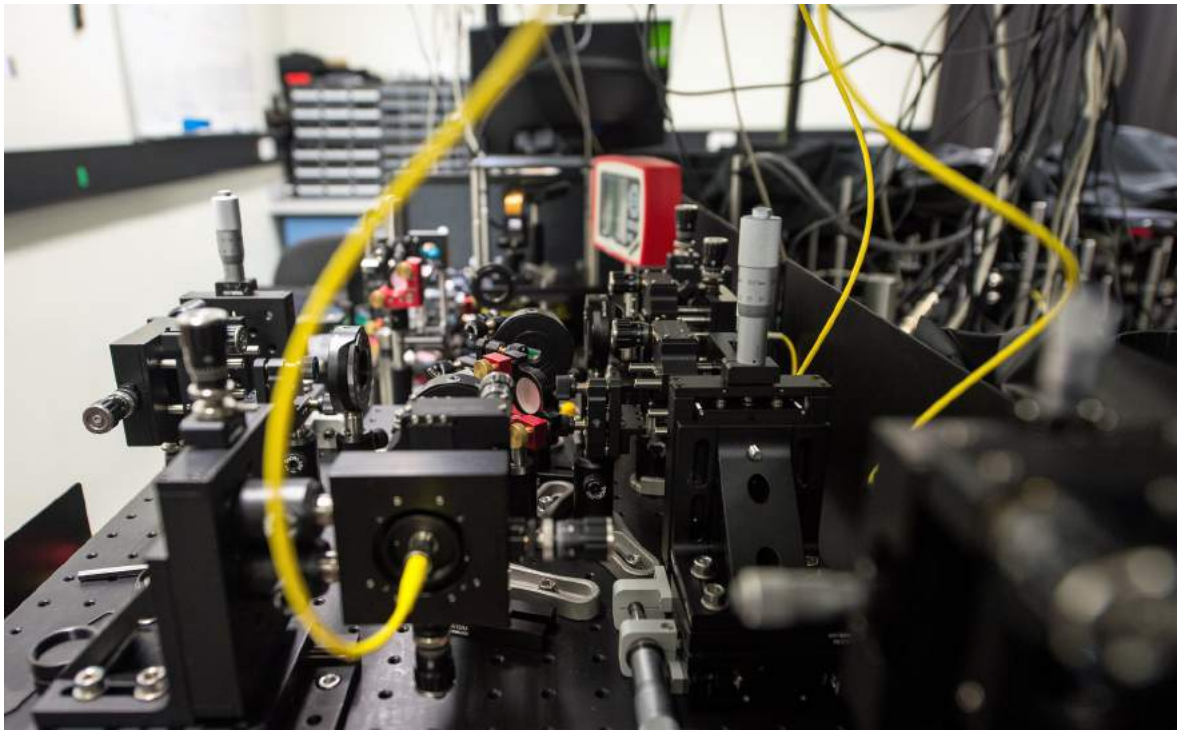

Figure 6.6: Experimental setup seen from the back of fiber coupler 2 (see caption of Fig. 6.5).

6.2.1 Future setup improvement.

When aligning and testing our setup we encountered several challenges, whose nature was mainly practical. We made some changes where possible, therefore improving the setup under aspects such as stability and efficiency (swapping from single mode fiber to spatial filter for Gaussian mode selection on the pump profile), measurement sensitivity (improving telescopes within image and Fourier lenses systems), and other smaller ones. However, some other changes could not be addressed due to limited time of the PhD program and sometimes also to limited space on the optical table. We very briefly mention them here for the sake of completeness, and as a guide for the future development of the experimental setup.

The lens systems used to implement both image and Fourier system could be improved. We designed them according to the specs of the lenses following the theory of ray optics. Which for practical purposes is not always accurate enough. On the top of that, the only experimental way to align the lenses is by using a technique know as back-propagation. Very briefly, one uses lasers beam back-propagating from the detector to the crystal for aligning all the optics in between, in place of using the beams that will eventually be detected (which of course travel from the crystal to the detectors). This is useful when the target light is invisible because of its frequency and/or low intensity (as in the case of SPDC). The problem is that the alignment cannot be perfect since the beams used for alignment and the target one to be detected do not have exactly the same physical characteristics.

After testing our setup, we realised that the image system creates an image which is too small; on the other hand, the Fourier system makes the momentum distribution too big. Here "*too*" small and "*too*" big refers to the fact that optimally we would like to fill the entire area of the SLM (in order to count on its high-resolution in pixels) but at the same time being careful not to clip part of the beam hitting the edges of the SLM.

The 50/50 BS mentioned in the previous section is only necessary in the 4-photon setup. The 2-photon experiments would benefit from the substitution of the beam splitter with a standard dielectric mirror. The reason is that in the 2-photon case we only couple the reflected beams of signal and idler incident the BS. Using a BS implies that probabilistically the event of signal and idler being *both* reflected happens only in the 25% of the cases. Therefore being able to swap from BM to standard mirror for the two-photon measurements would reduces the losses by 75%.

The last aspect we want to mention regards the nonlinear crystal. To increase the number of spatial modes in the downconverted fields, the easiest approach requires to increase the pump beam waist (some experimental comparisons between SPDC produced by small and large pump beam waists were addressed in the two previous chapters *Spatial entanglement detection using raster scan with a phase-slit* and *Direct detection of the moments of spatial probability distribution*. Also, a plot of the number of spatial modes available as a function of the pump beam waist is shown in 2.6). However, it can happen that the transverse profile of the pump touches the edges of the crystal itself when entering or exiting it, especially when using long nonlinear crystal (our is $20mm$ long). The only company we found producing the crystals that we needed could provide just one transverse size, that is $1 \times 2mm^2$. Using a larger crystal would allow to populate higher spatial modes in the downconverted field as well as facilitate alignment and improve stability of the setup.

7
Conclusions.

The paradox *is only a conflict between reality and your feeling of what reality "ought to be".*

Richard Phillip Feynman

Within this thesis we described the process of designing, engineering and testing of a sophisticated optical setup for the generation and control of quantum light. We built two experiments based on spontaneous parametric down conversion. In both cases we were interested in study the spatial degree of freedom of the generated quantum states as a source of multidimensional entanglement.

The setup is fully functioning and flexible for different kind of measurements and experimental parameters setting such as pump beam waist (small/large), pump laser (CW/pulsed), and pump transverse profile (Gaussian/Hermite-Gaussian). Another form of flexibility is introduced by the use of a spatial light modulator in the detection part. Thanks to its full programmability, we can easily engineer different kind of measurements such as the phase-slit scan presented in chapter 4 and the direct measurement of the moments of the distribution presented in chapter 5.

We elaborated a full characterization of the states produced by our source via bidimensional spatial tomography in position and momentum, highlighting strong correlations in position (see for instance the plots on the left column of Figure 4.7) and anticorrelation in momentum (right column of the same Figure). We also shown that we have control on the correlation, that is we can decide to create correlate or not-correlated photons by simply changing an experimental parameter - which is the pump beam waist in the Gaussian profile configuration. We have shown full experimental control on this important parameter, as we already pointed out in the conclusions drawn in section 4.5, at the end of chapter 4. The same result about the control on spatial correlations has been confirmed with the experimental method of direct measurements of the moments of probability distribution, which is clear when comparing the results presented in the subsections *Small Gaussian pump profile* and *Large Gaussian pump profile* of section 5.4.1.

Thanks to the flexibility in transverse spatial profile of the pump, we could run some study about states produced in SPDC when pumping the crystal with structured light. While the standard experiment uses Gaussian beam profile, employing higher modes can highlight interesting features of the downconverted fields. This peculiar behaviour is nicely addressed by the six plots in Figure 2.7 (simulations). In the third and fourth subsections of section 4.3 we have presented some of the results we had when measuring with the raster-scan method. The spatial profile of the pump was a first-order Hermite-Gaussian (HG) beam. According to the theoretical model for SPDC presented in chapter 2, the trnsverse distribution of the pump is mapped into the transverse distribution of the downconverted fields. The plots in Figures 4.11 show correlations in the real space and anticorrelations in the Fourier space in higher spatial modes of the downconverted fields. By comparing the results obtained for small and large Hermite-Gaussian profiles, we can see that it is not possible to "switch-off" correlations by downsizing the waist of the pump (as we did for the Gaussian pump case). This is an indicator of the stronger entanglement that is possible to create with Hermite-Gaussian fields with respect to the one found in Gaussian modes.

The results presented in chapter 5, in particular in section 5.4.2, are a demonstration of the reliability of the two experimental procedures presented in this thesis. In particular, we have showed that in our setup we have full control on the spatial correlations of the quantum photon produced via SPDC not only in the generation part, but also in the detection. Being able to count on two conceptually different methods for measuring spatial properties of very weak fields is definitely a remarkable strength of our setup. At this regard we have also shown that the direct method is superior to the more standard raster-scan at least under two aspects: the experimental errors are much lower, and the temporal duration of the full measurement is much shorter (couple of hours against 12+ hours for the double-slit scan method). The first aspect is clear when comparing the estimated variances in different experiments (presented in Tables 5.7, 5.6, 5.9, 5.12, and 5.12).

The hot topic and final goal of this thesis has always been the generation of 4-photon states genuinely entangled in a spatial degree of freedom. That is the direction always followed by us, but it has been very hard to conclude in time. Technical issues such as a broken crystal or the need of more sophisticated interference crystals, the need of more stability in the filtering of the pump, the necessity of ordering and testing a new piece of equipment on the go (the spatial light modulator) and other smaller issues slowed down the finalisation of the experimental setup. However, it is now ready for the 4-photon experiments in the sense that it just need to be aligned and tested. While this has been the main limitation for being able to publish any paper from the work done during this PhD project, now the setup is ready to run amazing experiments. One of which, unique in its genre, could be in the direction of investigating 4-photon states by pumping the crystal with Hermite-Gaussian modes.

In conclusion, from the data presented we can draw few important remarks:

I The estimated quantities from the experimental measurements match the values calculated from the theoretical model. This result validates the direct method employed in our setup and justifies its employment in following experiments.

II The two experimental methods provided similar results within the experimental errors. This is an empirical confirmation of the direct method with respect to a more intuitive, more employed one. Furthermore, this result indirectly shows that our own procedure for the phase-slit raster scan is reliable against the theoretical predictions. We also refer to the process data analysis of the result, which is the main difference and fundamental

aspect to take into account when considering a phase-slit with respect to the standard metallic slit.

III The error bars show that the direct method is more accurate. In particular, the uncertainties in the direct method are not proportional to the order of the moment measured as in the case of raster scan. Furthermore, this innovative method is five times faster than the standard double-raster.

IV The two experimental methods have been applied for the first time to Hermite-Gaussian correlations.

V We have full control on both generation and detection of the SPDC photons. This paves the next step, which is starting to detect entanglement in 4-photon states.

7.1 Outlook.

Within this PhD thesis we presented a setup at the forefront for the exploration of spatial properties of entangled photons. Thanks to the elasticity introduced by the utilization of a Spatial Light Modulator on the downconverted fields, the setup is suitable for measuring directly any higher order moment of the spatial probability distribution, both in near and far field. This, in conjunction with the possibility of generating entanglement in higher spatial modes, paves the way to deeper analysis of the spatial properties of the fields generated via SPDC. At this regard we showed the results of measurements in the peculiar experimental conditions of first-order Hermite-Gauss pump beam. However, that is just a starting point towards the exploration of high-dimensional entanglement, and the setup is ready to be pushed to the boundaries.

Even greater expectations are placed in the multipartite genuine entanglement that this setup is capable of. The cutting edge solutions proposed and tested for the 2-photon states, are fully applicable to the states of 4-photon. A full range of innovative experiments in the field of multi-photon *and* multidimensional entangled states can be designed based on our setup.

As an immediate application of the structured states produced by our setup we see several quantum nanophotonics experiments. For instance, the idea of using the already characterized higher modes states (as presented in this thesis) to proceed with our study of the interaction of quantum light with nanoholes, is very straight forward. Furthermore, most of the research ongoing in this field is limited to entangled states of 2-photon. With our setup, one can utilize spatially entangled states of four photons for the same nanophotonic experiments. In our particular case, we will be able to shine some light on the unexpected quantum effects already observed and submitted in the form of a paper written by some components of our research group [52].

References

[1] D. Bouwmeester, J.-W. Pan, K. Mattle, M. Eibl, H. Weinfurter, and A. Zeilinger. *Experimental quantum teleportation*. Nature **390**(6660), 575 (1997).

[2] T. Jennewein, C. Simon, G. Weihs, H. Weinfurter, and A. Zeilinger. *Quantum cryptography with entangled photons*. Physical Review Letters **84**(20), 4729 (2000).

[3] D. Naik, C. Peterson, A. White, A. Berglund, and P. G. Kwiat. *Entangled state quantum cryptography: eavesdropping on the ekert protocol*. Physical Review Letters **84**(20), 4733 (2000).

[4] R. Cleve, D. Gottesman, and H.-K. Lo. *How to share a quantum secret*. Physical Review Letters **83**(3), 648 (1999).

[5] J.-W. Pan, D. Bouwmeester, M. Daniell, H. Weinfurter, and A. Zeilinger. *Experimental test of quantum nonlocality in three-photon greenberger–horne–zeilinger entanglement*. Nature **403**(6769), 515 (2000).

[6] N. D. Mermin. *Extreme quantum entanglement in a superposition of macroscopically distinct states*. Physical Review Letters **65**(15), 1838 (1990).

[7] P. Walther, J.-W. Pan, M. Aspelmeyer, R. Ursin, S. Gasparoni, and A. Zeilinger. *De broglie wavelength of a non-local four-photon state*. Nature **429**(6988), 158 (2004).

[8] M. W. Mitchell, J. S. Lundeen, and A. M. Steinberg. *Super-resolving phase measurements with a multiphoton entangled state*. Nature **429**(6988), 161 (2004).

[9] T. Nagata, R. Okamoto, J. L. O'Brien, K. Sasaki, and S. Takeuchi. *Beating the standard quantum limit with four-entangled photons*. Science **316**(5825), 726 (2007).

[10] P. G. Kwiat, K. Mattle, H. Weinfurter, A. Zeilinger, A. V. Sergienko, and Y. Shih. *New high-intensity source of polarization-entangled photon pairs*. Physical Review Letters **75**(24), 4337 (1995).

[11] H. Weinfurter and M. Żukowski. *Four-photon entanglement from down-conversion*. Physical Review A **64**(1), 010102 (2001).

[12] J.-W. Pan, M. Daniell, S. Gasparoni, G. Weihs, and A. Zeilinger. *Experimental demonstration of four-photon entanglement and high-fidelity teleportation*. Physical Review Letters **86**(20), 4435 (2001).

[13] J. C. Matthews, A. Politi, D. Bonneau, and J. L. O'Brien. *Heralding two-photon and four-photon path entanglement on a chip*. Physical review letters **107**(16), 163602 (2011).

[14] F. Steinlechner, P. Trojek, M. Jofre, H. Weier, D. Perez, T. Jennewein, R. Ursin, J. Rarity, M. W. Mitchell, J. P. Torres, *et al. A high-brightness source of polarization-entangled photons optimized for applications in free space*. Optics express **20**(9), 9640 (2012).

[15] A. Mair, A. Vaziri, G. Weihs, and A. Zeilinger. *Entanglement of the orbital angular momentum states of photons*. Nature **412**(6844), 313 (2001).

[16] H. D. Riedmatten, V. Scarani, I. Marcikic, A. Acín, W. Tittel, H. Zbinden, and N. Gisin. *Two independent photon pairs versus four-photon entangled states in parametric down conversion*. journal of modern optics **51**(11), 1637 (2004).

[17] A. Lamas-Linares, J. C. Howell, and D. Bouwmeester. *Stimulated emission of polarization-entangled photons*. Nature **412**(6850), 887 (2001).

[18] A. Einstein, B. Podolsky, and N. Rosen. *Can quantum-mechanical description of physical reality be considered complete?* Physical review **47**(10), 777 (1935).

[19] J. C. Howell, R. S. Bennink, S. J. Bentley, and R. Boyd. *Realization of the einstein-podolsky-rosen paradox using momentum-and position-entangled photons from spontaneous parametric down conversion*. Physical review letters **92**(21), 210403 (2004).

[20] D. Bohm. *Quantum theory* (Courier Corporation, 1951).

[21] J. S. Bell. *On the einstein podolsky rosen paradox* (1964).

[22] J. S. Bell. *On the problem of hidden variables in quantum mechanics*. Reviews of Modern Physics **38**(3), 447 (1966).

[23] J. F. Clauser, M. A. Horne, A. Shimony, and R. A. Holt. *Proposed experiment to test local hidden-variable theories*. Physical review letters **23**(15), 880 (1969).

[24] M. A. Nielsen and I. L. Chuang. *Quantum computation and quantum information* (Cambridge university press, 2010).

[25] R. Raussendorf and H. J. Briegel. *A one-way quantum computer*. Physical Review Letters **86**(22), 5188 (2001).

[26] X.-L. Wang, L.-K. Chen, W. Li, H.-L. Huang, C. Liu, C. Chen, Y.-H. Luo, Z.-E. Su, D. Wu, Z.-D. Li, *et al. Experimental ten-photon entanglement*. arXiv preprint arXiv:1605.08547 (2016).

[27] B. Lanyon, M. Zwerger, P. Jurcevic, C. Hempel, W. Dür, H. Briegel, R. Blatt, and C. Roos. *Experimental violation of multipartite bell inequalities with trapped ions*. Physical review letters **112**(10), 100403 (2014).

[28] J. Kelly, R. Barends, A. Fowler, A. Megrant, E. Jeffrey, T. White, D. Sank, J. Mutus, B. Campbell, Y. Chen, *et al. State preservation by repetitive error detection in a superconducting quantum circuit*. Nature **519**(7541), 66 (2015).

[29] X.-C. Yao, T.-X. Wang, P. Xu, H. Lu, G.-S. Pan, X.-H. Bao, C.-Z. Peng, C.-Y. Lu, Y.-A. Chen, and J.-W. Pan. *Observation of eight-photon entanglement*. Nature Photonics **6**(4), 225 (2012).

[30] D. M. Greenberger, M. A. Horne, and A. Zeilinger. *Going beyond Bell's theorem*. In *Bell's theorem, quantum theory and conceptions of the Universe*, pp. 69–72 (Springer, 1989).

[31] C. Zhang, Y.-F. Huang, Z. Wang, B.-H. Liu, C.-F. Li, and G.-C. Guo. *Experimental Greenberger-Horne-Zeilinger-type six-photon quantum nonlocality*. Physical review letters **115**(26), 260402 (2015).

[32] R. Jozsa and N. Linden. *On the role of entanglement in quantum-computational speed-up*. In *Proceedings of the Royal Society of London A: Mathematical, Physical and Engineering Sciences*, vol. 459, pp. 2011–2032 (The Royal Society, 2003).

[33] D. Bruß and C. Macchiavello. *Multipartite entanglement in quantum algorithms*. Physical Review A **83**(5), 052313 (2011).

[34] M. Malik, M. Erhard, M. Huber, M. Krenn, R. Fickler, and A. Zeilinger. *Multi-photon entanglement in high dimensions*. Nature Photonics **10**(4), 248 (2016).

[35] A. A. Klyachko, M. A. Can, S. Binicioğlu, and A. S. Shumovsky. *Simple test for hidden variables in spin-1 systems*. Physical review letters **101**(2), 020403 (2008).

[36] R. Lapkiewicz, P. Li, C. Schaeff, N. K. Langford, S. Ramelow, M. Wieśniak, and A. Zeilinger. *Experimental non-classicality of an indivisible quantum system*. Nature **474**(7352), 490 (2011).

[37] C. Schaeff, R. Polster, R. Lapkiewicz, R. Fickler, S. Ramelow, and A. Zeilinger. *Scalable fiber integrated source for higher-dimensional path-entangled photonic qunits*. Optics Express **20**(15), 16145 (2012).

[38] M. Krenn, R. Fickler, M. Huber, R. Lapkiewicz, W. Plick, S. Ramelow, and A. Zeilinger. *Entangled singularity patterns of photons in ince-gauss modes*. Physical Review A **87**(1), 012326 (2013).

[39] R. Fickler, R. Lapkiewicz, W. N. Plick, M. Krenn, C. Schaeff, S. Ramelow, and A. Zeilinger. *Quantum entanglement of high angular momenta*. Science **338**(6107), 640 (2012).

[40] S. Zhao, L. Gong, Y. Li, H. Yang, Y. Sheng, X. Dong, F. Cao, and B. Zheng. *Experimental realization of large-alphabet quantum key distribution protocol using orbital angular momentum entanglement*. arXiv preprint arXiv:1205.0851 (2012).

[41] J. Romero, D. Giovannini, S. Franke-Arnold, S. Barnett, and M. Padgett. *Increasing the dimension in high-dimensional two-photon orbital angular momentum entanglement*. Physical Review A **86**(1), 012334 (2012).

[42] G. Molina-Terriza, J. P. Torres, and L. Torner. *Twisted photons*. Nature Physics **3**(5), 305 (2007).

[43] S. Gröblacher, T. Jennewein, A. Vaziri, G. Weihs, and A. Zeilinger. *Experimental quantum cryptography with qutrits*. New Journal of Physics **8**(5), 75 (2006).

[44] N. J. Cerf, M. Bourennane, A. Karlsson, and N. Gisin. *Security of quantum key distribution using d-level systems*. Physical Review Letters **88**(12), 127902 (2002).

[45] M. Mirhosseini, O. S. Magaña-Loaiza, M. N. O'Sullivan, B. Rodenburg, M. Malik, M. P. Lavery, M. J. Padgett, D. J. Gauthier, and R. W. Boyd. *High-dimensional quantum cryptography with twisted light*. New Journal of Physics **17**(3), 033033 (2015).

[46] M. Huber and J. I. de Vicente. *Structure of multidimensional entanglement in multipartite systems*. Physical review letters **110**(3), 030501 (2013).

[47] M. Malik and R. W. Boyd. *Quantum imaging technologies*. arXiv preprint arXiv:1406.1685 (2014).

[48] A. C. Dada, J. Leach, G. S. Buller, M. J. Padgett, and E. Andersson. *Experimental high-dimensional two-photon entanglement and violations of generalized bell inequalities*. Nature Physics **7**(9), 677 (2011).

[49] M. Krenn, M. Huber, R. Fickler, R. Lapkiewicz, S. Ramelow, and A. Zeilinger. *Generation and confirmation of a (100× 100)-dimensional entangled quantum system*. Proceedings of the National Academy of Sciences **111**(17), 6243 (2014).

[50] A. Büse, N. Tischler, M. L. Juan, and G. Molina-Terriza. *Where are photons created in parametric down-conversion? on the control of the spatio–temporal properties of biphoton states*. Journal of Optics **17**(6), 065201 (2015).

[51] N. Tischler, A. Büese, L. G. Helt, M. L. Juan, N. Piro, J. Ghosh, M. J. Steel, and G. Molina-Terriza. *Measurement and shaping of biphoton spectral wave functions*. Physical review letters **115**(19), 193602 (2015).

[52] A. Büese, M. L. Juan, N. Tischler, F. Sciarrino, L. Marrucci, and G. Molina-Terriza. *Quantum control of photonic entanglement with a single sub-wavelength structure*. In Preparation .

[53] A. Büese. *Quantum interference through plasmonic nanostructures*. PhD Thesis (2016).

[54] H. D. Riedmatten, V. Scarani, I. Marcikic, A. Acín, W. Tittel, H. Zbinden, and N. Gisin. *Two independent photon pairs versus four-photon entangled states in parametric down conversion*. journal of modern optics **51**(11), 1637 (2004).

[55] S. P. Walborn, C. Monken, S. Pádua, and P. S. Ribeiro. *Spatial correlations in parametric down-conversion*. Physics Reports **495**(4), 87 (2010).

[56] A. Tabacchini, M. L. Juan, and G. Molina-Terriza. *Engineering source of multi-photon, multidimensional oam entangled states for quantum control of nanostructures*. In *Research in Optical Sciences*, p. JW2A.64 (Optical Society of America, 2014). URL http://www.osapublishing.org/abstract.cfm?URI=QIM-2014-JW2A.64.

[57] W. Löffler, M. J. de Dood, and B. Hiesmayr. *Transverse-mode entanglement of four photons*. In *Research in Optical Sciences*, p. QW4A.4 (Optical Society of America, 2014). URL http://www.osapublishing.org/abstract.cfm?URI=QIM-2014-QW4A.4.

[58] B. Hiesmayr, M. de Dood, and W. Löffler. *Observation of four-photon orbital angular momentum entanglement*. Physical review letters **116**(7), 073601 (2016).

[59] M. Hor-Meyll, J. de Almeida, G. Lemos, P. S. Ribeiro, and S. Walborn. *Ancilla-assisted measurement of photonic spatial correlations and entanglement*. Physical review letters **112**(5), 053602 (2014).

[60] W. Heisenberg. *Über den anschaulichen inhalt der quantentheoretischen kinematik und mechanik*. Zeitschrift für Physik **43**(3-4), 172 (1927).

[61] N. Mott and R. Peierls. *Werner Heisenberg. 5 december 1901–1 february 1976*. Biographical Memoirs of Fellows of the Royal Society **23**, 213 (1977).

[62] E. P. Tryon. *Is the universe a vacuum fluctuation?* Nature **246**, 396 (1973).

[63] C. Law and J. Eberly. *Analysis and interpretation of high transverse entanglement in optical parametric down conversion*. Physical review letters **92**(12), 127903 (2004).

[64] C. Hong and L. Mandel. *Theory of parametric frequency down conversion of light*. Physical Review A **31**(4), 2409 (1985).

[65] L. Wang. Ph.D. thesis, University of Rocghester (1992).

[66] R. W. Boyd. *Nonlinear optics, 3rd* (2008).

[67] R. Loudon. *The quantum theory of light* (OUP Oxford, 2000).

[68] P. N. Butcher and D. Cotter. *The elements of nonlinear optics*, vol. 9 (Cambridge university press, 1991).

[69] N. Bloembergen. *Nonlinear optics* (World Scientific, 1996).

[70] Y.-R. Shen. *Principles of nonlinear optics* (1984).

[71] L. Mandel and E. Wolf. *Optical coherence and quantum optics* (Cambridge university press, 1995).

[72] B. E. Saleh, M. C. Teich, and B. E. Saleh. *Fundamentals of photonics*, vol. 22 (Wiley New York, 1991).

[73] J. Goodman. *Introduction to fourier optics, mcgaw-hill physical and quantum electronics series* (1968).

[74] M. Born and E. Wolf. *Principles of optics: electromagnetic theory of propagation, interference and diffraction of light* (CUP Archive, 2000).

[75] D. Stoler. *Operator methods in physical optics*. JOSA **71**(3), 334 (1981).

[76] D. Marcuse. *Light transmission optics* (1972).

[77] C. H. Monken, P. S. Ribeiro, and S. Pádua. *Transfer of angular spectrum and image formation in spontaneous parametric down-conversion*. Physical Review A **57**(4), 3123 (1998).

[78] H. D. L. Pires and M. van Exter. *Near-field correlations in the two-photon field*. Physical Review A **80**(5), 053820 (2009).

[79] E. Gómez, W. Nogueira, C. Monken, and G. Lima. *Quantifying the non-gaussianity of the state of spatially correlated down-converted photons*. Optics express **20**(4), 3753 (2012).

[80] S. Straupe, D. Ivanov, A. Kalinkin, I. Bobrov, and S. Kulik. *Angular schmidt modes in spontaneous parametric down-conversion*. Physical Review A **83**(6), 060302 (2011).

[81] K. Chan, J. Torres, and J. Eberly. *Transverse entanglement migration in hilbert space*. Physical Review A **75**(5), 050101 (2007).

[82] D. Tasca, S. Walborn, P. S. Ribeiro, and F. Toscano. *Detection of transverse entanglement in phase space*. Physical Review A **78**(1), 010304 (2008).

[83] D. Tasca, S. Walborn, P. S. Ribeiro, F. Toscano, and P. Pellat-Finet. *Propagation of transverse intensity correlations of a two-photon state*. Physical Review A **79**(3), 033801 (2009).

[84] S. Walborn, D. Ether, R. de Matos Filho, and N. Zagury. *Quantum teleportation of the angular spectrum of a single-photon field*. Physical Review A **76**(3), 033801 (2007).

[85] L. Zhang, L. Neves, J. S. Lundeen, and I. A. Walmsley. *A characterization of the single-photon sensitivity of an electron multiplying charge-coupled device*. Journal of Physics B: Atomic, Molecular and Optical Physics **42**(11), 114011 (2009).

[86] S. Walborn, S. Pádua, and C. Monken. *Conservation and entanglement of hermite-gaussian modes in parametric down-conversion*. Physical Review A **71**(5), 053812 (2005).

[87] S. Walborn and C. Monken. *Transverse spatial entanglement in parametric down-conversion*. Physical Review A **76**(6), 062305 (2007).

[88] F. M. Miatto, T. Brougham, and A. M. Yao. *Cartesian and polar schmidt bases for down-converted photons*. The European Physical Journal D **66**(7), 1 (2012).

[89] M. Van Exter, A. Aiello, S. Oemrawsingh, G. Nienhuis, and J. Woerdman. *Effect of spatial filtering on the schmidt decomposition of entangled photons*. Physical Review A **74**(1), 012309 (2006).

[90] R. Gomes, A. Salles, F. Toscano, P. S. Ribeiro, and S. Walborn. *Quantum entanglement beyond gaussian criteria*. Proceedings of the National Academy of Sciences **106**(51), 21517 (2009).

[91] P. G. Kwiat. *Hyper-entangled states*. Journal of modern optics **44**(11-12), 2173 (1997).

[92] M. Atatüre, G. Di Giuseppe, M. D. Shaw, A. V. Sergienko, B. E. Saleh, and M. C. Teich. *Multiparameter entanglement in femtosecond parametric down-conversion*. Physical Review A **65**(2), 023808 (2002).

[93] E. Schmidt. *Zur theorie der linearen und nichtlinearen integralgleichungen. i. teil: Entwicklung willkÃijrlicher funktionen nach systemen vorgeschriebener*. Mathematische Annalen **63**, 433 (1907). URL http://eudml.org/doc/158296.

[94] G. Stewart. *Fredholmf, Hilbert, Schmidth three fundamental papers on integral equations translated with commentary by G.W. Stewart* (2014).

[95] M. Fedorov and N. Miklin. *Schmidt modes and entanglement*. Contemporary Physics **55**(2), 94 (2014).

[96] H. Huang and J. Eberly. *Correlations and one-quantum pulse shapes in photon pair generation*. Journal of Modern Optics **40**(5), 915 (1993).

[97] R. Grobe, K. Rzazewski, and J. Eberly. *Measure of electron-electron correlation in atomic physics*. Journal of Physics B: Atomic, Molecular and Optical Physics **27**(16), L503 (1994).

[98] A. Ekert and P. L. Knight. *Entangled quantum systems and the schmidt decomposition*. American Journal of Physics **63**(5), 415 (1995).

[99] A. Pathak. *Elements of quantum computation and quantum communication* (Taylor & Francis, 2013).

[100] A. Peres. *Quantum theory: concepts and methods*, vol. 57 (Springer Science & Business Media, 2006).

[101] E. Shchukin and W. Vogel. *Inseparability criteria for continuous bipartite quantum states*. Physical review letters **95**(23), 230502 (2005).

[102] A. Peres. *Separability criterion for density matrices*. Physical Review Letters **77**(8), 1413 (1996).

[103] M. Horodecki, P. Horodecki, and R. Horodecki. *Separability of mixed states: necessary and sufficient conditions*. Physics Letters A **223**(1), 1 (1996).

[104] P. Horodecki. *Separability criterion and inseparable mixed states with positive partial transposition*. arXiv preprint quant-ph/9703004 (1997).

[105] L.-M. Duan, G. Giedke, J. I. Cirac, and P. Zoller. *Inseparability criterion for continuous variable systems*. Physical Review Letters **84**(12), 2722 (2000).

[106] R. Simon. *Peres-Horodecki separability criterion for continuous variable systems*. Physical Review Letters **84**(12), 2726 (2000).

[107] S. Mancini, V. Giovannetti, D. Vitali, and P. Tombesi. *Entangling macroscopic oscillators exploiting radiation pressure*. Physical review letters **88**(12), 120401 (2002).

[108] P. Hyllus and J. Eisert. *Optimal entanglement witnesses for continuous-variable systems*. New Journal of Physics **8**(4), 51 (2006).

[109] D. McCoy and M. Arrigoni. *Peak power in non-linear microscopy: Unraveling the rhetoric*. https://www.coherent.com/lasers/laser/chameleon-family/chameleon-ultra-family .

[110] G. Lima, A. Vargas, L. Neves, R. Guzmán, and C. Saavedra. *Manipulating spatial qudit states with programmable optical devices*. Optics Express **17**(13), 10688 (2009).

[111] D. Tasca, R. Gomes, F. Toscano, P. S. Ribeiro, and S. Walborn. *Continuous-variable quantum computation with spatial degrees of freedom of photons*. Physical Review A **83**(5), 052325 (2011).

[112] J. Leach, B. Jack, J. Romero, A. K. Jha, A. M. Yao, S. Franke-Arnold, D. G. Ireland, R. W. Boyd, S. M. Barnett, and M. J. Padgett. *Quantum correlations in optical angle–orbital angular momentum variables*. Science **329**(5992), 662 (2010).

[113] V. D'Ambrosio, F. Cardano, E. Karimi, E. Nagali, E. Santamato, L. Marrucci, and F. Sciarrino. *Test of mutually unbiased bases for six-dimensional photonic quantum systems*. arXiv preprint arXiv:1304.4081 (2013).

[114] J. Romero, D. Giovannini, D. Tasca, S. Barnett, and M. Padgett. *Tailored two-photon correlation and fair-sampling: a cautionary tale*. New Journal of Physics **15**(8), 083047 (2013).

[115] M. L. Jepsen. *A technology rollercoaster: Liquid crystal on silicon*. Nature Photonics **1**(5), 276 (2007).

[116] M. Zukowski, A. Zeilinger, M. Horne, and A. Ekert. *"event-ready-detectors" Bell experiment via entanglement swapping*. Physical Review Letters **71**(26), 4287 (1993).

[117] S. Friberg, C. Hong, and L. Mandel. *Measurement of time delays in the parametric production of photon pairs*. Physical review letters **54**(18), 2011 (1985).

[118] E. Hecht. *Optics, 4th*. International edition, Addison-Wesley, San Francisco **3** (2002).

[119] M. DâĂŹAngelo, Y.-H. Kim, S. P. Kulik, and Y. Shih. *Identifying entanglement using quantum ghost interference and imaging*. Physical review letters **92**(23), 233601 (2004).

[120] G. A. Howland and J. C. Howell. *Efficient high-dimensional entanglement imaging with a compressive-sensing double-pixel camera*. Physical review X **3**(1), 011013 (2013).

[121] F. Just, A. Cavanna, M. V. Chekhova, and G. Leuchs. *Transverse entanglement of biphotons*. New Journal of Physics **15**(8), 083015 (2013).

[122] M. P. Edgar, D. S. Tasca, F. Izdebski, R. E. Warburton, J. Leach, M. Agnew, G. S. Buller, R. W. Boyd, and M. J. Padgett. *Imaging high-dimensional spatial entanglement with a camera*. Nature communications **3**, 984 (2012).

[123] D. S. Tasca, M. P. Edgar, F. Izdebski, G. S. Buller, and M. J. Padgett. *Optimizing the use of detector arrays for measuring intensity correlations of photon pairs*. Physical Review A **88**(1), 013816 (2013).

[124] R. S. Aspden, D. S. Tasca, R. W. Boyd, and M. J. Padgett. *Epr-based ghost imaging using a single-photon-sensitive camera*. New Journal of Physics **15**(073032), 073032 (2013).

[125] A. F. Abouraddy, M. Nasr, B. E. Saleh, A. V. Sergienko, and M. C. Teich. *Demonstration of the complementarity of one-and two-photon interference*. Physical Review A **63**(6), 063803 (2001).

[126] R. Fickler, M. Krenn, R. Lapkiewicz, S. Ramelow, and A. Zeilinger. *Real-time imaging of quantum entanglement*. Scientific reports **3** (2013).

[127] E. Paul, M. Hor-Meyll, P. S. Ribeiro, and S. Walborn. *Measuring spatial correlations of photon pairs by automated raster scanning with spatial light modulators*. Scientific reports **4** (2014).

[128] A. Abouraddy, G. Di Giuseppe, T. Yarnall, M. Teich, and B. Saleh. *Implementing one-photon three-qubit quantum gates using spatial light modulators*. Physical Review A **86**(5), 050303 (2012).

[129] J. Schneeloch, P. B. Dixon, G. A. Howland, C. J. Broadbent, and J. C. Howell. *Violation of continuous-variable einstein-podolsky-rosen steering with discrete measurements*. Physical review letters **110**(13), 130407 (2013).

[130] D. Tasca, Ł. Rudnicki, R. Gomes, F. Toscano, and S. Walborn. *Reliable entanglement detection under coarse-grained measurements*. Physical review letters **110**(21), 210502 (2013).

[131] S. Walborn, F. Toscano, *et al. Heisenberg uncertainty relation for coarse-grained observables*. EPL (Europhysics Letters) **97**(3), 38003 (2012).

[132] S. Machado, P. Milman, and S. Walborn. *Interferometric scheme for direct measurement of moments of transverse spatial variables of photons*. Physical Review A **87**(5), 053834 (2013).

[133] P. B. Dixon, G. A. Howland, J. Schneeloch, and J. C. Howell. *Quantum mutual information capacity for high-dimensional entangled states*. Physical review letters **108**(14), 143603 (2012).

[134] S. L. Braunstein and P. Van Loock. *Quantum information with continuous variables*. Reviews of Modern Physics **77**(2), 513 (2005).

[135] G. Adesso and F. Illuminati. *Entanglement in continuous-variable systems: recent advances and current perspectives*. Journal of Physics A: Mathematical and Theoretical **40**(28), 7821 (2007).

[136] H. M. Ozaktas, Z. Zalevsky, and M. A. Kutay. *The fractional Fourier transform* (Wiley, Chichester, 2001).

[137] G. B. Lemos, J. de Almeida, S. Walborn, P. S. Ribeiro, and M. Hor-Meyll. *Characterization of a spatial light modulator as a polarization quantum channel*. Physical Review A **89**(4), 042119 (2014).

[138] T. M. Cover and J. A. Thomas. *Elements of information theory* (John Wiley & Sons, 2012).

[139] A. J. van der Torren, S. C. Yorulmaz, J. J. Renema, M. P. van Exter, and M. J. de Dood. *Spatially entangled four-photon states from a periodically poled potassium-titanyl-phosphate crystal*. Physical Review A **85**(4), 043837 (2012).